

University of Southampton Research Repository  
ePrints Soton

Copyright © and Moral Rights for this thesis are retained by the author and/or other copyright owners. A copy can be downloaded for personal non-commercial research or study, without prior permission or charge. This thesis cannot be reproduced or quoted extensively from without first obtaining permission in writing from the copyright holder/s. The content must not be changed in any way or sold commercially in any format or medium without the formal permission of the copyright holders.

When referring to this work, full bibliographic details including the author, title, awarding institution and date of the thesis must be given e.g.

AUTHOR (year of submission) "Full thesis title", University of Southampton, name of the University School or Department, PhD Thesis, pagination

**UNIVERSITY OF SOUTHAMPTON**

**FACULTY OF ENGINEERING, SCIENCE &  
MATHEMATICS**

**OPTOELECTRONICS RESEARCH CENTRE**

**Thiolate self-assembled monolayers  
studied with a Tuneable Infrared Low  
Temperature Laser Driven Scanning  
Tunnelling Microscope**

by

**Howard John Millman**

A thesis submitted to the University of Southampton  
for the degree of Doctor of Philosophy.

September 2005

UNIVERSITY OF SOUTHAMPTON

ABSTRACT

FACULTY OF ENGINEERING, SCIENCE AND MATHEMATICS  
OPTOELECTRONICS RESEARCH CENTRE

Doctor of Philosophy

Thiolate self-assembled monolayers studied with a Tuneable Infrared Low  
Temperature Laser Driven Scanning Tunnelling Microscope.

By Howard John Millman

This work describes the investigation of self-assembled monolayers (SAMs) with scanning tunnelling microscopy/spectroscopy (STM/S) and infrared laser-driven STM (LDSTM). As a tool STM is uniquely able to resolve atoms on a surface. Illuminating an STM with infrared radiation tuned to match modes in the SAM used as the sample provides a unique opportunity to investigate the combination of the well understood character of organic molecules with the atomic scale resolution of an STM.

SAMs were prepared with octanethiol and dimethyl disulphide on Au(111) substrates. STM images and STS spectra of these samples recorded at 78K are presented. Typical surface features are observed in the octanethiolate monolayers. The results of STS experiments with an octanethiolate monolayer reveal correlations between surface features and conductivity at -1.0V. The differences between these STS data and equivalents from uncoated samples reveal the effect of the molecules upon the electronic surface states of the samples. Images of samples prepared with dimethyl disulphide show previously unseen low density structures and individual molecules scattered across the surface. Correlations are made between these low density structures and the reconstruction of the underlying gold surface. Comparisons with previously calculated models are used to identify these isolated molecules. STS data collected across a section of sample show how topography data can be used to categorise STS data.

The response of the laser-STM interaction to the laser modulation is presented and compared with that of the STM alone. The modulation of the tunnelling current is found to be proportional to the equilibrium tunnelling current which is consistent with theoretical models. This response of the laser-STM interaction to the laser modulation frequency was found to differ between Au(111) substrates uncoated and coated with a methylthiolate SAM. Correlations were observed between the frequency response of the laser-STM interaction and the STS data.

## DECLARATION OF AUTHORSHIP

I, **HOWARD JOHN MILLMAN** declare that the thesis entitled:

“Thiolate self-assembled monolayers studied with a Tuneable Infrared Low Temperature Laser Driven Scanning Tunnelling Microscope”

and the work presented in it, are my own.

I confirm that:

- this work was done wholly or mainly while in candidature for a research degree at this University;
- where any part of this thesis has previously been submitted for a degree or any other qualification at this University or any other institution, this has been clearly stated;
- where I have consulted the published work of others, this is always clearly attributed;
- where I have quoted from the work of others, the source is always given. With the exception of such quotations, this thesis is entirely my own work;
- I have acknowledged all main sources of help;
- where the thesis is based on work done by myself jointly with others, I have made clear exactly what was done by others and what I have contributed myself;
- none of this work has been published before submission.

Signed: .....

Date: 7<sup>th</sup> September 2005

## Acknowledgements

Despite only having one name on the cover, this thesis would not have been possible without the input of others whose assistance has been invaluable.

Firstly a huge thanks to Dr. Naruo Yoshikawa who enabled this project to progress much faster than it otherwise might have and taught me virtually everything I know about UHV systems. Thanks to Dr. Peter Stone for starting the work with the LTSTM and getting us up to speed with its operation. Thanks to Dr. Lefteris Danos for assisting me in starting the work with the OPO and to Dr. Martin O'Connor for his insightful advice.

A big thanks to Dr. Bill Brocklesby and Dr. Jeremy Frey for coming up with the crazy idea to do this and keeping watchful eyes over the whole project. Thanks to the EPSRC for paying for all of this.

Thanks to Prof. Brian Hayden and the various past and present members of his group for advice and assistance in the laboratory and all things UHV related. Specifically thanks to Dr. Mike Rendall for teaching me everything else about UHV that Dr. Yoshikawa did not and for various IT skills that I have found invaluable; thanks to D. Scott Bazley and Ben Wilkinson for their assistance in manhandling the LTSTM and thanks to Duncan Smith for the use of the infrared camera which made beam alignment a lot less painful.

Huge thanks to Jamie Robinson and Kieron Taylor for their programming knowledge and assistance. I owe you several instances of \$BEVERAGE. Thanks to Esther Rousay and Adrian Wiley for the Perl script to generate Figure 1.1.

Thanks to my family for starting me off on this journey of scientific discovery and being there along the way. Thanks to Suzanne Elliman for allowing me the time to finish this work.

Finally the greatest thanks must go to יהָנָן, his Son and the Holy Spirit without whom there would not be this complicated world to investigate and explore, and no-one to investigate it.

## Abbreviations

AC	-	alternating current
AFM	-	atomic force microscope/microscopy
BCC	-	body centred cubic
DC	-	direct current
DMDS	-	dimethyl disulphide
FCC	-	face centred cubic
FEG-SEM	-	field emission gun scanning electron microscope
FTIR	-	Fourier transform infrared (spectroscopy)
HOPG	-	highly oriented pyrolytic graphite
IETS	-	inelastic tunnelling spectroscopy
LDAFM	-	laser driven atomic force microscope/microscopy
LDSTM	-	laser driven scanning tunnelling microscope/microscopy
LEED	-	low energy electron diffraction
LTSTM	-	low temperature scanning tunnelling microscope/microscopy
OPO	-	optical parametric oscillator
SAM(s)	-	self-assembled monolayer(s)
SEM	-	scanning electron microscope/microscopy
SNOM	-	scanning near field microscope/microscopy
SPM	-	scanning probe microscope/microscopy
STM	-	scanning tunnelling microscope/microscopy
STS	-	scanning tunnelling spectroscopy
TISE	-	time-independent Schrödinger equation
TSP	-	titanium sublimation pump
UHV	-	ultra-high vacuum
WKB	-	Wentzel, Kramers and Brillouin
XPS	-	X-ray photoelectron spectroscopy

# Contents

<b>Acknowledgements</b>	<b>iv</b>
<b>Abbreviations</b>	<b>v</b>
<b>Contents</b>	<b>vi</b>
<b>List of Figures</b>	<b>x</b>
<b>1 Chapter 1: Introduction</b>	<b>1</b>
1.1 Chapter Introduction	2
1.2 Overview of the Work	5
1.3 Outline of Thesis	5
1.3.1 Chapter 1: Introduction	5
1.3.2 Chapter 2: Technologies and Techniques Used	5
1.3.3 Chapter 3: Scanning Tunnelling Microscopy Tips	6
1.3.4 Chapter 4: Au(111) Samples	6
1.3.5 Chapter 5: Thiol Self-Assembled Monolayers	7
1.3.6 Chapter 6: Laser Driven Scanning Tunnelling Microscopy Experiments	7
1.3.7 Conclusions	7
1.4 References	8
<b>2 Chapter 2: Techniques and Technologies Used</b>	<b>10</b>
2.1 Chapter Introduction	11
2.2 Scanning Tunnelling Microscopy	11
2.2.1 A Brief History	11
2.2.2 An Overview of STM	13
2.2.3 A Theoretical Approach	14
2.2.3.1 The Rectangular Barrier	15
2.2.3.2 The Barrier Height (Workfunction)	19
2.2.3.3 The WKB Model	21
2.2.3.4 The Tersoff and Hamann Model	24
2.2.4 STM Spectroscopy	28
2.2.5 STM Equipment	34
2.2.5.1 Low Temperature Ultra High Vacuum STM	35

2.2.5.2	Tip Manufacture	42
2.3	Optical Parametric Oscillators	45
2.3.1	Overview	45
2.3.2	Background & Theory	46
2.3.3	Specific Details of the OPO Used for This Work	50
2.4	Self-Assembled Monolayers	57
2.5	Laser-Driven Scanning Tunnelling Microscopy (LDSTM)	60
2.5.1	Thermal Effects	61
2.5.2	Other LDSTM Responses	64
2.6	Chapter Summary	66
2.7	References	66
<b>3</b>	<b>Chapter 3: The Manufacture and Imaging of Scanning Tunnelling Microscopy Tips</b>	<b>74</b>
3.1	Chapter Introduction	75
3.2	Experimental Methods Used	75
3.3	Results and Discussion	76
3.3.1	Optical Microscope Images of STM Tips	76
3.3.1.1	Tungsten Tips Etched with Alternating Current	76
3.3.1.2	Tungsten Tips Etched with Direct Current	79
3.3.2	FEG-SEM images of STM tips.	81
3.3.3	STM Images Produced With Etched STM Tips	85
3.4	Conclusions and Future Work	86
3.5	References	87
<b>4</b>	<b>Chapter 4: Au(111) Surfaces</b>	<b>90</b>
4.1	Chapter Introduction	91
4.2	Preparing Au(111) Surfaces	91
4.2.1	Experimental Method	91
4.2.2	Results and Discussion	93
4.3	Spectroscopy of Au(111) Surfaces	96
4.3.1	Experimental Methods	96
4.3.2	Results and Discussion	97
4.4	Conclusions	100
4.5	Further Work	101
4.6	References	102

<b>5</b>	<b>Chapter 5 Thiols on Au(111) Surfaces</b>	<b>104</b>
5.1	Chapter Introduction	105
5.2	Octanethiol on Au(111)	106
5.2.1	Preparation of Octanethiol Self-Assembled Monolayers	106
5.2.1.1	Experimental Method	106
5.2.1.2	Results and Discussion	107
5.2.2	Spectroscopy Experiments with Octanethiol on Au(111)	113
5.2.2.1	Experimental Methods	113
5.2.2.2	Results and Discussion	114
5.3	Dimethyl Disulphide on Au(111)	121
5.3.1	Preparation of Dimethyl Disulphide	
	Self-Assembled Monolayers	121
5.3.1.1	Experimental Method	121
5.3.1.2	Results and Discussion	123
5.3.2	Spectroscopy Experiments	
	of Dimethyl Disulphide on Au(111)	129
5.3.2.1	Topographically Varying	
	Scanning Tunnelling Spectroscopy	130
5.3.2.1.1	Experimental Method	130
5.3.2.1.2	Results and Discussion	130
5.3.2.2	Scanning Tunnelling Spectroscopy	
	Conducted on a Complete Monolayer	133
5.3.2.2.1	Experimental Method	133
5.3.2.2.2	Results and Discussion	133
5.4	Conclusions	136
5.5	Future Work	139
5.6	References	140
<b>6</b>	<b>Chapter 6: Laser Driven Scanning Tunnelling Microscopy</b>	<b>142</b>
6.1	Chapter Introduction	143
6.2	Experimental Methods	143
6.2.1	General Principles	143
6.2.2	Specific Procedures Used	146
6.2.2.1	Laser Modulation Frequency	148
6.2.2.2	STM Electronics	148

6.2.2.3	Tunnelling Current	149
6.2.2.4	Applied Tunnelling Voltage	150
6.2.2.5	Laser Wavelength	150
6.2.2.6	Chemical Nature of the Sample	150
6.2.2.7	Surface Topography	150
6.3	Results and Discussion	151
6.3.1	Laser Modulation Frequency and Applied Tunnelling Voltage	151
6.3.2	STM Electronics	153
6.3.3	Tunnelling Current	155
6.3.4	Chemical Nature of the Sample	157
6.3.5	Laser Wavelength	158
6.4	Conclusions and Future Work	160
6.5	References	163
<b>7</b>	<b>Chapter 7: Conclusions</b>	<b>165</b>
7.1	References	169
<b>A</b>	<b>Appendix A: Manufacture of STM Tips</b>	<b>171</b>
<b>B</b>	<b>Appendix B: Etching Circuit Diagrams</b>	<b>173</b>
<b>C</b>	<b>Appendix C: Microscope Images of the PPLN OPO Crystals</b>	<b>175</b>
<b>D</b>	<b>Appendix D: MATLAB® Code for Processing Topographically Varying Scanning Tunnelling Spectroscopy Data</b>	<b>176</b>
<b>E</b>	<b>Appendix E: MATLAB® Code for Processing Scanning Tunnelling Spectroscopy Data</b>	<b>203</b>

## List of Figures

Figure	Caption	Page
1.1	An example a self-assembled monolayer of methanethiolate on gold. This cartoon is based upon a unit cell by De Renzi et al.[6] used for calculating the positions of the thiolate species on the surface.	3
2.1	Schematic of the tunnelling set-up. A very sharp metal tip is positioned very close to the surface and a voltage is applied between the two, as the tip is raster scanned across the surface whilst the current is measured.	13
2.2	Illustrating the simple case of tunnelling through a rectangular shaped barrier. The electron is considered to travel from the left to the right along the $x$ axis. Between $x = 0$ and $x = L$ there is a potential barrier with a height of energy $V_0$ .	15
2.3	Showing a wavefunction tunnelling through a barrier of arbitrary shape. This scenario can be described with the WKB model but only if the electron energy is not near the height of the barrier.	21
2.4	The WKB approximation can be made to work when the electron energy is close to the barrier height if a linear barrier is used. Removing the restriction on the electron energy comes at a cost of only being able to use a barrier with a linear shape.	21
2.5	Typical relative sizes of $5d_{z^2}$ and $6s$ orbitals in atoms in the tip. Doyen suggests that the radius of the $6s$ orbital is too large to explain the atomic resolution seen in some STM images.	27
2.6	Schematic STS curves showing how they are affected by a vibrational mode on a surface. The gradient of the $I$ vs. $V$ curve increases when the electron energy matches the energy of the vibrational mode. Such a change in the $I$ vs. $V$ curve will lead to $\frac{dI}{dV}$ vs. $V$ and $\frac{d^2I}{dV^2}$ vs. $V$ curves with shapes as shown. The symmetry of these curves is due to the fact that the interaction of the mode with the tunnelling electrons is independent of the	30

	direction of the electrons across the tunnelling junction.	
2.7	This is a copy of the $I$ vs. $V$ curve from Figure 5.30 that is used as an example of how the number of measurements recorded is adequate to lower the signal to noise ratio.	32
2.8	A stylised diagram showing some of the components of the LTSTM.	35
2.9	Photograph of the STM head unit. The piezoelectric stack is in the centre of the image. A tip holder (with tip) would sit on top of it in the place marked by the blue dot. The silver vertical rods to the left, right and rear (obscured) can be lowered such that the head detaches from the inner cryostat at the places marked with the blue line and becomes suspended on springs.	36
2.10	A schematic diagram showing how the various electronic components used for the STS experiments are connected together.	39
2.11	A highly stylised plan of the rig. Descriptions of the numbered components are included in the text.	40
2.12	Showing how the thermocouple and resistive heater are used with the manipulator arm to gently heat samples. The shaded cylinder represents the screw thread which can be moved in the direction shown by the arrow to raise and lower the resistive heater (dark loop protruding from the cylinder) and the thermocouple wire (thin line protruding from the cylinder). The loop of resistive heating wire is narrow enough to fit between the two parallel tungsten rods. (This figure is based upon Figure 20 from the Multiprobe® Surface Science Systems User's Guide Version 1.5, OMICRON Vakuumphysik GmbH. Used with permission.)	41
2.13	Diagram of the AC tip etching apparatus.	43
2.14	Close-up photograph of the beaker, tungsten ring and wire, shown in the previous Figure showing how the wire is positioned with respect to the ring.	43
2.15	A schematic diagram of the apparatus used for DC etching.	44
2.16	Showing the plastic beaker and smaller stainless ring used for DC etching.	45

2.17	Comparing the power output from a non-linear parametric process with different types of phasematching.	48
2.18	Stylised representation of a mask used for the poling of a lithium niobate crystal. Here are shown three sets of gratings each with a different period spacing to provide a tuning capability for the OPO. This mask would be placed on the side of a lithium niobate crystal and a high voltage applied across the crystal through the mask.	49
2.19	This is a stylised representation of the top grating in a Periodically Poled Lithium Niobate (PPLN) crystal made with the above mask and viewed from above. The arrows and shading indicate the orientation of the optical axis in the crystal.	49
2.20	Schematic showing the layout of the OPO	51
2.21	Photograph of the OPO used in this work. The coloured arrows show the paths of the different beams travelling through the OPO. The green arrows correspond to the path of the incident pump beam. The blue arrows as in Figure 2.19 show the path of the signal photons though the cavity. The orange arrow shows the path of the output beam from the OPO which contains components at several wavelengths	51
2.22	Showing how by using different gratings in PPLN crystal 1 at different temperatures the OPO can emit a wide range of wavelengths.	53
2.22	Showing how by using different gratings in PPLN crystal 2 at different temperatures the OPO can emit a wide range of wavelengths.	53
2.24	This shows how the OPO beam leaves the OPO and is manipulated before being passed through to the STM. The details of the numbered components are described in the text.	56
2.25	A stylised representation of octanethiol molecules lying flat on an Au surface at low surface coverage. The diagonal zigzag lines are the carbon chains, the yellow S's are the sulphur atoms and the horizontal wavy line is the metal surface.	59

3.1	Showing three AC etched tips with a well formed tip cone. (The top right image is a higher magnification image of the tip in the top left.) (Scales are in microns.)	77
3.2	Examples of AC etched macroscopic double tips. (Scale is in microns.)	77
3.3	AC manufactured tips showing changes in the tip angle part way down the tip cone. (Scales are in microns.)	78
3.4	An example of an AC etched tip with a multi-step tip shape. (Scale is in microns.)	78
3.5	Two blunt DC etched tips. (Scales are in microns.)	80
3.6	Three examples of tips exhibiting a 'neck' due to incomplete etching. (The bottom right image is a magnified section from the bottom left image.) (Scales are in microns.)	80
3.7	Four images of tips with good microscopic shape. (Scales are in microns.) The lower right image is a higher magnification image of the tip in the lower left image. The tip in these lower images was not treated with HF(aq) after etching. The deposits on the side of the tip are oxide and hydroxide by-products from the etching process. Higher magnification images of this tip are shown in Figure 3.16 to Figure 3.18. Despite the presence of contaminants on this last tip these show the microscopic consistency of the DC etching process.	81
3.8	Three examples of AC etched tips. They show the variation possible between tips produced by the same AC etching method.	82
3.9	This shows a larger scale image of the same type of tip as in the previous Figure.	82
3.10	A typical DC etched tip.	82
3.11	A more detailed image of the tip shown in the previous Figure.	82
3.12	A second example of a DC etched tip showing the consistency of the ball shaped end between different tips.	83
3.13	An example of a good DC etched tip that does not have a 'ball-shaped' end.	83
3.14	Another image of a DC etched tip showing the profile of the tip.	83

	Note how on this scale the circumference of the wire seems rough compared to the profile of the tip.	
3.15	A higher magnification image of the tip in the previous Figure showing that it does not have a 'ball-shaped' end.	83
3.16	A DC etched tip showing the presence of (hydr)oxide on part of its base.	84
3.17	A higher magnification image of the tip shown in the previous Figure.	84
3.18	The end of the tip shown in the previous Figure. The presence of a DC etched tip can be seen buried underneath the thick (hydr)oxide coating.	85
3.19	A $10.0\text{nm} \times 9.82\text{nm}$ image of an Au(111) surface recorded with an AC etched tip at 78K, showing a section of herringbone reconstruction.	85
3.20	A $5\text{nm} \times 5\text{nm}$ enlarged area of the surface shown in Figure 3.19 showing the individual gold atoms on the surface demonstrating that atomic resolution can be achieved with an AC etched tip. (STM parameters: $U_{gap} = 1\text{V}$ , $I = 0.2\text{nA}$ )	86
3.21	A $4.00\text{nm} \times 4.00\text{nm}$ atomic resolution STM image of an Au(111) surface recorded at 78K with a DC etched tip. (STM parameters: $U_{gap} = 79.6\text{mV}$ , $I = 1.9\text{nA}$ )	86
3.22	A $20\text{nm} \times 20\text{nm}$ image of another Au(111) surface. This was imaged with a DC etched tip at 78K and shows (a modified version of) the herringbone reconstruction. (STM parameters: $U_{gap} = 99\text{mV}$ , $I = 10.5\text{nA}$ )	86
4.1	A $400\text{nm} \times 400\text{nm}$ STM image of an Au sample, which was prepared by annealing with $\text{H}_2/\text{O}_2$ flame without removing it from the flame. The structure shown in this image is typical of all images recorded from this sample and shows the amalgamation of smaller microcrystalline regions into a larger one indicating that this method of preparation does not produce good Au(111) structure. (STM parameters: $U_{gap} = 0.1\text{V}$ , $I = 0.13\text{nA}$ )	93
4.2	A $5\mu\text{m} \times 5\mu\text{m}$ topographical AFM image of an Au sample before	94

annealing, showing a nanocrystalline structure.	
4.3 A $5\mu\text{m} \times 5\mu\text{m}$ topographical AFM image of an Au sample after annealing. This image shows the large domains as well as some 'lumpy' features both produced by the annealing process.	94
4.4 A $2\mu\text{m} \times 2\mu\text{m}$ phase AFM image of an annealed Au sample, showing an area of Au(111) in the upper part of the image.	95
4.5 A $40\text{nm} \times 40\text{nm}$ image of an Au sample that had been removed from the flame for 30s as part of the annealing process. No good quality areas of Au(111) were found on this sample. (STM parameters: $U_{gap} = 0.12\text{V}$ , $I = 10.5\text{nA}$ )	95
4.6 A room temperature $500\text{nm} \times 500\text{nm}$ STM image of a sample removed from the flame 7 times whilst it was being annealed. This image shows detailed Au(111) triangle structure. (STM parameters: $U_{gap} = 86\text{mV}$ , $I = 1.9\text{nA}$ )	95
4.7 A room temperature $50\text{nm} \times 50\text{nm}$ STM image of a sample that had been removed from the flame 9 times whilst it was being annealed. The 'noise' of the image is due to it being recorded at room temperature. (STM parameters: $U_{gap} = 97\text{mV}$ , $I = 15.4\text{nA}$ )	95
4.8 A $4\text{nm} \times 4\text{nm}$ 'grainy' room temperature atomic resolution image of the sample that had been removed from the flame 9 times during its annealing process. (STM parameters: $U_{gap} = 95\text{mV}$ , $I = 15.4\text{nA}$ )	96
4.9 A section of Au(111) showing a single atom defect. (STM parameters: $U_{gap} = 80\text{mV}$ , $I = 1.9\text{nA}$ )	96
4.10 $I$ vs. $V$ and $\frac{dI}{dV}$ vs. $V$ curves for Au(111)	97
4.11 STM images of $4\text{nm} \times 4\text{nm}$ sections of Au(111) terraces recorded with similar tunnelling parameters. In the left image the changes in the electronic structure is recorded as dark and light areas that give the corrugation a 'cobblestone' appearance whereas in the image on the right the light areas are more centred on the lattice positions. The difference in appearance might indicate differences in the tip structure.	100

5.1	Showing a stylised representation of a SAM of octanethiol. The diagonal zigzag lines are the carbon chains, the yellow S's are the sulphur atoms and the horizontal wavy line is the metal surface.	106
5.2	A 50nm × 50nm STM image of an octanethiol on gold sample, made using 1mM octanethiol solution showing 'holes' in the surface. (STM parameters: $U_{gap} = 426\text{mV}$ , $I = 219\text{pA}$ )	107
5.3	Another 50nm × 50nm image of the sample in shown in Figure 4.34, which shows another example of these 'holes' in the thiol layer. (STM parameters: $U_{gap} = 393\text{mV}$ , $I = 122\text{pA}$ )	107
5.4	A 200nm × 200nm STM image of an octanethiol on Au sample, made with a 10mM solution of octanethiol. The 'holes' can clearly be seen in the gold terrace. (STM parameters: $U_{gap} = 401\text{mV}$ , $I = 411\text{pA}$ )	108
5.5	A 100nm × 100nm enlarged section of the sample in Figure 4.36 showing a detailed image of a step edge. The surface density of holes in the 10mM sample appears to be greater than in the 1mM sample. (STM parameters: $U_{gap} = 418\text{mV}$ , $I = 210\text{pA}$ )	108
5.6	A 20.0nm × 10.9nm STM image of an octanethiol on Au sample, made with a 100nM octanethiol solution. A 'hole' shown in black can clearly be seen towards the top of the image. The 'holes' in this sample appear to be due to a change in the packing of the octanethiol molecules. (STM parameters: $U_{gap} = 435\text{mV}$ , $I = 504\text{pA}$ )	109
5.7	A 10nm × 10nm STM image of an octanethiol SAM on gold. It was made with a by immersing a gold sample into a 1mM solution of octanethiol overnight in a refrigerator. (STM parameters: $U_{gap} = 491\text{mV}$ , $I = 101\text{pA}$ )	109
5.8	A 10nm × 10nm STM image of an octanethiol SAM on gold sample recorded with the same STM but prior to this study and made in a similar way to the sample in Figure 5.7. Note that the spacing between the molecules is similar to that in Figure 5.7. (STM parameters: $U_{gap} = 1\text{V}$ , $I = 108\text{pA}$ )	110
5.9	A stylised representation of octanethiol molecules covering a	112

	surface of gold with a gap in the uppermost atomic layer. The distance between the atomic layers is $\approx 2\text{\AA}$ .	
5.10	A stylised representation of octanethiol molecules on a gold surface with some of the molecules at a different angle to the surface than the others showing how such a difference can produce depressions in the surface.	112
5.11	This is the first of two images showing the part of the surface where the octanethiol on Au(111) spectroscopy was recorded. The green and blue dots show the locations where the STS data was recorded presented as the green and blue curves in Figure 5.14. (STM parameters: $U_{gap} = 1.03\text{V}$ , $I = 518\text{pA}$ )	114
5.12	This is the second of two images showing the part of the surface where the octanethiol on Au(111) spectroscopy was recorded. The green and black dots show the locations where the STS data recorded presented as the red and black curves in Figure 5.14. (STM parameters: $U_{gap} = 1.03\text{V}$ , $I = 518\text{pA}$ )	115
5.13	Black curves: $I$ vs. $V$ and $\frac{dI}{dV}$ vs. $V$ STS spectroscopy data from the positions marked by dots shown Figure 5.11 and Figure 5.12. These curves are aggregates of the data at all locations. Red curves: $I$ vs. $V$ and $\frac{dI}{dV}$ vs. $V$ STS spectroscopy data from an unexposed Au(111) sample. (Repeated from Figure 4.10)	116
5.14	Showing the similarity in the overall shape of the $\frac{dI}{dV}$ vs. $V$ curves recorded using the compensation box and the lock-in amplifier (left) and calculated from the $\frac{I}{V}$ vs. $V$ curves (right).	117
5.15	$I$ vs. $V$ and $\frac{dI}{dV}$ vs. $V$ curves of STS spectroscopy data from the positions marked by dots shown Figure 5.11 and Figure 5.12, Blue Curves: Depressed areas (blue dots) in Figure 5.11, Green Curves: Non-depressed areas (green dots) in Figure 5.11, Black Curves: Raised areas (black dots) in Figure 5.12, Red Curves: Non-raised areas (green dots) in Figure 5.12	119
5.16	A $200\text{nm} \times 200\text{nm}$ section of an Au(111) surface covered with dimethyl disulphide.	124

5.17	A 50nm × 50nm image of the same sample as in the previous Figure.	124
5.18	A 50nm × 50nm image of a section of Au(111) for comparison with the previous Figure. (STM Parameters: $U_{gap} = 80\text{mV}$ , $I = 2.2\text{nA}$ )	124
5.19	A 20nm × 20nm section of Au(111) surface showing some features in the Au surface and a line of adsorbed molecules.	126
5.20	A 10nm × 10nm section of another part of the surface showing the Au atoms with some thiol molecules adsorbed on the surface. Note the relative orientations of the molecules to one another.	126
5.21	A 5nm × 5nm section of Au(111) surface showing more clearly five of the molecules in the previous Figure.	126
5.22	An image of the surface slightly displaced from that in the previous Figure.	126
5.23	Showing two possible orientations of DMDS molecules on the Au(111) surface.	127
5.24	Showing two methyl sulphide groups attached to the Au(111) surface. Note that here the S C bonds are perpendicular with the surface.	128
5.25	Showing a single methyl sulphide unit attached to the Au(111) surface, with the angle of the S C bond approximately 50° to the surface normal as suggested by Akinaga, Nakajima, and Hirao.	128
5.26	A 200nm × 200nm image of an methanethiolate coated Au(111) sample.	129
5.27	A differentiated version of the image in Figure 5.26. This is similar to Figure 4 from Dishner <i>et al.</i> <sup>[12]</sup> suggesting that the surface is coated with methanethiolate as expected. <sup>[13]</sup>	129
5.28	Showing the area of the surface where the topographically varying scanning tunnelling spectroscopy was recorded. The spectra were recorded to attempt to determine the nature of the feature on the left hand side in the image. (STM Parameters: $U_{gap} = 200\text{mV}$ , $I = 150\text{pA}$ )	131
5.29	Scanning tunnelling spectra collected from the area shown in	132

Figure 5.28	
5.30	An $I$ vs. $V$ curve and a $\frac{dI}{dV}$ vs. $V$ plot of the spectroscopy data collected from the Au sample coated with a methylthiolate SAM. 134
5.31	$I$ vs. $V$ curves and $\frac{dI}{dV}$ vs. $V$ plots of the spectroscopy data collected from an uncoated Au sample. The red and blue curves correspond to two sets of measurements made with the same tip on the same surface. 134
5.32	A section of the $\frac{d^2I}{dV^2}$ vs. $V$ curve calculated from the $\frac{dI}{dV}$ vs. $V$ curve overlaid with the $\frac{dI}{dV}$ vs. $V$ curve. Due to the method of calculation there is a slight offset between the two curves. 135
6.1	A plot showing the frequency and voltage dependence of the LDSTM response represented on the vertical axis as the magnitude output of the lock-in amplifier. The horizontal axis shows the modulation frequency of the AOM. Note the logarithmic scale on both axes. Experimental conditions: $I = 2\text{nA}$ , $\tau = 1\text{s}$ , feedback loop gain = 3%, laser power = 10mW and $\lambda = 2974\text{cm}^{-1} = 3.362\mu\text{m}$ . 152
6.2	Identical to the previous Figure but with the addition of the black curve displaying data from an experiment in which the tunnelling current was varied by a modulated applied voltage rather than a modulated laser beam. This shows the frequency response of the STM electronics and allows the LDSTM data to be seen in context of the characteristics of the STM. 154
6.3	This shows the results of LDSTM experiments recording the effect of the tunnelling current on $R$ . They were recorded with experimental conditions of: Methylthiolate on gold sample. Tunnelling voltage: 0.5V, $\tau = 1\text{s}$ , feedback loop gain = 3%, $\lambda = 2974\text{cm}^{-1} = 3.362\mu\text{m}$ , laser power = 10mW. 155
6.4	This shows the same data as in the previous Figure but with the lock-in magnitude output as a function of the modulation frequency. Experimental conditions as described in the caption for the previous Figure. 156

6.5 Showing the difference between the LDSTM responses for gold samples coated and uncoated with methylthiolate. Other experimental conditions: Tunnelling voltage = 0.5V, feedback loop gain = 3%,  $\lambda = 3.362\mu\text{m} = 2974\text{cm}^{-1}$ ,  $\tau = 1\text{s}$ ,  $I = 1\text{nA}$ , laser power = 10mW. The same tip was used for both samples. 157

6.6 Showing the LDSTM response to the wavelength of the laser. Samples: coated and uncoated Modulation frequency: ■ = 3.23 kHz, ▲ = 4.6 kHz. Other experimental conditions:  $\tau = 1\text{s}$ ,  $I = 1\text{nA}$ , feedback loop gain = 3%, laser power = 10mW. The black data points show additional data for laser wavelengths between  $3.16\mu\text{m}$  and  $3.36\mu\text{m}$ . These were generated by varying the temperature of the  $29.75\mu\text{m}$  grating from  $100^\circ\text{C}$  to  $190^\circ\text{C}$ . 158

6.7 Showing how the change in gradient at 0.42V in the methylthiolate  $\frac{dI}{dV}$  vs.  $V$  spectrum occurs at a similar energy to the increase in modulation of the tunnelling current of the coated sample. The insert is a copy of Figure 5.27. The main figure shows a section of this  $\frac{dI}{dV}$  vs.  $V$  curve from 0.25V to 0.5V (black curve, right axis) overlaid with data from Figure 5.27 (red and blue data, left axis). 160

# **Chapter 1**

## **Introduction**

1.1	Chapter Introduction.....	2
1.2	Overview of the Work .....	5
1.3	Outline of Thesis .....	5
1.3.1	Chapter 1: Introduction.....	5
1.3.2	Chapter 2: Technologies and Techniques Used .....	5
1.3.3	Chapter 3: Scanning Tunnelling Microscopy Tips.....	6
1.3.4	Chapter 4: Au(111) Samples .....	6
1.3.5	Chapter 5: Thiol Self-Assembled Monolayers .....	7
1.3.6	Chapter 6: Laser Driven Scanning Tunnelling Microscopy Experiments.....	7
1.3.7	Conclusions .....	7
1.4	References .....	8

## 1.1 Chapter Introduction

The pursuit of knowledge about the world around us is relentless and our drive to understanding the building blocks of the universe results in large sums of money being spent on multi-national ‘big science’ projects such as the new Large Hadron Collider at CERN<sup>[1]</sup>. However despite the discoveries made of these exotic subatomic particles, it is not possible to use these to derive all the characteristics about the atoms and molecules that form the basis of the world that we experience day to day. There are still many things of importance to learn from the latter. Until relatively recently almost all of the research in this area focussed upon studying macroscopic quantities of these atoms or molecules. In biological situations particularly, the situation is made more complicated by the necessity to study mixtures as provided by nature with only limited ways of controlling the molecular species in a system under investigation. There is great value in being able to study a single molecule (whether it is large or small) to cut through the averaging that takes place within a macroscopic sample.

For hundreds of years microscopy has been used as a way of studying our world. The samples examined have become smaller and smaller as the optical technology has improved. However the resolution of this technique is fundamentally limited by diffraction. Confocal microscopy can, to a limited degree overcome this problem and combined with partial selective tracing of biological molecules of interest can even track the movement of individual molecules. More recently a range of scanning probe microscopy (SPM) techniques has been developed, the first of which, scanning tunnelling microscopy (STM), still has the highest spatial resolution of a few Å. This is able to manipulate and record single molecules. With the advent of SPM the need arose to be able to manipulate systems on the nanoscale in a controlled way to provide suitable test samples (examples of which are described below) that could be studied with these new techniques.

For several decades prior to this self-assembled monolayers (SAMs)<sup>[2-4]</sup> had been available. They possess a regular array of molecules constrained into two dimensions (see Figure 1.1). Various surface science techniques can be applied to a SAM to measure their properties. However the spatial resolution of these techniques such as LEED (Low Energy Electron Diffraction) and XPS (X-ray

Photoelectric Spectroscopy) is limited. Although LEED can accurately determine the dimensions of a repeating structure, it is not able as a consequence of the diffraction process to record details of individual molecules or surface defects. With XPS the situation is better. It is possible to conduct imaging with XPS but at best the resolution is limited to  $\approx 120\text{nm}$ .<sup>[5]</sup>

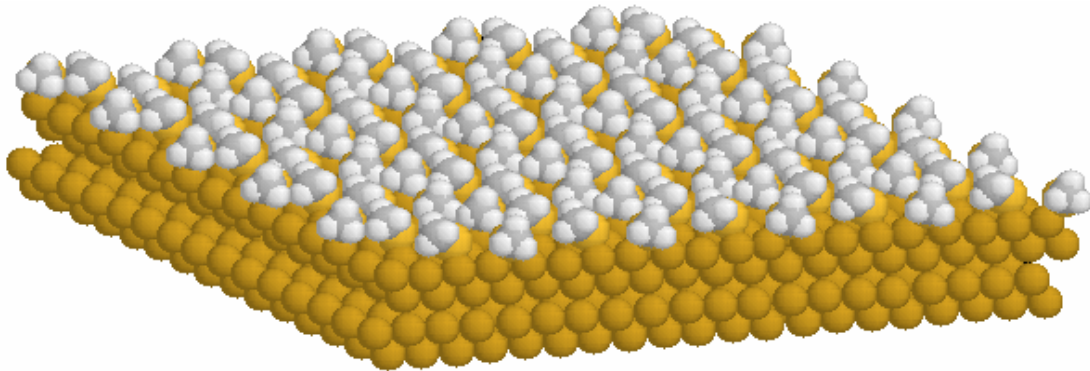


**Figure 1.1: An example of a self-assembled monolayer of methanethiolate on gold. This cartoon is based upon a unit cell by De Renzi *et al.*<sup>[6]</sup> used for calculating the positions of the thiolate species on the surface.**

With the advent of SPM and STM in particular the structure of such surfaces could be investigated at a molecular scale provided that suitable substrates are used. This gave an opportunity to start to work with individual molecules and atoms. STM provides an opportunity to find out how the individual properties of the constituent atoms and molecules combine together to give the macroscopic measurement. Although STM can image individual molecules, often it is difficult to resolve their substructure. This makes it difficult to identify a molecule found on a surface, without knowing what was put into the ultra high vacuum (UHV) chamber in the first place, particularly when the size of an atom or molecule is determined by its total electron density, rather than the electron density at the energy of the tunnelling electrons. The latter being the characteristic that the STM measures.

Some conventional spectroscopic techniques (e.g. FTIR, Raman) measure the vibrational modes in a macroscopic quantity of molecules this is a very successful way of determining their identity. In the last few years some STM work has been published that manages to identify such vibrational modes in individual molecules<sup>[7]</sup>, but this technique has only been applied to a few different types of

molecules partially because of the selection rules that restrict its use to certain vibrational transitions<sup>[8-10]</sup>. Conventional spectroscopic techniques are better able to record information to distinguish between different species, but even when incorporated with a near field technique (SNOM) the resolution cannot approach that of an STM. Here the sharp (metallic) tip enhances the electric field in its immediate proximity and a small area of the surface underneath the tip modifies the scattered radiation from this tip. The microscopic shape of the tip limits the size of this area and consequently the spatial resolution obtained. This interaction of radiation between the tip and the sample is such that it is the near field radiation from near this surface that the tip is able to scatter into the far field whilst maintaining the spatial resolution of the near field information. Alternatively, illuminating an STM tip with laser radiation and detecting its effect, as a modulation of the tunnelling current should yield higher spatial resolution because the resolution is determined by the resolution of the STM.

Over the last 15 years many groups have conducted experiments that couple a laser with the tip of an STM<sup>[11]</sup>. Although for conventional macroscopic spectroscopic techniques a broadband radiation source is often used, for laser driven STM (LDSTM) work a laser source is chosen, partially out of ease of being able to control the path of the radiation onto the STM tip. For some of the groups the motivation derived from wanting to understand the interaction between a laser and the metal-insulator-metal formed by the tip, vacuum gap and sample.<sup>[12-14]</sup> Later, other groups had considered using such a system as a spectroscopic tool and worked on initial experiments to study the various other effects (mostly thermal expansion) that occur with a laser and an STM that do not depend greatly upon the laser wavelength<sup>[15-20]</sup>. More recently experiments have been carried out investigating the effect that a visible laser light source has on the tunnelling characteristics of dyes<sup>[21, 22]</sup>. This second example describes the response of the tip sample distance to the wavelength of the laser. This type of experiment is made easier by the fact that such dyes have broad emission and absorption lines hence simplifying the process of matching up lasers with dyes. Vibrational transitions have much narrower bands than electronic ones and are also in the infrared, which means that dye lasers are not suitable. This provides the motivation for using an optical parametric oscillator in this work, which can be tuned to access these vibrational modes.

## 1.2 Overview of the Work

The high spatial resolution available with an STM and the chemical information available from infrared spectroscopy leads to a description of the aim of this project: to use an Optical Parametric Oscillator (OPO) as a tuneable infrared laser source coupled with an STM to probe the response of samples to the infrared radiation with the spatial resolution of the STM. This project works towards a technique for identifying singular molecular species and studying their interaction with the surface. Typical samples are expected to be metal substrates partially or completely covered with molecules with vibrational modes accessible by the OPO.

## 1.3 Outline of Thesis

### 1.3.1 Chapter 1: Introduction

This chapter introduces the aim of the project in the context of a brief summary of work conducted previously and lists outlines of the chapters in this thesis.

### 1.3.2 Chapter 2: Technologies and Techniques Used

Conducting experiments at low temperatures improves the quality of the images and STM spectroscopy recorded<sup>[23]</sup> due to the reduction of the atoms' thermal motion and the narrowing of the vibrational modes. As a consequence it was decided to use a low temperature STM (LTSTM) to take advantage of this. §2.1 provides an overview of STM and describes details of the particular LTSTM used in this study.

§2.3 describes how an OPO can be used as a tuneable infrared source and provides details of the specific OPO used in this work.

Self-assembled monolayers (SAMs) prepared on gold were used as the basis for the samples used, mostly as a consequence of the restricted types of substrate available for use with this STM. For an overview of SAMs and their manufacture see §2.4.

Coupling a laser with an STM forms the key experiment conducted as part of this work. §2.5 provides a history of this type of experiment and describes a theoretical basis for its use.

### 1.3.3 Chapter 3: Scanning Tunnelling Microscopy Tips

The STM tip is a critical component of the STM. Manufacturing tips with reproducible quality is not easy but it is important that this is achieved. Chapter 3 describes the procedures developed for making the tips used in the STM. Optical and electron microscope images of these tips are used to show the effectiveness of the tip etching methods. STM images recorded with these tips are included to illustrate their quality. Conclusions are drawn from these various images and suggestions are made for potential future improvements.

### 1.3.4 Chapter 4: Au(111) Samples

The low reactivity of gold makes it available as a suitable substrate that can be prepared outside the ultra-high vacuum (UHV) chamber before being loaded into the chamber for the purposes of experiments. §3.2 describes how these gold substrates are prepared for the experiments. STM images are included to show the effectiveness of the different process variations of making the gold samples. Details are given of STM spectroscopy experiments conducted upon these samples. There is some discussion into what the spectroscopy data reveals about the tip structure.

### 1.3.5 Chapter 5: Thiol Self-Assembled Monolayers

Although the reactivity of gold is quite low it will react readily with thiol molecules (containing sulphur atoms) either as an –S-H group or as a dithiol (-S-S-) group. §5.2 describes the preparation of self-assembled monolayers of octanethiol onto gold substrates and their subsequent imaging with the STM. This section also includes details of scanning tunnelling spectroscopy experiments conducted on the octanethiolate samples. §5.3 describes experiments conducted with samples of dimethyl disulphide deposited onto Au(111) including details of the method used to make these samples. The experiments used include STM imaging and STM spectroscopy. The chapter concludes with discussions of the results of the experiments conducted and makes suggestions for future experiments.

### 1.3.6 Chapter 6: Laser Driven Scanning Tunnelling Microscopy Experiments

A key part of the area of interest of this thesis is the nature of the interaction between the beam from an OPO and the tunnelling junction in an STM. This chapter describes the details of the experiments that combine the laser with the STM. A series of subsections highlight a range of key variables and the experiments used to investigate them. The chapter concludes with a discussion of the results collected from these experiments and makes suggestions for further work.

### 1.3.7 Conclusions

This chapter summarises the experimental results drawing them together and highlights conclusions that follow from the whole body of results.

## 1.4 References

1. Rogers, P., *To the LHC and beyond*. Physics World, 2004. **17**(9): p. 64.
2. Emmons, H., Trans. Am. Inst. Chem. Eng., 1939. **35**: p. 109-.
3. Schmidt, E., W. Schurig, W. Sellschopp, Tech. Mech. Thermodyn., 1930. **1**: p. 53-.
4. Nagle, W.M., T. B. Drew, Trans. Am. Inst. Chem. Eng., 1933. **30**: p. 217-.
5. Escher, M., et al., *NanoESCA: imaging UPS and XPS with high energy resolution*. Journal of Electron Spectroscopy and Related Phenomena, 2005. **144-147**: p. 1179-1182.
6. De Renzi, V., et al., *Ordered (3 x 4) high-density phase of methylthiolate on Au(111)*. Journal of Physical Chemistry B, 2004. **108**(1): p. 16-20.
7. Ho, W., *Single-molecule chemistry*. The Journal of Chemical Physics, 2002. **117**(24): p. 11033-11061.
8. Mingo, N., *Calculation of the Inelastic Scanning Tunneling Image of Acetylene on Cu(100)*. Phys. Rev. Letters, 2000. **84**(16): p. 3694-3697.
9. Lorente, N. and M. Persson, *Theory of single molecule vibrational spectroscopy and microscopy*. Physical Review Letters, 2000. **85**(14): p. 2997-3000.
10. Lorente, N., et al., *Symmetry Selection Rules for vibrationally Inelastic Tunneling*. Physical Review Letters, 2001. **86**(12): p. 2593-2596.
11. Grafström, S., *Photoassisted scanning tunneling microscopy*. J. Appl. Phys., 2002. **91**(4): p. 1717-1753.
12. Kroo, N., et al., *Decay Length of Surface-Plasmons Determined with a Tunneling Microscope*. Europhysics Letters, 1991. **15**(3): p. 289-293.
13. Grafström, S., et al., *Thermal expansion of scanning tunneling microscopy tips under laser illumination*. Journal of Applied Physics, 1998. **83**(7): p. 3453-3460.
14. Krieger, W., et al., *Generation of Microwave-Radiation in the Tunneling Junction of a Scanning Tunneling Microscope*. Physical Review B, 1990. **41**(14): p. 10229-10232.
15. Grafström, S., *Analysis and compensation of thermal effects in laser-assisted scanning tunneling microscopy*. Journal of Vacuum Science & Technology B, 1991. **9**(2): p. 568-572.

16. Grafström, S., et al., *Investigation of laser-induced effects in molecular layers by scanning tunneling microscopy*. Applied Physics A-Materials Science & Processing, 1998. **66**: p. S1237-S1240.
17. Amer, N.M., A. Skumanich, and D. Ripple, *Photothermal modulation of the gap distance in scanning tunneling microscopy*. Applied Physics Letters, 1986. **49**(3): p. 137-139.
18. Specht, M., et al., *Scanning Plasmon near-Field Microscope*. Physical Review Letters, 1992. **68**(4): p. 476-479.
19. Gutjahr-Loser, T., et al., *Ferrimagnetic resonance excitation by light-wave mixing in a scanning tunneling microscope*. Journal of Applied Physics, 1999. **86**(11): p. 6331-6334.
20. Landi, S.M. and O.E. Martinez, *Quenching the thermal contribution in laser assisted scanning tunneling microscopy*. Journal of Applied Physics, 2000. **88**(8): p. 4840-4844.
21. Moltgen, H. and K. Kleinermanns, *Resonance enhanced scanning tunneling (REST) spectroscopy of molecular aggregates on graphite*. Physical Chemistry Chemical Physics, 2003. **5**(12): p. 2643-2647.
22. Smith, D.A. and R.W. Owens, *Laser-assisted scanning tunnelling microscope detection of a molecular adsorbate*. Applied Physics Letters, 2000. **76**(25): p. 3825-3827.
23. Ferris, J.H., et al., *Design, operation, and housing of an ultrastable, low temperature, ultrahigh vacuum scanning tunneling microscope*. Review of Scientific Instruments, 1998. **69**(7): p. 2691-2695.

## Chapter 2

### Techniques and Technologies Used

2.1	Chapter Introduction .....	11
2.2	Scanning Tunnelling Microscopy .....	11
2.2.1	A Brief History.....	11
2.2.2	An Overview of STM.....	13
2.2.3	A Theoretical Approach.....	14
2.2.3.1	The Rectangular Barrier.....	15
2.2.3.2	The Barrier Height (Workfunction) .....	19
2.2.3.3	The WKB Model.....	21
2.2.3.4	The Tersoff and Hamann Model .....	24
2.2.4	STM Spectroscopy .....	28
2.2.5	STM Equipment .....	34
2.2.5.1	Low Temperature Ultra High Vacuum STM .....	35
2.2.5.2	Tip Manufacture.....	42
2.3	Optical Parametric Oscillators .....	45
2.3.1	Overview .....	45
2.3.2	Background & Theory.....	46
2.3.3	Specific Details of the OPO Used for This Work .....	50
2.4	Self-Assembled Monolayers .....	57
2.5	Laser-Driven Scanning Tunnelling Microscopy (LDSTM).....	60
2.5.1	Thermal Effects.....	61
2.5.2	Other LDSTM Responses .....	64
2.6	Chapter Summary.....	66
2.7	References .....	66

## 2.1 Chapter Introduction

This chapter describes the equipment and the experimental techniques used to conduct the experiments. It is comprised of four sections. It starts by introducing the technique of scanning tunnelling microscopy and describes details of the specific STM used to collect the data included in this work. A sub-section is included describing how STM spectroscopy can be conducted on samples by varying the tunnelling conditions. Section 2.3 introduces the optical parametric oscillator as the laser source used to irradiate the sample during the laser driven scanning tunnelling microscopy (LDSTM) experiments. Section 2.4 describes self-assembled monolayers (SAMs) and why they are a useful system to study with LDSTM. The chapter concludes with a look at LDSTM itself. An overview and history of part of the field is discussed highlighting how the technique is an improvement over conventional spectroscopy or STM techniques alone.

## 2.2 Scanning Tunnelling Microscopy

### 2.2.1 A Brief History

Scanning tunnelling microscopy (STM) is a unique technique that can be used to image and investigate surfaces at the atomic scale. It was developed in the early 1980's<sup>[1]</sup> by Binnig *et al.*, from earlier work with metal-oxide-metal interfaces<sup>[2, 3]</sup>. In STM a sharp metal tip is positioned very close to a conducting surface. A voltage is applied between the tip and the sample. Electrons will tunnel from the tip to the sample. The rate of electron tunnelling is approximately exponentially dependent on the distance between the sample and the tip. Raster scanning the tip across the sample yields the variation in the electron density across the surface.

Some of the characteristics recorded in experiments with metal-oxide-metal interfaces can also be recorded in STM experiments. For example, the ability to measure vibrational modes in the insulating oxide layer by means of inelastic

tunnelling<sup>[4]</sup> can also be applied to STM. However, since with an STM the current ideally only tunnels through one atom the signal-to-noise ratio will be significantly worse. It is only in the last few years that STM technology has caught up and been used to do similar experiments on a single molecular scale<sup>[5]</sup>. In the years that followed, other groups started work with STM using any conductive sample that could be prepared with a regular structure e.g. graphite, III-V semiconductors, and metals prepared with (111), (110) or (100) surfaces. Although well-ordered surfaces are easier to study, many surface chemical and physical processes take place at the defects that exist on the surfaces. STM provided a way of studying these defects individually providing greater insight into such processes.

As the features of simple surfaces had been reasonably well understood, the attention of those using STM moved to surfaces that were more complicated, typically involving a metal substrate with other atoms or molecules on its surface<sup>[6, 7]</sup>. These additional atoms on the surface could either be scattered sparingly or as a monolayer or as a multilayer. Some of IBM's most famous work required a low concentration of atoms on the metal surface.<sup>[8]</sup> Initially these experiments were designed to demonstrate successes in actively positioning atoms on a surface.<sup>[8]</sup> Later the electron standing waves produced by a specific arrangement of atoms became of interest.<sup>[7, 9-11]</sup> Currently the 'cutting edge' of the field includes work based around single molecule inelastic tunnelling experiments exploring the possibilities of initiating reactions with one molecule of each reagent<sup>[12]</sup>.

As the progress of STM experiments proceeded over the years, ideas for the theoretical understanding of STM were developed in parallel. Initially these were derived from tunnelling electron flow between the two metals in a metal-oxide-metal 'sandwich'.<sup>[13]</sup> By the 1980's they had become more sophisticated, adding effects due to the different spatial arrangements between metal-oxide-metal and STM systems<sup>[14]</sup>. More recently efforts have focussed on the role of the character of the tip in influencing the STM images<sup>[15-17]</sup>.

In short, history has shown that STM is a powerful technique for studying small numbers of atoms and molecules. The next few sections describe how this technique works.

### 2.2.2 An Overview of STM

In STM a potential difference is applied between a conducting surface and a very fine point (tip) a few Ångstroms just above the surface (Figure 2.1). The voltage applied is enough to enable electrons to tunnel across the vacuum gap between the surface and the tip (or vice versa). The particular polarity and magnitude of the voltage for any given experiment will depend upon the sample used and what is of particular interest in that sample. The number of electrons that tunnel from the surface to the tip (or vice versa) is exponentially dependent upon the distance between the surface and the tip<sup>[14]</sup>; i.e. the further away the tip is from the surface the lower the current will be. The tip is raster scanned across a section of sample surface and the current between the surface and the tip is measured continuously (see Figure 2.1). This tunnelling current is dependent on the electronic properties of the tip and sample and approximately exponentially dependent upon the distance between the tip and the sample.

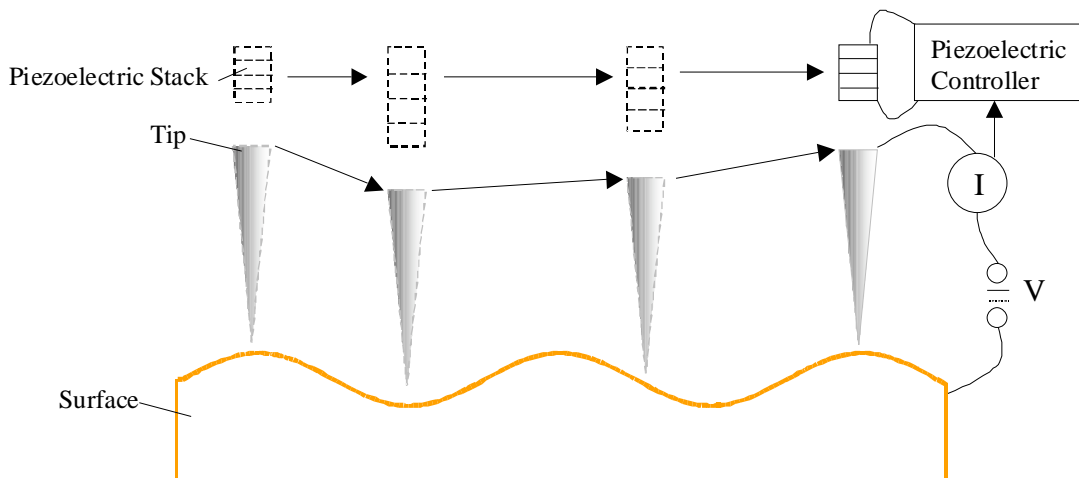


**Figure 2.1: Schematic of the tunnelling set-up. A very sharp metal tip is positioned very close to the surface and a voltage is applied between the two, as the tip is raster scanned across the surface whilst the current is measured.**

Although the vertical position of the tip can be held constant while the current measurements are taken, it is usual to include a feedback mechanism that keeps the current constant, by moving the tip up and down so that it follows the contours of the surface as it scans. This method can cope with large variations in the

topography of the surface without the tip colliding into the surface. The tip is moved in three dimensions with a stack of piezoelectric material. Applying a voltage across the stack in an appropriate direction moves one end of this material, onto which the tip is attached. The distance that the piezoelectric stack has to move to keep the current constant is recorded and plotted to produce a topographical map of the surface.

STM experiments can be carried out under a wide range of different conditions: air<sup>[18]</sup>, liquid (both polar<sup>[19]</sup> and non-polar<sup>[20]</sup>) and ultra-high vacuum (UHV)<sup>[18]</sup>. Images recorded from experiments conducted in air tend to be of poorer quality than those conducted in UHV due to species in the atmosphere contaminating the sample but it is much more convenient to work in air than in UHV so conducting experiments in air can still be useful. For STM experiments in liquids the issue of contamination is more acute due to the surface being continuously in contact with the species present in the liquid used. This requires that the liquid does not contain any undesirable species that would adsorb on the surface for an appreciable length of time. STM experiments are only usually conducted in liquids in order to investigate the interaction of the sample with the constituents of the liquid.<sup>[21]</sup> As a consequence of the reduced risk of contamination, experiments run in UHV produce images with better quality, which is why the experiments documented in this report took place in UHV. In addition, it is more difficult to image the atoms in a surface at room temperature since the STM is sensitive enough to measure their thermal motion. Consequently, much of the data included in this report has been recorded with the apparatus cooled to 77K (with N<sub>2(l)</sub>) and some of it was recorded with the apparatus cooled to  $\approx$ 5K (with He<sub>(l)</sub>).

### 2.2.3 A Theoretical Approach

In order to fully understand and appreciate the results of an experiment it is vital to have some theoretical understanding or model of the system under investigation. For STM there are a range of different models that have been developed with varying levels of complexity.

### 2.2.3.1 The Rectangular Barrier

At the simplest level, the tunnelling process can be described in one dimension with a rectangular shaped potential barrier. The energy of the wavefunction of the tunnelling electron is kept constant. This simple case can be described best in a time independent manner. For a simple rectangular barrier, there are three regions of interest that have the following time-independent Schrödinger equations and associated wavefunctions for an electron of mass  $m$  and energy  $E$ <sup>[22]</sup> (see Figure 2.2),:

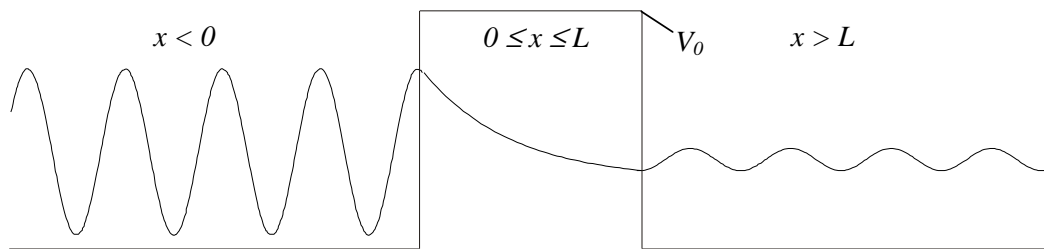


**Figure 2.2: Illustrating the simple case of tunnelling through a rectangular shaped barrier. The electron is considered to travel from the left to the right along the  $x$  axis. Between  $x = 0$  and  $x = L$  there is a potential barrier with a height of energy  $V_0$ .**

The probability of transmission for the electron is calculated by matching the wavefunctions and their first derivatives at the interfaces between these three regions.

#### 1. Left hand side of barrier ( $x < 0$ ):

Equation 2.1 and Equation 2.2 show the Time Independent Schrödinger Equation (TISE) and the electron wavefunction for this region respectively.

$$\frac{-\hbar^2}{2m} \frac{d^2\Psi_1}{dx^2} = E\Psi_1 \quad \text{Equation 2.1}$$

$$\Psi_1 = e^{i(kx-\omega t)} + A e^{-i(kx+\omega t)} \quad \text{where} \quad k^2 = \frac{2mE}{\hbar^2} \quad \text{Equation 2.2}$$

The two parts of  $\Psi_1$  show that it has two components, one incident to and the other reflected from the barrier. The  $A$  in the second, reflected part enables these two components to have different magnitudes.

2. *In the barrier ( $0 \leq x \leq L$ ):*

Equation 2.3 and Equation 2.4 show the TISE and the electron wavefunction for this region respectively. Note the addition of the terms containing  $V_0$  (barrier height or workfunction) due to the presence of the wavefunction in the potential barrier.

$$\frac{-\hbar^2}{2m} \frac{d^2\Psi_2}{dx^2} + V_0\Psi_2 = E\Psi_2 \quad \text{Equation 2.3}$$

$$\text{where } k'^2 = \frac{2m(V_0 - E)}{\hbar^2} \quad \text{Equation 2.4}$$

Also the exponential parts of Equation 2.4 are real resulting in the exponential shape of the wavefunction inside the barrier compared to the periodic shape outside the barrier.

3. *Right hand side of the barrier ( $x > L$ ):*

Equation 2.5 (the TISE for this region) has a similar form to Equation 2.1 due to the absence of the potential for  $x > L$ . Equation 2.6, the expression for  $\Psi_3$  only contains one term due to the electrons in this region only propagating away from the barrier. Note the  $x - L$  term used to describe the position of the electron to displace the origin of the wavefunction from  $x = 0$  to  $x = L$ .

$$\frac{-\hbar^2}{2m} \frac{d^2\Psi_3}{dx^2} = E\Psi_3 \quad \text{Equation 2.5}$$

$$\Psi_3 = De^{i(k(x-L)-\alpha x)} \text{ where } k^2 = \frac{2mE}{\hbar^2} \quad \text{Equation 2.6}$$

The proportion of electrons that tunnel through the barrier is given by the transmission coefficient  $T$ , given by:

$$T = \frac{j_t}{j_i} \quad \text{Equation 2.7}$$

where  $j_t$  is the transmitted current density and  $j_i$  is the incident current density. In the one dimensional case current density,  $j$  (sometimes referred to as particle flux) is given by<sup>[23]</sup>:

$$j = \frac{-i\hbar}{2m} \left( \Psi^* \frac{d\Psi}{dx} - \Psi \frac{d\Psi^*}{dx} \right) \quad \text{Equation 2.8}$$

For  $j_t$ ,  $\Psi = \Psi_3$ :

$$j_t = \frac{-i\hbar}{2m} \left( \Psi_3^* \frac{d\Psi_3}{dx} - \Psi_3 \frac{d\Psi_3^*}{dx} \right) \quad \text{Equation 2.9}$$

More explicitly:

$$j_t = \frac{-i\hbar}{2m} \left( D e^{-i(k(x-L)-\omega t)} \frac{d}{dx} (D e^{i(k(x-L)-\omega t)}) - D e^{i(k(x-L)-\omega t)} \frac{d}{dx} (D e^{-i(k(x-L)-\omega t)}) \right) \quad \text{Equation 2.10}$$

This simplifies to:

$$j_t = \frac{\hbar k}{m} |D|^2 \quad \text{Equation 2.11}$$

For  $j_i$ ,  $\Psi$  equals the first term in  $\Psi_1$ :

$$j_i = \frac{-i\hbar}{2m} \left( e^{-i(kx-\omega t)} \frac{d}{dx} (e^{i(kx-\omega t)}) - e^{i(kx-\omega t)} \frac{d}{dx} (e^{-i(kx-\omega t)}) \right) \quad \text{Equation 2.12}$$

This simplifies to:

$$j_i = \frac{\hbar k}{m} \quad \text{Equation 2.13}$$

Therefore:

$$T = |D|^2 \quad \text{Equation 2.14}$$

The wavefunctions  $\Psi_1$ ,  $\Psi_2$ , and  $\Psi_3$  have boundary conditions that require the wavefunctions and their first derivatives to be matched at the interfaces between these three regions. Satisfying these boundary conditions for Equation 2.1 to Equation 2.6 leads to four simultaneous equations for  $A$ ,  $B$ ,  $C$ , &  $D$ .

$$I + A = B + C \quad \text{Equation 2.15}$$

$$ik - ikA = k'C - k'B \quad \text{Equation 2.16}$$

$$Be^{-k'L} + Ce^{k'L} = D \quad \text{Equation 2.17}$$

$$k'C e^{k'L} - k'B e^{-k'L} = ikD \quad \text{Equation 2.18}$$

Equation 2.15 to Equation 2.18 can be solved to yield  $D$  and consequently  $|D|^2$ . To do this, Equation 2.15 and Equation 2.16 are combined to eliminate  $A$  and rearranged:

$$C = \frac{2ik + B(k' - ik)}{k' + ik} \quad \text{Equation 2.19}$$

Inserting Equation 2.19 into Equation 2.17 and rearranging for  $B$  yields:

$$B = \frac{(k' + ik)D - 2ike^{k'L}}{2k' \cosh(k'L) - 2ik \sinh(k'L)} \quad \text{Equation 2.20}$$

Inserting Equation 2.19 into Equation 2.18 and rearranging for  $B$  yields:

$$B = \frac{(ik'k - k^2)D - 2ik'ke^{k'L}}{2k'^2 \sinh(k'L) - 2ik'k \cosh(k'L)} \quad \text{Equation 2.21}$$

Setting Equation 2.20 equal to Equation 2.21 and rearranging for  $D$  gives:

$$D = \frac{2ik'k}{(k'^2 + k^2) \sinh(k'L) - 2ik'k \cosh(k'L)} \quad \text{Equation 2.22}$$

Consequently  $T$  is given by:

$$T = |D|^2 = \frac{4k'^2 k^2}{(k'^2 + k^2)^2 \sinh^2(k'L) + 4k'^2 k^2 \cosh^2(k'L)} \quad \text{Equation 2.23}$$

For the scenarios described in this thesis the de Broglie wavelength of the tunnelling electrons is less than the barrier width. In this regime Equation 2.23 becomes:

$$T \approx \frac{4E(V_0 - E)}{V_0^2 + 4E(V_0 - E)} e^{-\frac{2}{\hbar} \sqrt{2m(V_0 - E)} L} \quad \text{Equation 2.24}$$

Despite the simplicity of this model some important points can be drawn from it. In this approximate expression for  $T$  the exponential part dominates. The exponential dependence of  $T$  on the barrier width  $L$  is what enables an STM to resolve the variation of the electron density on a surface with such high spatial resolution.  $T$  is similarly exponentially dependent upon the square root of the effective barrier height  $\sqrt{V_0 - E}$ . The exponential dependence of the probability of tunnelling upon the effective barrier height is also true for barriers with a more general shape. This is shown in §2.2.3.3 which describes the Wentzel, Kramers and Brillouin (WKB) model.<sup>[24]</sup>

### 2.2.3.2 The Barrier Height (Workfunction)

It is important to realise that a spatial variation in the barrier height ( $V_0$ ) will affect the tunnelling current measured across a sample and that in the operation of an STM it is not normally configured to measure this change so that localised changes in workfunction are incorrectly recorded as localised changes in the tip-sample separation ( $L$ ). However it is possible to make an approximate local

measurement of the barrier height (workfunction) by making use of a simplified version of Equation 2.24. If the workfunction ( $V_0$ ) is significantly larger than  $E$  then the exponential component of this expression can be considered to be independent of the electron energy and the pre-exponential factor simplifies to  $4\frac{E}{V_0}$  implying that the tunnelling probability (and consequently the tunnelling current) is linearly dependent upon the electron energy. At a fixed value of the electron energy  $E$  this can be expressed in the following form:

$$I \propto E e^{-\frac{2}{\hbar} \sqrt{2mV_0} L} \quad \text{Equation 2.25}$$

Despite the simplicity of such a model it does provide a good approximation and experimentally the tunnelling current can in many cases be found to be linearly dependent upon the applied voltage. If the approximation of regarding the exponential part as independent of  $E$  is assumed to be valid then this provides a simple way of measuring the workfunction. At a fixed value of  $E$ , Equation 2.25 can be simplified further to:

$$I \propto e^{-\frac{2}{\hbar} \sqrt{2m\phi} L} \quad \text{Equation 2.26}$$

where  $\phi$  is an effective workfunction (barrier height). By recording the tunnelling current ( $I$ ) for different values of the tip sample separation ( $L$ ),  $\phi$  can be calculated from gradient of a plot of  $\ln I$  vs.  $L$ . As described above this model is intended to be used when  $V_0$  is much larger than  $E$ . When  $V_0$  is only slightly larger than  $E$  a more complex expression should be used<sup>[25]</sup>:

$$I \propto \left(V_0 - \frac{E}{2}\right) e^{\left[-\frac{2L}{\hbar} \sqrt{2m(V_0 - \frac{E}{2})}\right]} - \left(V_0 + \frac{E}{2}\right) e^{\left[-\frac{2L}{\hbar} \sqrt{2m(V_0 + \frac{E}{2})}\right]}$$

$$\text{Equation 2.27}$$

However from calculations performed using these two forms the difference between them is not great indicating that Equation 2.26 provides a good approximation of the workfunction.

### 2.2.3.3 The WKB Model

This model is more sophisticated than the rectangular barrier case in that it considers a barrier with an arbitrary shape (see Figure 2.3). This treatment allows the shape of the potential barrier to be included in order to more accurately model the tunnelling process and provides a better estimate of the pre-exponential factor. However, this flexibility comes at a price and this is that the model does not work when the energy of the electrons is close to that of the potential barrier. This limitation can be overcome by restricting the barrier to one with a linear shape, but of course this removes the flexibility of working with an arbitrarily shaped barrier (see Figure 2.4).

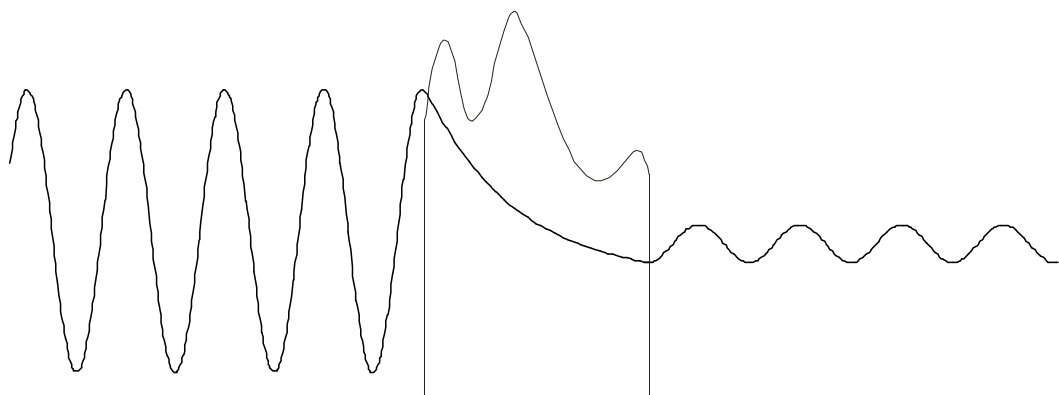


**Figure 2.3 (Above):** Showing a wavefunction tunnelling through a barrier of arbitrary shape. This scenario can be described with the WKB model but only if the electron energy is not near the height of the barrier.

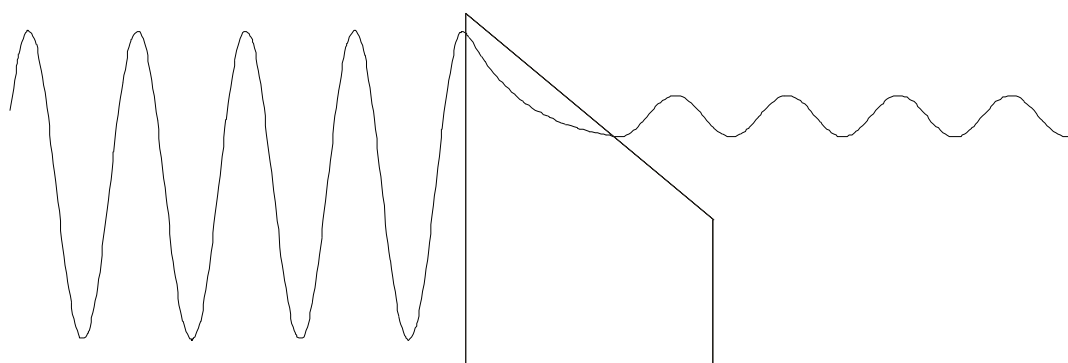


**Figure 2.4 (Above):** The WKB approximation can be made to work when the electron energy is close to the barrier height if a linear barrier is used. Removing the restriction on the electron energy comes at a cost of only being able to use a barrier with a linear shape.

To illustrate how the WKB model works let us assume a wavefunction of the form:

$$\psi = e^{iS(x)+T(x)} \quad \text{Equation 2.28}$$

Here just the spatially dependent part is included for clarity. The wavefunction is a combination of periodic and exponential components.

Firstly take the Time Independent Schrödinger Equation (TISE):

$$\frac{-\hbar^2}{2m} \frac{d^2\psi}{dx^2} + V\psi = E\psi \quad \text{Equation 2.29}$$

and rearrange it:

$$\frac{d^2\psi}{d\psi} = \frac{-2m(E-V)}{\hbar^2} \psi \quad \text{Equation 2.30}$$

Insert the wavefunction  $\psi$ :

$$\left( i \frac{d^2S}{dx^2} + \frac{d^2T}{dx^2} - \left( \frac{dS}{dx} \right)^2 + 2i \frac{dS}{dx} \frac{dT}{dx} + \left( \frac{dT}{dx} \right)^2 \right) \psi = \frac{-2m(E-V)}{\hbar^2} \psi \quad \text{Equation 2.31}$$

Cancelling  $\psi$  and writing the real and imaginary parts separately yields:

$$- \left( \frac{dS}{dx} \right)^2 + \frac{d^2T}{dx^2} + \left( \frac{dT}{dx} \right)^2 + k^2 = 0 \quad \text{Equation 2.32}$$

and:

$$\frac{d^2S}{dx^2} + 2 \frac{dS}{dx} \frac{dT}{dx} = 0 \quad \text{Equation 2.33}$$

where:

$$k^2 = \frac{2m(E-V(x))}{\hbar^2} \quad \text{Equation 2.34}$$

Let us consider cases where the oscillation of the wave function is very rapid compared to any non-periodic changes in its amplitude, i.e. when the wavelength,  $\lambda$  is small (and correspondingly the momentum,  $p$  is large). In this case

$\frac{d^2T}{dx^2} \ll \frac{dS}{dx}$  and  $\frac{dT}{dx} \ll \frac{dS}{dx}$ . These can be used to approximate Equation 2.32 to

$\left(\frac{dS}{dx}\right)^2 = k^2$ , leading to:

$$\frac{dS}{dx} = \pm k. \quad \text{Equation 2.35}$$

Integrating Equation 2.35 gives:

$$S(x) = \pm \int k dx \quad \text{Equation 2.36}$$

and differentiating Equation 2.35 gives:

$$\frac{d^2S}{dx^2} = \pm \frac{dk}{dx} \quad \text{Equation 2.37}$$

Inserting Equation 2.35 and Equation 2.37 into Equation 2.33 and rearranging gives:

$$2k \frac{dT}{dx} = - \frac{dk}{dx} \quad \text{Equation 2.38}$$

Integrating Equation 2.38 gives:

$$T = -\frac{1}{2} \ln k + c \quad \text{Equation 2.39}$$

(c = constant of integration)

Rearranging:

$$e^{T(x)} = \frac{A}{\sqrt{k}} \quad \text{Equation 2.40}$$

( $A = e^c$ )

Inserting Equation 2.36 and Equation 2.40 into Equation 2.28 and substituting for  $k$  gives:

$$\psi = \frac{A}{\sqrt{\frac{\sqrt{2m(E-V(x))}}{\hbar}}} e^{\pm i \frac{\sqrt{2m}}{\hbar} \int \sqrt{E-V(x)} dx} \quad \text{Equation 2.41}$$

For a given expression of  $V(x)$ , Equation 2.41 can be inserted into expressions for  $j_t (x = L)$  and  $j_i (x = 0)$ . From this the transmission coefficient  $T$  can be calculated. Comparing Equation 2.24 with Equation 2.41 shows that they both contain the exponential dependence upon the effective barrier height and the barrier width but with the WKB description they are included as an integral allowing an arbitrary shaped barrier to be modelled.

### 2.2.3.4 The Tersoff and Hamann Model

Bardeen developed a more advanced model still, using first order perturbation theory<sup>[13]</sup>. This allows for specific wavefunctions for the sample and the tip allowing for a more accurate description of the tunnelling process.

This can be seen by starting with a new Hamiltonian, which equals the original one plus a ‘small’ perturbation.

$$\hat{H} = \hat{H}_0 + \hat{H}' \quad \text{Equation 2.42}$$

Expanding the time-dependent Schrödinger equation with Equation 2.42:

$$\hat{H}\Psi = i\hbar \frac{\partial\Psi}{\partial t} = \hat{H}_0\Psi + \hat{H}'\Psi \quad \text{Equation 2.43}$$

Using (2) from Bardeen’s paper<sup>[13]</sup> for  $\Psi$  and reinserting  $\hbar$ .

$$\Psi = a(t)\Psi_0 e^{-iW_0t/\hbar} + \sum_{mn} b_{mn}(t)\Psi_{mn} e^{-iW_{mn}t/\hbar}$$

**Equation 2.44**

Inserting Equation 2.43 into Equation 2.44:

$$\begin{aligned} & \left( i\Psi_0 \frac{\partial a(t)}{\partial t} + \Psi_0 W_0 a(t) \right) e^{-iW_0t/\hbar} + \sum_{mn} \left( i \frac{\partial b(t)}{\partial t} \Psi_{mn} + \Psi_{mn} W_{mn} b(t) \right) e^{-iW_{mn}t/\hbar} \leftarrow \\ & = a(t)W_0\Psi_0 e^{-iW_0t/\hbar} + \sum_{mn} b_{mn}(t)W_{mn}\Psi_{mn} e^{-iW_{mn}t/\hbar} + \leftarrow \\ & a(t)\hat{H}'\Psi_0 e^{-iW_0t/\hbar} + \sum_{mn} b_{mn}(t)\hat{H}'\Psi_{mn} e^{-iW_{mn}t/\hbar} \end{aligned}$$

**Equation 2.45**

$$\text{Where } \hat{H}_0\Psi_0 = W_0\Psi_0 \quad \text{Equation 2.46}$$

$$\& \quad \hat{H}_0\Psi_{mn} = W_{mn}\Psi_{mn} \quad \text{Equation 2.47}$$

Cancelling some terms:

$$i\Psi_0 \frac{\partial a(t)}{\partial t} e^{-iW_0t/\hbar} + \sum_{mn} \Psi_{mn} i \frac{\partial b(t)}{\partial t} e^{-iW_{mn}t/\hbar} = a(t)\hat{H}'\Psi_0 e^{-iW_0t/\hbar} + \sum_{mn} b_{mn}(t)\hat{H}'\Psi_{mn} e^{-iW_{mn}t/\hbar}$$

**Equation 2.48**

Multiplying by  $\Psi_0^*$  and integrating over all space:

$$i \frac{\partial a(t)}{\partial t} e^{-iW_0t/\hbar} = a(t)H'_{00} e^{-iW_0t/\hbar} + \sum_{mn} b_{mn}(t)H'_{mn} e^{-iW_{mn}t/\hbar} \quad \text{Equation 2.49}$$

where:

$$H'_{00} = \int \Psi_0^* \hat{H}' \Psi_0 d\tau \quad \text{Equation 2.50}$$

and:

$$H'_{mn} = \int \Psi_0^* \hat{H}' \Psi_{mn} d\tau = \int \Psi_0^* (\hat{H} - \hat{H}_0) \Psi_{mn} d\tau = \int \Psi_0^* (\hat{H} - W_{mn}) \Psi_{mn} d\tau \quad \text{Equation 2.51}$$

Tersoff and Hamann took this expression for the transition matrix element  $H'_{mn}$  and used it to derive an expression for the tunnelling current ( $I$ ) in an STM. as<sup>[14]</sup>:

$$I = \frac{e}{h} \sum_{\mu, \nu} f(E_\mu) [1 - f(E_\nu + eV)] |M_{\mu\nu}|^2 \delta(E_\mu - E_\nu) \quad \text{Equation 2.52}$$

Where  $h$  is Planck's constant,  $e$  is the fundamental charge unit,  $f(E)$  is the Fermi function,  $V$  is the applied voltage,  $M_{\mu\nu}$  is the tunnelling matrix element between states  $\psi_\mu$  of the probe and  $\psi_\nu$  of the surface and  $E_\mu$  is the energy of state  $\psi_\mu$  in the absence of tunnelling. The  $\delta()$  part means that only expressions in the summation where  $E_\mu$  equals  $E_\nu$  are valid

They then made some simplifications and inserted expressions for the matrix element in an attempt to come up with a practical theoretical model for STM. Their analysis had several limitations that restricted its accuracy. They approximated the tip wavefunction using a spherical wavefunction, which produces a reasonable solution; however it does restrict the resolution a little. Doyen raises this issue<sup>[26]</sup> based on work by Chen<sup>[27, 28]</sup> and shows that using a d-orbital wavefunction in the model improves its resolution providing a better fit to experimental data. This is because in the end tip atom the electrons tunnel via one of the large lobes of the  $5d_{z^2}$  orbital which has a smaller radius than that of the 6s orbital (see Figure 2.5). Doyen proposes that the 6s orbital is too large to resolve the atoms seen in some STM images but the resolution can be explained if the electrons are tunnelling through the  $5d_{z^2}$  orbital.

Tersoff and Hamann insert an example expression for the surface wave function in order to illustrate their model. However using this model to describe a sample consisting of an adsorbate on substrate system, which is the case for much of the work described in this thesis, requires a much more complicated expression. Trying to use accurate models for a tip substrate system in order to model contemporary experimental results is non-trivial and forms an active research area in itself<sup>[29, 30]</sup>. It is important to remember that Bardeen's perturbation theory treatment is an approximation and is only valid if the perturbation is small, i.e. where the overlap of the tip and sample wavefunctions is small. This corresponds to a relatively large tip sample separation and/or low tunnelling current. If the tip sample distance is reduced then the wavefunction overlap becomes larger and the perturbation approach will start to break down.

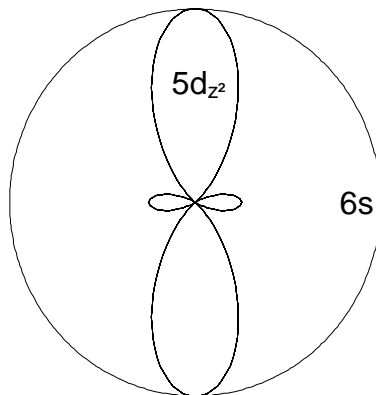


**Figure 2.5: Typical relative sizes of  $5d_z^2$  and  $6s$  orbitals in atoms in the tip. Doyen suggests that the radius of the  $6s$  orbital is too large to explain the atomic resolution seen in some STM images<sup>[26]</sup>.**

More recently, work has been conducted by Hofer that looks at the significance of the chemical element used for the tip upon STM images<sup>[15-17]</sup>. Despite the advances in the field, something as fundamental as the choice of tip still poses a challenge for those trying to model an STM and sample system.

Despite these limitations Bardeen's perturbation model and its application to STM by Tersoff and Hamann introduces some important principles in understanding how the sample and the applied voltage affect the tunnelling characteristics. The most important of these is that the tunnelling current is dependent upon the (surface) density of states of the tip and sample. The dependence upon the sample states enables STM to be a useful tool for characterising surface electronic structure. However the dependence upon the tip density of states could prove problematic if there is variation between different tips of the density of states at the tip apex.

In summary, there is a range of theoretical descriptions for the STM, ranging from the simplest one-dimensional barrier through to highly modified versions of the transfer Hamiltonian method. They describe how tunnelling works and as they have become more sophisticated, they have been able to incorporate more subtle features of the tips and samples used in STM experiments giving insight into the complex processes taking place.

### 2.2.4 STM Spectroscopy

From the theory of the STM, it can be shown that the current ( $I$ ) flowing between the tip and the sample is proportional to the integral of the density of states of the tip and the sample at the place of tunnelling at the energy ( $eV$ ) of the tunnelling electron. The surface density of the states at the energy of the tunnelling electron is not homogeneous and its spatial variation yields important information about the physical and chemical processes that can take place at the surface. By measuring  $I$  (and consequently  $\frac{dI}{dV}$ ) for different tunnelling electron energies at specific points across the surface an STM can provide a mechanism for measuring the density of states at the surface with high spatial resolution. This procedure is known as STM spectroscopy or Scanning Tunnelling Spectroscopy (STS). Even for a sample with a clean substrate surface this technique can be used to record the subtle changes in the density of states due to different parts of the surface structure<sup>[31]</sup>. This effect is particularly noticeable for semiconductors<sup>[32]</sup> where their band structure influences the shape of STS curves recorded at different parts of the sample.

The results from STS experiments where the sample is made from a substrate with molecules adsorbed onto it are more interesting still. When electrons tunnel from the sample to the tip (or vice versa) they will interact with the energy levels of those adsorbed molecules, as well as those of the tip and substrate. This means that an  $I$  vs.  $V$  plot for a particular sample will be different to that of the bare substrate because of the adsorbate (see Ref. [33] for an example). This difference is characteristic of the adsorbate, and in these situations, it is usual to present the data as  $\frac{dI}{dV}$  vs.  $V$  curves rather than  $I$  vs.  $V$ , in order to compare different curves for different adsorbates. This is because the differences between the  $I$  vs.  $V$  curves for different adsorbates are quite subtle and can often only be seen when comparing  $\frac{dI}{dV}$  vs.  $V$  curves. This technique has been applied frequently to self-assembled monolayers (SAMs) on gold (e.g. Ref. [34]). Despite the capability of an STM to record STS curves at different places on the surface, normally, for such a sample, the lateral position of the tip (relative to the surface feature positions) is not

considered to be that important when conducting the STM spectroscopy experiments on SAMs.

In order to resolve features well in  $\frac{dI}{dV}$  vs.  $V$  plots a good signal-to-noise ratio is needed in the  $I$  signal recorded. In order to achieve this various parameters of the experimental setup need to be carefully controlled. For this work the STM used was a carefully specified low temperature model constructed with high quality low noise electronic components to increase the signal to noise of an individual measurement.<sup>[35]</sup>

In addition it is normal to modulate the applied voltage at a relatively high frequency that is too fast for the STM feedback loop to detect. The tunnelling current will consequently also possess this modulation and phase sensitive detection can be used to extract this signal. The lock-in amplifier used to do this phase sensitive detection generates the  $\frac{dI}{dV}$  signal from the  $I$  signal as part of the process. Generating the  $\frac{dI}{dV}$  signals numerically from  $I$  data introduces systematic errors, as a consequence of the algorithms used which are avoided if phase sensitive detection is used.

If the tunnelling electrons have sufficient energy to excite a vibrational transition in a molecule then some will tunnel as if there was no molecule there but others will excite the mode from one state to the next and as a consequence, lose energy. The number of electrons that can tunnel via this second, inelastic, process depends upon the tip and surface density of states at the energy of the electron after the process. The total tunnelling current for an applied initial energy of the electrons is the sum of the currents for these two channels. On a curve of  $I$  against  $V$  for such a sample, the effect of the adsorbed molecule(s) is to increase the magnitude of the gradient of the graph where the electron energy is equal to the energy of the vibrational mode. As an example for a C-H vibrational mode ( $\approx 2900\text{cm}^{-1}$  or  $3.4\mu\text{m}$ ) this would happen at  $\approx 0.36\text{eV}$ . The first differential of this  $I$  vs.  $V$  curve should therefore show a step change at this energy and in the second  $\left(\frac{d^2I}{dV^2}\right)$  peaks should appear at the same energy. This is illustrated in Figure 2.6.

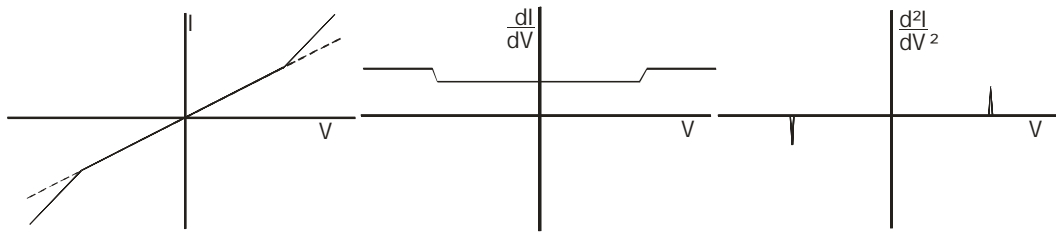


**Figure 2.6:** Schematic STS curves showing how they are affected by a vibrational mode on a surface. The gradient of the  $I$  vs.  $V$  curve increases when the electron energy matches the energy of the vibrational mode. Such a change in the  $I$  vs.  $V$  curve will lead to  $\frac{dI}{dV}$  vs.  $V$  and  $\frac{d^2I}{dV^2}$  vs.  $V$  curves with shapes as shown. The symmetry of these curves is due to the fact that the interaction of the mode with the tunnelling electrons is independent of the direction of the electrons across the tunnelling junction.

As described earlier, STS data are normally presented as  $\frac{dI}{dV}$  vs.  $V$  curves but when the data is intended to show vibrational modes the data are usually presented as second differential curves<sup>[12]</sup>. In order to record the fine details of such data it is vital to apply a modulation to the tunnelling voltage and use phase sensitive detection to extract the corresponding component in the tunnelling current. This technique of measuring the change in conductivity of systems containing vibrational modes with the same energy as the tunnelling electrons is known as Inelastic Tunnelling Spectroscopy (IETS). It is important to note that the widths of the peaks in the  $\frac{d^2I}{dV^2}$  vs.  $V$  curves are dependent upon the temperature ( $T$ ) at which the experiment was recorded according to the following expression<sup>[36]</sup>:

$$W^2 \cong W_I^2 + (1.7V_{ac})^2 + \left(\frac{5.4k_B T}{e}\right)^2 \quad \text{Equation 2.53}$$

where  $W$  is the measured width of the peak,  $W_I$  is the intrinsic line-width of the peak,  $V_{ac}$  is the rms bias modulation,  $k_B$  is Boltzmann's constant and  $e$  is the charge of the electron. When data are presented as  $\frac{dI}{dV}$  vs.  $V$  curves the peaks in the  $\frac{d^2I}{dV^2}$  vs.  $V$  curves appear as steps. In Chapter 5 the results of the STS experiments are presented as  $\frac{dI}{dV}$  vs.  $V$  curves where the temperature dependence governs the width of the steps.

The increase in current due to the inelastic channel is very small and in order to measure it the signal to noise ratio needs to be large enough to be sensitive to this increase. It is possible to repeat the experiments many times and average the results but the signal to noise ratio only increases as the square root of the number of experiments performed. This means that to increase the signal to noise ratio significantly requires collecting data for a long period of time. This can cause problems if the drift is large; by the time the required number of experiments have been conducted, the tip has moved away from the area chosen for the experiments. If the experiments are conducted at reduced temperatures this reduces the drift in addition to reducing the widths of the second differential peaks. However it is not possible to observe these subtle inelastic tunnelling effects just by using averaging and cryogenic cooling. It is necessary to use an STM with an intrinsically low noise floor and low drift e.g.  $\approx 0.6\text{\AA}/\text{hour}$  at 4.2K for single molecule STS<sup>[12]</sup>. This is because it is necessary to be able to have sub-molecular precision in the placement of the tip. The STS signal recorded can vary at different places upon the molecule<sup>[12]</sup>. The low temperature STM used in this work was specifically chosen to possess these properties. Its native specifications were enhanced by fitting it with anti-vibration legs on a concrete base. This design has in the past been used to conduct spatially resolved STS<sup>[37]</sup>. As an example of how these enhancements reduced the noise floor of the STM; from data recorded to produce the plot in Figure 2.7 it should be possible to measure a 1% change in the tunnelling current, with a signal to noise ratio of 10:1, after 409 measurements (which is less than the number of measurements recorded on this sample). For this experiment this would correspond to 74 minutes of capturing data. This experiment was conducted at  $\approx 78\text{K}$  increasing the lateral ( $x - y$ ) drift up to  $\approx 2\text{\AA}/\text{hour}$ . It is not clear that this increase is significant because the experiment was conducted on a whole thiol monolayer and it is not certain whether the spatial constraints that apply to single molecules also apply to monolayers since inelastic tunnelling has been observed in experiments conducted with metal-insulator-metal systems<sup>[38]</sup>.

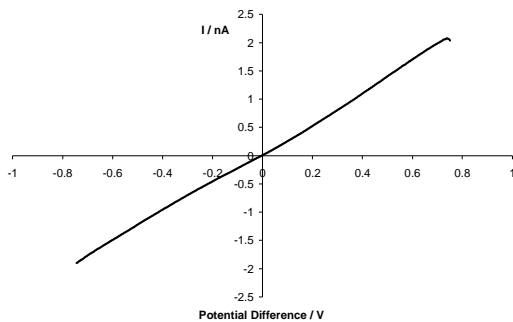


**Figure 2.7:** This is a copy of the  $I$  vs.  $V$  curve from Figure 5.30 that is used as an example of how the number of measurements recorded is adequate to lower the signal to noise ratio.

As with other techniques that measure the vibrational modes of molecules, IETS has selection rules that govern which modes can be observed and which cannot. IETS is still a new technique and the interpretation of the experimental results is still not fully understood. As described previously above a certain threshold voltage an additional inelastic channel is opened up for systems containing vibrational modes. However, it is not obvious what the cross-section will be for a given scenario. Detailed calculations have been performed on three different systems that describe the three main types of IETS behaviour of molecules adsorbed onto metal surfaces<sup>[39]</sup>. From these calculations not only is it clear that the size of the inelastic channel can vary but also that the conventional elastic channel can also vary with applied voltage. The reason for this is due to subtleties in the mixing of the tunnelling electron wavefunction with those of the adsorbed molecule and metal surface. For most of the vibrational modes, the increase in the tunnelling current due to the opened up inelastic channel is cancelled out by the reduction of the elastic channel. However for a few modes, e.g. C-H antisymmetric stretch for ethyne on Cu(100), the increase in the tunnelling current is large enough compared to the decrease in the elastic channel that the mode can be seen in IETS experiments[40]. In this situation, this is due to a large resonance originating from the  $\pi^*$  orbitals of the molecule mixing with electronic states in the metal surface around the Fermi level.

Alternatively, for some situations the tunnelling current can decrease with respect to the clean substrate. For example O<sub>2</sub> on Ag(110) shows a decrease in current at tunnelling energies corresponding to vibrational modes in the molecule<sup>[41]</sup>. This is due to a sharp resonance at the Fermi level caused by the molecular  $\pi g$  orbital hybridising with surface electronic states. Here the decrease in the elastic tunnelling channel is greater than the increase in the inelastic channel so the

current decreases. A third type of system has a molecule adsorbed onto the surface that does not have any electronic states near the Fermi level e.g. NH<sub>3</sub> on Cu(100)<sup>[39]</sup>. Here calculations show that the change in the tunnelling current due to the inelastic channel is small and undetectable with presently available technology.

The calculations performed in Refs. [39-41] show that despite the energy of the vibrational mode being within that accessible by the tunnelling electrons this does not always mean that this mode will induce a response in an STS experiment. The extent to which a vibrational mode will induce a measured response depends upon the interaction between the molecules electronic states and the surface electronic states. Additional factors not mentioned so far are the significance of the number of molecules adsorbed onto the surface and the position of the tip relative to the adsorbed molecules when the experiments are conducted. Although some early STM spectroscopy experiments mostly focussed upon SAMs on metals<sup>[42-46]</sup>, the more recent experiments that are able to record or model the vibrational transitions are configured to record the properties of just one isolated molecule on a sparsely covered surface. The latter reveal that it is clear that the relative positions of the tip and the molecule do make a difference to the data recorded. This suggests that there might be some value in repeating the experiments with SAMs with greater control over the position of the tip on the surface. The fact that these IETS experiments have so far been conducted on single molecules raises the issue of whether if a whole SAM was used, the  $\frac{d^2I}{dV^2}$  vs. V curves would still show the peaks seen in the single molecule case. A modern variation of the metal-insulator-metal type experiment where the electrons tunnel though a pore of diameter  $\approx 50\text{nm}$  filled with a SAM recorded these peaks at 4.2K<sup>[38]</sup> suggesting that it should be possible to also measure them with an STM.

The new research described in this work concerns illuminating such systems with infrared radiation at a frequency corresponding to the vibrational transitions in these molecules. It is not clear how this would affect the IETS characteristics of the systems investigated, one possibility is that the laser would interrupt the IETS process removing the features in the  $\frac{dI}{dV}$  vs. V curves. If a vibrational mode that would normally be involved in an IETS process is in its first excited state rather than its ground state as a consequence of the laser then it would not contribute in

the same way to the IETS process. However it is also expected that the heating effect of the laser on the sample and tip would be significant and prior to doing the experiments it is not clear how these two effects would work together hence providing an extra complexity to the analysis of the experimental results.

In summary, STM spectroscopy can be used to measure the conductivity characteristics of a sample, which can be used as a guide for its surface density of states. The spatial resolution of an STM enables the measurement of how the density of states varies across the surface. A special case of STM spectroscopy, IETS is able to record the presence of inelastic channels in the tunnelling current due to vibrational modes present in molecules adsorbed to the surface. These are usually presented as peaks in  $\frac{d^2I}{dV^2}$  vs.  $V$  plots. An additional complication is the extent to which the molecular orbitals interact with those of the substrate. This controls the size of both the inelastic and elastic channels around the energy of the vibrational mode in the molecule. The relative sizes of these two channels around this energy determine the size and direction of any peaks in a  $\frac{d^2I}{dV^2}$  vs.  $V$  plot.

Although IETS has been demonstrated to work with single molecules, it might be initially more useful to conduct experiments with greater coverage, when the position of the tip does not need to be as tightly controlled, providing a greater degree of flexibility when investigating the interaction with the laser tuned a vibrational mode of interest in the sample.

## 2.2.5 STM Equipment

This section is divided into two parts. The first and largest part describes the details of the low temperature ultra high vacuum (UHV) STM and associated equipment used as part of this work. The second, smaller part, describes the equipment used to make the tips for the STM.

### 2.2.5.1 Low Temperature Ultra High Vacuum STM

So far, STM has been described in general terms that would apply to many types of STM in use. This section describes some of the details of the specific STM used as part of this study. The STM is an Omicron LTSTM unit mounted in a UHV chamber as shown in Figure 2.8.

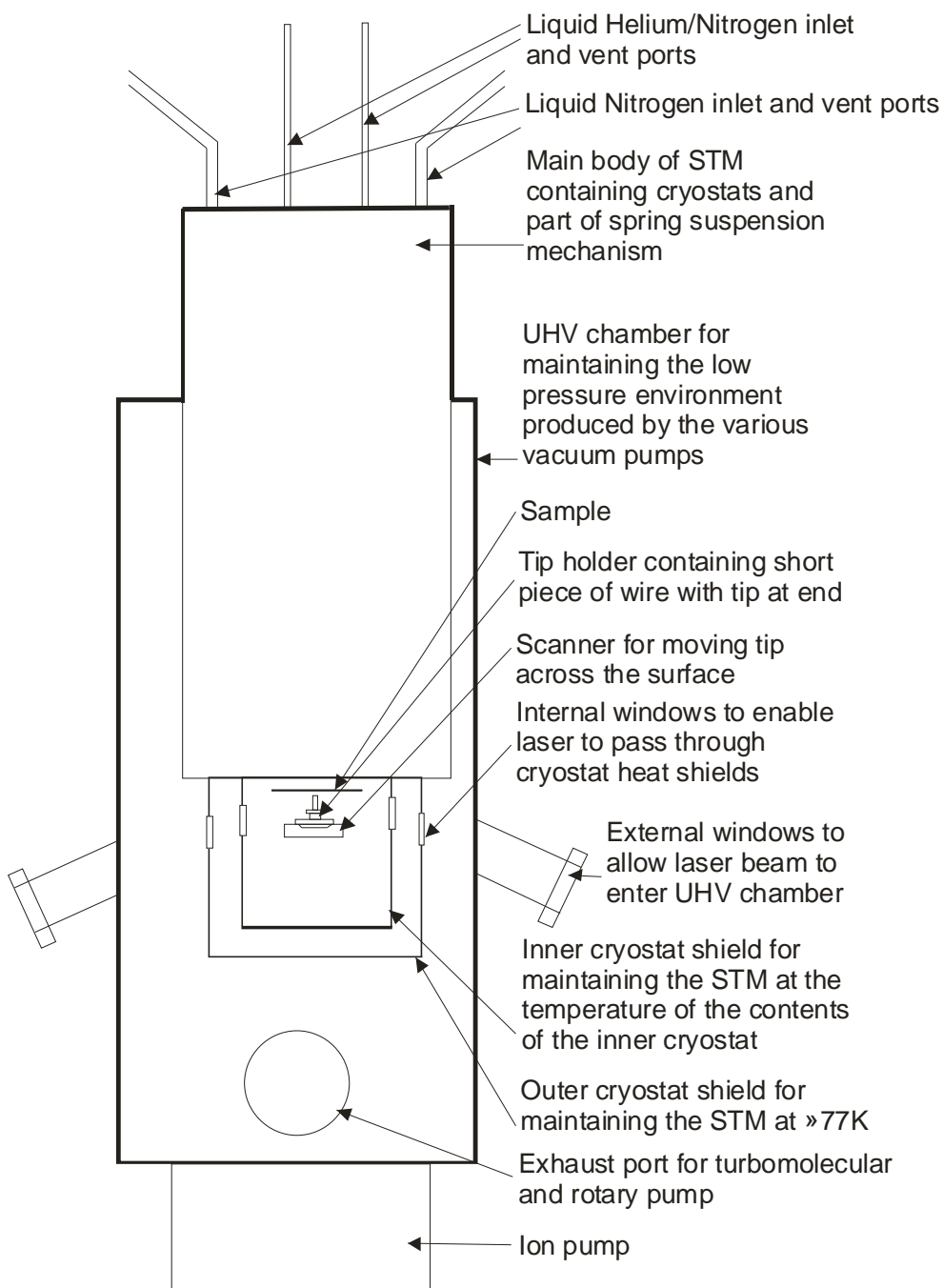
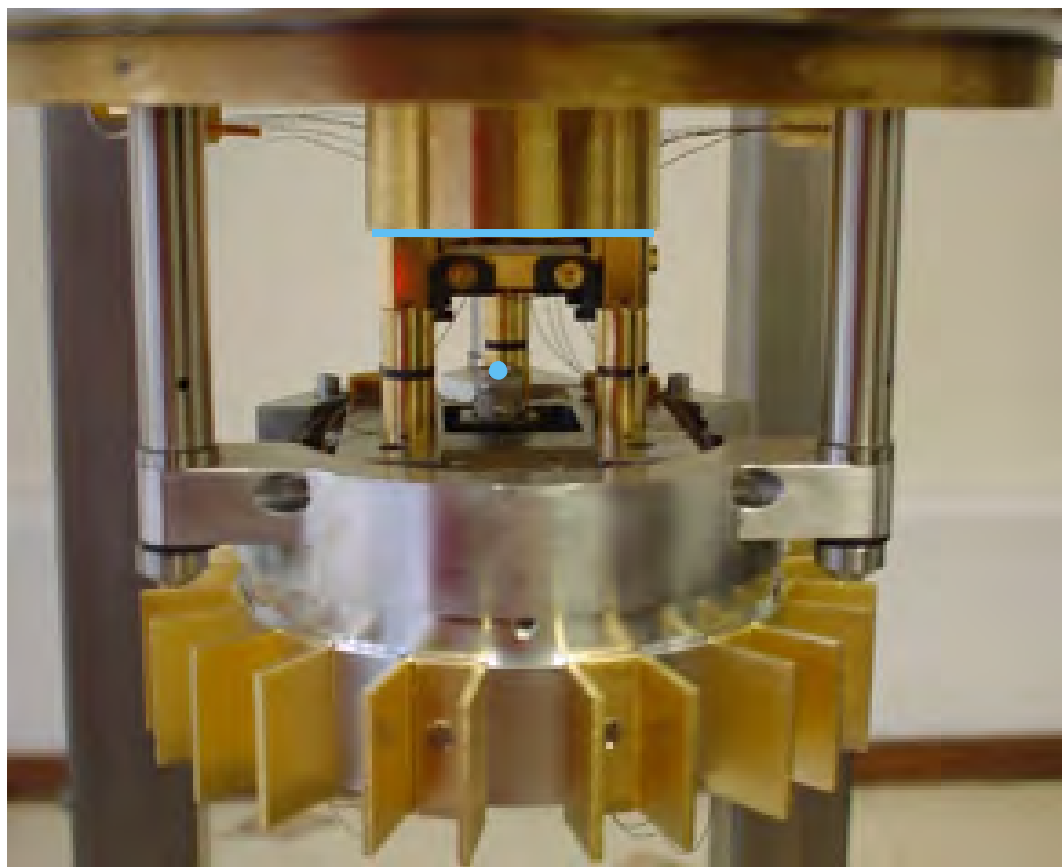


Figure 2.8: A stylised diagram showing some of the components of the LTSTM.

The STM head unit is suspended on springs during use. Figure 2.9 shows a photograph of the STM head unit showing where the head unit detaches from the cryostat.



**Figure 2.9: Photograph of the STM head unit. The piezoelectric stack is in the centre of the image. A tip holder (with tip) would sit on top of it in the place marked by the blue dot. The silver vertical rods to the left, right and rear (obscured) can be lowered such that the head detaches from the inner cryostat at the places marked with the blue line and becomes suspended on springs.**

Firstly, it needs to be explained why it was decided to use a UHV STM. This adds significantly to the complexity of aspects of the experiments conducted and must provide a significant benefit to the project in order to justify this. Examining samples in UHV significantly reduces any contamination of the surface of the sample used. For some of the samples this may not be that critical but possessing this facility allows greater flexibility in the samples that can be investigated. For example in the next chapter, some of the samples that are described are made

using gas dosing, which is only possible in a vacuum environment. If such procedures were conducted in a lower quality vacuum environment, there would be too much contamination to confidently know the identity of species observed on the surface. This reduced risk of contamination becomes even more important when another feature of this STM is taken into consideration.

The STM has two nested cryostats with which it is possible for the STM to be cooled to  $\approx 5\text{K}$ . However, as described in §2.2.2, most of the work conducted with this STM was conducted with the inner cryostat filled with liquid nitrogen. This is primarily for cost reasons but also out of a desire to develop procedures that work in the more manageable 77K to 80K range. Although it initially might be better to develop highly successful techniques that require liquid helium cooling, it will be more difficult to extend these techniques such that they can be used routinely. In addition, at these low temperatures the probability that unwanted species will adsorb onto the surface becomes much greater.

Even under UHV conditions, it is still possible over several months to accumulate unwanted species on a sample surface. For example, this means that care needs to be taken when transferring tips and samples into the chamber so that as much water vapour is removed as possible. Despite the important role played by the presence of a UHV chamber and the facility to cool the sample, of greater importance is the ability to isolate the STM head from external vibrations. Figure 2.9 shows the rods that are lowered to detach the head from the cryostat.

The particular UHV chamber used is a Multiprobe® Surface Science System unit (OMICRON Vakuumphysik GmbH; [www.omicron.de](http://www.omicron.de)).

Main pumping is provided by a series arrangement of a rotary and a turbo-molecular pump. Due to the sensitivity of the STM to vibrations it is not possible to maintain the vacuum with these pumps so a Varian Vaclon Plus 300 ion pump is used for this purpose. (This is mounted in the cuboid base underneath the UHV chamber.) Additional pumping is provided by a Titanium Sublimation Pump (TSP), used mostly for removing hydrogen and minimising the effect of adding small amounts of air whenever samples or tips are loaded into/removed from the chamber.

Another important feature of this specific LTSTM is the electronic equipment used when conducting spectroscopy experiments (see §2.2.4). Due to design faults

and limitations of the electronics in the STM, it does not measure the data for  $I$  vs.  $V$  curves accurately. This is only a small defect and cannot easily be seen in the  $I$  vs.  $V$  curves themselves but is more evident in the  $\frac{dI}{dV}$  vs.  $V$  curves. Due to UHV and cryo-mechanical constraints, the wires that carry the voltage and current to the tip and sample are too weakly shielded to protect the electronic signals from cross-talk with other electronic components in the in the STM. This adds a frequency component to the  $I$  vs.  $V$  signals that can be clearly seen in the  $\frac{dI}{dV}$  vs.  $V$  curve. To overcome this problem additional electronics are used to add an identical frequency component  $180^\circ$  out of phase with the one generated by the electronics inside the STM. The box containing this additional electronics (compensation box) is not used on its own; instead, it is combined with a lock-in amplifier in order to operate correctly. The compensation box does not just add a compensatory frequency component to the current signal; it also adds a reference signal to the applied voltage signal. The lock-in amplifier compares this reference signal with the current signal, and then extracts the component at the frequency of the reference signal from the current signal, before sending to the one of the external inputs of the STM. As a consequence of this process, the signal that it sends to the external input is a  $\frac{dI}{dV}$  vs.  $V$  signal rather than a current signal. None of the  $\frac{dI}{dV}$  vs.  $V$  graphs shown in the results section for all the different samples are calculated from the  $I$  vs.  $V$  graphs but are measured directly from this external input. Figure 2.10 shows how the various pieces of equipment are connected together for STS experiments.

Starting with this present paragraph the remainder of §2.2.5.1 now focuses upon the modifications made to the original specifications in order to conduct the experiments chosen as part of this project. Figure 2.11 shows some of accessories attached to the main chamber that contains the STM. Modifications to the original design are labelled as follows:

## 1. Gas/liquid dosing line

This dosing line is used to add CO, O<sub>2</sub> or a vaporised liquid into the chamber in a controlled manner. Some of this material will be deposited upon the sample where it can be studied with the STM. Initially liquids were dosed

using this dosing line but there was some concern that the chemicals used would have an undesired effect upon the components of the STM so this facility was not used for the collection of the data in this thesis. It was replaced with a second liquid dosing facility (marked as **2** in Figure 2.11) attached to the loading arm. When a sample was dosed here the chemicals to be used will only be exposed to the inside of the loading arm and not to the contents of the main chamber.

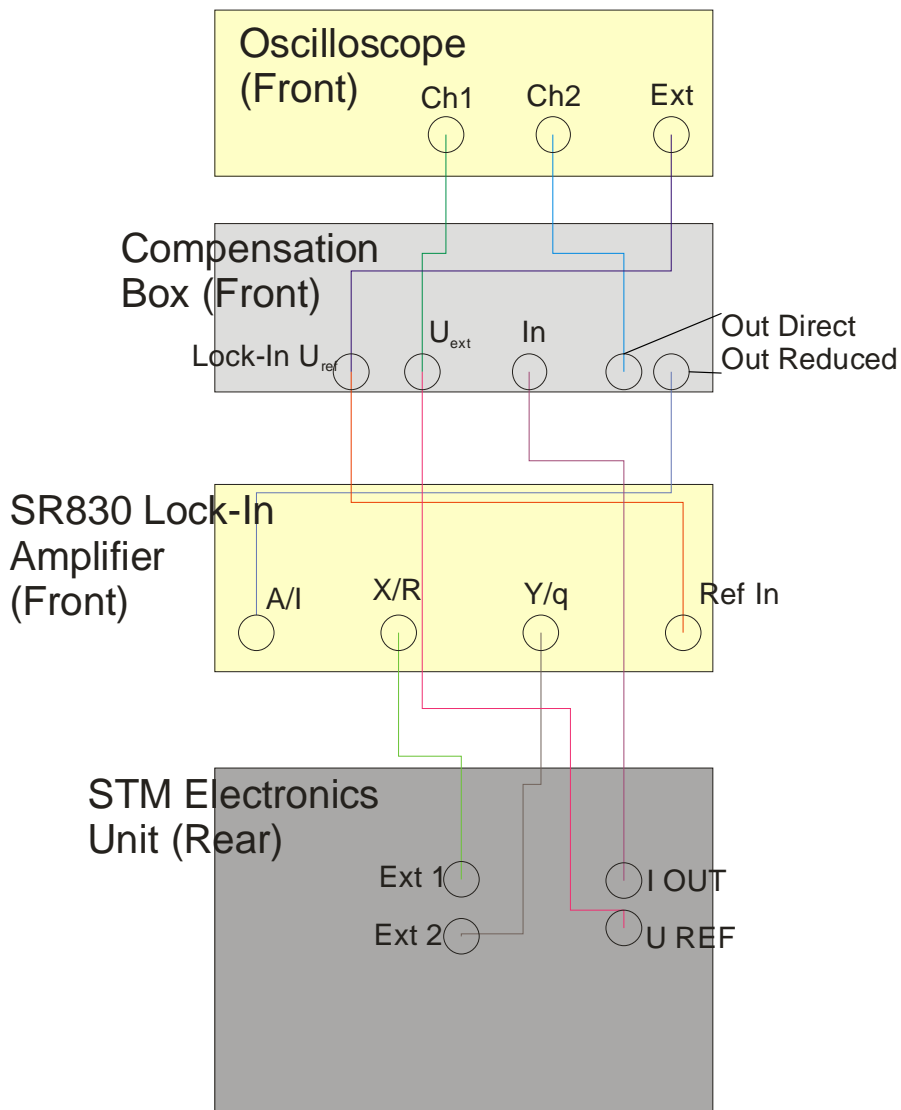


**Figure 2.10:**  
A schematic diagram showing how the various electronic components used for the STS experiments are connected together.

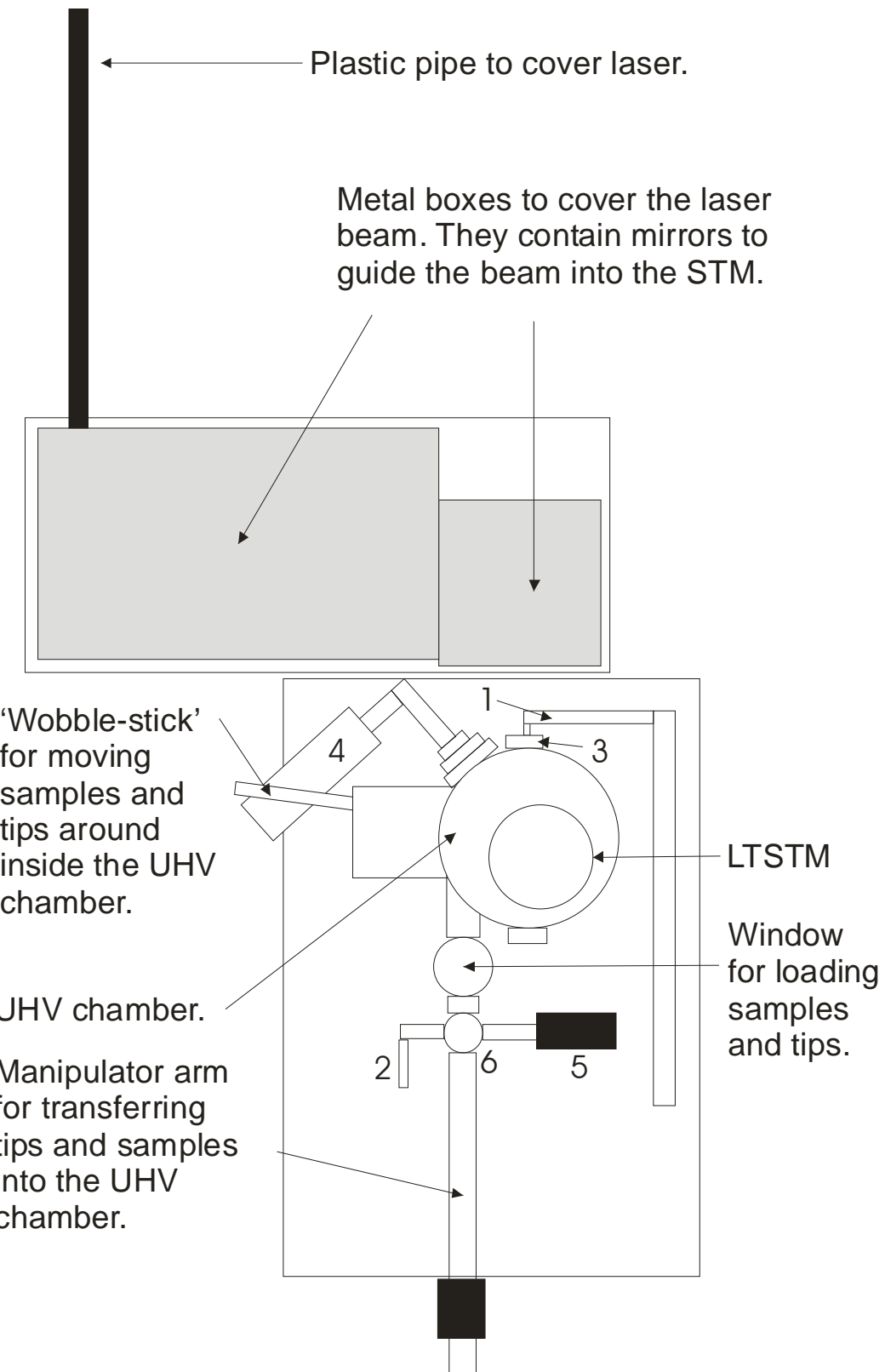


**Figure 2.11:** A highly stylised plan of the rig. Descriptions of the numbered components are included in the text.

## 2. Liquid dosing line

This dosing line was used for all the work presented on dimethyl disulfide (DMDS). It consists of a glass bulb moulded to a ‘mini-flange’ adaptor, a ‘Swagelock’ valve and a bleed valve. A vapour pressure of dimethyl disulfide would build up behind the bleed valve, which is then used to carefully control the quantity of DMDS released into the loading arm.

## 3. $\text{CaF}_2$ infrared transparent window

The window was replaced with one made from calcium fluoride ( $\text{CaF}_2$ ) since this window needs to be transparent to infrared radiation. (See §2.3.3)

## 4. Mass spectrometer

This enables the quantitative identification of the species in the chamber. This is extremely helpful when dosing material into the chamber or searching for leaks.

## 5. Mass spectrometer & pressure gauge

This was used to measure the total and partial pressures of species in the loading arm.

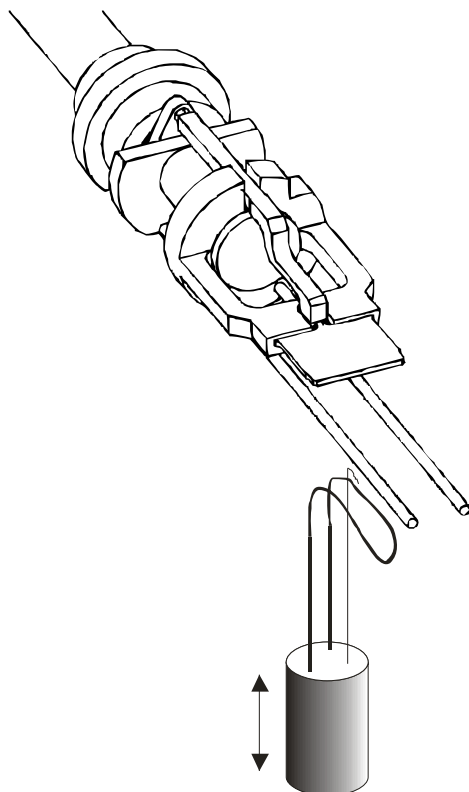


**Figure 2.12:** Showing how the thermocouple and resistive heater are used with the manipulator arm to gently heat samples. The shaded cylinder represents the screw thread which can be moved in the direction shown by the arrow to raise and lower the resistive heater (dark loop protruding from the cylinder) and the thermocouple wire (thin line protruding from the cylinder). The loop of resistive heating wire is narrow enough to fit between the two parallel tungsten rods. (This figure is based upon Figure 20 from the Multiprobe® Surface Science Systems User’s Guide Version 1.5, OMICRON Vakuumphysik GmbH. Used with permission.)

## 6. Sample heating system

This was used to heat the sample to  $\sim 55^{\circ}\text{C}$  whilst dosing it with dimethyl disulfide to increase the proportion of molecules that chemisorb onto the surface. It consists of a thermocouple and a resistive heating filament mounted on a screw thread that controls their vertical position. When they are lowered, the sample can be positioned over them with the manipulator arm. Raising the screw thread allows the thermocouple to touch the back of the sample plate and brings the filament closer to the sample. Both the thermocouple and the filament can pass through the parallel tungsten rods that form part of the manipulator head mechanism (see Figure 2.12). The samples used are all gold deposited on borosilicate glass with a thin  $\sim 3\text{nm}$  layer of chromium in between the gold and the glass. The glass will slightly hinder the heat flow between the back of the sample plate, meaning that the thermocouple reading is a little high relative to the sample temperature. The thermocouple and the filament are connected to the outside of the apparatus via ceramic feedthroughs.

### 2.2.5.2 Tip Manufacture

One of the most crucial parts of an STM experiment is the tip that is used to image the surface. This is a very delicate component and is very difficult to manufacture correctly. In STM, tips can be made by cutting or etching a piece of wire. Ideally, if a wire of suitable composition (e.g. Pt/Ir) is cut in a certain way then its very end will be rough enough to have a high likelihood of being atomically sharp. However this process is not very reproducible so etching of a piece of wire (e.g. W) is preferred. With etching an electrochemical process is used to remove material from the end of the wire to leave behind a sharp point.

The text below describes the equipment developed for making etched tips. For a description of how this equipment is used see Appendix A. The electrochemical process to make etched tips uses an AC or DC low voltage electrical supply. The equipment used for these two methods is broadly similar for both but there are

some important differences. The simplest method of these two uses an AC supply; see Figure 2.13 and Figure 2.14:

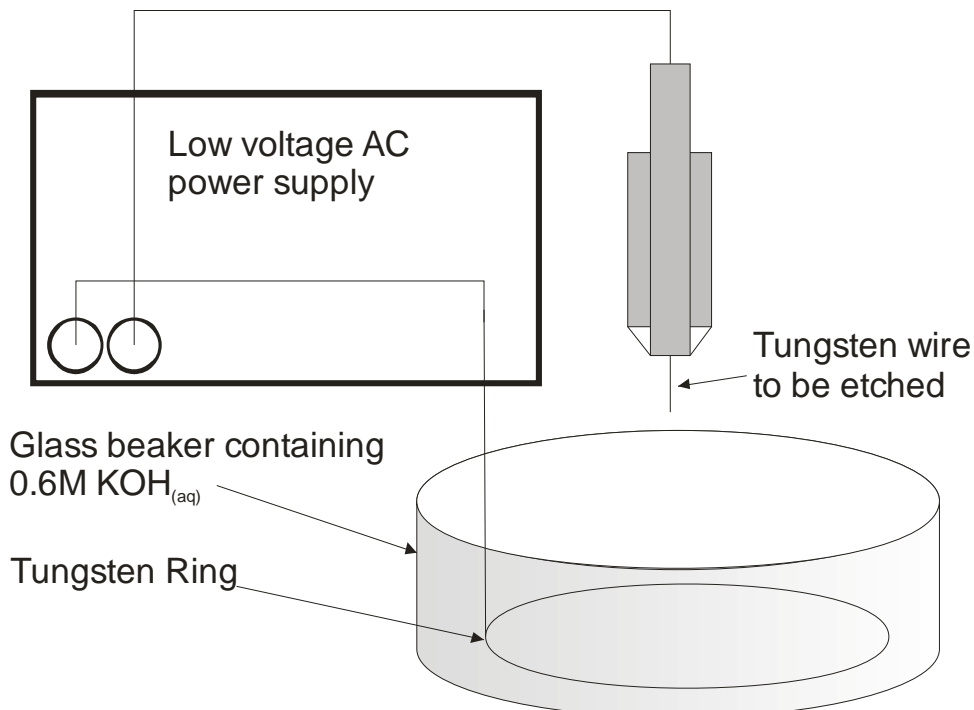


**Figure 2.13: Diagram of the AC tip etching apparatus.**

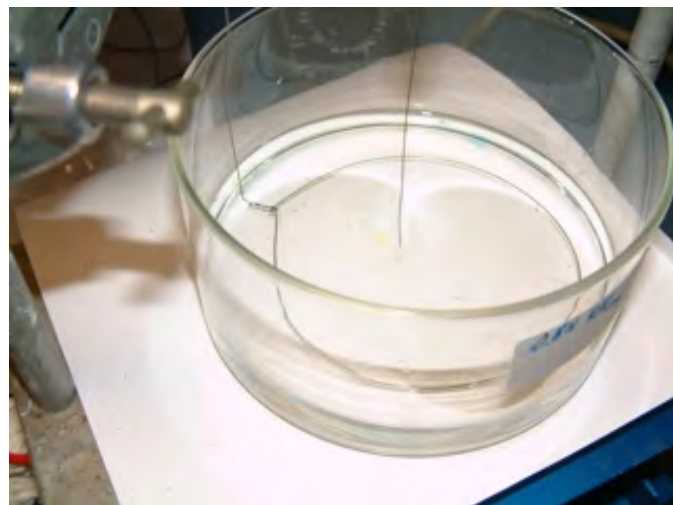


**Figure 2.14: Close-up photograph of the beaker, tungsten ring and wire, shown in the previous Figure showing how the wire is positioned with respect to the ring.**

The setup for using a DC supply is similar but a little more complicated; see Figure 2.15 & Figure 2.16. Due to the etching reaction proceeding via a different

mechanism, this setup has to use a special type of power supply to control the current flow (see Appendix B for the circuit diagram of this supply).

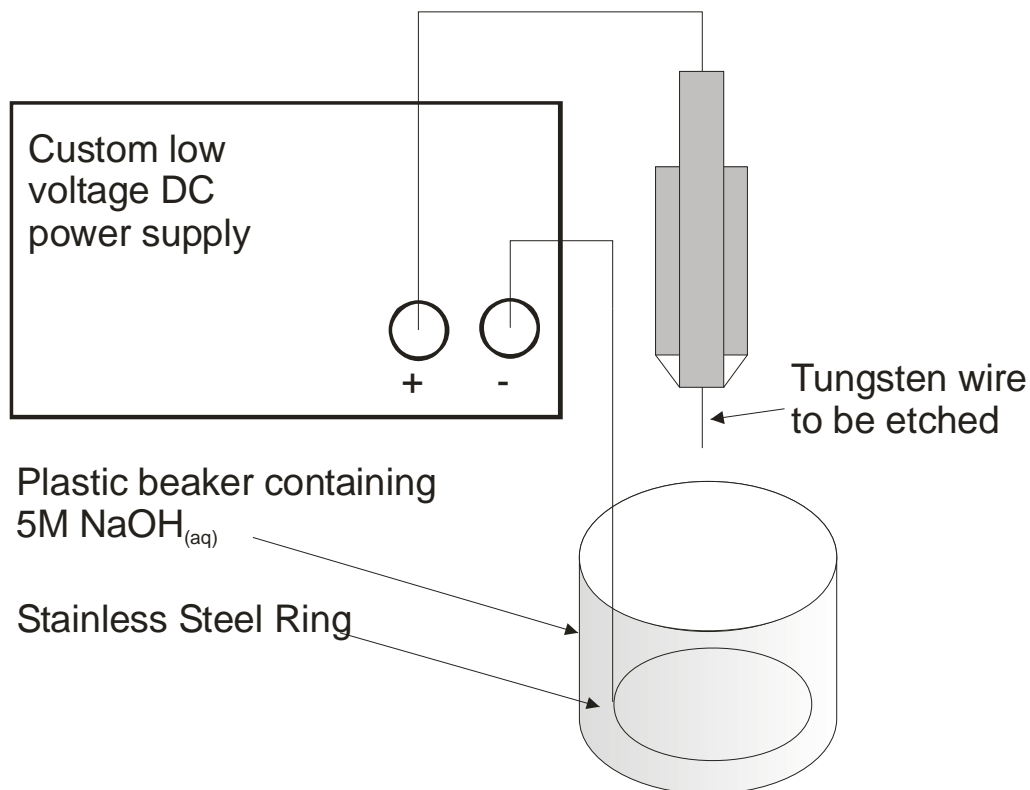


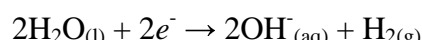
**Figure 2.15: A schematic diagram of the apparatus used for DC etching.**

The DC process still uses a metal ring in a hydroxide solution but this time the ring is smaller and is made of stainless steel (as per the instructions given by the STM manufacturer); the hydroxide solution is a much more concentrated 5M  $\text{NaOH}_{(\text{aq})}$ .

In both instances the electron flow drives the etching process by oxidising the tungsten atoms to soluble  $\text{WO}_4^{2-}$  ions. In the DC etching case the half-reaction at the tungsten wire is:



And the half-reaction at the stainless steel wire is:



This gives an overall reaction process of:



In the case of AC etching both half-reactions take place at both the wire and the ring, alternating between each 50 times a second. This means that the tungsten ring is slowly etched away too.

To see what kind of tips this equipment produces and images of samples collected with them see Chapter 3.



**Figure 2.16:** Showing the plastic beaker and smaller stainless ring used for DC etching.

## 2.3 Optical Parametric Oscillators

### 2.3.1 Overview

An important feature of this research is the ability to expose the sample (especially the area around the tip) to modulated infrared radiation with an energy corresponding to the energy of vibrational transitions in the species on the surface.

Since the native wavelength of an ‘off-the-shelf’ monochromatic laser is unlikely to match the vibrational transition of interest, a tuneable laser source is required.

An Optical Parametric Oscillator (OPO) is such a source. These devices provide a good way of producing a wide range of wavelengths of electromagnetic radiation from the infrared through to the visible.

There are various different types of OPOs in existence but they all have several characteristics in common:

1. They all make use of the optical properties of a crystal, which converts an incident photon into two photons, the energies of which sum to the energy of the incident photon.
2. They all contain a cavity that is resonant with one of the photons produced by the crystal.
3. The vast majority have some way of adjusting the balance of energy between the two photons produced by the crystal. This provides the tuning capability of the OPO.

This chapter provides an overview of what OPOs are and how they work particularly with respect to the specific OPO used in this work. This description is not intended to be fully comprehensive but is designed to be a starting point on the subject. For a more comprehensive treatment on the subject see Ref. [47, 48].

### 2.3.2 Background & Theory

Key to the operation of an OPO is the non-linear behaviour of the crystal in the centre of its cavity. In conventional optical materials the polarisation (**P**) induced in the material is linearly dependent upon the incident electric field (**E**):

$$\mathbf{P} = \epsilon_0 \chi(\omega) \mathbf{E} \quad \text{Equation 2.54}$$

where  $\epsilon_0$  is the permittivity of free space,  $\chi(\omega)$  the polarizability of the material and  $\omega$  is the frequency of the radiation. At large values of  $E$ ,  $P$  no longer increases linearly and is better represented as a series expansion:

$$\mathbf{P} = \epsilon_0(\chi_1 \mathbf{E} + \chi_2 \mathbf{E} \cdot \mathbf{E} + \chi_3 \mathbf{E} \cdot \mathbf{E} \cdot \mathbf{E} + \dots) \quad \text{Equation 2.55}$$

The values of  $\chi_n$  tend to decrease with increasing values of  $n$ . For most materials the value of  $\chi_2$  and higher order terms of  $\chi$  are small so this non-linear effect only appears at large values of  $E$ . However some materials have higher values of  $\chi$ , this reduces the value of  $E$  required to introduce a non-linear response in  $P$ . The key term in Equation 2.55 for the operation of an OPO is  $\chi_2 E \cdot E$ . In some circumstances both values of  $E$  are the same; this results in the generation of radiation at twice the incident frequency. In other situations these two values of  $E$  have different frequencies and this is the case with optical parametric generation. In order for a material to facilitate such a non-linear parametric process with significant power output, a condition called ‘phasematching’ must be satisfied inside the crystal. This is described by the following equation:

$$c\Delta k = n(\omega_p)\omega_p - n(\omega_s)\omega_s - n(\omega_i)\omega_i \quad \text{Equation 2.56}$$

Where  $\omega_p$ ,  $\omega_s$  and  $\omega_i$  are the angular frequencies of the pump (incident/input), signal and idler (output) photons respectively;  $n$  is the refractive index of the material (at angular frequencies  $\omega_p$ ,  $\omega_s$  and  $\omega_i$ ) and  $c$  is the vacuum speed of light. The labels of  $\omega_s$  and  $\omega_i$  are chosen such that  $\omega_s > \omega_i$ . When the phasematching condition is met,  $\Delta k$  equals zero and the power of the output photons is of the form shown in the green curve in Figure 2.17.

If the phase matching condition is not met then the power of the output photons will be modulated along the length of the crystal with a characteristic length of  $L_c = \pi/\Delta k$  (see black curve in Figure 2.17). Apart from a few special cases, this phasematching condition is not met in most crystals with non-linear optical properties. This necessitates another approach: Quasi-Phasematching. This solution provides an alternative to fulfilling the full phasematching condition but

as a consequence the output power is slightly reduced. If, in the crystal, the direction of the optical axis can be inverted after distance  $L_c$  then instead of the output power dropping back to zero after distance  $2L_c$  the output power will increase. Continuing this sequence along the crystal produces an output power curve in the shape of the red curve in Figure 2.17.

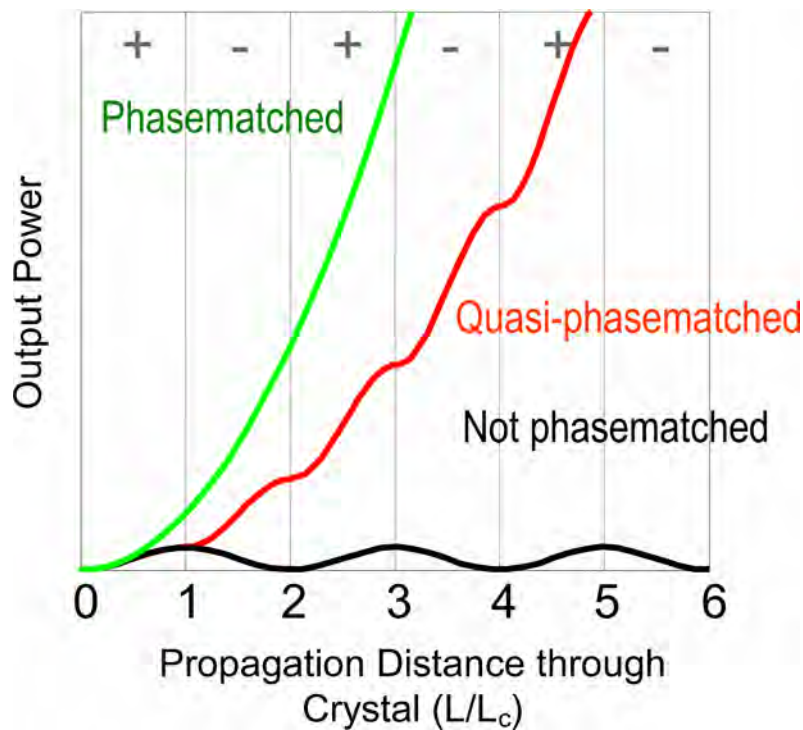


**Figure 2.17: Comparing the power output from a non-linear parametric process with different types of phasematching.**

In general it is not possible to modify the optical axis of most crystals into an alternating pattern like this. There are a few exceptions and lithium niobate ( $\text{LiNbO}_3$ ) is one of them. It is possible to change the direction of the optical axis by applying a large electric field and it is also possible to do this to some parts of a crystal whilst leaving others as they were.

During the manufacture of a crystal of  $\text{LiNbO}_3$  a permanent electric field is applied across it. This ensures the orientation of the crystal's optical axis is known with respect to its physical dimensions. After the crystal has been cut up into individual samples with the required orientation, it is exposed to another electric field through a metal mask, in the opposite direction to the first. This process is

known as poling. The mask has a series of gratings e-beam etched through it (see Figure 2.18).

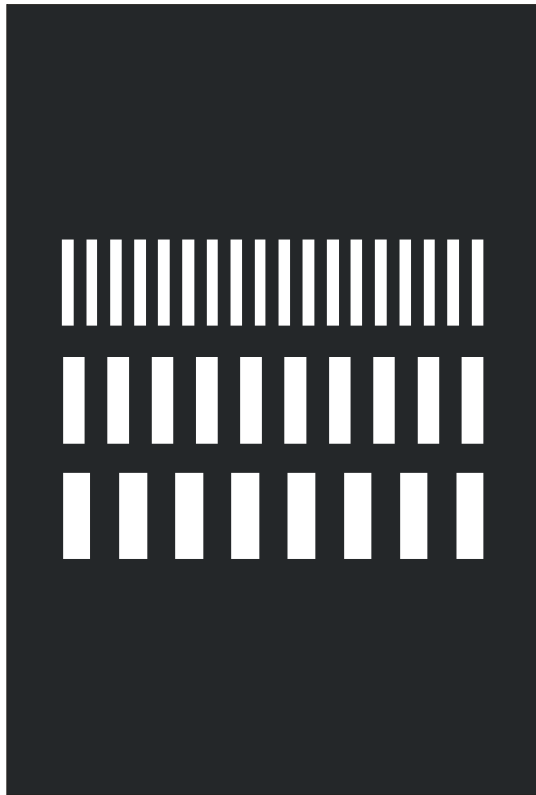


**Figure 2.18:** Stylised representation of a mask used for the poling of a lithium niobate crystal. Here are shown three sets of gratings each with a different period spacing to provide a tuning capability for the OPO. This mask would be placed on the side of a lithium niobate crystal and a high voltage applied across the crystal through the mask.

The effect of the electric field is to reverse the optical axis in the crystal where the gaps are in the gratings (Figure 2.19).

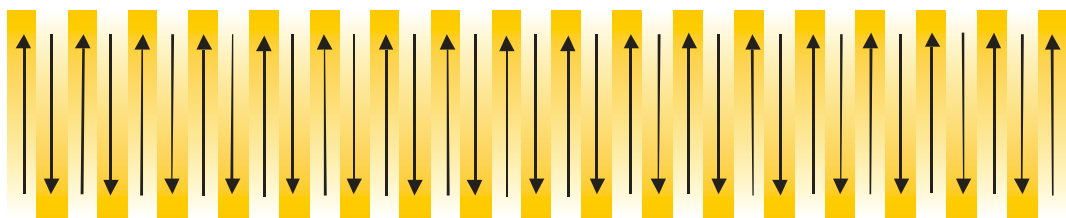


**Figure 2.19:** This is a stylised representation of the top grating in a Periodically Poled Lithium Niobate (PPLN) crystal made with the above mask and viewed from above. The arrows and shading indicate the orientation of the optical axis in the crystal.

The period spacing of the gratings in the mask corresponds to selected values of  $2L_c$ . Ordinarily this would mean that only certain output wavelengths of photons could be produced depending on the period spacing. However the refractive index

of the crystal changes with temperature so heating the crystal changes the frequencies at which phasematching occurs. Thus changing the temperature of the crystal provides a tuning mechanism for an OPO. As might be expected the range of available temperatures is limited so each grating patterned into the crystal has a finite wavelength range. By designing a mask where each grating has a different pitch and controlling where the input laser passes through the crystal allows the tuning of an OPO over several microns.

The non-linear properties of the crystal also allow for sum frequency generation processes. Combinations of any two of the pump, signal and idler photons are achieved in the crystal to produce other infrared and visible photons. These are potentially useful but they have very low efficiency, reducing the likelihood that they can be used in an experiment.

The efficiency of the non-linear processes in the crystal is greatly improved if the crystal is installed in a cavity that is resonant with either the signal or idler photons. This is due to another non-linear process that takes place inside the crystal: Difference Frequency Generation. In this process, the crystal converts two photons into a third with an energy equal to the difference between the energies of the first two. In the context of an OPO this means that some of the signal photons in the cavity combine with more pump photons to create more idler photons increasing the idler output power.

### 2.3.3 Specific Details of the OPO Used for This Work

In the OPO used in these experiments the PPLN crystal is mounted inside a folded cavity as shown in Figure 2.20 and Figure 2.21. The cavity is formed by mirrors M3 to M6 and the path that the beam takes through this cavity is indicated by the blue arrows. These mirrors are highly reflective for the signal photons and >80% transmissive for pump and idler photons. The cavity is synchronously pumped and is designed such that its round trip time is just under 17ns. This means that signal photons created in the crystal with one laser pulse pass around the cavity and then interact with the next but one laser pulse. The temperature and the grating of the

crystal used determine the wavelength of the signal photons produced by the crystal.

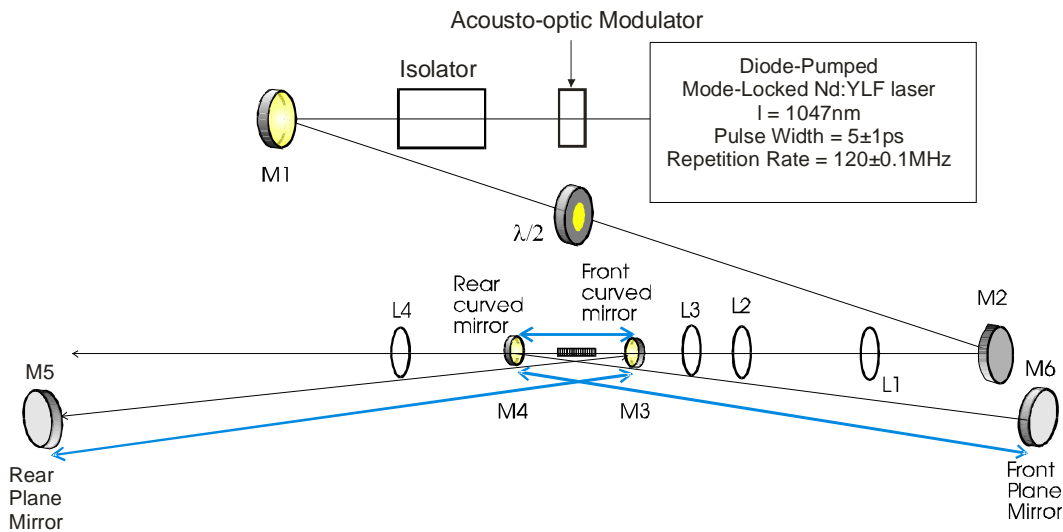


Figure 2.20: Schematic showing the layout of the OPO

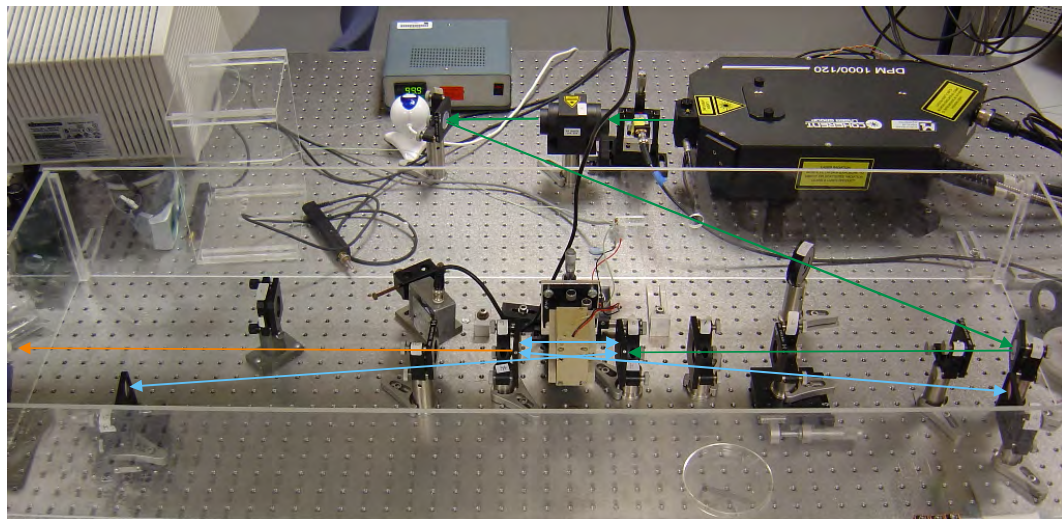


Figure 2.21: Photograph of the OPO used in this work. The coloured arrows show the paths of the different beams travelling through the OPO. The green arrows correspond to the path of the incident pump beam. The blue arrows as in Figure 2.20 show the path of the signal photons through the cavity. The orange arrow shows the path of the output beam from the OPO which contains components at several wavelengths: pump, signal, idler and combinations of these.

The position of M5 is adjustable so that the round trip time of the signal photons in the cavity can always be matched to the time between two photons in the pulse train from the pump laser. This raises an important issue in relation to the repetition rate of the laser.

In a non-linear process the output power is determined by the peak power of the laser source and in many applications the repetition rate of the pump laser is much smaller (e.g. 10Hz) in order to produce a higher peak power. Although increased peak power would be useful for the non-linear processes taking place inside the crystal, a repetition rate of 10Hz would require an impractically large cavity to maintain its synchronously pumped characteristics.

Figure 2.22 and Figure 2.23 show the idler wavelength range for each of the two types of crystals used. The ‘Grating’ figures inside the plot areas correspond to the pitch of each grating. (These charts are reprinted as originally provided by the designer of this OPO.<sup>[49]</sup> They include no information about the power of the laser beam at these different wavelengths. For the 29.0 $\mu\text{m}$  to 29.75 $\mu\text{m}$  gratings the laser power available was  $\approx$ 95mW but for the 30 $\mu\text{m}$  and 30.25 $\mu\text{m}$  gratings the power was only a few mW and therefore not usable for experiments. The reason for this is because when these two gratings are used the wavelengths of the corresponding signal photons are outside the limits of the reflective coatings on the cavity mirrors. Consequently it was not appropriate to verify the idler wavelengths produced by these wavelengths and the corresponding trendlines.)

Despite some of the data points in Figure 2.23 being recorded for temperatures below 100°C the crystal can only be safely operated at temperatures between 100°C to 200°C. Below the lower limit of 100°C the pump beam damages the crystal. This damage is not permanent. Restoring OPO operation to above 100°C will undo the damage. When operating the crystal within the normal temperature range of 100°C to 200°C the thermal energy in the crystal is able to compensate for the damage induced by the pump beam. Above 200°C the degradation to the insulation of the wires that provide power to the crystal heaters becomes too severe. The ‘domain wall’ between two regions in the crystal with opposing optical axes can be seen with a microscope. Appendix C shows composite microscope images of the two crystals that were initially supplied with the OPO.

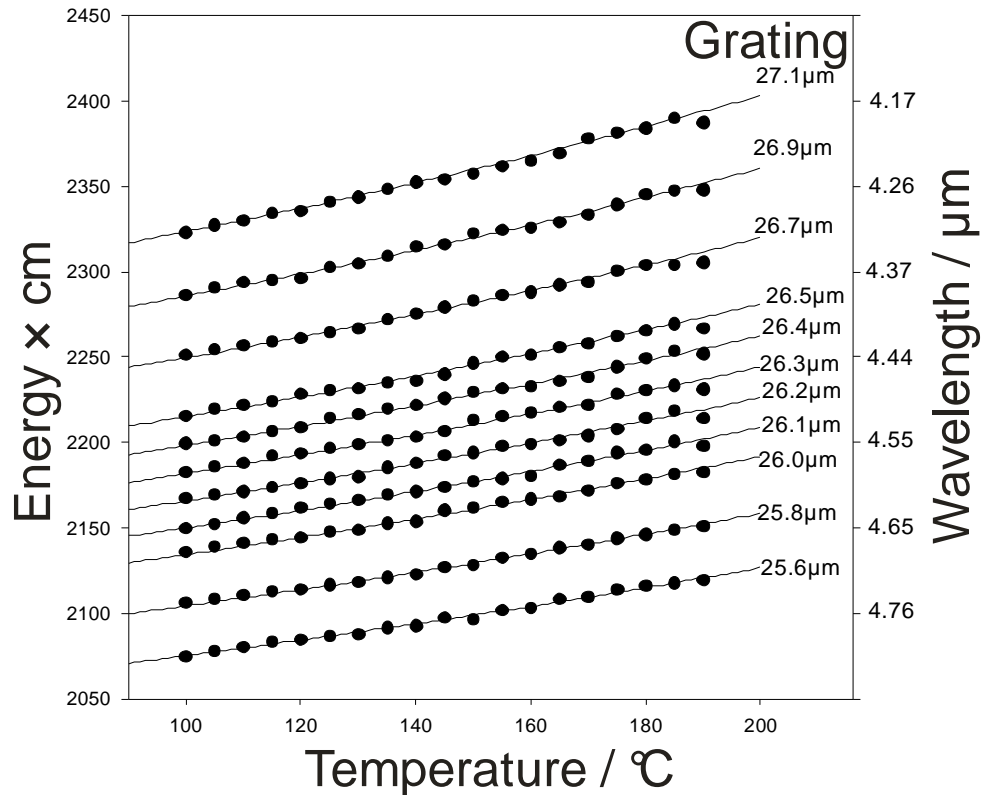


Figure 2.22: Showing how by using different gratings in PPLN crystal 1 at different temperatures the OPO can emit a wide range of wavelengths.

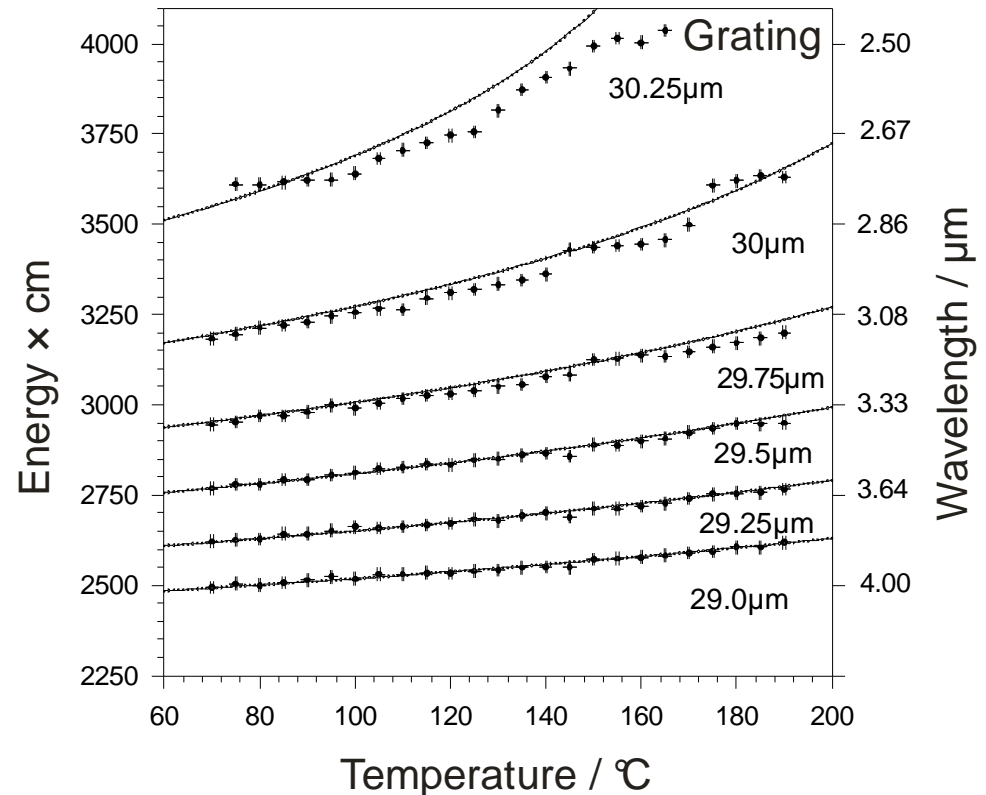


Figure 2.23: Showing how by using different gratings in PPLN crystal 2 at different temperatures the OPO can emit a wide range of wavelengths.

	Pump (1047nm)	Signal (1.34 $\mu$ m to 1.80 $\mu$ m)	Idler (2.50 $\mu$ m to 4.80 $\mu$ m)
Pump (1047nm)	523.5nm	587.6nm to 662.2nm	738.0nm to 859.5nm
Signal (1.34 $\mu$ m to 1.80 $\mu$ m)	587.6nm to 662.2nm	670nm to 900nm	1047nm (Pump)
Idler (2.5 $\mu$ m to 4.8 $\mu$ m)	738.0nm to 859.5nm	1047nm (Pump)	<i>1.25<math>\mu</math>m to 2.40<math>\mu</math>m</i>

**Table 2.1:** This shows the different wavelengths of radiation that can be emitted from the OPO. The figures in italics indicate photons that have a wavelength that is too long to be detected by the spectrometer.

As described earlier, in addition to the parametric processes, sum frequency generation processes take place inside the crystal. The table above shows the wavelengths of the photons produced in this way. The incoming photons in this process are along the top and the side of the table and the outgoing photons are in its main body. The wavelengths of the visible photons are measured by a spectrometer and this enables the wavelengths of the signal and idler photons to be calculated. The figures in italics indicate photons that have a wavelength that is too long to be detected by the spectrometer.

For the sake of completeness, it is worth describing how the beam from the OPO is directed into the STM. Figure 2.23 shows a schematic representation of the OPO and the optics that directs the beam towards the hole in the wall where it continues towards the STM. In Figure 2.23 the numbered features are as follows:

1. Pump laser.
2. Plastic box containing OPO.
3. Filter to remove all wavelengths from the OPO beam except the idler for use LDSTM experiments.
4. 25mm gold mirror.

5. Combination of 25mm diameter, -50mm focal length CaF<sub>2</sub> lens and 50mm diameter, 135mm focal length CaF<sub>2</sub> lens.
6. 50mm gold mirror.
7. Plastic pipe for covering the beam as it passes from the edge of the optical table to a hole in the wall.
8. Filter mounted on a shutter just in front of the hole in the wall. This filter removes all infrared components of the beam to enable alignment of the beam with the visible components. The filter is part of an interlock mechanism that only withdraws the infrared blocking filter when the all the beam covers on the other side of the wall (Figure 2.11) are engaged.
9. 12mm diameter hole in the wall to enable the beam to pass from the OPO laboratory to the laboratory containing the STM.

Gold mirrors and CaF<sub>2</sub> lenses are used to enable the propagation of radiation at all the wavelengths produced by the OPO to the STM.

The beam coming from the OPO has an initial beam size of  $\approx 60\mu\text{m}$  and has a small divergence, but due to the size of the distance between the OPO and the hole in the wall, the beam's diameter at the hole (with no additional lenses) is too large to cleanly pass through it.

Consequently the combination of lenses labelled as 5 in Figure 2.24 are used to emulate a convex lens with a long focal length required to bring the beam to a focus inside the pipe covering the beam in Figure 2.11. In order to do this, the divergent -50mm lens expands the visible beam to a size of  $\approx 10\text{mm}$  by the time the beam reaches the 50mm diameter lens. Despite the size of the visible beam being only  $\approx 10\text{mm}$  in diameter it is necessary to use a lens of 50mm diameter due to poor co-linearity of the components in the beam. Due to the way that the different wavelengths are generated inside the OPO they each propagate in slightly different directions. The pump beam follows the path of the mirrors and lenses that launch it into the chamber. The signal beam follows a path through the crystal that matches the round trip path of the cavity.

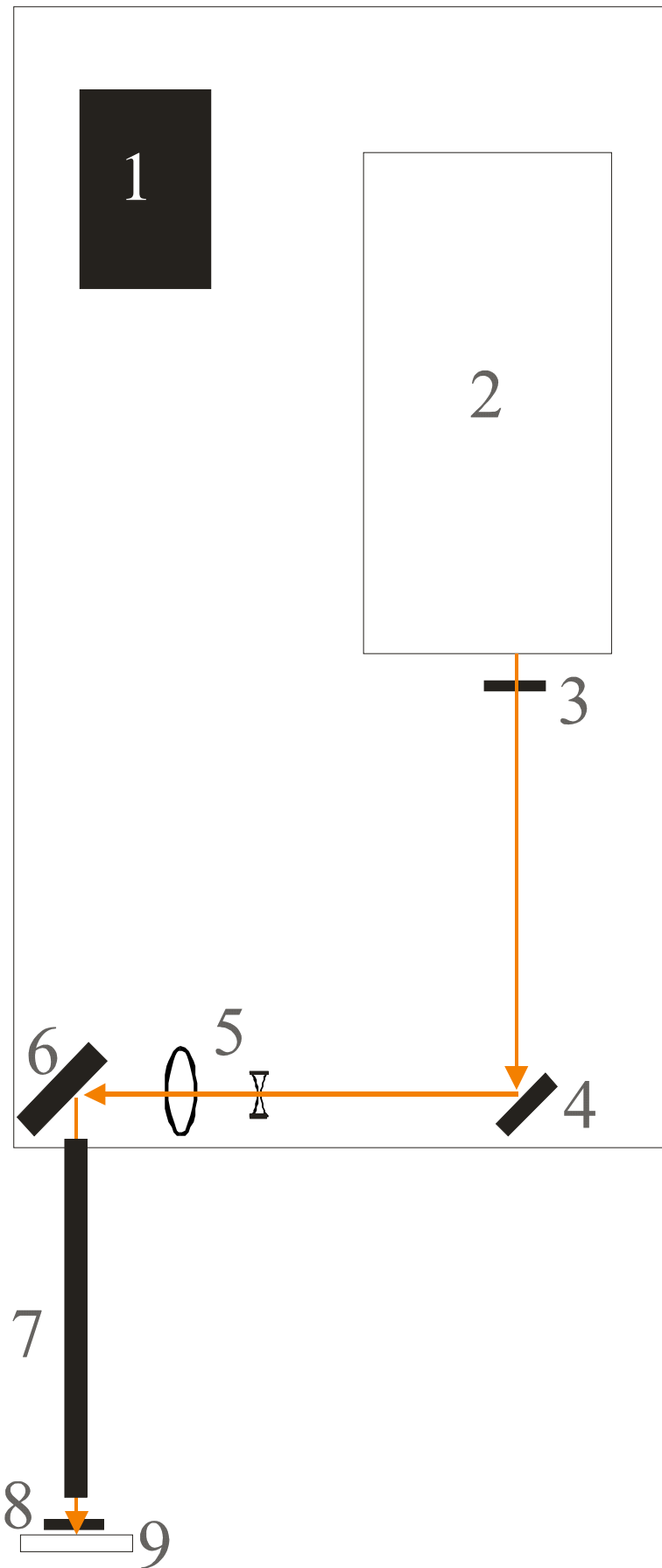


**Figure 2.24:**  
This shows how the OPO beam leaves the OPO and is manipulated before being passed through to the STM. The details of the numbered components are described in the text.

The direction of the idler beam is determined by vector addition of the direction of the pump and signal beams. The direction of any visible beam is determined by vector addition of the two infrared beams that combine to form it. The extent to which the beam paths of these components deviate from one another, increases with increasing size of the components in the beam. Below a beam size of  $\approx 1\text{mm}$  the components are approximately collinear but when the size of the components is increased to  $\approx 10\text{mm}$  the some visible components of the beam no longer overlap with the idler components of the beam. So although the size of each of the components of the beam is  $\approx 10\text{mm}$  the combined diameter of all of the beams is greater than  $25\text{mm}$  and hence a  $50\text{mm}$  diameter lens is needed to refocus the beam. At the point where the beam meets the second gold mirror the combined beam size is still substantial and so it needs to be  $50\text{mm}$  in diameter too.

Once the beam has passed through the hole in the wall it propagates down the pipe on the other side of the wall and through the metal boxes directed by three more gold mirrors (Figure 2.11). These mirrors finally direct the beam into the chamber via the infrared transparent window (marked as 3 in Figure 2.11). Before the second of these mirrors an iris is used to adjust the power of the beam. Since the beam has a waist inside the plastic pipe the beam is divergent at this point so a final  $25\text{mm}$  diameter,  $300\text{mm}$  focal length  $\text{CaF}_2$  lens is used to bring the beam to a focus at the sample.

In summary, this section has described how OPOs operate and how these principles are applied to the OPO used in this study. Details are given describing how the output from the OPO is directed into the STM.

## 2.4 Self-Assembled Monolayers

This section introduces the field of self-assembled monolayers, what they are, and why they are useful as samples to test this new variant of laser driven scanning tunnelling microscopy. As described in the introduction, when developing a new technique such as tuneable infrared LDSTM, it is important to have a system that

can be used as a control sample. Self-assembled monolayers were suggested as suitable candidates for this.

A self-assembled monolayer is a single layer film of a chemical that forms automatically on a surface when the surface is exposed to the chemical. The conditions under which this occurred determine the extent of the ordering of these molecules. Typically these layers will always be ordered in the direction perpendicular to the surface but in directions parallel to the surface the extent of the ordering can vary.

This type of system has been available in one form or another for many years. Originally, the interest in organic monolayers was due to their ability to control the wetting behaviour of vertical metal plates in the condensers of steam engines<sup>[50-52]</sup>. Coating these metal plates with such substances replaced the hydrophilic metal surface with a hydrophobic organic one. As the steam condensed into water on these coated plates, it formed droplets that fell down and came off the plate by gravity, thus freeing up an area on the plate to continue the condensation process. In contrast, when steam condensed on uncoated plates it formed a film of water that insulates the steam from the cold plate, hence hindering the condensation process. More recently, these coatings are being investigated as a way of constructing nanoscale structures as part of a ‘bottom-up’ approach. There is an ongoing trend amongst the disciplines of chemistry and biochemistry to conduct experiments on a smaller and smaller scale.<sup>[53]</sup> This requires structures in which, and with which, to do this. They can be made in two ways, a ‘top-down’ and a ‘bottom-up’<sup>[54]</sup> approach. The ‘top-down’ approach takes a larger structure and uses fabrication techniques to modify it into a desired structure. Conversely the ‘bottom-up’ approach takes small components such as organic molecules and connects them together in such a way to form the desired structure.

Of the different types of chemicals used to make monolayers those investigated most extensively have been alkanethiols. SAMs of alkanethiols have been investigated predominately on surfaces of gold, specifically Au(111), due to the ease of their manufacture and characterisation. Initially these monolayers were made by immersing gold (Au) surfaces into solutions of alkane thiol. As STM technology developed in UHV, it became possible to make these SAMs *in situ*,

which allows for a greater control over the amount of coverage of the sample. Many papers have been published over the years on the different ways that the molecules pack on the surface as the density of molecules increases<sup>[55-58]</sup>. The packing structure of the molecules on the surface progresses through a series of ‘phases’ as their surface density increases. Some of the phases are ordered; others are not. The transition between two ordered phases is usually via a disordered phase and occurs by the formation of ‘islands’ of the more dense structure in the ‘sea’ of the less dense phase. When the surface concentration of the thiols is low, the molecules are thought to lie horizontally on the surface<sup>[56, 59]</sup> (see Figure 2.25). As the surface density increases the angle between the carbon backbones of the molecules increases and the structure becomes a bit like a carpet (see Figure 5.1).

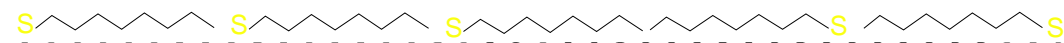


**Figure 2.25: A stylised representation of octanethiol molecules lying flat on an Au surface at low surface coverage. The diagonal zigzag lines are the carbon chains, the yellow S's are the sulphur atoms and the horizontal wavy line is the metal surface.**

For a variety of reasons, it was decided to use alkanethiols on gold as a test sample for this new type of LDSTM experiment:

1. It is relatively easy to make this Au(111) surface form of gold in air. (For more details see §3.3)
2. These Au(111) samples are air stable enough to survive the transit from their manufacture into the UHV chamber. For most metals when a clean metal surface is produced on a sample it will quickly react with constituents of the atmosphere (principally O<sub>2</sub> and H<sub>2</sub>O) before it can be loaded into the chamber. Consequently the preparation of a surface of most metals has to be conducted inside the UHV chamber itself. This requires a special preparation chamber which was not available for the work in this thesis.
3. These thiol molecules react with the surface to make strong covalent S-Au bonds with the surface. This means that the sample can be made at room

temperature and that the adsorbed molecules are less likely to move about on the surface.

4. The chemistry of the molecules is very simple making it easier to assign recorded phenomena with molecular structure.
5. The wavelength of the OPO can be tuned to the C-H stretching vibrational transition.
6. It is possible to create partially covered surfaces so that the response to the laser of the covered areas can be compared with the uncovered areas.

In summary, SAMs provide a suitable system that can be investigated with this new technique given the constraints of the equipment available.

## ***2.5 Laser-Driven Scanning Tunnelling Microscopy (LDSTM)***

As stated in the introduction there is much to be gained from combining a laser with an STM. Some work has been done in this area<sup>[60-76]</sup> however there are still significant gaps that as yet have not been explored. Some of the work in this thesis concerns the interaction of an STM and sample with infrared radiation with a wavelength designed to match vibrational modes in the sample.

This sub-section reviews work in two key areas that relates to the work in this thesis: firstly, the thermal effect that the laser has on the tip and the sample and secondly, other responses that the sample and tip can have to the laser.

In light of what follows in this section it is important to remember the difference between LDSTM and other types of experiments that investigate the difference between a localised probe and a laser. For example another mature SPM (scanning probe microscopy) technique, SNOM (scanning near-field microscopy) records the local response of a sample to an incident laser but detects this as a modulation in the radiation scattered from the sample. A second example is LDAFM (laser driven atomic force microscopy). In a conventional AFM experiment the surface topography is recorded as perturbations to the oscillations

of a local sharp tip as a consequence of sample-tip van der Waals forces. With LDAFM the tip and sample are illuminated with a laser. The light scattered from them is modulated by the local properties of the sample and the oscillation of the AFM tip. By decoupling the scattered light at the oscillation frequency of the tip, the localised optical response of the sample can be extracted. In contrast to this LDSTM is implemented in a different way. The laser illuminates the tip-sample region and the effect of the tip is detected as a change in the tunnelling current. This difference is significant. Since the tip is used to detect the response it cannot be used to modulate the laser beam.

In practice conducting experiments such as SNOM or LDAFM is generally easier than an LDSTM experiment as a consequence of not having to modulate the incident laser beam. (Modulation of the laser beam as discussed in more detail in §2.5.1 can cause thermal expansion which can mask some LDSTM phenomena.) However both SNOM and LDAFM possess characteristics that fundamentally limit their resolution to that lower than achievable with STM. In the case of SNOM a very narrow aperture optical fibre is used to either illuminate the sample or collect the scattered light. If the aperture becomes too small ( $\leq 50\text{nm}$ ) then it becomes increasingly difficult to illuminate the sample or collect this scattered light, reducing the signal-to-noise of the radiation measured. In the case of LDAFM the scattered radiation is influenced by the overall nanoscopic shape of the tip rather than the sub-nanoscale structure of the end of the tip. With STM however the resolution is only limited by a single atom (usually part of a relatively rough structure) on the end of tip with a nanoscopic radius. This demonstrates the importance of developing an experimental procedure to record a localised laser response.

### 2.5.1 Thermal Effects

In addition to any other effect that takes place when a laser illuminates a tip, the tip will thermally expand as a consequence of the adsorption of the radiation. This expansion will therefore change the tunnelling gap width and consequently the

tunnelling current. This effect is not usually significant if the tip is constantly illuminated since here the feedback loop just retracts the tip slightly to compensate. It is significant however if the laser is modulated in some way as is the case in the present work. For studying certain phenomena this thermal modulation is useful, for example laser-excited surface plasmons<sup>[60]</sup>, STM junction frequency mixing<sup>[62, 63]</sup>, and nanostructuring<sup>[64, 65]</sup>. However, for others it becomes a hindrance, particularly if the laser is intentionally modulated so that phase-sensitive detection can be used to improve sensitivity.

For the scenario where the tip and sample are illuminated by a modulated laser beam and a lock-in amplifier is used to detect the change in the tunnelling current, the output of the lock-in amplifier can be shown to be proportional to the magnitude of the tunnelling current. Approximating the tunnelling current to being exponentially dependent upon the gap between the tip and the sample gives:

$$I = I_0 e^{-cz} \quad \text{Equation 2.57}$$

Where  $I$  is the tunnelling current,  $I_0$  is an equilibrium current,  $z$  is the tip sample gap and  $c$  is a positive proportionality constant. Since the modulation of the laser beam modulates the tip sample distance, the lock-in amplifier essentially calculates the change in the tunnelling current ( $\Delta I$ ) with respect to the change in  $z$  ( $\Delta z$ ), or:

$$\frac{dI}{dz} = -cI_0 e^{-cz} = -cI. \quad \text{Equation 2.58}$$

The thermal LDSTM response was first investigated by Amer *et al.*, who reported that it was the sample rather than the tip that underwent thermal expansion<sup>[66]</sup>. As other groups carried out further work, it became clear that although the sample has some effect on the thermal response of the STM in most cases it is dominated by the effect of the tip. Robins *et al.* conducted a detailed treatment of the laser-tip interaction<sup>[68]</sup> where they take into consideration that not all of the beam will hit the tip. There has been some treatment of the expansion of the sample in response to the laser<sup>[69, 71]</sup> which has been found to match experimental data<sup>[71]</sup>. Trying to

apply the principles from these works to the work described in this thesis is not trivial. Landi *et al.*<sup>[71]</sup> used HOPG (highly oriented pyrolytic graphite) and gold foil samples not the gold on glass samples used in this thesis. These samples will respond to the incident radiation in different ways, the glass will not conduct heat away from the surface as well as metal, so the heating effect would be greater.

Some important experimental work was published by Grafström *et al.*<sup>[67]</sup> in which they were able to focus their laser to a tight enough spot size to be able to direct it either on the tip or the sample. They studied a range of different samples and tips and of relevance for the work here is that gold on mica samples significantly increase the thermal response over bulk gold samples such that the sample contribution is almost as large as that of the tip.<sup>[67]</sup> Also reported was the expected roll-off of the thermal expansion with increasing modulation frequency.

If it is expected that this thermal response would mask other LDSTM effects then it is desirable to find some way to compensate for them so that these other effects can be investigated more easily. One of the ways to do this is to modulate the laser with a frequency greater than  $\approx 10$  kHz. The exact roll-off frequency will vary depending on the exact conditions. However in some STM systems their internal electronics act as a high pass filter removing high frequency signals above  $\approx 10$  kHz thus eliminating this as a solution. Another way as described by Grafström *et al.* is to use two lasers the where the modulation of one is  $180^\circ$  out of phase with the other. The wavelength of one laser is chosen to match an adsorption mode in the sample while the other is chosen so that it does not match any of the adsorption modes.<sup>[67]</sup> By adjusting the power of the two lasers the thermal effect on the tip and sample can be kept constant.

Prior to conducting experiments to investigate the frequency response of the LTSTM it was not known whether rapid modulation of the laser beam is going to be effective in compensating for the thermal effect. With respect to the two beam solution it is unlikely that such a solution could be used with the LTSTM and OPO. In order for it to succeed the power and size of two different components of the OPO beam would have to be matched to one another and modulated with the required  $180^\circ$  relative phase shift. This would be difficult for the idler beam since few components are available to modulate beams at this wavelength.

In short there is some information available describing the thermal response of an STM to a laser stimulus but how much is applicable to the experimental setup described in this thesis is not completely clear prior to running experiments with this equipment.

### 2.5.2 Other LDSTM Responses

If the thermal response of an STM to a laser beam can be compensated for then it is possible to record other types of LDSTM response. Despite the ability of an STM to resolve surface features with high spatial resolution not all LDSTM experiments make use of this. Most of these experiments investigate samples coated with species that have an electronic transition that absorbs radiation at the frequency of the laser used.

For example Smith and Owens<sup>[76]</sup> used a system where the sample was mounted onto a prism so that the tunnelling junction could be illuminated from the rear of the sample in order to minimise the effect of the heating effect of the laser. They used samples of 1,1'-diethyl-2,2'-cyanine bromide (PIC bromide) mounted onto a silver substrate and PIC bromide mounted onto a 11-mercaptoundecanoic acid SAM on silver substrate. They also used a rhodamine 110 cw dye laser modulated with a chopper at 120Hz. By varying the wavelength of the laser they recorded a peak-to-peak laser induced vertical modulation of the tip position of  $\approx 0.31\text{\AA}$  and  $\approx 0.27\text{\AA}$  respectively for the two samples above around a peak wavelength of  $\approx 582\text{nm}$ . The samples used had the same composition across the surface so no investigation was made into how this LDSTM response varied across the surface.

Some similarities exist between these experiments and those conducted by Möltgen and Kleinermanns<sup>[61]</sup>. For their test samples they used Malachite Green and 4-4'-azoxyanisole on highly orientated pyrolytic graphite (HOPG). Technically the experiments they performed were not true LDSTM experiments since they used a Xe-lamp with a monochromator (focussed down to a 1mm spot size) instead of a laser source. The sample was illuminated from above and no modulation was applied to the radiation. Despite this lack of modulation Möltgen and Kleinermanns were able to record responses in the voltage applied to the  $z$ -

piezoelectric signal (used to keep the sample-tip separation constant) correlated to the UV/VIS absorption spectra for both molecules. As with the Smith and Owens data no images were presented showing how the response to the radiation varies across the surface.

However Grafström *et al.*<sup>[75]</sup> have managed to do this using their twin laser system to record the non-thermal response of a dye and a liquid crystal combination across a  $60 \times 60 \text{ nm}^2$  section of surface. They coated a HOPG substrate with a perylene-tetracarboxylic-dianhydride (PTCDA) dye and then coated this dye with the liquid crystal octylcyanobiphenyl (8CB). The interaction between these two species produced a layer probed by the STM tip that contained regions of both structures. The two lasers used to illuminate the sample were an  $\text{Ar}^+$  laser (488nm) and a dye laser (590nm). The PTCDA dye absorbed the radiation from the  $\text{Ar}^+$  laser but not the dye laser. They were able to measure the tunnelling current across this  $60 \times 60 \text{ nm}^2$  section of surface and decouple it with respect to the switching frequency of the two lasers rapidly enough to build up a picture of the LDSTM response across this surface. The change in surface composition in the topography image was clearly seen in the LDSTM response image.

It is important to compare this LDSTM data from Grafström *et al.* with LDAFM data from Taubner, Hillenbrand and Keilmann<sup>[77-79]</sup> and from Knoll and Keilmann<sup>[80]</sup>. In the case of the LDAFM data the variation in composition of the sample is detected as changes in the light scattered off the tip in the vicinity of the surface. In contrast to this the LDSTM data records how the interaction of the tunnelling region with the incident laser light is coupled into a change in the tunnelling current.

The LDSTM experiments presented in this thesis were chosen to work towards experiments similar to those by Grafström *et al.* except using an infrared laser with a wavelength in the ‘fingerprint’ region and samples that are sensitive to this wavelength. As described in the Introduction it is the response of molecules to radiation in this ‘fingerprint’ region that is a powerful tool in their identification. Only by developing a technique that allows the combination of an STM with an infrared wavelength laser can molecules be investigated with the high resolution of an STM.

## 2.6 Chapter Summary

This chapter has described an overview of scanning tunnelling microscopy both theoretically and with reference to the equipment used in this study. Spectroscopy based upon STM has also been described as an additional characterisation technique. An introduction to the theory behind the workings of an optical parametric oscillator (the coherent infrared radiation source) has been given along with details of the specific unit used for this work and how it is coupled to the STM.

Self-assembled monolayers are introduced as type of system that can be used as a starting point for developing suitable samples to be investigated with this new LDSTM system.

Finally the current progress in LDSTM has been reviewed indicating where this new work fits in with previous studies.

## 2.7 References

1. Binnig, G., et al., *Surface Studies by Scanning Tunneling Microscopy*. Physical Review Letters, 1982. **49**(1): p. 57-61.
2. Jaklevic, R.C. and J. Lambe, *Molecular Vibration Spectra by Electron Tunneling*. Physical Review Letters, 1966. **17**(22): p. 1139-1140.
3. Lambe, J. and R.C. Jaklevic, *Molecular Vibration Spectra by Inelastic Electron Tunneling*. Physical Review, 1968. **165**(3): p. 821-832.
4. Hansma, P.K., *Inelastic electron tunneling*. Physics Reports, 1977. **30**(2): p. 145-206.
5. Stipe, B.C., *A variable-temperature scanning tunneling microscope capable of single-molecule vibrational spectroscopy*. Review of Scientific Instruments, 1999. **70**(1): p. 137-143.
6. Kim, Y.-T., R.L. McCarley, and A.J. Bard, *Scanning tunneling microscopy studies of gold(111) derivatized with organothiols*. Journal of Physical Chemistry, 1992. **96**(18): p. 7416-7421.

7. Crommie, M.F., D.M. Lutz, and D.M. Eigler, *Confinement of Electrons to Quantum Corrals on a Metal Surface*. *Science*, 1993. **262**(5131): p. 218-220.
8. Eigler, D.M. and E.K. Schweizer, *Positioning single atoms with a scanning tunnelling microscope*. *Nature*, 1990. **344**: p. 524-526.
9. Hasegawa, Y. and P. Avouris, *Direct Observation of Standing Wave Formation at Surface Steps Using Scanning Tunneling Spectroscopy*. *Physical Review Letters*, 1993. **71**(7): p. 1071-1074.
10. Collins, G.P., *STM Rounds Up Electron Waves At The QM Corral*. *Physics Today*, 1993.
11. Crommie, M.F., C.P. Lutz, and D.M. Eigler, *Imaging standing waves in a two-dimensional electron gas*. *Nature*, 1993. **363**: p. 524-527.
12. Ho, W., *Single-molecule chemistry*. *The Journal of Chemical Physics*, 2002. **117**(24): p. 11033-11061.
13. Bardeen, J., *Tunnelling from a Many-Particle Point of View*. *Physical Review Letters*, 1961. **6**(2): p. 57-59.
14. Tersoff, J. and D.R. Hamann, *Theory of the scanning tunneling microscope*. *Physical Review B*, 1985. **31**(2): p. 805-813.
15. Hofer, W.A. and J. Redinger, *Electronic structure of a realistic STM tip: the role of different apex atoms*. *Philosophical Magazine B-Physics of Condensed Matter Statistical Mechanics Electronic Optical and Magnetic Properties*, 1998. **78**(5-6): p. 519-525.
16. Hofer, W.A., J. Redinger, and R. Podloucky, *Modeling STM tips by single absorbed atoms on W(100) films: 3d and 4d transition-metal atoms*. *Physical Review B (Condensed Matter and Materials Physics)*, 2001. **64**(12): p. 125108-7.
17. Hofer, W.A., J. Redinger, and P. Varga, *Modeling STM tips by single absorbed atoms on W(100) films: 5d transition metal atoms*. *Solid State Communications*, 1999. **113**(5): p. 245-250.
18. Hallmark, V.M., et al., *Observation of Atomic Corrugation on Au(111) by Scanning Tunneling Microscopy*. *Physical Review Letters*, 1987. **59**(25): p. 2879-2882.

19. Penner, R.M., et al., *Mechanistic investigations of nanometer-scale lithography at liquid-covered graphite surfaces*. Applied Physics Letters, 1991. **58**(13): p. 1389-1391.
20. Giancarlo, L.C. and G.W. Flynn, *Scanning tunneling and atomic force microscopy probes of self-assembled, physisorbed monolayers: Peeking at the peaks*. Annu. Rev. Phys. Chem., 1998. **49**(1): p. 297-336.
21. Yau, S.L., et al., *Atomic-Resolution Scanning Tunneling Microscopy and Infrared- Spectroscopy as Combined In situ Probes of Electrochemical Adlayer Structure - Carbon-Monoxide on Rhodium(111)*. J. Am. Chem. Soc., 1991. **113**(16): p. 6049-6056.
22. Wiesendanger, R., *Scanning Probe Microscopy and Spectroscopy*. 1994. p. 15-17.
23. Rae, A.I.M., *Quantum Mechanics*. Third ed. 1996, Bristol: Institute of Physics Publishing. 178-179.
24. Calvert, J.B., *The WKB Approximation*. 2001: <http://www.du.edu/~jcalvert/phys/wkb.htm>.
25. Simmons, J.G., *Generalized Formula for the Electric Tunnel Effect between Similar Electrodes Separated by a Thin Insulating Film*. Journal of Applied Physics, 1963. **34**(6): p. 1793-1803.
26. Doyen, G., *The Scattering Theoretical Approach to the Scanning Tunneling Microscope*, in *Scanning Tunneling Microscopy III*, R.W.H.-J. Güntherodt, Editor. 1996, Springer-Verlag. p. 23-50.
27. Chen, C.J. *Microscopic view of scanning tunneling microscopy*. in *Topical Conference on Nanometer Scale Properties of Surfaces and Interfaces*. 1991. Boston, Massachusetts (USA): AVS.
28. Chen, C.J., *Origin Of Atomic Resolution On Metal-Surfaces In Scanning Tunneling Microscopy*. Physical Review Letters, 1990. **65**(4): p. 448-451.
29. Hofer, W.A., *Challenges and errors: interpreting high resolution images in scanning tunneling microscopy*. Progress in Surface Science, 2003. **71**(5-8): p. 147-183.
30. Hofer, W.A., et al., *Surface Relaxations, Current Enhancements, and Absolute Distances in High Resolution Scanning Tunneling Microscopy*. Physical Review Letters, 2001. **87**(23): p. 236104-4.

31. Everson, M.P., R.C. Jaklevic, and W.D. Shen, *Measurement of the Local Density of States on a Metal-Surface - Scanning Tunneling Spectroscopic Imaging of Au(111)*. Journal of Vacuum Science & Technology A-Vacuum Surfaces and Films, 1990. **8**(5): p. 3662-3665.
32. Feenstra, R.M., *Scanning tunneling spectroscopy*. Surface Science, 1994. **299-300**: p. 965-979.
33. Gaudioso, J., L.J. Lauhon, and W. Ho, *Vibrationally mediated negative differential resistance in a single molecule*. Physical Review Letters, 2000. **85**(9): p. 1918-1921.
34. Labonté, A.P., et al., *Scanning tunneling spectroscopy of insulating self-assembled monolayers on Au(111)*. Journal of Physical Chemistry B, 2002. **106**(34): p. 8721-8725.
35. Becker, T., et al., *Applications with a new low-temperature UHV STM at 5 K*. Applied Physics A: Materials Science & Processing, 1998. **66**(0): p. S27.
36. Lauhon, L.J. and W. Ho, *Effects of temperature and other experimental variables on single molecule vibrational spectroscopy with the scanning tunneling microscope*. Review of Scientific Instruments, 2001. **72**(1): p. 216-223.
37. Hovel, H., et al., *Tunneling spectroscopy on silver clusters at T=5 K: size dependence and spatial energy shifts*. Surface Science, 2000. **463**(1): p. L603-L608.
38. Wang, W.Y., T. Lee, and M.A. Reed, *Elastic and inelastic electron tunneling in alkane self-assembled monolayers*. Journal of Physical Chemistry B, 2004. **108**(48): p. 18398-18407.
39. Lorente, N., *Mode excitation induced by the scanning tunnelling microscope*. Applied Physics A-Materials Science & Processing, 2004. **78**(6): p. 799-806.
40. Stipe, B.C., *Single-Molecule Vibrational Spectroscopy and Microscopy*. Science, 1998. **280**: p. 1732-1735.
41. Hahn, J.R., H.J. Lee, and W. Ho, *Electronic resonance and symmetry in single-molecule inelastic electron tunneling*. Physical Review Letters, 2000. **85**(9): p. 1914-1917.

42. Rohwerder, M., et al., *Adsorption of self-assembled monolayers of mercaptan on gold*. Thin Solid Films, 1995. **264**(2): p. 240-245.
43. Fenter, P., A. Eberhardt, and P. Eisenberger, *Self-Assembly of N-Alkyl Thiols as Disulfides on Au(111)*. Science, 1994. **266**(5188): p. 1216-1218.
44. Durig, U., et al., *Electronic and Mechanical Characterization of Self-Assembled Alkanethiol Monolayers by Scanning-Tunneling-Microscopy Combined with Interaction-Force-Gradient Sensing*. Physical Review B, 1993. **48**(3): p. 1711-1717.
45. Widrig, C.A., C.A. Alves, and M.D. Porter, *Scanning Tunneling Microscopy of Ethanethiolate and Normal-Octadecanethiolate Monolayers Spontaneously Adsorbed at Gold Surfaces*. Journal of the American Chemical Society, 1991. **113**(8): p. 2805-2810.
46. Hallmark, V.M., et al., *Structure and Topography of Molecular Assemblies on Solid Substrates by Infrared-Spectroscopy and Scanning Tunneling Microscopy*. Mikrochimica Acta, 1988. **2**(1-6): p. 39-42.
47. Ebrahimzadeh, M., *Mid-infrared ultrafast and continuous-wave optical parametric oscillators*, in *Solid-State Mid-Infrared Laser Sources*. 2003, Springer-Verlag Berlin: Berlin. p. 179-218.
48. Myers, L.E., R. C. Eckardt, M. M. Fejer, R. L. Byer, W. R. Bosenberg, J. W. Pierce,, *Quasi-phase-matched optical parametric oscillators in bulk periodically poled LiNbO<sub>3</sub>*. Journal of the Optical Society of America B, 1995. **12**(11): p. 2102-2116.
49. Britton, P., *Synchronously pumped PPLN based optical parametric oscillator*. 2000, University of Southampton: Southampton.
50. Emmons, H., Trans. Am. Inst. Chem. Eng., 1939. **35**: p. 109-.
51. Schmidt, E., W. Schurig, W. Sellschopp, Tech. Mech. Thermodyn., 1930. **1**: p. 53-.
52. Nagle, W.M., T. B. Drew, Trans. Am. Inst. Chem. Eng., 1933. **30**: p. 217-.
53. Gooding, J.J., et al., *Self-assembled monolayers into the 21(st) century: Recent advances and applications*. Electroanalysis, 2003. **15**(2): p. 81-96.
54. Chryssolouris, G., et al., *Nanomanufacturing processes: a critical review*. International Journal of Materials & Product Technology, 2004. **21**(4): p. 331-348.

55. Poirier, G.E., E. D. Pylant, *The Self-Assembly Mechanism of Alkanethiols on Au(111)*. Science, 1996. **272**(5265): p. 1145-1148.
56. Poirier, G.E., *Coverage-Dependent Phases and Phase Stability of Decanethiol on Au(111)*. Langmuir, 1999. **15**: p. 1167-1175.
57. Poirier, G.E., *Mechanism of Formation of Au Vacancy Islands in Alkanethiol Monolayers on Au(111)*. Langmuir, 1997. **13**: p. 2019-2026.
58. Poirier, G.E., *Characterization of Organosulfur Molecular Monolayers on Au(111) using Scanning Tunneling Microscopy*. Chemical Reviews, 1997. **97**: p. 1117-1127.
59. Pflaum, J., et al., *Structure and electronic properties of  $CH_3$ - and  $CF_3$ -terminated alkanethiol monolayers on Au(111): a scanning tunneling microscopy, surface X-ray and helium scattering study*. Surface Science, 2002. **498**(1-2): p. 89-104.
60. Möller, R., et al., *Detection of Surface-Plasmons by Scanning Tunneling Microscopy*. Journal of Vacuum Science & Technology B, 1991. **9**(2): p. 506-509.
61. Möltgen, H. and K. Kleinermanns, *Resonance enhanced scanning tunneling (REST) spectroscopy of molecular aggregates on graphite*. Physical Chemistry Chemical Physics, 2003. **5**(12): p. 2643-2647.
62. Arnold, L., W. Krieger, and H. Walther, *Laser-Frequency Mixing in the Junction of a Scanning Tunneling Microscope*. Applied Physics Letters, 1987. **51**(11): p. 786-788.
63. Arnold, L., W. Krieger, and H. Walther, *Laser-Frequency Mixing Using the Scanning Tunneling Microscope*. Journal of Vacuum Science & Technology A-Vacuum Surfaces and Films, 1988. **6**(2): p. 466-469.
64. Yau, S.T., D. Saltz, and M.H. Nayfeh, *Scanning Tunneling Microscope Laser Fabrication of Nanostructures*. Journal of Vacuum Science & Technology B, 1991. **9**(2): p. 1371-1375.
65. Yau, S.-T., D. Saltz, and M.H. Nayfeh, *Laser-assisted deposition of nanometer structures using a scanning tunneling microscope*. Applied Physics Letters, 1990. **57**(27): p. 2913-2915.

66. Amer, N.M., A. Skumanich, and D. Ripple, *Photothermal modulation of the gap distance in scanning tunneling microscopy*. Applied Physics Letters, 1986. **49**(3): p. 137-139.
67. Grafström, S., *Analysis and compensation of thermal effects in laser-assisted scanning tunneling microscopy*. Journal of Vacuum Science & Technology B, 1991. **9**(2): p. 568-572.
68. Robins, E.S., M.J.G. Lee, and P. Langlois, *Effect of Optical Diffraction on Laser-Heating of a Field Emitter*. Canadian Journal of Physics, 1986. **64**(1): p. 111-117.
69. Bragas, A.V., et al., *Spectroscopic response of photoinduced currents in a laser-assisted scanning tunneling microscope*. Journal of Applied Physics, 1997. **82**(9): p. 4153-4158.
70. Bragas, A.V., *Field Enhancement in Laser Assisted Scanning Tunneling Microscope*. Phys. Low-Dim. Struct, 1998. **9/10**(1): p. 1-16.
71. Landi, S.M., *Avoiding photothermal noise in laser assisted scanning tunneling microscopy*. Ultramicroscopy, 1999. **77**: p. 207-211.
72. Landi, S.M. and O.E. Martinez, *Quenching the thermal contribution in laser assisted scanning tunneling microscopy*. Journal of Applied Physics, 2000. **88**(8): p. 4840-4844.
73. Grafström, S., *Photoassisted scanning tunneling microscopy*. J. Appl. Phys., 2002. **91**(4): p. 1717-1753.
74. Grafström, S., et al., *Investigation of laser-induced effects in molecular layers by scanning tunneling microscopy*. Applied Physics A-Materials Science & Processing, 1998. **66**: p. S1237-S1240.
75. Grafström, S., et al., *Thermal expansion of scanning tunneling microscopy tips under laser illumination*. Journal of Applied Physics, 1998. **83**(7): p. 3453-3460.
76. Smith, D.A. and R.W. Owens, *Laser-assisted scanning tunnelling microscope detection of a molecular adsorbate*. Applied Physics Letters, 2000. **76**(25): p. 3825-3827.
77. Taubner, T., R. Hillenbrand, and F. Keilmann, *Nanoscale polymer recognition by spectral signature in scattering infrared near-field microscopy*. Applied Physics Letters, 2004. **85**(21): p. 5064-5066.

78. Taubner, T., R. Hillenbrand, and F. Keilmann, *Performance of visible and mid-infrared scattering-type near-field optical microscopes*. Journal of Microscopy, 2003. **210**(3): p. 311-314.
79. Hillenbrand, R., T. Taubner, and F. Keilmann, *Phonon-enhanced light-matter interaction at the nanometre scale*. 2002. **418**(6894): p. 159-162.
80. Knoll, B. and F. Keilmann, *Scanning microscopy by mid-infrared near-field scattering*. Applied Physics a-Materials Science & Processing, 1998. **66**(5): p. 477-481.

## **Chapter 3**

### **The Manufacture and Imaging of Scanning Tunnelling Microscopy Tips**

3.1	Chapter Introduction .....	75
3.2	Experimental Methods Used .....	75
3.3	Results and Discussion.....	76
3.3.1	Optical Microscope Images of STM Tips.....	76
3.3.1.1	Tungsten Tips Etched with Alternating Current .....	76
3.3.1.2	Tungsten Tips Etched with Direct Current .....	79
3.3.2	FEG-SEM images of STM tips.....	81
3.3.3	STM Images Produced With Etched STM Tips .....	85
3.4	Conclusions and Future Work.....	86
3.5	References .....	87

### **3.1 Chapter Introduction**

The sharp tip in an STM is one of its key components. For the optimum operation of the STM, these tips need to be of high quality. When starting to work on this thesis the existing procedures for manufacturing STM tips within the group were not satisfactory so a new method needed to be developed to produce better quality tips more reliably. This chapter describes two new methods used and the tips made with them as well as the images produced with these tips.

### **3.2 Experimental Methods Used**

At the beginning of this study the tips were made by cutting platinum/iridium wire ( $\phi = 0.25$  mm) in the hope that the rough end of the wire would have a cluster of atoms that protruded more than the others, forming a useable tip. However, this method was not very reliable which made its use inefficient. The alternative was to electrochemically etch tungsten (W) wire ( $\phi = 0.25$  mm or 0.35 mm) to make tips using AC or DC. There are many different ways that W tips can be made<sup>[1]</sup> and different groups with STMs often develop their own variation of existing methods in an attempt to find the optimum tips for their STM.<sup>[2-16]</sup> For the STM used in this study the optimum method was found to be an amalgamation of a modified version of the procedure recommended by the manufacturer and the use of a special power supply based upon a design from Dartmouth College, New Hampshire, USA. The circuit diagram for this design from Dartmouth College and the modified design used to make the tips for this study can be found in Appendix B. For more details of procedures used to make tips by the cutting and etching methods see Appendix A.

The special power supply was needed for etching with DC because it was important that the supply voltage was switched off at a critical point in the etching reaction. This is because AC and DC etching proceed in different ways. With AC etching the metal is removed from across the whole of the cross-section of the wire and it is etched back to a sharp point. However, with DC etching the wire is

thinned to a narrow filament with a ‘neck’ at the surface of liquid. Finally, the neck is etched away and the filament falls to the bottom of the beaker leaving behind a sharp tip on the end of the wire. At this point the current flow decreases rapidly and the power supply unit needs to detect this and switch off the applied voltage. The switch off takes place within a few  $\mu$ s. If the etch is allowed to continue then the sharp tip will be etched away further and become blunt.

In order to find the optimum settings for the two variable resistors in the new power supply and the optimum applied voltage for the AC etching, tips were made with both AC and DC methods with varying experimental conditions. Images of these were recorded with an optical microscope and a Field Emission Gun - Scanning Electron Microscope (FEG-SEM). From these images the optimum etching conditions could be determined. A selection of these images are included in §3.3.

### **3.3 Results and Discussion**

#### **3.3.1 Optical Microscope Images of STM Tips**

This subsection shows optical microscope images of tips made with both AC and DC etching. With these images are given descriptions of the quality of the STM images that were produced with such tips. From these it was possible to determine the optimum etching conditions for good macroscopic tip shape.

##### **3.3.1.1 Tungsten Tips Etched with Alternating Current**

When the etching process is working well the tips have shapes as seen in Figure 3.1. These tips have a consistent tip angle and the top left image shows how the tip narrows from the full width of the wire to a point (as resolved at this magnification). Tips with this type of macroscopic shape were necessary to image the sample surfaces with good resolution (see the good quality images in Figure

3.19 and Figure 3.20). Deviation from this shape results in the inability of the tips to image the surface with good quality. For example Figure 3.2 shows extreme examples when the etching process produces double tips. Despite one of the tips protruding more than the other, they were unusable as STM tips.

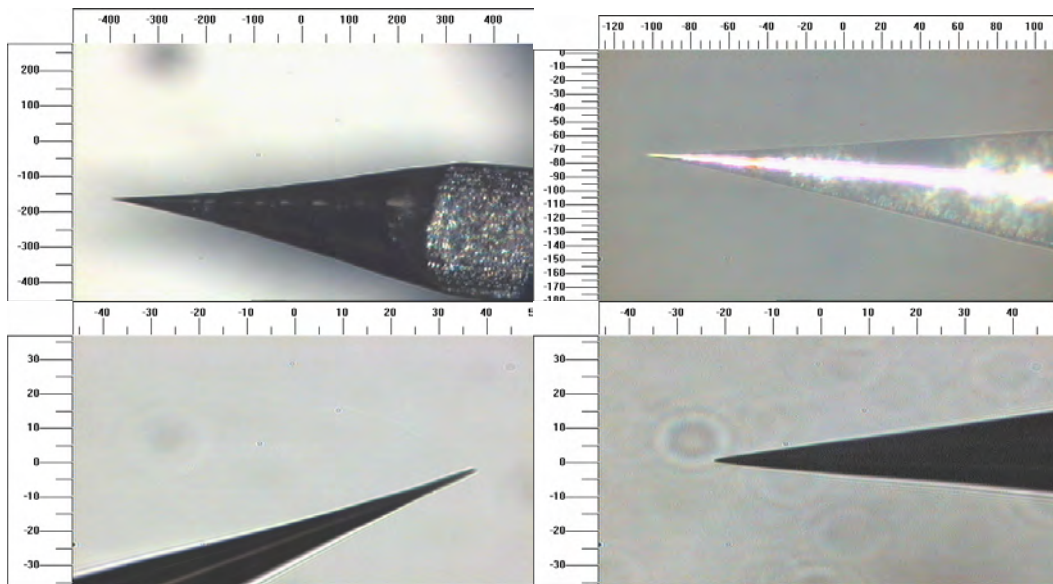


**Figure 3.1 (Above):** Showing three AC etched tips with a well formed tip cone. (The top right image is a higher magnification image of the tip in the top left.) (Scales are in microns.)

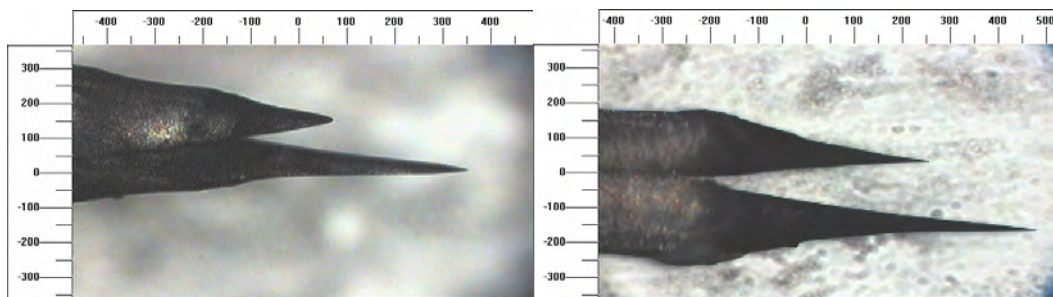


**Figure 3.2 (Above):** Examples of AC etched macroscopic double tips. (Scale is in microns.)

The AC power supply used was unregulated which means that the voltage applied through the electrolytic solution initially decreased as the wire was lowered into the solution completing the circuit. Due to the removal of material from the wire during the etching process the resistance of the wire increases and consequently the applied voltage increases as the etching process progressed. The tips in Figure 3.1 were made by configuring the power supply to supply a particular voltage

prior to lowering the wire into the solution. This voltage was allowed to vary as the etching process progressed. If the supplied voltage was adjusted during the etching process to compensate for the unregulated power supply then the tips had profiles as shown in Figure 3.3. It seems that adjusting the applied voltage produces a change in the tip angle. The quality of tips produced like this is so poor that they are not suitable for use in an STM.

It seems that it is more important to get the initial conditions correct and allow the applied voltage to drift rather than trying to optimise how to adjust the applied voltage during the etching process. This can be seen in Figure 3.4.

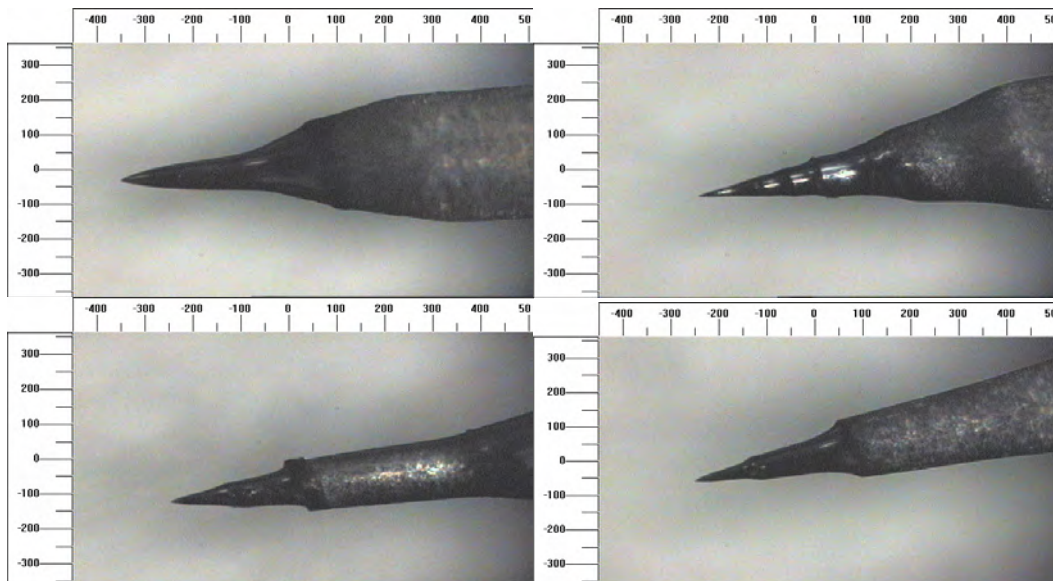


**Figure 3.3 (Above):** AC manufactured tips showing changes in the tip angle part way down the tip cone. (Scales are in microns.)

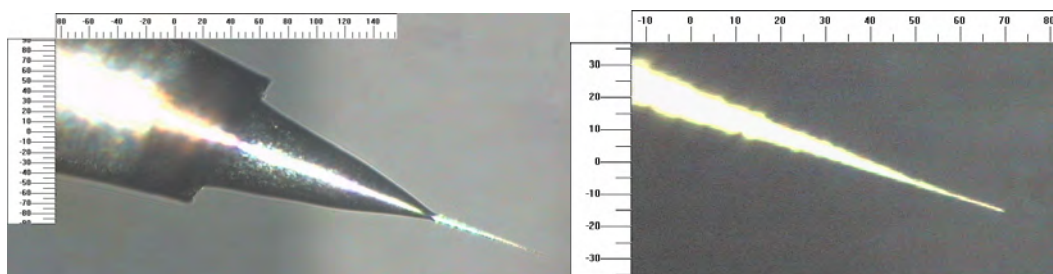


**Figure 3.4 (Above):** An example of an AC etched tip with a multi-step tip shape. (Scale is in microns.)

Here changes in the applied voltage produced step changes in the shape of the tip as before except in this instance the last part of the tip appears to be sharper than those in Figure 3.1. However this apparent improvement in microscopic shape did not yield a corresponding improvement in its sub-nanoscale quality since it was not possible to record good STM images with this tip. This suggests that it is the consistency of the cone angle that is the best macroscopic indicator of a tip's nanoscopic properties.

From reviewing these different tip shapes it was concluded that as far as the etching conditions are concerned it seems that it is not necessary to continually compensate for the unregulated nature of the power supply by adjusting the etching voltage to match those specified by the manufacturer. Satisfactory tips were produced by simply setting the initial conditions to the manufacturer's recommendations then allowing the voltage and current to drift. Even with the optimum etching conditions it is usual to find that for any given batch of tips that they only have consistently good quality after ~4 poor quality tips have been made from that batch. These poor quality tips are discarded.

### **3.3.1.2 Tungsten Tips Etched with Direct Current**

With DC etching the process of optimising the macroscopic shapes of the tips is more difficult due to the electronic equipment required. There are two variable resistors in the electronic circuitry (Appendix B). The first of these, VR1 controls the amount of current flowing through the tungsten wire, the other, VR2 controls the sensitivity of the cut-off mechanism. Both needed to be optimised to produce good tips. As with the description of AC made tips, a series of images of DC etched tips are included below, along with comments linking the macroscopic tip shapes with the settings of VR1 and VR2.

Fortunately as with the AC process, it was found that adjusting VR1 so that the initial etching conditions were in line with those recommended, yielded a satisfactory setting for VR1. Optimising VR2 proved more difficult. Figure 3.5 shows what happened when it was set too low. The etching process does not stop

when the correct amount of metal has been removed from the tip and the continuing etching process removes more material making the tip blunt. At the other extreme are the kind of tips seen in Figure 3.6 which possess a 'neck' due to the electronics box cutting off too early. This happens when VR2 is set to too high a value whereas blunt tips are made if VR2 is set too low. Its optimum setting seemed to be at 85% of its  $5k\Omega$  rating.

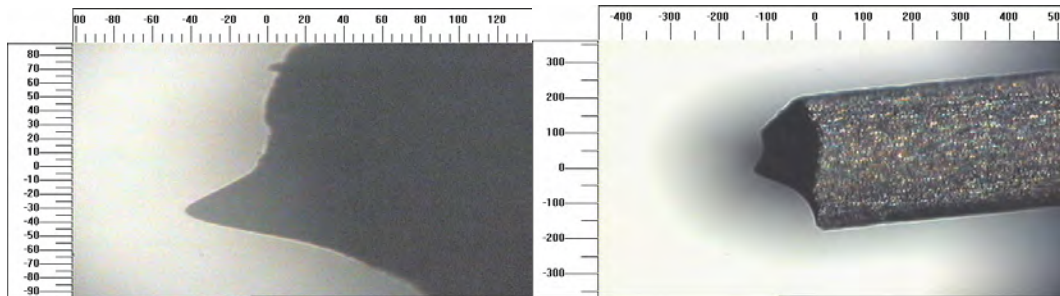


Figure 3.5 (Above): Two blunt DC etched tips. (Scales are in microns.)

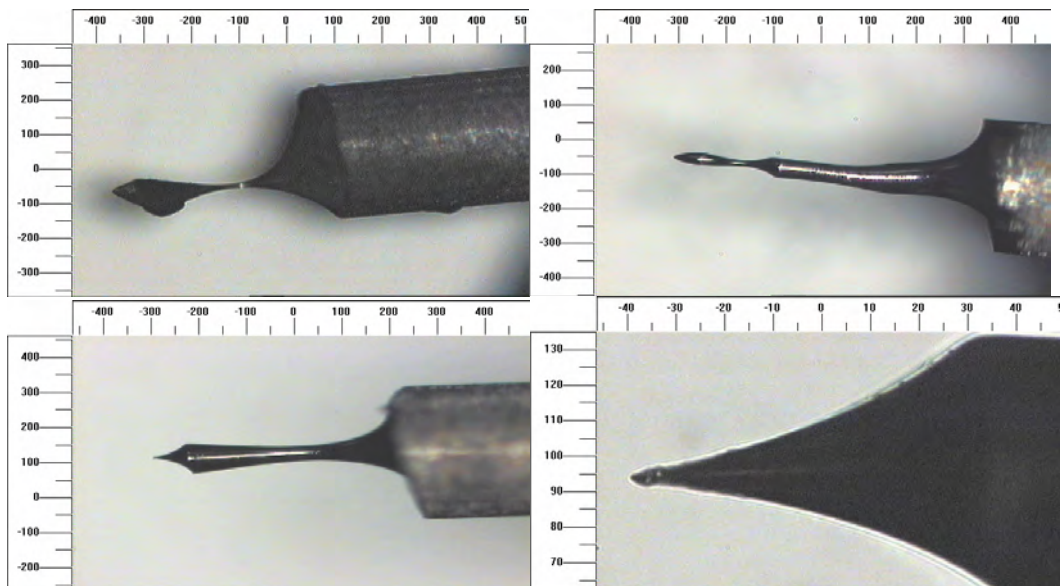
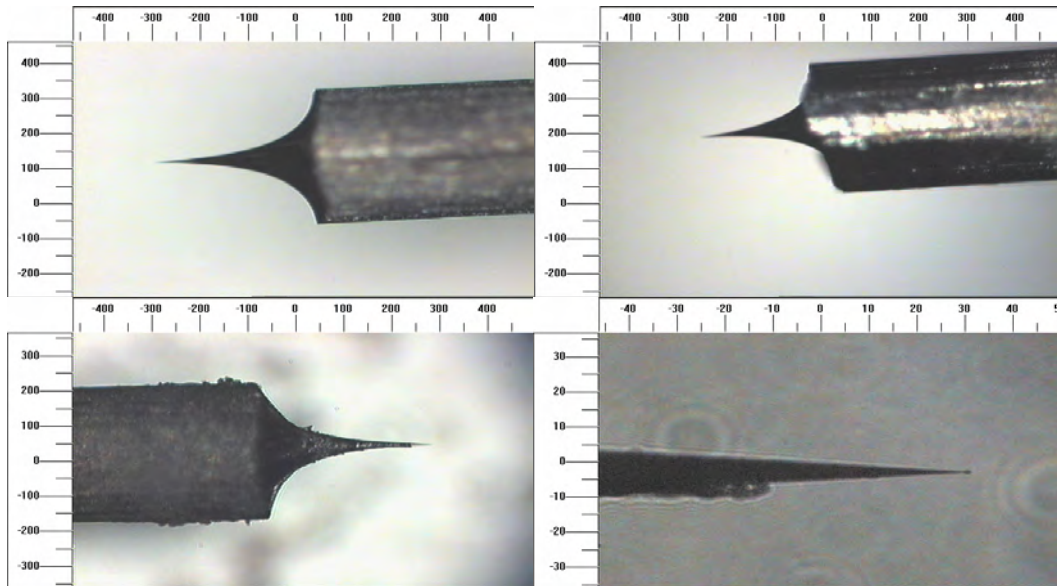


Figure 3.6: Three examples of tips exhibiting a 'neck' due to incomplete etching. (The bottom right image is a magnified section from the bottom left image.) (Scales are in microns.)

When the conditions were correctly optimised then the tips appeared as shown in Figure 3.7. Note how small the lengths of the tips are compared to AC etched tips. The lower two images show the importance of the post-etch  $HF_{(aq)}$  treatment. The material coating the tip is sodium hydroxide. Due to surface tension some of the

etching solution stays on the tip after the etching process has finished. The  $\text{HF}_{(\text{aq})}$  is then used to remove this along with any partially oxidised tungsten.

Of course it is entirely possible that tips that look satisfactory with an optical microscope will be blunt at the nanoscopic scale. The next section describes how a Field Emission Gun Scanning Electron Microscope (FEG-SEM) was used to probe their dimensions on a smaller scale to try and better ascertain their quality.



**Figure 3.7:** Four images of tips with good microscopic shape. (Scales are in microns.) The lower right image is a higher magnification image of the tip in the lower left image. The tip in these lower images was not treated with  $\text{HF}_{(\text{aq})}$  after etching. The deposits on the side of the tip are oxide and hydroxide by-products from the etching process. Higher magnification images of this tip are shown in Figure 3.16 to Figure 3.18. Despite the presence of contaminants on this last tip these show the microscopic consistency of the DC etching process.

### 3.3.2 FEG-SEM images of STM tips.

The images of the tips collected with the FEG-SEM can be seen in Figure 3.8 to Figure 3.18. In the legend at the bottom of each image, the length of the white bar represents the distance written underneath it.

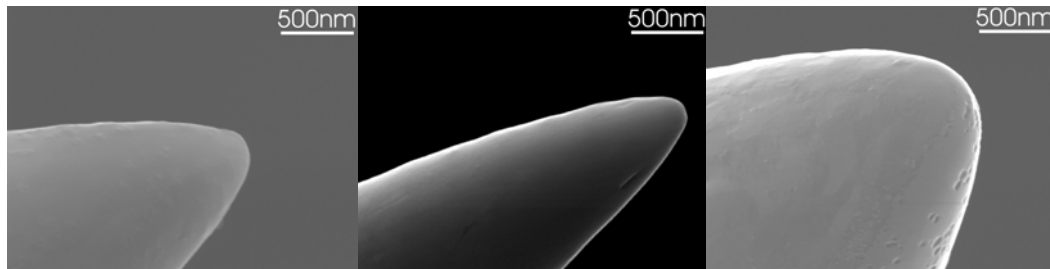
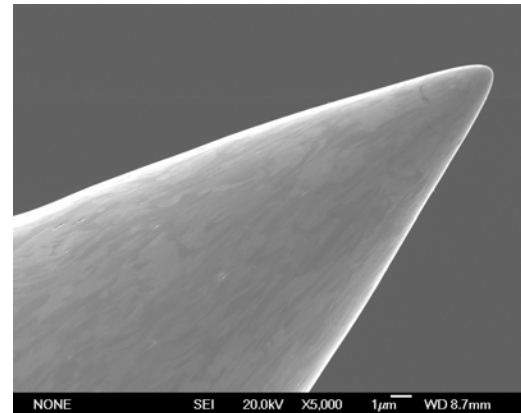


**Figure 3.8 (Above):** Three examples of AC etched tips. They show the variation possible between tips produced by the same AC etching method.

**Figure 3.9: (Right)**

This shows a larger scale image of the same type of tip as in the previous Figure.



Although the number of tips included here is relatively small, some important general trends can be identified. Firstly that the tips produced by AC etching have a much larger tip radius than the DC etched tips. This suggests that it would be more difficult to obtain high-resolution images with such a type of tip. This is consistent with experimental experience of these tips.

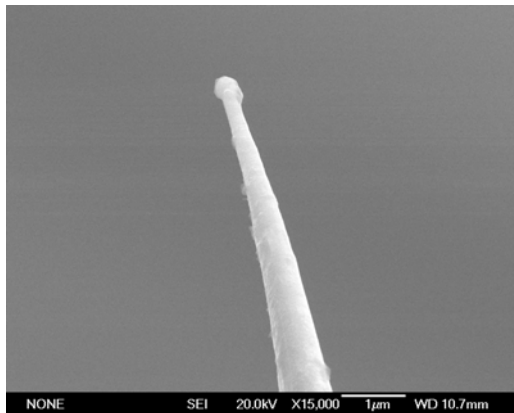


**Figure 3.10:**  
A typical DC etched tip.

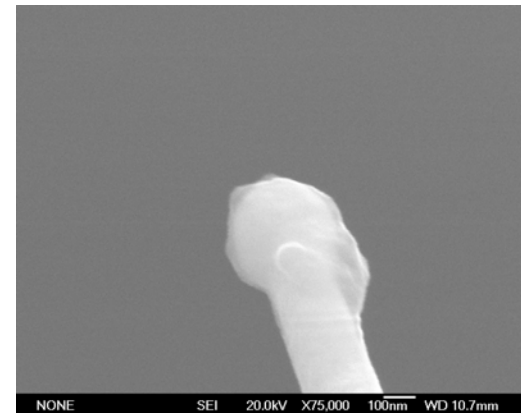


**Figure 3.11:** A more detailed image of the tip shown in the previous Figure.

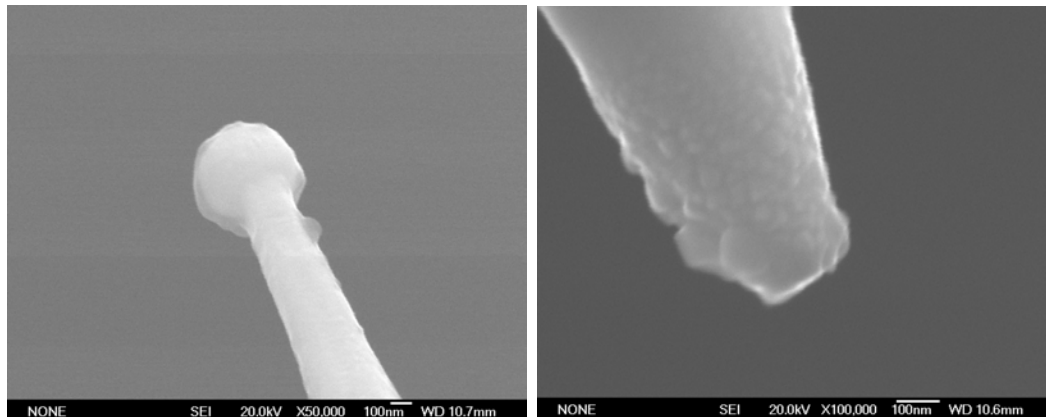


**Figure 3.12:** A second example of a DC etched tip showing the consistency of the ball shaped end between different tips.

**Figure 3.13:** An example of a good DC etched tip that does not have a 'ball-shaped' end.

Some very good atomic resolution images have been observed with these tips but this appears to be the exception rather than the rule. It is likely that this relates to the roughness of the ends of these AC tips. If they are nanoscopically smooth then the tip radius will be too large to resolve the atoms on the surface. Only if the end of the tip is rough with a cluster of atoms protruding further than the others will the effective tip radius be reduced and the resolution improved.

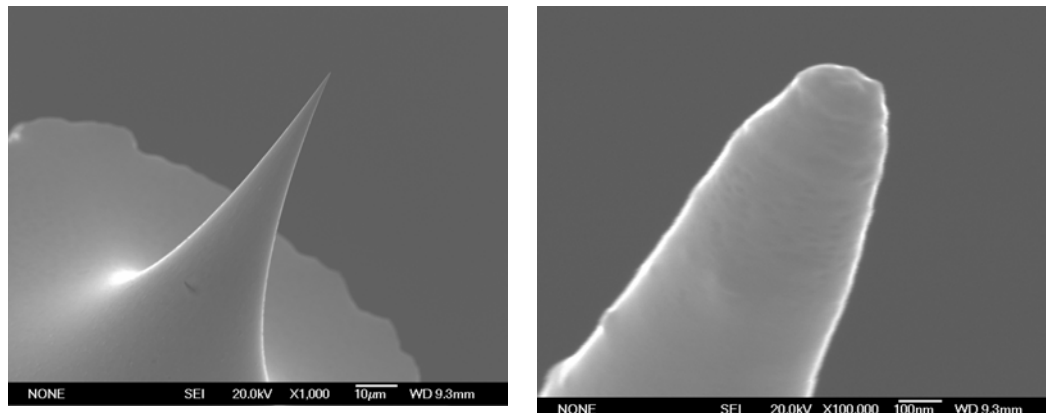


**Figure 3.14:** Another image of a DC etched tip showing the profile of the tip. Note how on this scale the circumference of the wire seems rough compared to the profile of the tip.

**Figure 3.15:** A higher magnification image of the tip in the previous Figure showing that it does not have a 'ball-shaped' end.

The DC etched tips with their smaller tip radius should more reliably produce good quality images. This was consistent with experimental experience. However a number of the DC etched tips possess a narrow neck and a rounded end. This is not unexpected and has been seen in previously published SEM images of such tips.<sup>[1]</sup> From the images that have been recorded it seems that this is not always a problem. This seems to be due to the fact that these rounded ends are not smooth. Protrusions on their ends have similar effective tip radii to the tips without the rounded ends enabling atomic resolution imaging of the surface.

Serendipitously the condition of one of the tips was such that it revealed why it is important to ensure that the tips are washed and HF treated before they are used. Figure 3.16 shows an image of a tip that at first glance looks reasonable. There are some deposits attached to the base of the tip but they are away from the end of the tip and should not affect the conduction properties of the tip too much. However, two higher magnification images of the end of the tip show that it is very rough. Indeed, it appears that there is an object with the expected shape of a DC tip.

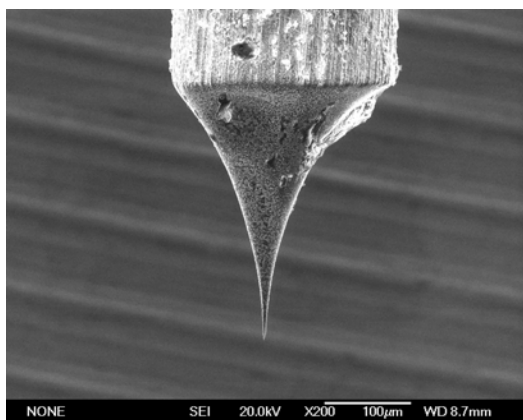


**Figure 3.16:** A DC etched tip showing the presence of (hydr)oxide on part of its base.

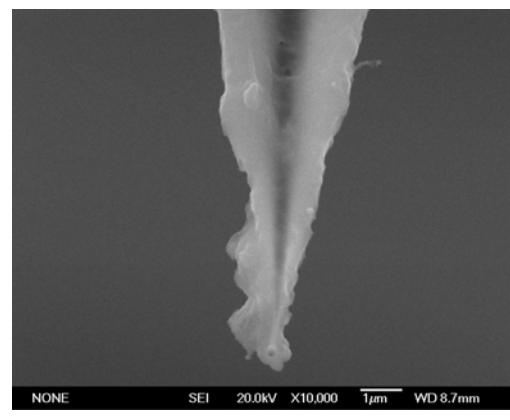


**Figure 3.17:** A higher magnification image of the tip shown in the previous Figure.

Figure 3.18 indicates that the object in the centre has a much higher density than the material around it. This image was produced using a technique that shows denser material as light parts on the image and less dense material as darker shades. Since only the central part of the tip is shown as bright, it would seem sensible to assume that the dense material in the centre is actually the tungsten tip and the area surrounding it is some sort of oxygen-containing compound. It would

be either an oxide of tungsten, or sodium hydroxide both of which are by-products of the etching process.

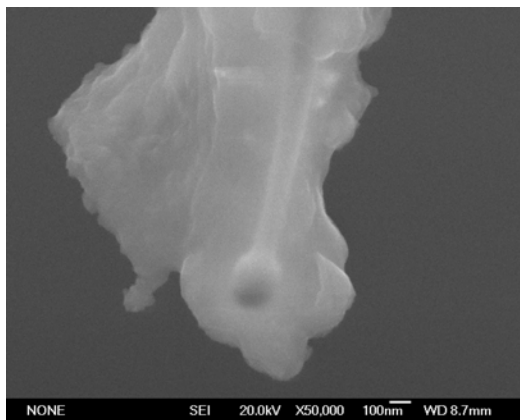


**Figure 3.18 (Left):** The end of the tip shown in the previous Figure. The presence of a DC etched tip can be seen buried underneath the thick (hydr)oxide coating.

### 3.3.3 STM Images Produced With Etched STM Tips

Good quality STM images were collected at 78K with tips produced using both of these etching methods. Figure 3.19 and Figure 3.20 show STM atomic resolution images of an Au(111) surface including the ‘herringbone’ reconstruction produced with a W tip manufactured using AC. Similar results were also achieved with DC etched tips. Figure 3.21 and Figure 3.22 show that DC etched tips can also be used to image herringbone structure and atomic resolution on an Au(111) surface.

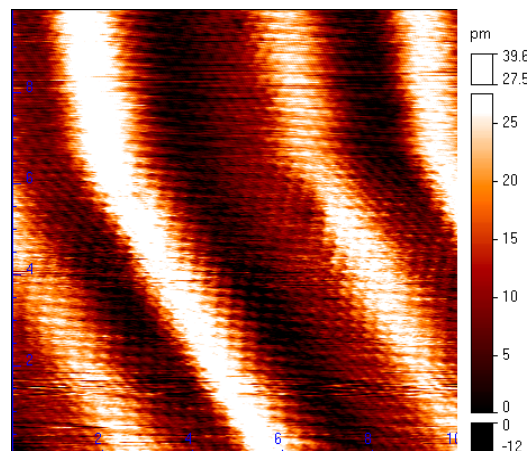


**Figure 3.19 (Right):** A 10.0nm x 9.82nm image of an Au(111) surface recorded with an AC etched tip at 78K, showing a section of herringbone reconstruction.

(STM parameters:  $U_{\text{gap}} = 1\text{V}$ ,  $I = 0.2\text{nA}$  )

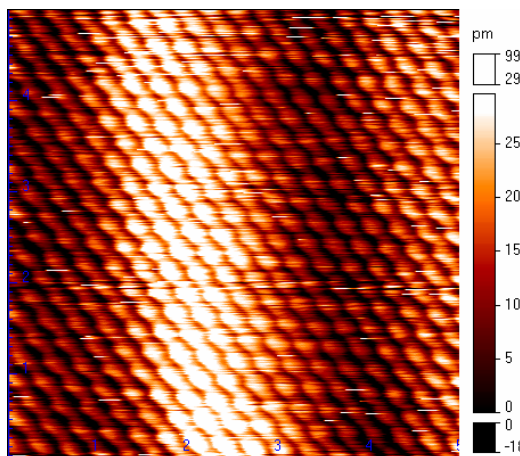


**Figure 3.20 (Left):** A  $5\text{nm} \times 5\text{nm}$  enlarged area of the surface shown in Figure 3.19 showing the individual gold atoms on the surface demonstrating that atomic resolution can be achieved with an AC etched tip. (STM parameters:  $U_{\text{gap}} = 1\text{V}$ ,  $I = 0.2\text{nA}$ )

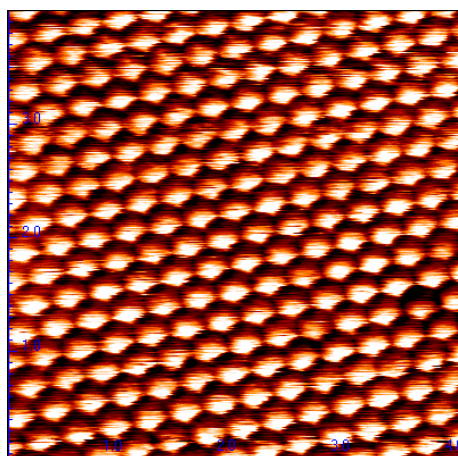


**Figure 3.21 (Above):** A  $4.00\text{nm} \times 4.00\text{nm}$  atomic resolution STM image of an  $\text{Au}(111)$  surface recorded at  $78\text{K}$  with a DC etched tip. (STM parameters:  $U_{\text{gap}} = 79.6\text{mV}$ ,  $I = 1.9\text{nA}$ )

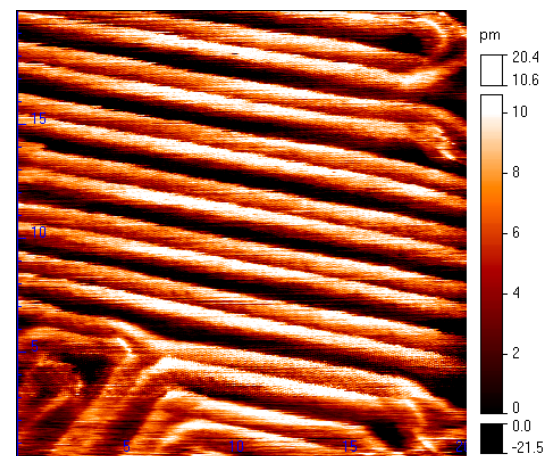


**Figure 3.22 (Above):** A  $20\text{nm} \times 20\text{nm}$  image of another  $\text{Au}(111)$  surface. This was imaged with a DC etched tip at  $78\text{K}$  and shows (a modified version of) the herringbone reconstruction. (STM parameters:  $U_{\text{gap}} = 99\text{mV}$ ,  $I = 10.5\text{nA}$ )

### 3.4 Conclusions and Future Work

This chapter has described how tungsten STM tips can be electrochemically etched with alkali metal hydroxide solutions. The equipment used is described including the need for a special power supply for the DC etching process. Optical microscope images are included showing the microscopic reproducibility of both

AC and DC etching methods. These images also show how deviating from the optimum etching conditions produces a detrimental effect on the microscopic tip shape. At the upper end of the nanoscopic scale FEG-SEM images of AC and DC tips reveal that the AC etched tips show more consistency than the DC tips. Despite occasional good success with AC tips their effective tip radius is frequently too large to resolve the test samples well. The variation in the shape of the DC tips at this scale does not appear to be significant; both shapes of tip seem to possess atomically sharp protrusions at their apexes.

Images recorded with the STM at 78K show how both types of tip can be used to record atomic resolution images.

Future development of tip manufacture could include the installation of a facility for tip self-sputtering<sup>[1]</sup> into the vacuum chamber (probably in the loading arm). In this process electrons are passed from the tip to a metal wire ring in the presence of a low pressure neon atmosphere. The electrons ionise the neon atoms, and the resulting ions are attracted to the tip. By carefully adjusting the voltage between the tip and the ring, the energy of the ions can be chosen to decapitate the tip. If the rounded end of a DC etched tip is too smooth and does not resolve the atoms on a surface then this process can be used to remove the rounded end to leave behind a tip with a smaller effective radius.

### 3.5 References

1. Ekvall, I., et al., *Preparation and characterization of electrochemically etched W tips for STM*. Measurement Science and Technology, 1999. **10**: p. 11-18.
2. Nam, A.J., et al., *Benign Making of Sharp Tips for STM and FIM - Pt, Ir, Au, Pd, and Rh*. Journal of Vacuum Science & Technology B, 1995. **13**(4): p. 1556-1559.
3. Morishita, S. and F. Okuyama, *Sharpening of Monocrystalline Molybdenum Tips by Means of Inert-Gas Ion Sputtering*. Journal of Vacuum Science & Technology A-Vacuum Surfaces and Films, 1991. **9**(1): p. 167-169.

4. Nakamura, Y., Y. Mera, and K. Maeda, *A reproducible method to fabricate atomically sharp tips for scanning tunneling microscopy*. Review of Scientific Instruments, 1999. **70**(8): p. 3373-3376.
5. Oliva, A.I., et al., *Electrochemical preparation of tungsten tips for a scanning tunneling microscope*. Review of Scientific Instruments, 1996. **67**(5): p. 1917-1921.
6. Song, J.P., et al., *A Development in the Preparation of Sharp Scanning Tunneling Microscopy Tips*. Review of Scientific Instruments, 1993. **64**(4): p. 900-903.
7. Melmed, A.J., *The Art and Science and Other Aspects of Making Sharp Tips*. Journal of Vacuum Science & Technology B, 1991. **9**(2): p. 601-608.
8. Liu, A.W., et al., *An improved control technique for the electrochemical fabrication of scanning tunneling microscopy microtips*. Review of Scientific Instruments, 1997. **68**(10): p. 3811-3813.
9. Bourque, H. and R.M. Leblanc, *Electrochemical Fabrication of Scanning-Tunneling-Microscopy Tips without an Electronic Shutoff Control*. Review of Scientific Instruments, 1995. **66**(3): p. 2695-2697.
10. Hockett, L.A. and S.E. Creager, *A Convenient Method for Removing Surface Oxides from Tungsten STM Tips*. Review of Scientific Instruments, 1993. **64**(1): p. 263-264.
11. Vasile, M.J., et al., *Scanning Probe Tips Formed by Focused Ion-Beams*. Review of Scientific Instruments, 1991. **62**(9): p. 2167-2171.
12. Paparazzo, E., et al., *Effects of HF attack on the surface and interface microchemistry of W tips for use in the STM microscope: a scanning Auger microscopy (SAM) study*. Vacuum, 1999. **52**(4): p. 421-426.
13. Zhang, R. and D.G. Ivey, *Preparation of sharp polycrystalline tungsten tips for scanning tunneling microscopy imaging*. Journal of Vacuum Science & Technology B, 1996. **14**(1): p. 1-10.
14. Klein, M. and G. Schwitzgebel, *An improved lamellae drop-off technique for sharp tip preparation in scanning tunneling microscopy*. Review of Scientific Instruments, 1997. **68**(8): p. 3099-3103.
15. Kar, A.K., S. Gangopadhyay, and B.K. Mathur, *A reverse electrochemical floating-layer technique of SPM tip preparation*. Measurement Science and Technology, 2000. **11**(10): p. 1426.

16. Ibe, J.P., et al., *On the Electrochemical Etching of Tips for Scanning Tunneling Microscopy*. Journal of Vacuum Science & Technology A-Vacuum Surfaces and Films, 1990. **8**(4): p. 3570-3575.

## **Chapter 4**

### **Au(111) Surfaces**

4.1	Chapter Introduction .....	91
4.2	Preparing Au(111) Surfaces .....	91
4.2.1	Experimental Method.....	91
4.2.2	Results and Discussion.....	93
4.3	Spectroscopy of Au(111) Surfaces.....	96
4.3.1	Experimental Methods .....	96
4.3.2	Results and Discussion.....	97
4.4	Conclusions .....	100
4.5	Further Work.....	101
4.6	References .....	102

## 4.1 Chapter Introduction

All of the experiments described in this thesis used Au(111) as a base substrate. This chapter includes descriptions of the efforts undertaken to attempt to reproducibly manufacture this surface as well as showing images of the surfaces produced.

STM spectroscopy experiments were run upon adsorbents on Au(111) surfaces. It will be necessary to have a good quality spectrum of the bare Au(111) surface for comparison. This chapter also includes experimental details of STM spectroscopy experiments conducted on the Au(111) surface, and the results collected from these experiments.

## 4.2 Preparing Au(111) Surfaces

### 4.2.1 Experimental Method

For most UHV STM experiments, the sample substrates used are prepared inside the UHV chamber with special equipment, due to the reactivity of the samples prepared. If the samples were exposed to air after being prepared, the surface would quickly react with the constituents in the atmosphere (principally water and oxygen) contaminating the surface. However, the UHV chamber used in this study does not have such sample preparation equipment. This requires that the samples are prepared outside the chamber. To prevent contamination it is vital to use an inert sample that will not react with atmospheric constituents during the transfer of the sample into the UHV chamber. Gold is suitable for this. When using gold as a substrate sample material in an STM it is useful for the atoms in the sample to be rearranged into ordered domains upon the surface. This is because an STM can record an image of a surface that is made up of small (100nm) disordered domains but not with atomic resolution. In order to do this, it is necessary to modify the surface so that it is made up of larger domains in which

the atoms are arranged in a regular pattern. To do this just requires the sample to be heated so that the atoms have enough energy to rearrange themselves into larger domains containing regions where the atoms are arranged into the (111) surface crystal structure. The preference for the (111) structure is because it has a lower energy than the (110) or (100) structures.

An investigation was conducted to see if this method of producing Au(111) surfaces (annealing) could be made more reliable. Au(111) surfaces were prepared by heating an Au on glass slab (purchased from Metallhandel Schröer GmbH) with an open hydrogen gas flame, with no other ambient light present, whilst ensuring that the slab is moved around in the flame to provide even heating for the slab. The exclusion of any other source of light other than the flame enables any colour changes of the surface to be observed more easily.

When heating an Au on silica slab, there are several experimental parameters that can be varied. Three that are more obvious are the length of the H<sub>2</sub>/O<sub>2</sub> flame (which mostly depends upon the H<sub>2</sub> pressure), the position of the slab in the flame and the length of time that the slab is in the flame. When the slab is heated the flame is narrow enough such that only a part of the slab will glow a bright yellow colour. The slab needs to be moved around relative to the position of the flame so that the slab is evenly heated whilst it is in the flame. The slab is not usually held in the flame for the entire annealing session. In fact when a sample had been prepared in this way no regions containing (111) facets could be found (see Figure 4.1).

Normally, once heated to a bright yellow colour, the slab would be removed from the flame for short periods before being reheated. Previously, a slab would be removed for a few seconds to allow the slab to cool so that it no longer glowed, before being returned to the flame. This cycle of heating and cooling would be repeated until the slab took about 3 seconds to cool to ‘black’. The colour of the gold only yields information about the temperature of the surface and not about the temperature of the glass substrate. As the slab is heated its temperature increases and this means that it takes longer for the gold to change colour outside the flame. The existing method using an H<sub>2</sub>/O<sub>2</sub> flame does not repeatedly produce good Au(111) surfaces. An alternative idea that was tried extended the time that the sample was removed from the flame to 30 seconds to give the slab a much longer time to cool between heating cycles.

A way of determining how long a slab should be heated, is to specify how long the slab should be removed from the flame and then to vary the number of times that it is removed from the flame. This method was tried, with the time that the sample should be removed from the flame set at  $\approx 3$  seconds. The sample was removed from the flame 3, 5, 7 or 9 times. The slab is only removed when it has a bright yellow colour. STM images from samples made in this way are shown in §4.2.2.

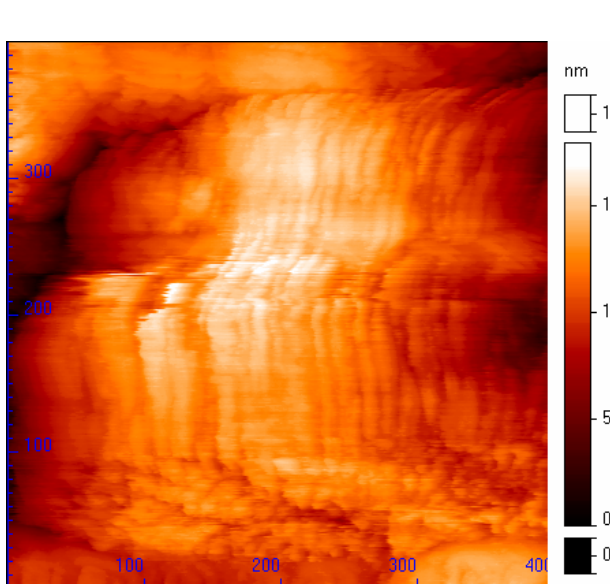


**Figure 4.1:** A  $400\text{nm} \times 400\text{nm}$  STM image of an Au sample, which was prepared by annealing with  $\text{H}_2/\text{O}_2$  flame without removing it from the flame. The structure shown in this image is typical of all images recorded from this sample and shows the amalgamation of smaller microcrystalline regions into a larger one indicating that this method of preparation does not produce good Au(111) structure. (STM parameters:  $U_{\text{gap}} = 0.1\text{V}$ ,  $I = 0.13\text{nA}$ )

## 4.2.2 Results and Discussion

As a way of gaining further insight into the annealing process, atomic force microscopy (AFM) images were recorded of Au slabs before and after treatment with the  $\text{H}_2/\text{O}_2$  flame (Figure 4.2 and Figure 4.3).

Before heat treatment the surface contains nanocrystalline regions nearly all of which are less than 200nm across. The heating process transforms these into much larger regions. Although the difference between these two images appears quite dramatic, in practice the situation is more complicated. In most cases only a part of the surface will be reformed into domains of Au(111) (Figure 4.4). The better

the annealing technique the greater the percentage of Au(111) structure and the larger the domains of Au(111).

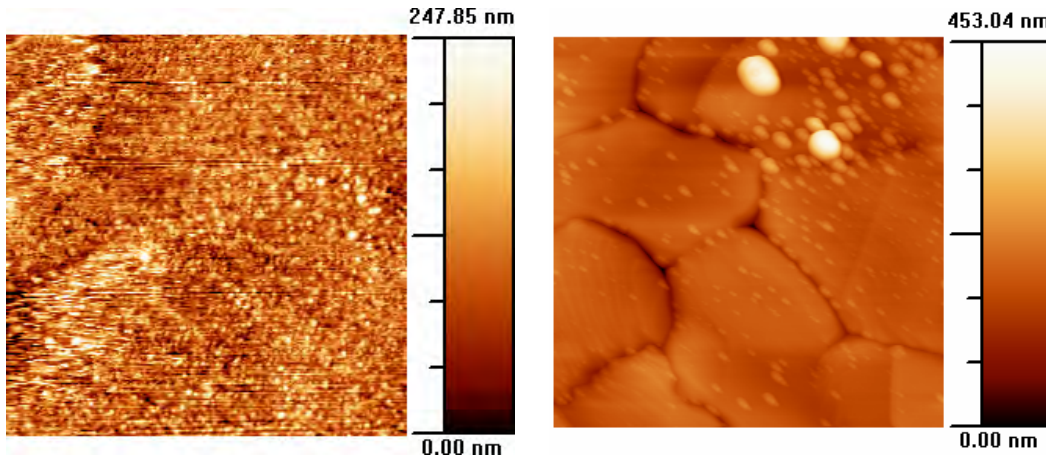


**Figure 4.2 (Above):** A  $5\mu\text{m} \times 5\mu\text{m}$  topographical AFM image of an Au sample before annealing, showing a nanocrystalline structure.<sup>[1]</sup>

**Figure 4.3 (Above):** A  $5\mu\text{m} \times 5\mu\text{m}$  topographical AFM image of an Au sample after annealing. This image shows the large domains as well as some 'lumpy' features both produced by the annealing process.<sup>[1]</sup>

With the gold on glass samples used, (when approaching the tip to the surface) the chance of the tip meeting an area of Au(111) depends upon the proportion of Au(111) on the surface. The original method for producing Au(111) did work sometimes as can be seen from Figure 3.19 but as mentioned previously this method was not readily repeatable. In the Experimental Method, a modification was described to the way that a sample was made, where the time that the sample removed from the flame was extended up to 30s. This did not yield an improvement in the quality of the samples (Figure 4.5) but this did reveal that there is an upper limit to how long the slab can be removed from the flame. Also, samples from slabs removed from the flame 3 or 5 times during annealing did not yield good Au(111) surfaces either.

Samples made from slabs that had been removed 7 or 9 times were better. The sample that had been removed from the flame 7 times revealed some triangular structures (Figure 4.6) but the sample that had been removed from the flame 9 times yielded the characteristic herringbone structure and atomic resolution of the structure even at room temperature (Figure 4.7 and Figure 4.8). With a second

sample that had been prepared with 9 cycles of heating and cooling, surfaces of a good enough quality were obtained, that with a good tip produced images such as Figure 4.9 showing a single atom defect within a section of Au(111).

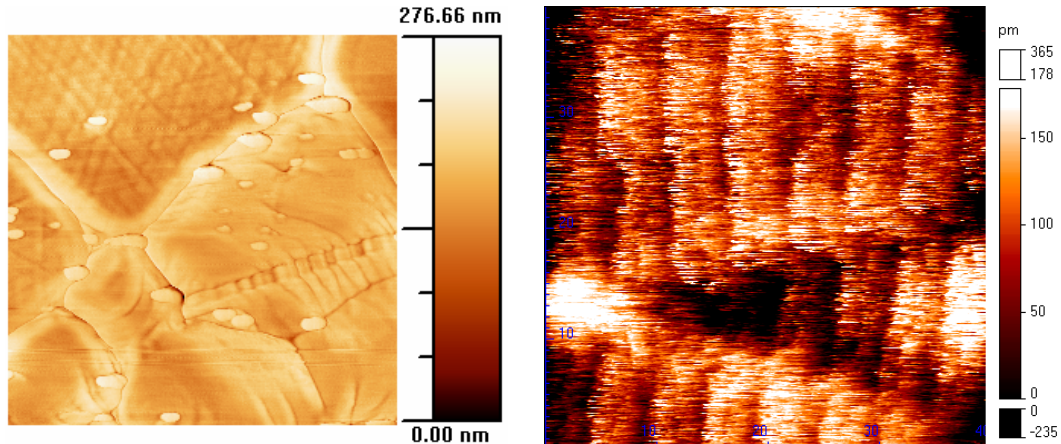


**Figure 4.4 (Above):** A  $2\mu\text{m} \times 2\mu\text{m}$  phase AFM image of an annealed Au sample, showing an area of Au(111) in the upper part of the image.<sup>[1]</sup>

**Figure 4.5 (Above):** A  $40\text{nm} \times 40\text{nm}$  image of an Au sample that had been removed from the flame for 30s as part of the annealing process. No good quality areas of Au(111) were found on this sample. (STM parameters:  $U_{\text{gap}} = 0.12\text{V}$ ,  $I = 10.5\text{nA}$ )

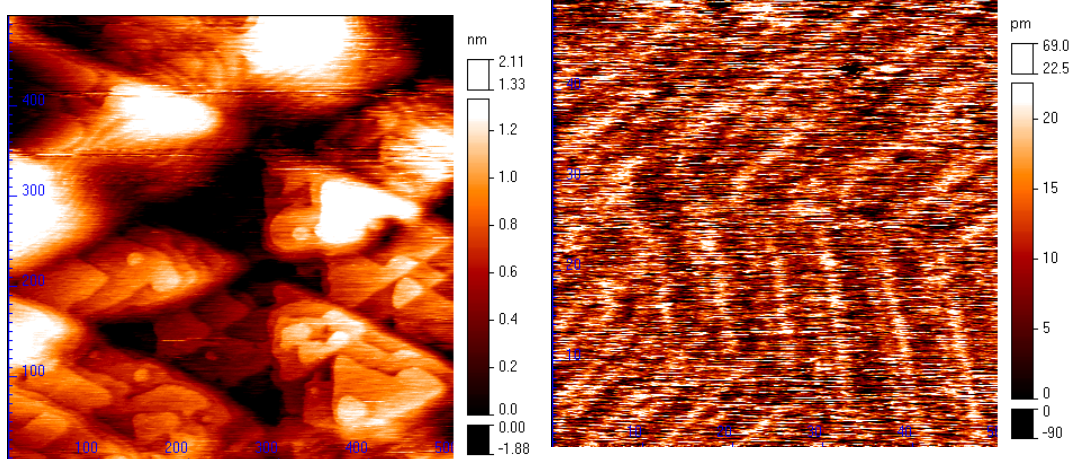


**Figure 4.6 (Above):** A room temperature  $500\text{nm} \times 500\text{nm}$  STM image of a sample removed from the flame 7 times whilst it was being annealed. This image shows detailed Au(111) triangle structure. (STM parameters:  $U_{\text{gap}} = 86\text{mV}$ ,  $I = 1.9\text{nA}$ )

**Figure 4.7 (Above):** A room temperature  $50\text{nm} \times 50\text{nm}$  STM image of a sample that had been removed from the flame 9 times whilst it was being annealed. The 'noise' of the image is due to it being recorded at room temperature. (STM parameters:  $U_{\text{gap}} = 97\text{mV}$ ,  $I = 15.4\text{nA}$ )

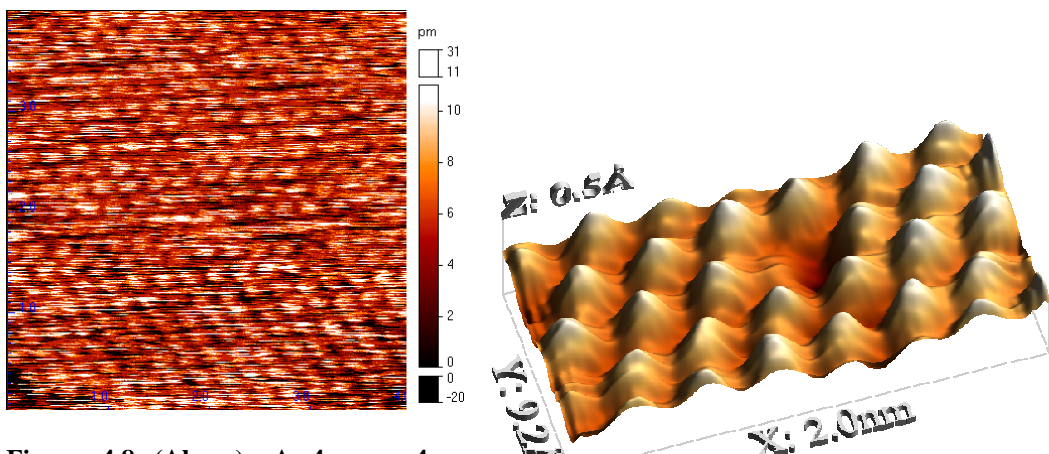


**Figure 4.8 (Above):** A 4nm  $\times$  4nm 'grainy' room temperature atomic resolution image of the sample that had been removed from the flame 9 times during its annealing process. (STM parameters:  $U_{\text{gap}} = 95\text{mV}$ ,  $I = 15.4\text{nA}$ )

**Figure 4.9 (Above):** A section of Au(111) showing a single atom defect. (STM parameters:  $U_{\text{gap}} = 80\text{mV}$ ,  $I = 1.9\text{nA}$ )<sup>[11]</sup>

### 4.3 Spectroscopy of Au(111) Surfaces

#### 4.3.1 Experimental Methods

Scanning Tunnelling Spectroscopy (STS) (or  $I$  -  $V$ ) experiments were conducted on Au(111) surfaces. This was done to provide background results to compare with STS experimental results from samples coated with organic molecules. For STM, spectroscopy is different from that normally used with visible or infrared radiation. (For more details see §2.2.4.) When recording spectra, the LTSTM is configured so that the  $I$  signal recorded is quite large to ensure a large signal-to-noise ratio. This brings the tip closer to the surface.

The spectra presented here show data for an applied voltage of  $-1\text{V}$  to  $+1\text{V}$ . For any given spectroscopy experiment, the signal-to-noise ratio is poor so the obvious way to improve it is to conduct many spectroscopy experiments and average the results. If the surface is assumed to be uniform over a small area (e.g. 5nm  $\times$  5nm) then it is most convenient to record spectroscopy data in a grid

pattern. For the Au(111) sample a 5 by 5 grid pattern was used (25 measurements in each grid). In each data file recorded there are measurements for two sets of grids corresponding to the forward and backward directions of the tip. In all, eight data files were recorded from the Au(111) sample used, resulting in 400 ( $8 \times 2 \times 25$ ) spectroscopy experiments that were conducted on a  $5\text{nm} \times 5\text{nm}$  area. The spectra were recorded at a temperature of between 4.2K and 5K. When collecting this data it was important to know what the surface looked like in order to confirm that the area underneath the tip was a section of Au(111) as required. Consequently prior to collecting the STS data, images were recorded of the surface to ensure that a suitable place was found.

### 4.3.2 Results and Discussion

A series of 400 STM spectroscopy experiments were conducted on a  $5\text{nm} \times 5\text{nm}$  part of a region (terrace) of Au(111) at 5K. Plots of  $I$  vs.  $V$  and  $\frac{dI}{dV}$  vs.  $V$  for the data recorded are shown in Figure 4.10.

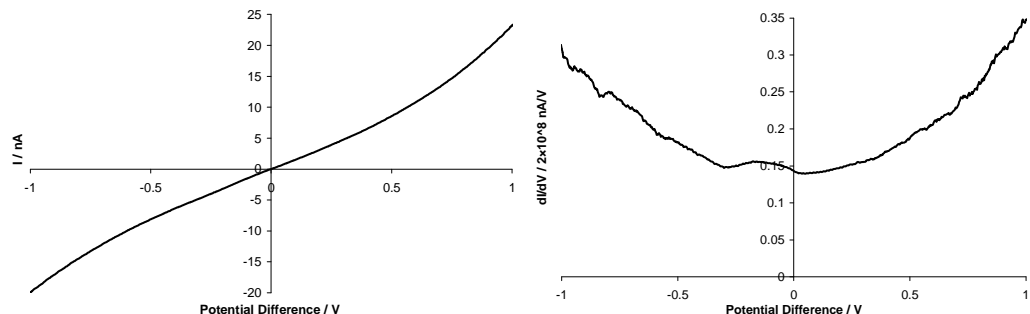


Figure 4.10:  $I$  vs.  $V$  and  $\frac{dI}{dV}$  vs.  $V$  curves for Au(111)

The  $I$  vs.  $V$  plot shows a gently sloping curve where the tunnelling current increases with increasing potential. This trend naturally shows itself in the  $\frac{dI}{dV}$  vs.  $V$  curve as an increase in the  $\frac{dI}{dV}$  vs.  $V$  signal with increasing magnitude of applied potential. In addition to this general trend there are small fluctuations at potentials larger than  $\pm 0.7\text{V}$ . There is also a broad peak at around  $-0.1\text{V}$ . Of the 400

experiments conducted the data from 4 of them were rejected for exceeding standard deviation threshold limits. Since the proportion of poor quality graphs is small (1%) we can be reasonably confident that the remainder represent the system under investigation.

The shape of this  $\frac{dI}{dV}$  vs.  $V$  curve is not as expected. Previous experiments on Au(111) have recorded a step in this curve at  $-0.5V$ <sup>[2, 3]</sup> both at 4K and 305K. This step is attributed to a surface state in electronic structure of the metal. The surface acts as a defect to the crystal structure introducing a perturbation in the electronic structure. The reason for the discrepancy between this data and that in [2, 3] could lie in work presented in a paper by Vázquez de Parga *et al*<sup>[4]</sup> which suggests that the crystal structure of the very end of the tip has a significant effect on the shape of the  $\frac{dI}{dV}$  vs.  $V$  curve. In their paper they present two versions of the  $\frac{dI}{dV}$  vs.  $V$  spectrum of a Cu(111) surface. Sometimes in their experiments they would record one type and at other times another. They do not describe any intentional experimental circumstances that could account for the two types of  $\frac{dI}{dV}$  vs.  $V$  curve recorded. They modelled what the spectra should look like for (111) FCC and (111) BCC arrangements of tip atoms. The calculated spectra for the two tip atom arrangements could be matched to the experimental data indicating that in some experiments the end of their tip had an FCC structure and in others a BCC structure. Whether the tip had an FCC or a BCC structure seemed to be due to whether the tip atoms had enough energy to decay from the meta-stable FCC structure to the more stable BCC structure. From the difference between the spectrum in Figure 4.10 and those in [4] it seems that it likely that the structure of the tip used to record the data in Figure 4.10 was neither FCC or BCC. This raises an important issue as to whether STM spectra ( $I$  vs.  $V$ ,  $\frac{dI}{dV}$  vs.  $V$ , or  $\frac{d^2I}{dV^2}$  vs.  $V$  plots) of species on top of a metal substrate can be presented without subtraction of the spectrum of the underlying substrate recorded with the same tip.

To complicate things further, work by Zhang and Ivey<sup>[5]</sup> suggests that tips become blunter through regular usage implying that the end tip structure of a given tip does not stay the same. This raises doubts as to whether it is sensible to conduct STS spectra on an uncoated metal sample and then use the same tip on a metal sample coated with an adsorbate if the structure of the tip has changed during the collection of the data from the uncoated sample. However the sample that Zhang

and Ivey were using contained many polycrystalline domains therefore was a much rougher surface than the samples that are used for this study.

As described in §4.2.1 the gold samples used (initially) possess a polycrystalline structure but the H<sub>2</sub>/O<sub>2</sub> flame heating process enlarges the domains and gives them a regular structure. Within one of these regular ordered domains the surface is flatter than an equivalent polycrystalline surface so it might be reasonable to assume that when imaging domains like this the tip is less likely to come into contact with the surface thus reducing the risk of structural changes to the tip. However in the process of trying to find one of these areas the tip will have to track over parts of the surface that will not be as flat. This increases the risk of the surface coming in contact with the tip and changing its shape.

When using the STM to just collect topography images these issues relating to changes in tip structure do not seem to be as significant. It is normal for the tip to be damaged occasionally as it approaches too close to a rough part of the surface. This does not always mean that the tip has to be replaced. It is sometimes possible to restore the quality by very briefly increasing the voltage between the sample and tip, to ten times its usual value. This switches the electron transfer mechanism from tunnelling to electron flow. In this mode the electrons flowing through the tip change its structure in an attempt to make it sharper. It is likely that the increased electron flow induces localised melting such that material is removed from the end of the tip. Normally the tip is put through several cycles of increasing the tunnelling voltage and then restoring the voltage back to its original value. Often this is adequate to restore the quality of the tip so that it can yield good quality images again. However it is possible that the tip structure has changed but this is not noticeable in the images.

It is worth noting that Vázquez de Parga *et al.* do not report any STM images showing differences in the topography due to the differences in tip structure. If they did not see any significant differences in the topography this would be in agreement with the data collected with the STM in this study. For example compare the images of the Au(111) surface in Figure 4.11. These show 4nm × 4nm sections of the Au(111) surface with the same arrangement of the metal atoms. However the *appearance* of the atoms in the two images is different. In the left image the contrast between light and dark areas gives the image a ‘cobblestone’ appearance whereas with the right image the bright regions are

more centred onto the lattice positions. This difference in appearance does not affect the lattice parameters so both surfaces can be identified as Au(111) structures but might indicate tip characteristics. This might explain why other users of STMs who just collect topography images of the surface have not seen evidence suggesting this sort of tip structure dependence

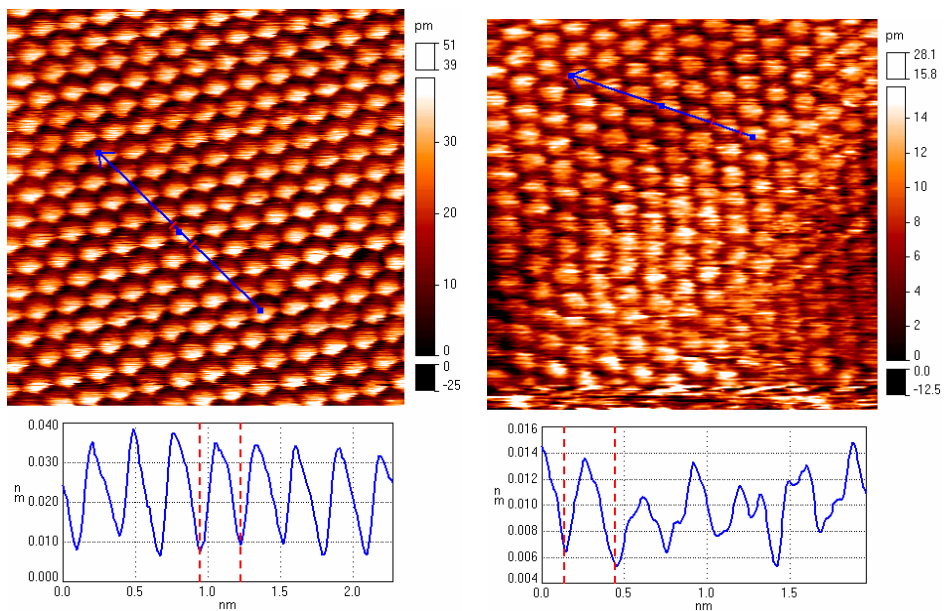


**Figure 4.11: STM images of  $4\text{nm} \times 4\text{nm}$  sections of Au(111) terraces recorded with similar tunnelling parameters. In the left image the changes in the electronic structure is recorded as dark and light areas that give the corrugation a ‘cobblestone’ appearance whereas in the image on the right the light areas are more centred on the lattice positions. The difference in appearance might indicate differences in the tip structure. Note the similar inter-atomic spacing of  $\approx 0.3\text{nm}$ .**

#### 4.4 Conclusions

In this chapter descriptions are given for reliable methods of manufacturing gold samples containing regions of Au(111). Only part of the surface was converted into the Au(111) reconstruction but typically the proportion was high enough so that finding these regions by scanning across the surface was reasonably trivial.

Evidence of the reconstruction of these regions is shown in a selection of STM images including images showing the characteristic  $22 \times \sqrt{3}$  “herringbone” reconstruction.

The results of STS experiments conducted at 5K on the Au(111) surface are given. There is some discussion into the reasons for the disparity between the data presented here and equivalent data published previously. The STS data suggests that the arrangement of the atoms at the apex of the tip is different to that seen in previously published work. No significant differences are seen between the STM images recorded with this STM and those published previously indicating that the process of collecting STM images is less sensitive to the tip structure than the STM spectroscopy.

## 4.5 Further Work

Although good images and spectra have been recorded from gold surfaces in the way anticipated there are still ways in which the manufacture of these samples can be improved. Despite the understanding of the optimum conditions for making the Au(111) samples, it is still common to find that on some samples a large proportion of the surface is not arranged into a good Au(111) structure. Consequently when samples are studied it sometimes can take a significant period of time to find a suitable area of the surface to work with. To make the experiments more time efficient it will be necessary to make the samples in a different way that produces flatter surfaces. The best way to do this would be to use solid metal single crystals of gold. These can be cut so that the exposed face of the crystal has the (111) structure. Rather than heating the sample on the outside and later loading into the UHV chamber, it is better if it is electrically heated, gradually, inside the chamber at approximately 800°C for 10 to 12 hours. By being solid metal the heat flow through the sample is very good ensuring even heating. Such a sample would have a much flatter surface and it is most unlikely that the tip would be positioned on a part of the surface that did not contain good Au(111) structure. However such an improvement comes at a price. These single crystal samples are more expensive than their gold-on-glass counterparts.

Therefore it is not really realistic to use such samples in the semi-disposable way that the metal-on-glass samples are used. It is necessary to have a facility to clean adsorbates off the surface so that the substrate can be reused. The best way to do this is with a noble gas (usually He or Ar) ion gun. It is also possible that such a device could be modified for use as a tip cleaning/sharpening tool<sup>[6]</sup>.

Although an STM can resolve the metal surface with atomic resolution it would be useful to have the facility to conduct Low Energy Electron Diffraction (LEED) experiments as an alternative way of checking the surface structure if the STM is not working correctly. This technique is analogous to x-ray diffraction except that it records the 2D crystal structure of a surface rather than the 3D crystal structure of a bulk solid.

In order to add the facilities to implement these various techniques to the existing UHV chamber, a separate chamber would be required on which to mount the new equipment.

## 4.6 References

1. processed with WSxM© <http://www.nanotec.es>.
2. Everson, M.P., R.C. Jaklevic, and W.D. Shen, *Measurement of the Local Density of States on a Metal-Surface - Scanning Tunneling Spectroscopic Imaging of Au(111)*. Journal of Vacuum Science & Technology A-Vacuum Surfaces and Films, 1990. **8**(5): p. 3662-3665.
3. Chen, W., *Scanning Tunneling Microscopy Observation of an Electronic Superlattice at the Surface of Clean Gold*. Phys. Rev. Letters, 1998. **80**(7): p. 1469-1472.
4. Vázquez de Parga, A.L., et al., *Electron Resonances in Sharp Tips and Their Role in Tunneling Spectroscopy*. Phys. Rev. Letters, 1998. **80**(2): p. 357-360.
5. Zhang, R. and D.G. Ivey, *Preparation of sharp polycrystalline tungsten tips for scanning tunneling microscopy imaging*. Journal of Vacuum Science & Technology B, 1996. **14**(1): p. 1-10.

6. Ekvall, I., et al., *Preparation and characterization of electrochemically etched W tips for STM*. Measurement Science and Technology, 1999. **10**: p. 11-18.

## Chapter 5

### Alkanethiols on Au(111) Surfaces

5.1	Chapter Introduction .....	105
5.2	Octanethiol on Au(111).....	106
5.2.1	Preparation of Octanethiol Self-Assembled Monolayers.....	106
5.2.1.1	Experimental Method.....	106
5.2.1.2	Results and Discussion.....	107
5.2.2	Spectroscopy Experiments with Octanethiol on Au(111).....	113
5.2.2.1	Experimental Methods .....	113
5.2.2.2	Results and Discussion.....	114
5.3	Dimethyl Disulphide on Au(111) .....	121
5.3.1	Preparation of Dimethyl Disulphide Self-Assembled Monolayers..	121
5.3.1.1	Experimental Method.....	121
5.3.1.2	Results and Discussion.....	123
5.3.2	Spectroscopy Experiments of Dimethyl Disulphide on Au(111)....	129
5.3.2.1	Topographically Varying Scanning Tunnelling Spectroscopy .	130
5.3.2.1.1	Experimental Method.....	130
5.3.2.1.2	Results and Discussion.....	130
5.3.2.2	Scanning Tunnelling Spectroscopy Conducted on a Complete Monolayer .....	133
5.3.2.2.1	Experimental Method.....	133
5.3.2.2.2	Results and Discussion.....	133
5.4	Conclusions .....	136
5.5	Future Work .....	139
5.6	References .....	140

## 5.1 Chapter Introduction

The essence of this work involves investigating the response of an STM to the ‘fingerprint’ region infrared radiation from an OPO. Such an experiment is made more interesting if the sample is expected to specifically absorb at the wavelength of the radiation emitted by the OPO. As a consequence of the LiNbO<sub>3</sub> crystals available for use with the OPO only part of the ‘fingerprint’ region is available. Some functional groups that have vibrational modes here are C≡N, C≡O, C≡C, and alkane C-H (sp<sup>3</sup> hybridised carbon). In order to make up a sample containing some C-H bonds it would be possible in principle to just coat a gold sample with a heavy hydrocarbon, which will not evaporate easily in the UHV conditions. However an STM would probably find it difficult to image such a sample due to the disordered arrangement of molecules on the surface. A better solution is to make use a self-assembled monolayer (SAM). This ensures a degree of order to the arrangement of molecules on the surface.

Octanethiol and dimethyl disulphide are examples of molecules that can be formed into SAMs. This chapter describes the preparation of SAMs of octanethiol and dimethyl disulphide and their investigation by recording STM images and spectra of the surface. The results of these investigations were used to determine the suitability of the molecules for laser driven STM experiments.

## 5.2 Octanethiol on Au(111)

### 5.2.1 Preparation of Octanethiol Self-Assembled Monolayers

#### 5.2.1.1 Experimental Method

The easiest way to prepare a SAM on gold is to use an alkanethiol. The Au–S bond enthalpy is high enough such that the S–H bond in the molecule will break and an Au–S bond will form. With enough molecules an ordered ‘carpet’ of alkanethiolate (R–S) molecule will form on the surface of the gold (see Figure 5.1).

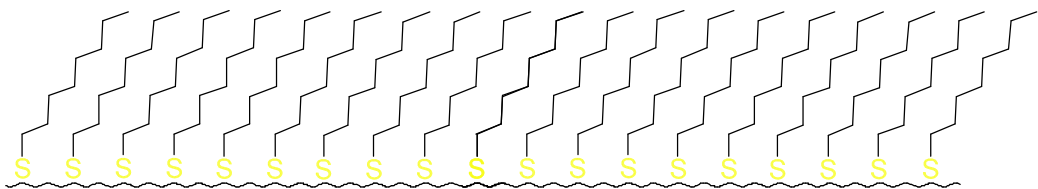


**Figure 5.1:** showing a stylised representation of a SAM of octanethiol. The diagonal zigzag lines are the carbon chains, the yellow S's are the sulphur atoms and the horizontal wavy line is the metal surface.

The easiest way to make such a system is to prepare an Au sample as described in §4.2.1 and when cooled immerse it into a dilute solution of an alkanethiol in ethanol. This method was applied for three Au samples each in a different concentration of octanethiol ( $\text{H}_3\text{C}(\text{CH}_2)_7\text{SH}$ ). These slabs were then immersed in a solution of octanethiol in ethanol for 16 to 20 hours. Once removed from the solution the samples are rinsed with ethanol before being loaded into the STM. Three different concentrations of octanethiol were used, to enable the production of three different types of octanethiol on Au(111) systems. It was anticipated that varying the concentration of octanethiol in the ethanol might affect the structure of the resulting octanethiol on Au(111) system when imaged with the STM.

Specifically the greater the concentration of octanethiol solution the greater the anticipated coverage of octanethiol on the Au(111). STM images of these samples are shown in §5.2.1.2.

### 5.2.1.2 Results and Discussion

Images of gold samples covered with a SAM of octanethiol are shown below. Where cross-sections are included they have been calculated with four nearest neighbour averaging. The different images correspond to different concentrations of octanethiol in ethanol used to make the sample.

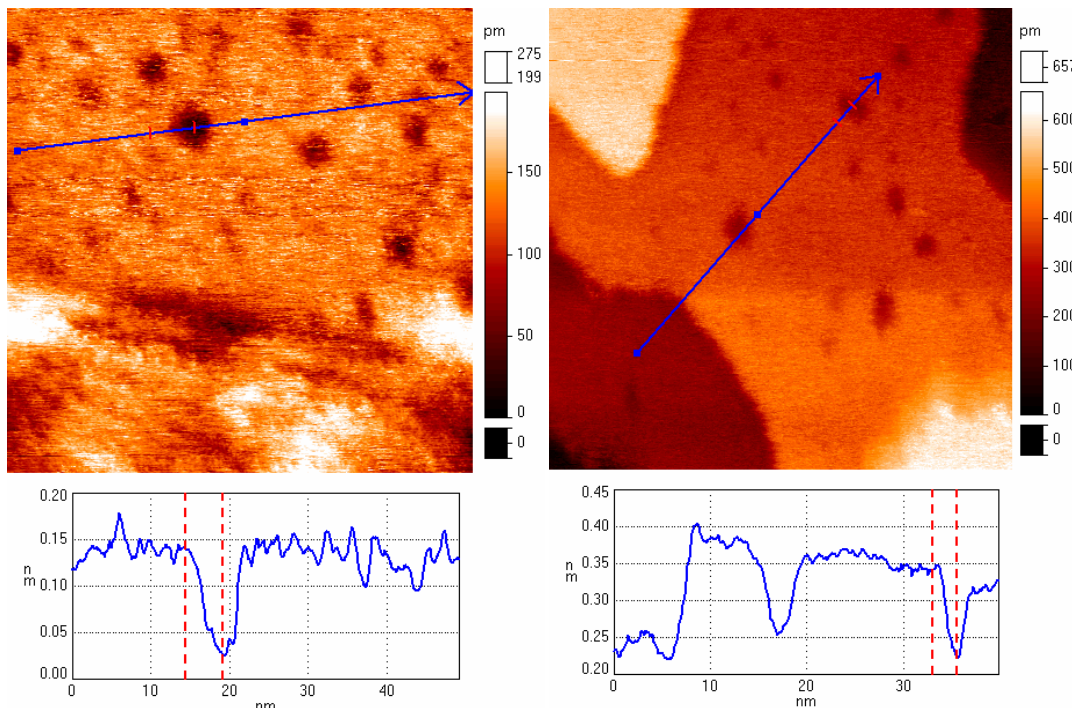


**Figure 5.2 (Above):** A 50nm × 50nm STM image of an octanethiol on gold sample, made using 1mM octanethiol solution showing 'holes' in the surface. (STM parameters:  $U_{\text{gap}} = 426\text{mV}$ ,  $I = 219\text{pA}$ )

**Figure 5.3 (Above):** Another 50nm × 50nm image of the sample in shown in Figure 5.2, that shows another example of these 'holes' in the thiol layer. (STM parameters:  $U_{\text{gap}} = 393\text{mV}$ ,  $I = 122\text{pA}$ )

The sample shown in Figure 5.2 and Figure 5.3 was made with 1mM octanethiol solution. The upper part of Figure 5.2 shows a covered terrace of Au(111) and the

sharp changes in contrast in Figure 5.3 indicate the edges of the layers of gold atoms. The dark patches on the surface are depressions in the thiol layer. Descriptions of the origin of these are given later in the text. The sample shown in Figure 5.4 and Figure 5.5 was made with a 10mM octanethiol solution. Again in both images the edge of atomic layers and the depressions in the thiol layer can clearly be seen. Note the ‘nibbled’ appearance of the atomic step edges in Figure 5.5.

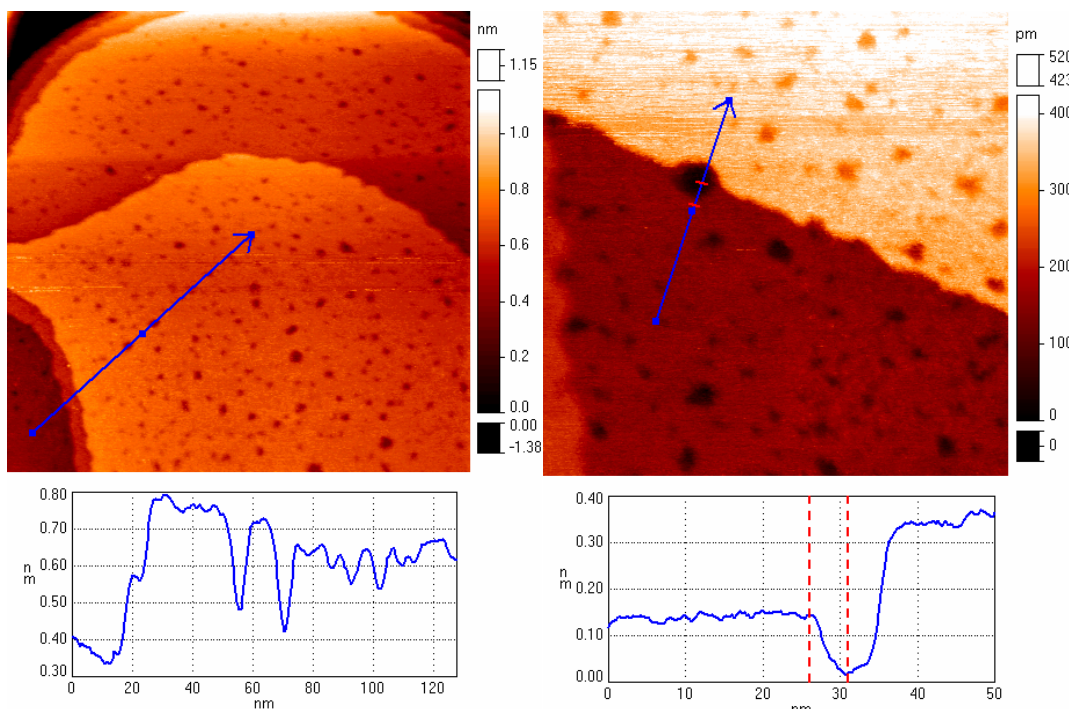


**Figure 5.4 (Above):** A 200nm × 200nm STM image of an octanethiol on Au sample, made with a 10mM solution of octanethiol. The ‘holes’ can clearly be seen in the gold terrace. (STM parameters:  $U_{\text{gap}} = 401\text{mV}$ ,  $I = 411\text{pA}$ )

**Figure 5.5 (Above):** A 100nm × 100nm enlarged section of the sample in Figure 4.36 showing a detailed image of a step edge. The surface density of holes in the 10mM sample appears to be greater than in the 1mM sample. (STM parameters:  $U_{\text{gap}} = 418\text{mV}$ ,  $I = 210\text{pA}$ )

Figure 5.6 shows a section of a sample made with a 100nM octanethiol solution. In this image some structure can be seen in the thiol layer. These images of octanethiol samples reveal that the STM could record molecular resolution images of the SAM of thiol molecules on the Au surface. Figure 5.7 shows a section of a SAM that in part shows individual molecules. The lattice spacing in the ordered

part of the surface  $\approx 0.5\text{nm}$  ( $= \sqrt{3} \times 0.3\text{nm}$  (Au(111) lattice spacing) *cf.* Figure 4.11). This thiol lattice spacing is consistent with work published previously<sup>[1, 2]</sup>.

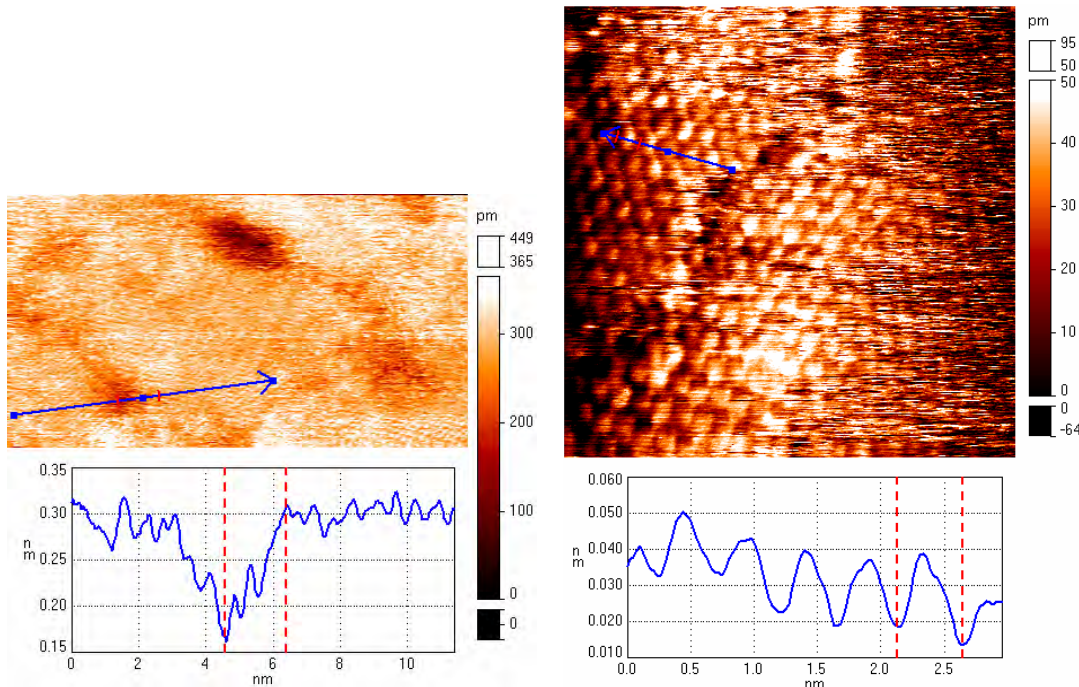


**Figure 5.6 (Above):** A  $20.0\text{nm} \times 10.9\text{nm}$  STM image of an octanethiol on Au sample, made with a  $100\text{nM}$  octanethiol solution. A ‘hole’ shown in black can clearly be seen towards the top of the image. The ‘holes’ in this sample appear to be due to a change in the packing of the octanethiol molecules. (STM parameters:  $U_{\text{gap}} = 435\text{mV}$ ,  $I = 504\text{pA}$ )

**Figure 5.7 (Above):** A  $10\text{nm} \times 10\text{nm}$  STM image of an octanethiol SAM on gold. It was made by immersing a gold sample into a  $1\text{mM}$  solution of octanethiol overnight in a refrigerator. Note the lattice spacing in the ordered part of the surface is  $\approx 0.5\text{nm}$  ( $\approx \sqrt{3} \times 0.3\text{nm}$  (Au(111) lattice spacing)) (STM parameters:  $U_{\text{gap}} = 491\text{mV}$ ,  $I = 101\text{pA}$ )

It is useful to compare this with Figure 5.8 also recorded with the same STM. The sample was made prior to this study but in the same way as that for Figure 5.7. This indicates that the technique used to make these samples coats the surface with the thiol molecules. An additional way to determine that the surface has been coated with thiol molecules is to conduct STM spectroscopy experiments upon them. Section 5.2.2 describes some experiments that were conducted on such samples and shows that the shape of these spectroscopy curves is very different to that for the unexposed sample, providing additional evidence that these samples have been coated with octanethiol molecules.

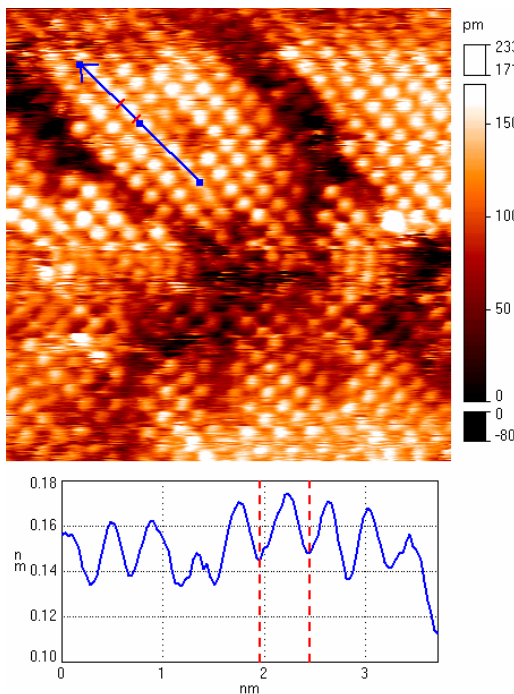


**Figure 5.8:** A  $10\text{nm} \times 10\text{nm}$  STM image of an octanethiol SAM on gold sample recorded with the same STM but prior to this study and made in a similar way to the sample in Figure 5.7. Note that the spacing between the molecules is similar to that in Figure 5.7. (STM parameters:  $U_{\text{gap}} = 1\text{V}$ ,  $I = 108\text{pA}$ )

Figure 5.7 highlights an important aspect of STM images of surfaces. In most cases STMs can only record molecular resolution images like this when the molecules are arranged in an ordered pattern on the surface. If the orientations of the molecules are in a 2D fluid phase and not locked together in the plane of the SAM then it is possible that they can be moved by the tip and are not immobile for long enough to be accurately imaged. The presence of this ordered arrangement in part of the image but with no significant height change between the ordered and disordered areas suggests that the localised conditions are not always right for the molecules to arrange themselves in an ordered pattern, despite the quality of the tip.

Information was recorded on how the thiol molecules arrange themselves on the surface of the Au, specifically the presence of ‘holes’ in the surface. The size and depth of these ‘holes’ can vary and is related to the concentration of the thiol solution used to prepare the samples. It is important to remember when examining depth measurements of these holes that they may not be accurate. The reason for this is that the addition of octanethiol changes the height of the potential barrier (workfunction) of the surface. In §2.2.3 it was stated that at a fixed applied voltage ( $U_{\text{gap}}$ ) the tunnelling current is related to the workfunction by the following expression (Equation 2.26):

$$I \propto e^{-\frac{2}{\hbar}\sqrt{2m\varphi}L}$$

The images in this present section were all recorded under the constant current regime. Assuming that the proportionality constant is identical in all areas of the image, the expression  $e^{-\frac{2}{\hbar}\sqrt{2m\varphi}L}$  will be constant at all places in the image. Note that  $L$  in the above expression relates to the distance between the tip and the sample, whereas the STM images record the distance that the tip has to move in order to keep the tunnelling current fixed. There is a small offset between these two quantities. In order for the feedback loop to correct for the variations in the surface it has to assume that  $\varphi$  is fixed across the surface. If  $\varphi$  is not fixed then the distance the tip has to move will not correspond to the topography of the surface. However if it is known how the workfunction varies across a surface then it is possible to correct for this. In the regime of constant current then the above expression can be rearranged to:

$$\varphi_1 L_1^2 = \varphi_2 L_2^2 \quad \text{Equation 5.1}$$

One possibility for these ‘holes’ is that they are gaps in the thiol layer, i.e. there are gold atoms at the bottom of these holes. If that is the case then the workfunction in the hole will be different to the surrounding area. The workfunction of gold is  $5.35\text{eV}^{[3]}$  and for octanethiol is  $1.17\text{eV}$  lower<sup>[4]</sup> ( $4.18\text{eV}$ ). Since the STM would assume that the workfunction in the holes is the same as the surrounding area Equation 5.1 reveals that the STM would measure the hole to be deeper than it really was. The length of an octanethiolate molecule is  $\approx 10\text{\AA}$  but the holes are no more than  $2\text{\AA}$  ruling out the possibility that the holes are unexposed regions of the gold substrate.

Another possibility is that there is a missing patch of Au atoms underneath the thiol molecules (see Figure 5.9). This has been previously suggested<sup>[5]</sup> and might explain why the thiol molecules can be seen in parts of the holes. This is likely to be the reason for the holes in Figure 5.4 since the depths of the ‘holes’ are  $\approx 2\text{\AA}$ . The regular triangle shape of the layers in Figure 5.5 has been perturbed and now the edges have a ‘nibbled’ appearance. The thiol molecules have restructured the

arrangement of gold atoms in the layer and consequently the straight edges of the gold layers have been lost.

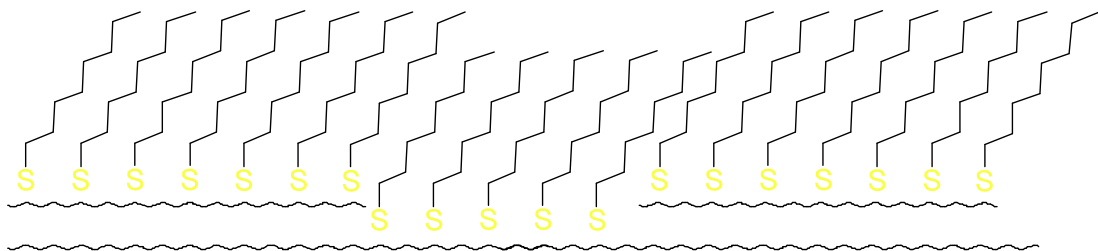


**Figure 5.9:** A stylised representation of octanethiol molecules covering a surface of gold with a gap in the uppermost atomic layer. The distance between the atomic layers is  $\approx 2\text{\AA}$ .

Another possibility is that some of the thiol molecules are not positioned at such a steep angle as usual on the surface (see Figure 5.10). This would explain the appearance of what appears to be molecules continuing into the highlighted depression in Figure 5.6.

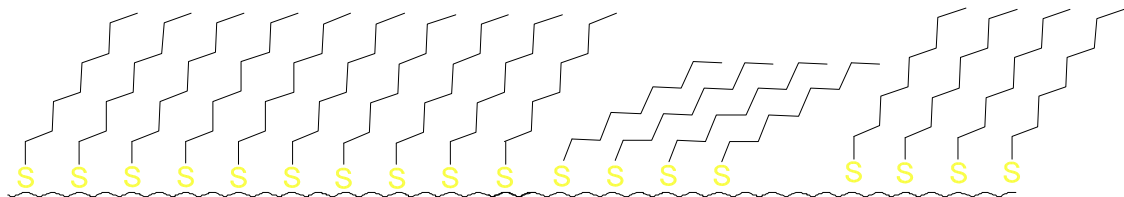


**Figure 5.10:** A stylised representation of octanethiol molecules on a gold surface with some of the molecules at a different angle to the surface than the others showing how such a difference can produce depressions in the surface.

The ‘holes’ indicated in Figure 5.2, Figure 5.3 and Figure 5.5 have depths of  $1.0\text{\AA}$ ,  $1.3\text{\AA}$  and  $1.2\text{\AA}$  respectively. Identifying the origin of these depressions is not trivial. It may not be possible to assign the origin of these depressions purely on depth alone since they are less than  $2\text{\AA}$  deep. If the profile of the tip is large enough then it will not be able to reach the bottom of a depression leading to a false measurement of its depth. These depressions may still be due to missing gold atoms despite their depth apparently not being deep enough.

Prior to conducting these experiments there was an expectation that that the ‘holes’ would be bare areas of gold and that by varying the concentration of octanethiol in ethanol the holes would vary in size. However it seems that the

holes are due to other effects and that varying concentration does not significantly change the sizes of the holes. It was primarily as a consequence of these results that the various vapour phase sample-dosing methods were developed in attempt to better control the quantity of any chemical added onto the gold surface.

## 5.2.2 Spectroscopy Experiments with Octanethiol on Au(111)

### 5.2.2.1 Experimental Methods

One of the ways of characterising a SAM with an STM is to conduct STS experiments on it to see how the monolayer changes the tunnelling characteristics of the surface. As described in §2.2.4 it is known that under certain conditions vibrational modes in molecular species on the surface can appear in STS spectra. Although the vibrational modes for the gas or liquid phase of octanethiol are well known sometimes these modes can shift when the molecules are adsorbed onto a surface. Also, the detection mechanism for these modes with STM is different to that for other surface science techniques such as low energy electron diffraction (LEED). Therefore it is useful to know whether these modes can be seen in STS experiments.

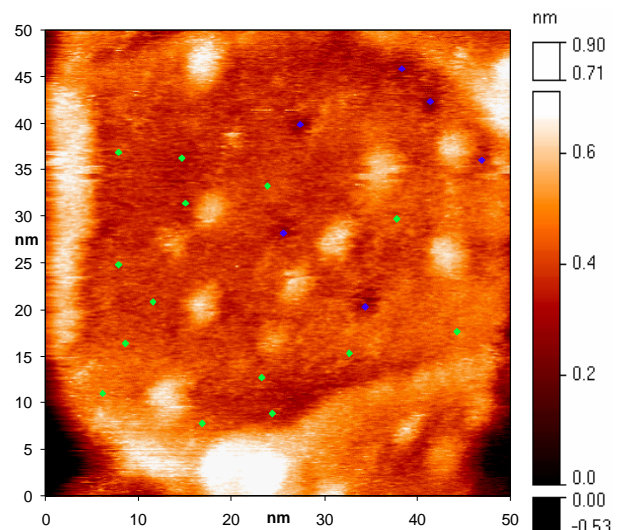
STS experiments were undertaken on a monolayer of octanethiol on Au(111) at 78K ( $\pm 1\text{K}$ ). As with the experiments on Au(111) many spectra were recorded, but this time they were not in a grid pattern. As images of the octanethiol on Au(111) surfaces were recorded, specific places on the surface were chosen at which to conduct the spectroscopy experiments. At each location 5 STS measurements were run sequentially. In this context an STS measurements consists of ramping the applied voltage from one predetermined extreme to the other whilst recording the  $I$  signal. Making several measurements at each location increases the signal to noise ratio for the data collected at that location. Ideally it would be better to collect more sets of data at each location on the surface but there is a limit (due to software constraints) to how much data can be collected at each location. At each

location up to 2000 data points can be recorded. These can be recorded as part of one STS measurement where the applied voltage is ramped from one extreme to the other with 2000 increments between these two extremes. This provides the highest available voltage (energy) resolution. However in an attempt to reduce the signal to noise of the data recorded at each location the average of five measurements recorded at each location was used. This reduced the voltage resolution between the two extremes to 400 increments. This trade off provides the optimum use of the 2000 data points that can be used at each chosen point of the surface. The spectroscopy data were recorded at the same time as the image of the surface. STM spectra were collected along with two images of the surfaces at 20 different points for each image resulting in 200 ( $5 \times 2 \times 20$ ) measurements conducted in all.

### 5.2.2.2 Results and Discussion

Several sets of STM spectroscopy experiments were run on a section of octanethiol on Au(111) SAM at  $78 \pm 1$  K. Figure 5.11 and Figure 5.12 are two images recorded one after another of a part of the surface of an octanethiol on Au(111) sample.

**Figure 5.11 (Right):** This is the first of two images showing the part of the surface where the octanethiol on Au(111) spectroscopy was recorded. The green and blue dots show the locations where the STS data was recorded presented as the green and blue curves in Figure 5.15. (STM parameters:  $U_{\text{gap}} = 1.03$  V,  $I = 518$  pA)



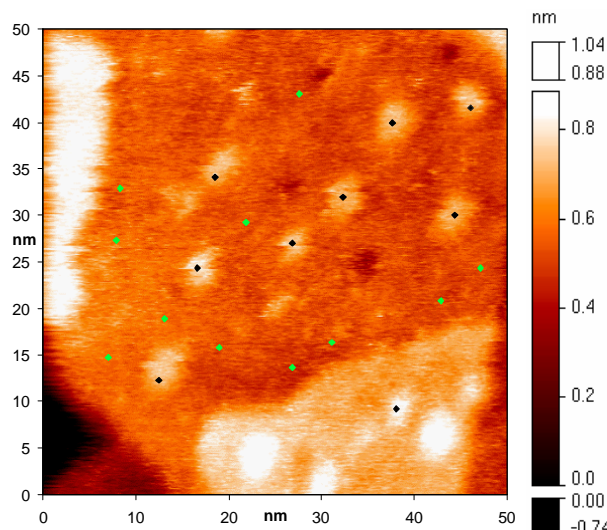


**Figure 5.12 (Left):** This is the second of two images showing the part of the surface where the octanethiol on Au(111) spectroscopy was recorded. The green and black dots show the locations where the STS data recorded presented as the red and black curves in Figure 5.15. (STM parameters:  $U_{\text{gap}} = 1.03\text{V}$ ,  $I = 518\text{pA}$ )

In the central parts of both images is an approximately level area light to dark orange in colour. It is important to remember that the height differences recorded in these images are only apparent. The STM measures the tunnelling current assuming that it only depends upon the distance between the tip and the sample. The tunnelling current can also depend upon the local workfunction so the change in contrast in Figure 5.11 and Figure 5.12 may not entirely be due to changes in surface topography. In the lower left hand corner is an apparently lower part of the surface one layer of Au atoms lower than the central part of the surface. Towards the other edges there are apparently raised areas. The shape of the area in the lower part of the image and the height difference between these raised areas and the central area suggests that the raised areas are one Au atomic layer higher than the central area. In the central area however there are some bright, apparently raised spots and also some darker, apparently depressed spots. Spectra were recorded as indicated by green dots in the main area as well as on these apparently raised and depressed areas. This was done as a test to see if the difference in apparent height on the surface made any difference to the spectroscopy recorded. As seen previously in images of SAMs of octanethiol on Au(111) the surface contains depressions. In previous images they appear to be due to some of the molecules being arranged at a slightly different angle to those that surround them. In addition to the apparent depressions in the surface, there are also apparently raised areas. These have only been seen before on a few occasions and we have yet to observe these areas in images of octanethiol on Au(111) which possess

atomic resolution. This may be more than a coincidence. It may well be that the process that creates these apparently raised areas also modifies the arrangement of the molecules on the surface, removing their regular lateral structure so they can be difficult to image with molecular resolution. It is also possible that these regions of apparently raised and depressed parts of the surface may instead be due to changes in the local workfunction or resistance. It is not possible to distinguish between these different effects using STM images alone.

Figure 5.13 shows the aggregate spectroscopy data from all the locations marked with the dots in Figure 5.11 and Figure 5.12. Comparing these plots with the those for Au(111) it is clear that they differ significantly.

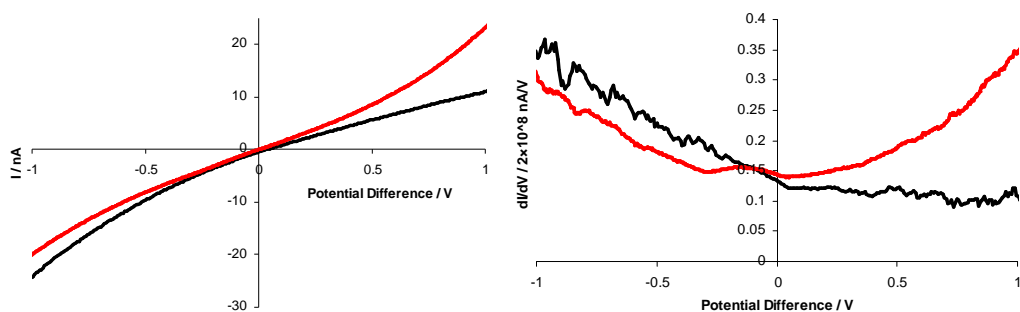


**Figure 5.13: Black curves:  $I$  vs.  $V$  and  $\frac{dI}{dV}$  vs.  $V$  STS spectroscopy data from the positions marked by dots shown Figure 5.11 and Figure 5.12. These curves are aggregates of the data at all locations. Red curves:  $I$  vs.  $V$  and  $\frac{dI}{dV}$  vs.  $V$  STS spectroscopy data from an unexposed Au(111) sample. (Repeated from Figure 4.10)**

The  $\frac{dI}{dV}$  vs.  $V$  spectrum of the octanethiolate sample shows much more asymmetry than the uncoated Au(111) sample. The shape of the  $\frac{dI}{dV}$  vs.  $V$  curve for the octanethiol sample is consistent with the shape of the  $\frac{I}{V}$  vs.  $V$  curve indicating that any difference between the shapes of the  $\frac{dI}{dV}$  vs.  $V$  curves is not due to an effect of the data collection method used. This is more clearly seen in Figure 5.14. The first curve is calculated from the  $I$  vs.  $V$ , the second was measured using the lock-in amplifier. The overall shapes of the curves in the two plots are the same showing that the settings used for the lock-in amplifier were correct. The difference in vertical scale is due to the different methods of data capture and the

detailed differences in the curves are probably due to systematic errors resulting from the approximate differentiation algorithm used.

The most obvious difference between the curves for octanethiol and those for Au(111) is the increased asymmetry in those for octanethiol. This is possibly due to the asymmetry of the tunnelling junction. Without the layer of octanethiol, the tunnelling junction possesses asymmetry due to the different shape and chemical composition.

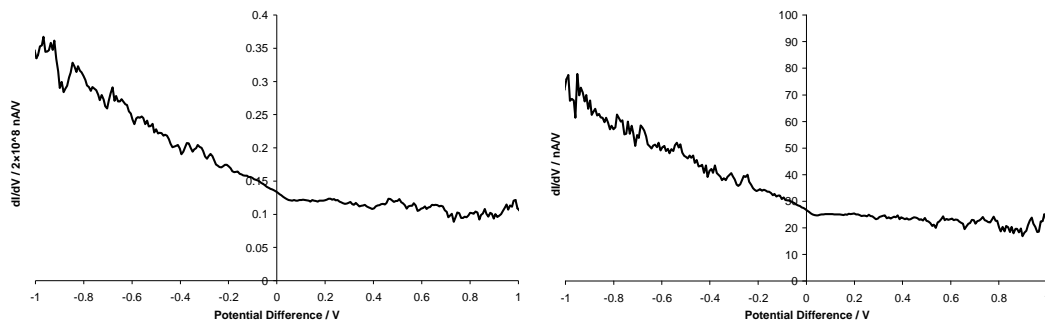


**Figure 5.14:** Showing the similarity in the overall shape of the  $\frac{dI}{dV}$  vs.  $V$  curves recorded using the compensation box and the lock-in amplifier (left) and calculated from the  $\frac{I}{V}$  vs.  $V$  curves (right).

This is the source of the asymmetry in the Au(111) STS curves. Adding the thiolate molecules increases this asymmetry. This might be due to the thiol molecules only having an S atom on one end and only being chemically bonded to one electrode. Some work has been conducted by Cui *et al.*<sup>[6]</sup> using conducting AFM to study octanethiol on Au(111) samples. They recorded spectra using gold coated silicon tips in a nitrogen atmosphere at room temperature over a range of -3V to +3V. At a tip bias of -1.5V they recorded a current of 10pA which was twice that recorded at +1.5V (5pA). In the voltage range of -1V to +1V the  $I$  vs.  $V$  curve recorded is more linear than that shown in Figure 5.13 but still shows some asymmetry. The tunnelling currents recorded by Cui *et al.* are much smaller than those in Figure 5.13. This is probably due to the equilibrium position of the AFM tip being further away from the surface than the equilibrium position of the STM tip. It is not clear whether this difference in tip-sample distance is adequate to explain the difference in shape between these two sets of data. The shape difference might be due to the difference in temperature at which the two sets of

experiments were conducted but this is less likely given results from Wang, Lee and Reed<sup>[7]</sup>. They conducted conductivity experiments on a metal-insulator-metal system, with Au electrodes and 1,8-octanedithiol as the insulator and with applied voltages in the range -1V to +1V. They recorded no significant difference in the shape of the  $I$  vs.  $V$  curves recorded between 290K and 4.2K.

From the octanethiol  $I$  vs.  $V$  data in Figure 5.13 it is clear that the curve does not pass through the origin. In the  $\frac{dI}{dV}$  vs.  $V$  curve this appears as a change in gradient at  $\approx 60$ mV. Such a feature is not seen in the spectrum for the Au(111) sample. In order for the  $I$  vs.  $V$  to not pass through the origin a tunnelling current must be induced across the junction with no applied voltage. It is not clear how adding the thiolate monolayer could modify the tunnelling junction to generate such a phenomenon. Neither is it clear how any potential flaws in the collection of the data could distort the data in this way.

Section 2.2.4 described how molecular vibrational modes can be manifest in STS data along with the experimental specifications required to see such modes. Despite the low noise floor of the STM used it is still necessary to average over several spectroscopy measurements in order to observe features originating from inelastic tunnelling processes. As a consequence of the method used to collect the data in Figure 5.12, Figure 5.13 and Figure 5.14 the number of spectroscopy measurements made (200) is not large enough to reduce the background noise enough to confidently resolve any features originating from inelastic tunnelling. For data collected in this way 1296 measurements would need to be recorded. As a consequence the curves only record how the thiol layer affects the electronic structure of the surface.

This STS data was collected by choosing particular locations on the surface based upon the features seen in the STM images. Four types of location were chosen to see if there was any difference between the spectra from the different locations. In Figure 5.11 two types of location were chosen, apparent depressions in the surface (marked with blue dots) and apparently non-depressed regions (marked with green dots). In Figure 5.12 the other two types chosen were apparently raised areas (marked with black dots) and apparently non-raised areas (marked with green dots). Figure 5.15 shows averages of the spectra for the four different environments.

Comparing the  $\frac{dI}{dV}$  vs.  $V$  curves from the different regions on the surface does not appear to show any significant difference between them once the number of spectra recorded for each different environment is taken into consideration. The curves for the apparently non-depressed (green) and apparently non-raised (red) are from the same type of environment so the differences between them provide an indicator of the noise level in the system. The curves for the apparently depressed (blue) and apparently raised (black) locations are produced from a lower number of spectra and just seem to be more noisy versions of the curves from the non-depressed and non-raised locations. This suggests that the different environments on the sample do not appear to make a significant difference to the STM spectra collected.

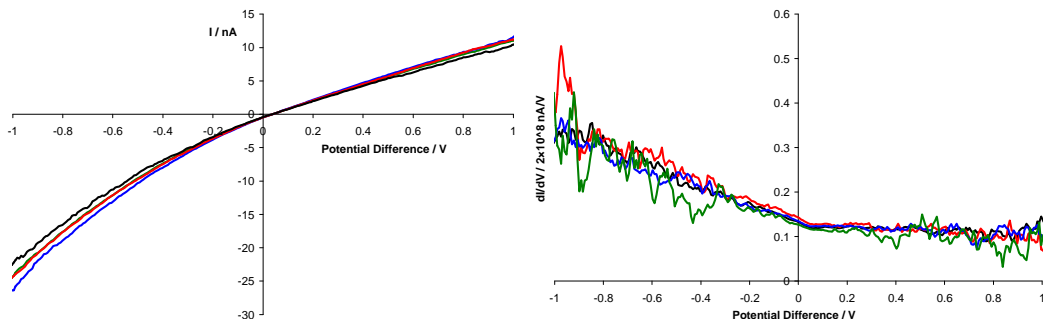


**Figure 5.15:  $I$  vs.  $V$  and  $\frac{dI}{dV}$  vs.  $V$  curves of STS spectroscopy data from the positions marked by dots shown Figure 5.11 and Figure 5.12,      Blue Curves: Depressed areas (blue dots) in Figure 5.11,    Green Curves: Non-depressed areas (green dots) in Figure 5.11,    Black Curves: Raised areas (black dots) in Figure 5.12,    Red Curves: Non-raised areas (green dots) in Figure 5.12**

However the  $I$  vs.  $V$  curves do show a difference between the different environments. The curves for the apparently non-depressed (green) and apparently non-raised (red) overlap one another. This is not surprising since that despite their different labels they are from the same environment. The curves for the apparently raised (black) and apparently depressed (blue) show a slightly different shape to the first two curves towards an applied voltage of -1V. It is not clear what these differences in shape are due to. The greater overlap of the curves at +1V is likely due to this being the voltage at which the STM images were collected so the conditions under which the STS data were recorded are similar to those when the

feedback loop was enabled. This should fix the curves so that they all pass through the same point on the graph. Although it is tempting to assign the variation in the curves at -1V to the variation in the apparent heights in the STM images where the data were recorded, trying to identify a mechanism by which this takes place is difficult. The variations in apparent height in the STM images could be due to several reasons including local variations in one or more of the following: workfunction, thickness and resistance of the thiol layer. However it is also important to note that the slight asymmetry in the  $I$  vs.  $V$  curves cannot be due to these three variables since they cannot introduce an asymmetric change in the  $I$  vs.  $V$  curves. Consequently any further model that can explain the asymmetry also needs to take into consideration any potential changes in workfunction, resistance and thiol layer thickness which will affect the tip sample separation. At present there is not enough information to construct such a model.

Overall the information from these spectroscopy experiments combined with the information gained from the images of the octanethiolate SAM structures suggests that they would not be ideal test samples for exploratory LDSTM experiments. From the images of the octanethiolate SAMs it seems that their method of manufacture does not produce partial layers and from the STS experiments no significant difference can be recorded between different types of feature on the surface. When conducting LDSTM experiments it is important to have a facility to control the extent of surface coverage of the test chemical used and this procedure for working with octanethiol does not provide this.

## 5.3 Dimethyl Disulphide on Au(111)

### 5.3.1 Preparation of Dimethyl Disulphide Self-Assembled Monolayers

#### 5.3.1.1 Experimental Method

The procedure used to make the octanethiol sample is limited to only making whole layers of molecules, but for ongoing study in this area there is a need for a facility to be able to make partial layers of thiols. It was anticipated that the most effective way to study the interaction of the infrared laser with the STM was to use substrates partially coated with thiolate so that a difference could be recorded between the coated and uncoated regions. As a consequence of this need the dosing technology described in §2.2.5 was developed. Instead of using octanethiol it was decided that a smaller molecule would be better because it was expected that the results collected from such a molecule would be simpler to understand than for octanethiol. Therefore ideally the best molecule to use is methanethiol ( $\text{HSCH}_3$ ) but its toxicity makes it difficult (and expensive) to work with. A better option is dimethyl disulphide (DMDS) ( $\text{H}_3\text{CSSCH}_3$ ). The S–S bond can experience fission to make two chemisorbed  $-\text{SCH}_3$  groups on the surface of a sample. Dimethyl disulphide was added to the sample via one of the two liquid dosing lines. To do this 1mL of liquid dimethyl disulphide was added to the Pyrex® dosing vial in a fume hood. Immediately afterwards a Swagelock® valve was bolted to the mini-flange fitting of the vial. This is to ensure that the vial can be transferred to the apparatus and stored detached from the apparatus (e.g. during baking the chamber) without the contents escaping into the environment. On each liquid dosing line there are at least two valves between the contents of the vial and the rest of the vacuum system. The Swagelock® valve is one of them; on the gas/liquid dosing line there is another Swagelock® valve and on the liquid dosing line there is a needle valve. These second valves enable the gas/liquid dosing line and the transfer/loading arm to be evacuated. The presence of the needle valve

allows careful control of the vapour released into the chamber as measured by the mass spectrometer (labelled 5 in Figure 2.10).

When the sample is cryogenically cooled the gold coated copper shutters (that form part of the base of the cryostat) are closed to keep the heat out. This restricts the size of the opening between the inside and the outside of the cryostat. Consequently when molecules are introduced into the main chamber for dosing purposes there will be a partial pressure difference between the inside and the outside of the cryostat. For the partial pressure of the vapour used the molecules will pass through these small openings in a relatively short time of a few minutes. However this pressure difference means that the mass spectrometry measurements, which are made outside the cryostat, do not exactly match the conditions on the inside where the sample is. However, this method does allow the sample to be imaged as molecules are dosed.

For both thermal and electrical purposes many of the components of the STM are coated with gold. Given the affinity of thiol molecules for gold, introducing thiol vapour into the main chamber would coat these components with thiol molecules. It was not clear whether the components would continue to work correctly with such a coating as this. As a consequence the other liquid dosing line on the transfer/loading arm was developed.

The gold samples were coated with DMDS with the liquid dosing line using a variation of the following procedure:

Once the vial had been attached to the transfer/loading arm it was put through four freeze-pump-thaw processes to remove unwanted (dissolved) gas from the vial. (This process only needed to be conducted after the Swagelock® valve was first bolted to the vial.) The sample was then loaded into the loading/transfer arm, either from the main chamber or via its loading port.

At the time when the first experiments were first conducted the sample heater had not been developed so the sample was simply coated by exposing it to a specified pressure of DMDS vapour for a specified time. One sample was exposed to a pressure of  $10^{-7}$  mbar for 12s. Images from this sample and a description of what they show are included in §5.3.1.2.

The electrons that pass from the filament to the grid inside the pressure gauge/mass analyser may have enough energy to break up the DMDS molecules. This means that leaving the analyser on during the dosing process would cause

some of the DMDS molecules to break up and not attach to the surface properly. So, once the correct vapour pressure has been set, the gauge/analyser was switched off for the remainder of the dosing period. (See Figure 2.10 for how these components are arranged relative to one another.)

For the later experiments the sample was heated while being dosed with DMDS. The DMDS molecules require a surface temperature of 320K in order for them to break in two and chemically bond (chemisorb) to the surface.<sup>[8]</sup> If this energy is not provided then many of the DMDS molecules will stay whole and physically attach (physisorb) to the surface. The procedure to heat the sample was as follows: A thermocouple mounted on a screw thread was raised until it touched the back of the sample plate. Current was passed through a filament that was also mounted on the screw thread. Electrons radiating from this filament were used to heat the back of the sample plate to  $\approx 60^{\circ}\text{C}$ . The thermal conductivity across the sample plate and the sample was low and it was possible that the temperature on the sample surface was only  $\approx 50^{\circ}\text{C}$ . This should have been enough for the DMDS molecules to fall apart into two  $-\text{CSH}_3$  units that chemically bond to the surface. Images of samples coated with this technique are shown at the end of §5.3.1.2.

### 5.3.1.2 Results and Discussion

As described in the previous section dimethyl disulfide (DMDS) was added to Au(111) samples in two different ways. Only in the latter was the sample heated during the dosing process to ensure that the molecules chemisorbed onto the surface. With the former method the molecules covered the surface but as time progressed many left the surface. Figure 5.16 and Figure 5.17 show a section of surface exposed to DMDS without heating the sample during the dosing process. These images were recorded at  $78\pm1\text{K}$ .

Most parts of the surface did not seem to show any regular features but occasionally features such as those in the figures could be seen. The height difference between the raised areas and the mid orange areas in Figure 5.16 is such that this image could show partial coverage of DMDS. However as discussed in §5.2.1.2 a change in the surface composition will change the local workfunction. For DMDS the workfunction reduces by  $1.0\text{eV}^{[3]}$  to  $4.35\text{eV}$ .

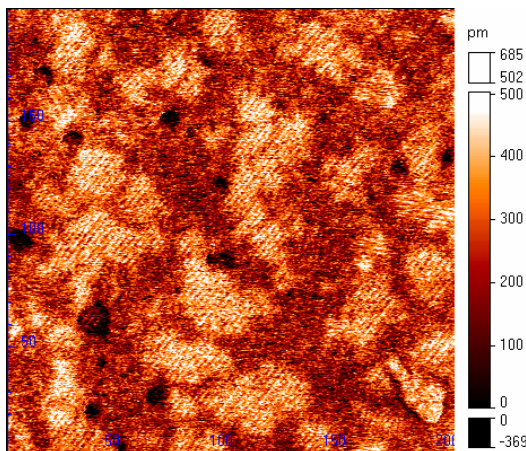


**Figure 5.16 (Left):** A  $200\text{nm} \times 200\text{nm}$  section of an Au(111) surface covered with dimethyl disulphide. (STM Parameters:  $U_{\text{gap}} = 400\text{mV}$ ,  $I = 4\text{nA}$ )

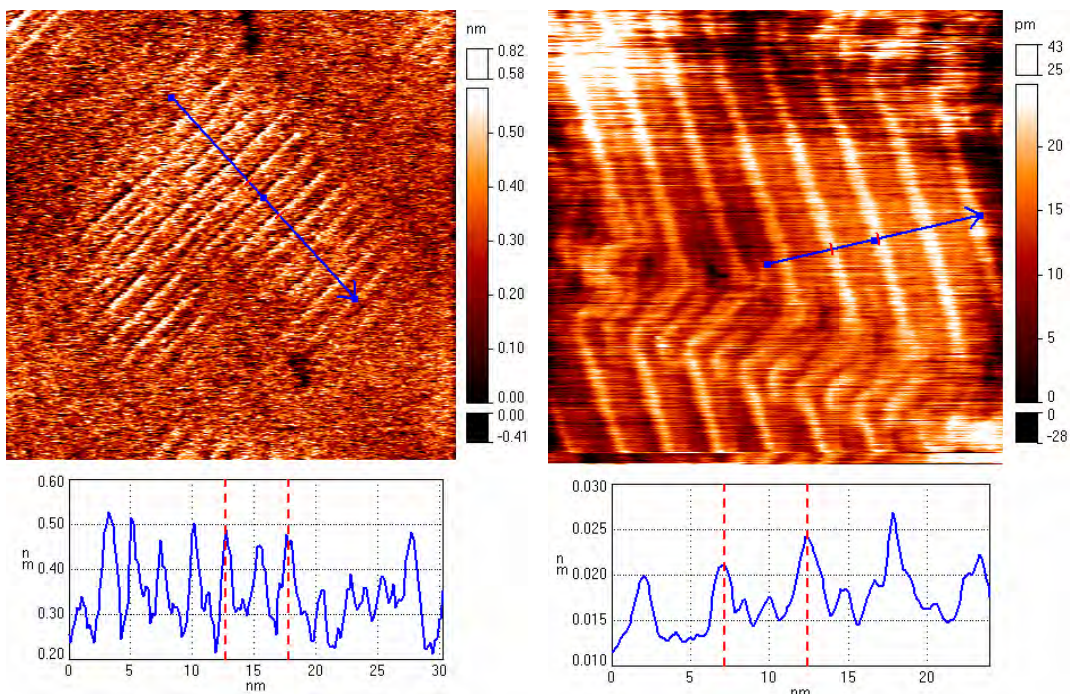


**Figure 5.17 (Above):** A  $50\text{nm} \times 50\text{nm}$  image of the same sample as in the previous Figure. (STM Parameters:  $U_{\text{gap}} = -100\text{mV}$ ,  $I = 5\text{nA}$ )

**Figure 5.18 (Above):** A  $50\text{nm} \times 50\text{nm}$  image of a section of Au(111) for comparison with the previous Figure. (STM Parameters:  $U_{\text{gap}} = 80\text{mV}$ ,  $I = 2.2\text{nA}$ )

From Equation 5.1 it can be seen that decreasing the workfunction increases the tip-sample separation in order to keep the tunnelling current constant. In the context of Figure 5.16 this would mean that the regions covered with DMDS would be raised considerably relative to the Au substrate. In Figure 5.16 the lighter regions are typically  $1.5\text{\AA}$  higher than their surroundings. If the molecule is assumed to be  $\sim 4\text{\AA}$  high off the surface<sup>[9]</sup> then this height difference of  $1.5\text{\AA}$  is too small to be a region of molecules even without the additional height difference

expected as a consequence of the variation of surface composition. There are several reasons why this might be the case. Firstly the topography recorded with an STM is likely not to match the dimensions of calculated molecular models due to the fact the energy of the tunnelling electrons is limited by the applied voltage so some states in the molecule may not be seen. Secondly the change in contrast in Figure 5.16 may not be due to patches of DMDS molecules, it may instead be due changes in the arrangements of the molecules on the surface. However it is not clear, even when taking the issue of the workfunction into consideration, how a change in the arrangement of molecules of identical size would yield regions that are  $1.5\text{\AA}$  higher than their surroundings. Further investigation would be required to clarify this issue probably involving topographically varying scanning tunnelling spectroscopy (see §5.3.2.1) to distinguish between the two regions.

The striped pattern more clearly seen in Figure 5.17 is intriguing. For alkanethiols it is quite normal to see striped features on the surface with sub monolayer coverage. These are due to the molecules lying flat in a regular arrangement on the surface. However the distance between the stripes (2.5nm) is too large for the size of molecules used ( $\approx 6\text{\AA}$ ). Comparing this result with a section of Au(111) on the same scale (Figure 5.18) shows that the distance between a ridge and the next but one ridge in the thiol covered sample (5.1nm) is approximately the same distance as between two ridges in the Au(111) sample (5.2nm). This suggests that at low coverage the molecules might be orientating themselves with the underlying gold  $22\times\sqrt{3}$  “herringbone” reconstruction. Another group that conducted STM work with DMDS on Cu(111) with a similar did not observe such striped features due to the Cu(111) surface not possessing an analogue to the Au(111)  $22\times\sqrt{3}$  reconstruction.<sup>[10]</sup>

In most cases the effect of the tip is considered to only have a small impact on the images recorded by an STM. The effect of the tip is most noticeable when the tip is blunt and the detail in the images is removed by the convolution effect of the tip. If the shapes of the features in Figure 5.20 and Figure 5.21 are due to a convolution effect of the tip then it is odd that there is no apparent change in the pattern of the gold substrate, since convolution effects of the tip should not make any distinction between the natures of the features on the surface.

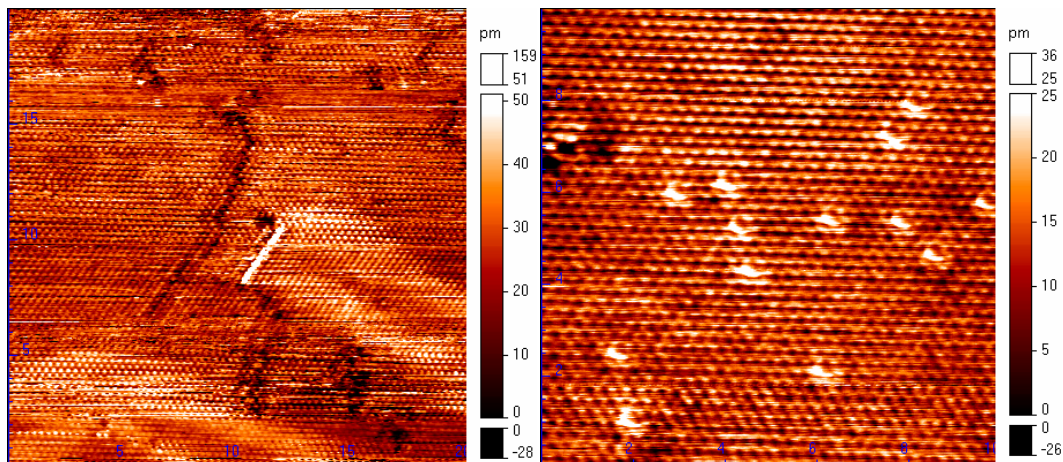


**Figure 5.19 (Above):** A 20nm × 20nm section of Au(111) surface showing some features in the Au surface and a line of adsorbed molecules.

(STM Parameters:  $U_{\text{gap}} = 150\text{mV}$ ,  $I = 4\text{nA}$ )

**Figure 5.20 (Above):** A 10nm × 10nm section of another part of the surface showing the Au atoms with some thiol molecules adsorbed on the surface. Note the relative orientations of the molecules to one another.

(STM Parameters:  $U_{\text{gap}} = 100\text{mV}$ ,  $I = 4\text{nA}$ )

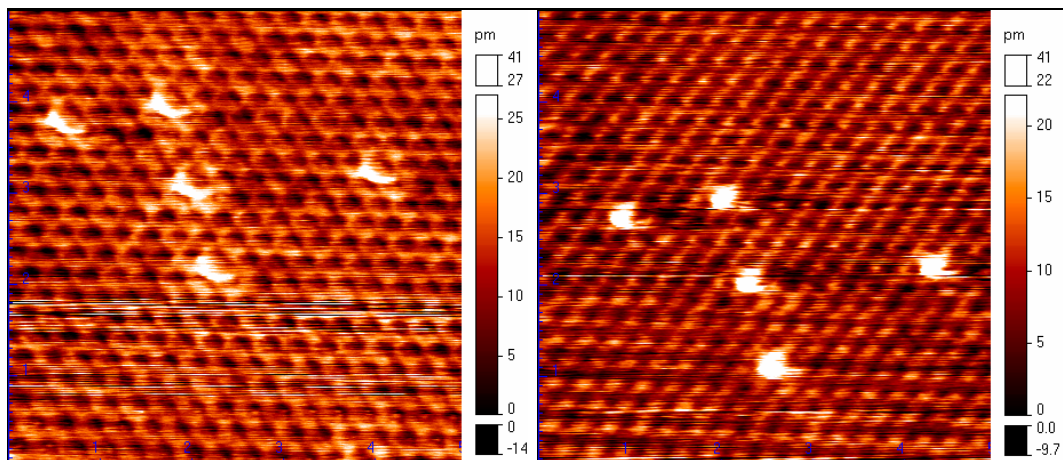


**Figure 5.21 (Above):** A 5nm × 5nm section of Au(111) surface showing more clearly five of the molecules in the previous Figure.

(STM Parameters:  $U_{\text{gap}} = 100\text{mV}$ ,  $I = 4\text{nA}$ )

**Figure 5.22 (Above):** An image of the surface slightly displaced from that in the previous Figure.

(STM Parameters:  $U_{\text{gap}} = 390\text{mV}$ ,  $I = 7\text{nA}$ )

Also Figure 5.22 shows the same molecules with a higher applied voltage. (The tunnelling current was increased in an attempt to keep the tip at the same height above the surface.) This higher voltage was chosen to attempt to match the energy of the C–H vibrational mode in the molecule. If the shapes of these features are due to a tip convolution effect then it is intriguing that this changes with applied

tunnelling voltage. This might reveal something about the shape of the energy states in the tip that the electrons tunnel through.

Alternatively if the shapes of these features are not due to a tip convolution effect then it might be possible to attempt to determine the structures in Figure 5.21 and Figure 5.22.

It is not trivial to determine whether these molecules are whole DMDS units or  $-\text{SCH}_3$  units since molecules imaged with STM usually look different from the space-filling computer rendered models often used to represent the shape of a molecule. This is because the STM only picks out the energy states in the molecule at the energy that the electrons tunnel at. Despite this, there is some value in comparing this image with a selection of models of various possible candidates on a metal surface. These are shown in Figure 5.23 to Figure 5.25, which are based upon work by Grönbeck, Curioni and Andreoni<sup>[9]</sup> who modelled how DMDS and methanethiol bond onto the Au(111) surface in order to determine their most favourable bonding locations. For DMDS they determined that if the S–S bond broke the orientation of the S–C bond was vertical with respect to the surface. In a separate study Akinaga, Nakajima, and Hirao<sup>[11]</sup> also calculated the optimum location and orientation of the  $\text{SCH}_3$  group on Au(111) and they determined that the S–C bond was tilted at an angle of 50° to the surface normal. To illustrate how this differs from the results from [9], one of the structures from [9] was modified with the information from [11] and is included as Figure 5.25.

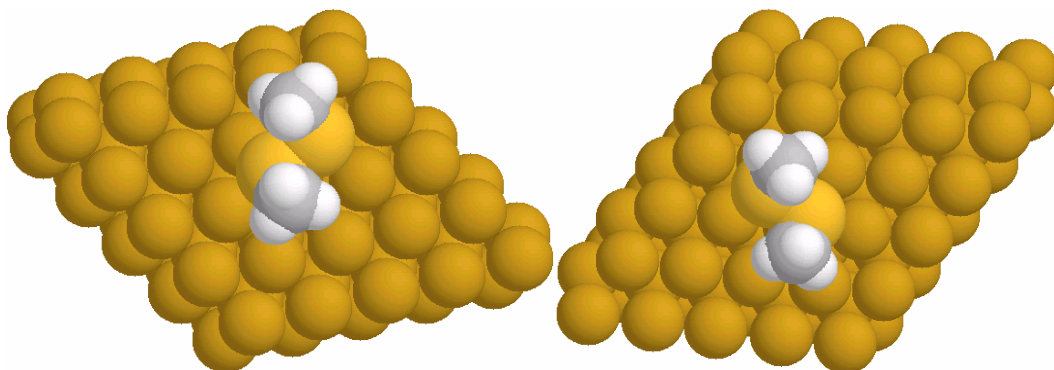
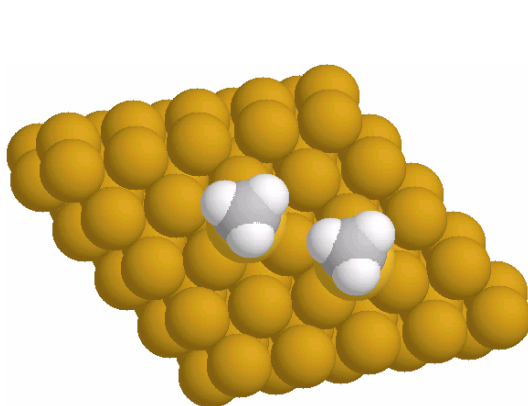
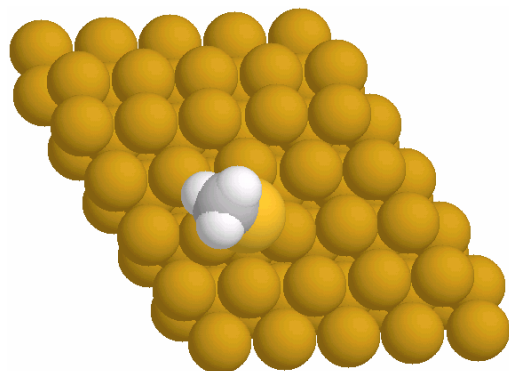


Figure 5.23: Showing two possible orientations of DMDS molecules on the Au(111) surface.



**Figure 5.24 (Above):** Showing two methyl sulphide groups attached to the Au(111) surface. Note that here the S-C bonds are perpendicular with the surface.



**Figure 5.25 (Above):** Showing a single methyl sulphide unit attached to the Au(111) surface, with the angle of the S-C bond approximately  $50^\circ$  to the surface normal as suggested by Akinaga, Nakajima, and Hirao.<sup>[11]</sup>

Comparing the STM images and these models suggests that the DMDS molecules are the wrong shape to produce the features seen in the STM images. The structures in Figure 5.21 do not appear to possess the  $180^\circ$  rotational symmetry present in the structures in Figure 5.23. Also the structures shown in Figure 5.24 seem too small laterally for the species in the STM images. This leaves the structure in Figure 5.25. This does not seem to match completely either. The difference between Figure 5.21 and Figure 5.22 shows the significance of changing the tunnelling voltage. This changes the energy states in the molecule that the electrons tunnel through. The energy states at 390meV seem to have a different shape to those at 100meV.

If the structures in the STM images are the  $\text{SCH}_3$  species then this would suggest the fission of the S-S bond occurred in a few of the DMDS molecules when the samples were prepared at room temperature. Given that the coverage of the sample was initially greater (Figure 5.16 and Figure 5.17) and then decreased over time (Figure 5.19 to Figure 5.22) this would suggest that initially the vast majority of the molecules were physisorbed to the sample and over time they left the surface leaving behind the few chemisorbed  $\text{SCH}_3$  species.

In order to resolve the issue of the structure of the molecules in the STM images it would be necessary to take the various models that have been made and calculate what they would be expected to look like with an STM modelled on the one in

this study. The STM images recorded are a convolution of the sample used and the characteristics of the STM. Only when the effect of the STM has been understood can fair comparisons be made between STM images and calculated models.

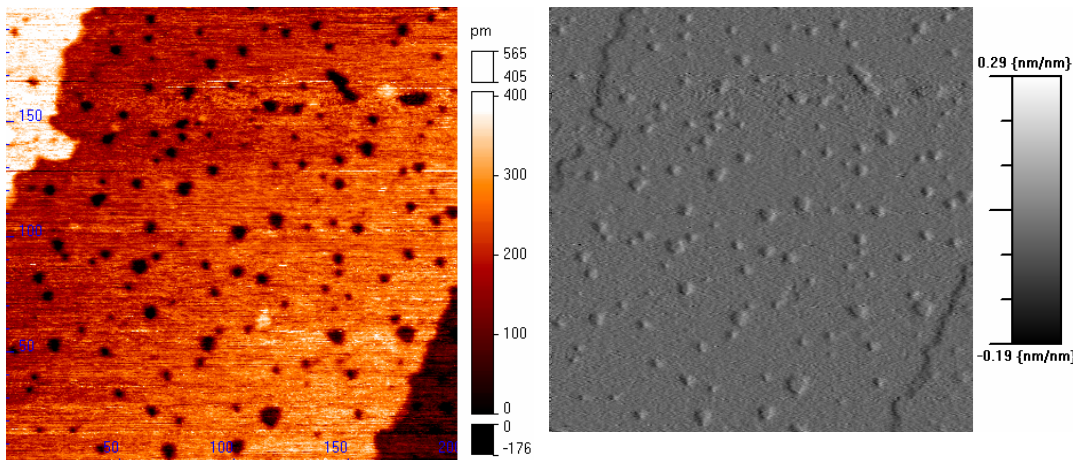


**Figure 5.26 (Above):** A  $200\text{nm} \times 200\text{nm}$  image of an methanethiolate coated Au(111) sample.

**Figure 5.27 (Above):** A differentiated version of the image in Figure 5.26. This is similar to Figure 4 from Dishner *et al.*<sup>[12]</sup> suggesting that the surface is coated with methanethiolate as expected.<sup>[13]</sup>

As described towards the end of §5.3.1.1 later experiments with dimethyl disulphide involved heating the sample to  $\approx 50^\circ\text{C}$  in an attempt to fully coat the sample. Images of such a sample are show in Figure 5.26 and Figure 5.27. The similarity of Figure 5.27 to Figure 4 from Dishner *et al.*<sup>[12]</sup> suggests that this method was successful in coating the sample in the required way.

### 5.3.2 Spectroscopy Experiments of Dimethyl Disulphide on Au(111)

As with octanethiol it was important to characterise the dimethyl disulphide samples with STS. This section describes the conditions used for these experiments.

### 5.3.2.1 Topographically Varying Scanning Tunnelling Spectroscopy

#### 5.3.2.1.1 Experimental Method

When recording images of a sample coated with DMDS (that had not been heated whilst dosing) some features were seen on the surface that did not appear to be consistent with the surface structure expected for an Au(111) surface. These features were clusters about 10nm across and almost 3nm high. It was not clear whether these were made up of gold atoms or DMDS molecules. To try and identify these features STS experiments were conducted on a 15nm by 15nm section of the surface that included a part of one of these clusters. As with the STS experiments conducted on the bare Au(111) sample they were recorded in a grid pattern. A 10 by 25 grid pattern was used for each direction (forward and back) and 123 data files were recorded resulting in 61500 ( $10 \times 25 \times 2 \times 123$ ) spectroscopy experiments in all. Unlike the case with the bare Au(111) sample, software was developed with MATLAB<sup>®</sup> that could analyse the topographical images and identify where the cluster is in the image. From this it divided up the spectroscopy data into two groups; those that are recorded over the cluster and those that are not. Aggregate totals were collected for these two scenarios so that they could be compared to see what difference (if any) could be seen. The MATLAB<sup>®</sup> code used for processing the data is included in Appendix D. These experiments were conducted at  $78 \pm 1$ K.

#### 5.3.2.1.2 Results and Discussion

Figure 5.28 shows a section of the sample that was suspected to be partially coated with DMDS. The raised feature can be seen on the left hand side of the image. The poor quality of the image is due to the fact that spectra were recorded at the same time as recording the image. Due to the time required for collecting data from each point in the grid when the feedback loop of the STM is switched off, the tip seems to drift slightly in space relative to the sample. Despite the feedback loop correcting for some of this when it is switched back on after

collecting spectroscopy data, there is still a detrimental effect on the image. This problem can be avoided by reducing the resolution or the energy range over which it is conducted. This of course reduces the quantity of information recorded.

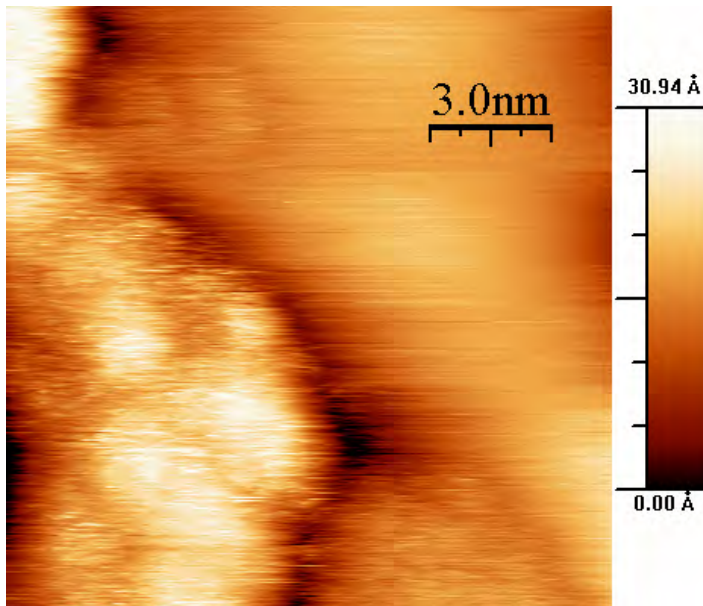


**Figure 5.28:** Showing the area of the surface where the topographically varying scanning tunnelling spectroscopy was recorded. The spectra were recorded to attempt to determine the nature of the feature on the left hand side in the image.<sup>[13]</sup> (STM Parameters:  $U_{\text{gap}} = 200\text{mV}$ ,  $I = 150\text{pA}$ )

Figure 5.29 shows the  $I$  vs.  $V$  and  $\frac{dI}{dV}$  vs.  $V$  spectroscopy curves recorded over this area. Of the 61500 measurements recorded, 13745 were recorded over the feature and the remainder were recorded off the feature. The significance of this data is that the data on the feature (blue curve) has a different shape to the data off the feature (red curve). This difference indicates that the feature has different electronic states compared to the region surrounding it. The ‘on feature’ curve is noisier than that from off the feature due to fewer measurements being recorded at the location of the feature. As described in §2.2.4 the drift of the STM was low enough that the tip remained over the feature of interest while all the data was collected. From individual measurements of the noise in the tunnelling current recorded during the experiment, it was determined that enough measurements had been recorded that the aggregates of the data should be sensitive enough to detect a 1% change in the tunnelling current. The lateral drift was no more than  $\approx 2\text{\AA}/\text{hour}$ . This figure is not too critical since the analysis software was able to track the location of the apparently raised area.

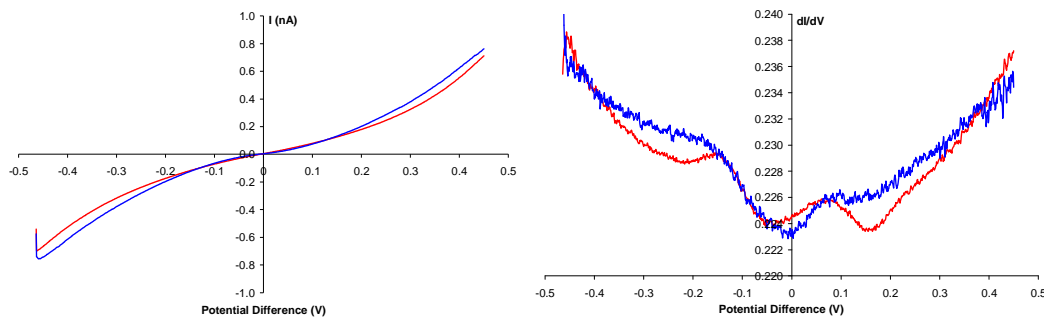


**Figure 5.29:** Scanning tunnelling spectra collected from the area shown in Figure 5.28. Red: Data from off the feature. Blue: Data from on the feature.

On examination of these curves two important points can be deduced. Firstly their overall shapes are different from that recorded when measuring the spectrum of Au(111) when the sample used was cooled to  $\approx 5\text{K}$ . This could well be a result of the same reason that the spectrum then did not match what was expected, i.e. the tip structure. If the structure of the very end of the tip used to collect this data was different from the structure of the tip used previously then this would explain the difference in the shape of the curves between then and now. This shows the advantage of conducting spectroscopy experiments on partially covered surfaces where comparisons can be made between spectra recorded on and off a feature of interest.

Secondly the difference between the two curves is not consistent with the descriptions given for features resulting from inelastic tunnelling give in §2.2.4. This suggests that the feature does not consist of thiol molecules at all. It is most likely that it is just a cluster of gold atoms and the difference between the blue and the red curves is due to the perturbation that the cluster makes to the electronic structure of the surface. The electronic states in the cluster are different from those of the bulk and the Au(111) surface so they induce a change in the spectra recorded.

It is also important to note that the overall shapes of all the curves are different. Overall this experiment shows that although the region of interest in the corner of the STM image did not appear to be due to a cluster of DMDS molecules it does illustrate the viability of distinguishing between the measurements in a set of data based upon the topography of the location where the measurement was made.

### 5.3.2.2 Scanning Tunnelling Spectroscopy Conducted on a Complete Monolayer

#### 5.3.2.2.1 Experimental Method

Spectroscopy experiments were also conducted on samples made by the second method where the sample was heated during the dosing procedure. This was to ensure that the DMDS molecules split into two methylthiolate units to form a more stable SAM on the gold substrate. Images of a sample coated in this way are shown in Figure 5.26 and Figure 5.27 which are consisted with previously published images of gold samples coated with methanethiolate.<sup>[12]</sup> As before the surface was imaged in order to find a suitable place then spectra were recorded in pairs of a 10 by 25 grid pattern. This time however the nature of the sample was uniform across the 10nm by 10nm area scanned so no topographical analysis was conducted on the data recorded. For comparative purposes some spectroscopy experiments were recorded under similar conditions on a separate bare Au(111) sample. As with the previous sample, these experiments were conducted at 78±1K and the  $\frac{dI}{dV}$  vs. V data was recorded with the lock-in amplifier. Again a MATLAB<sup>®</sup> script was used to process the data but the script was shorter as a consequence of not needing to do the topographical analysis. It can be found in Appendix E.

#### 5.3.2.2.2 Results and Discussion

1500 spectra were recorded from the methylthiolate SAM sample. From analysis of the noise in individual measurements of the tunnelling current it was determined that more than enough spectra were recorded to be able to measure 1% changes in the tunnelling current with a signal to noise ratio of 10:1. The lateral drift was no more than  $\approx 2\text{\AA}/\text{hour}$ . This is too high to record the spatial dependence of the STS data with the molecular features in the monolayer but would be

adequate to record phenomena if sub-molecular precision of the tip is not required. A MATLAB® script (Appendix E) was used to process the data post collection of the data. (In the script a value of 4 was used for the ‘StatsThreshold’ variable.) A plot of  $\frac{dI}{dV}$  vs. V is shown in Figure 5.30. In addition to the data processing by the MATLAB® script, 3-point smoothing has been applied to the data to reduce some of the noise in the  $\frac{dI}{dV}$  vs. V plot.

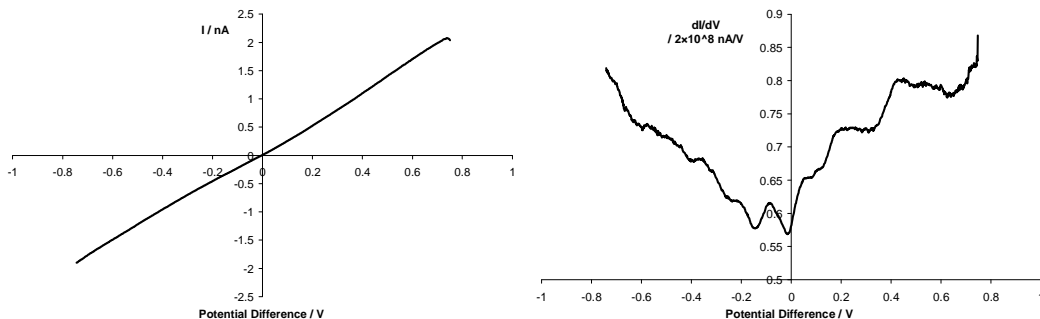


**Figure 5.30: An  $I$  vs.  $V$  curve and a  $\frac{dI}{dV}$  vs.  $V$  plot of the spectroscopy data collected from the Au sample coated with a methylthiolate SAM.**

In an attempt to try and identify which of these features were due to the underlying metal substrate and which were due to the thiol molecules further spectra were recorded on an unexposed Au sample. Figure 5.31 shows spectra recorded from this sample.

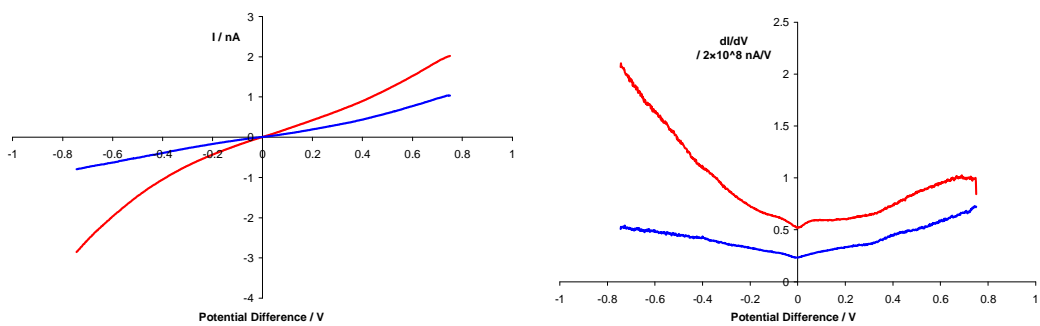


**Figure 5.31:  $I$  vs.  $V$  curves and  $\frac{dI}{dV}$  vs.  $V$  plots of the spectroscopy data collected from an uncoated Au sample. The red and blue curves correspond to two sets of measurements made with the same tip on the same surface.**

The blue and red curves are aggregates of 1500 and 500 spectra respectively, collected in the same way as for the DMDS coated sample. Again,  $\frac{dI}{dV}$  vs.  $V$

spectra are plotted to enable better quantitative comparison between the two curves and with the equivalent curve in Figure 5.30.

The  $I$  vs.  $V$  curve for the methylthiolate SAM sample (Figure 5.30) has a linear (ohmic) shape whereas the curves for the unexposed gold sample show changes in the gradient of the curve, particularly at around zero volts. This is more clearly seen in the  $\frac{dI}{dV}$  vs.  $V$  curves, where the maximum value of  $\frac{dI}{dV}$  for the SAM coated sample is less than for the uncoated sample. These  $\frac{dI}{dV}$  vs.  $V$  curves also show that the curve for the SAM covered sample contains much more structure than for the uncoated sample and is made more visible by the lack of any overall change in gradient in the  $I$  vs.  $V$  curve. In this structure there is a dip around zero volts. This dip is also present in the gold sample curves indicating that this feature is due to the gold substrate. In order to try and understand the origin of the steps on the  $+V$  part of the  $\frac{dI}{dV}$  vs.  $V$  curve for the coated samples a  $\frac{d^2I}{dV^2}$  vs.  $V$  curve was calculated from the  $\frac{dI}{dV}$  vs.  $V$  curve. This is shown in Figure 5.32. The widths of these broad peaks are consistent with the temperature dependence of inelastic peaks in  $\frac{d^2I}{dV^2}$  vs.  $V$  curves<sup>[14]</sup>. However at this temperature the peaks are too broad to easily verify that they originate from an inelastic process. One of the consequences of having narrower peaks at colder temperatures (~5K) is that they are much narrower than the electronic states and therefore easier to extract from the background signal. In order to determine whether these features in the data from the methanethiolate sample originate from inelastic processes it would be necessary to repeat the experiments at a lower temperature.

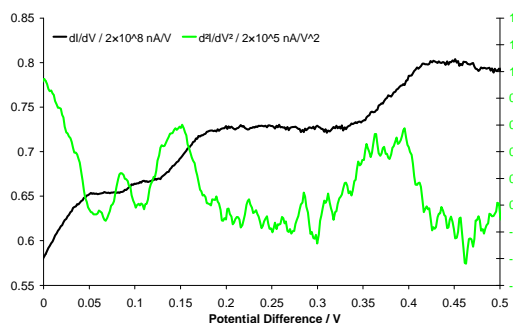


**Figure 5.32: A section of the  $\frac{d^2I}{dV^2}$  vs.  $V$  curve calculated from the  $\frac{dI}{dV}$  vs.  $V$  curve overlaid with the  $\frac{dI}{dV}$  vs.  $V$  curve. Due to the method of calculation there is a slight offset between the two curves.**

From Figure 5.31 the two different curves illustrate that despite attempting to keep all the experimental parameters the same there can still be significant

variation between two sets of data. As highlighted in §4.3.2 it is possible for the structure of the tip to change during the process of scanning across the surface. From the data in §4.3.2 it appears that the shape of the spectroscopy curve depends upon the structure of the end of the tip, this would explain why the two curves have different shapes to one another. This makes it difficult to make good comparisons between the spectrum from the SAM coated sample and the spectra from the uncoated sample with the current experimental procedure.

There are two ways of overcoming this problem. One is to prepare the substrates in a different way so that they are not as rough such that as the tip scans across the surface there is less chance of the end atoms on the tip coming in contact with the surface. The samples used at present have a thin layer of metal on a glass substrate added with a vapour deposition technique. This results in a polycrystalline arrangement of the atoms on the surface. The sample has to be heated *evenly*, to a temperature of at least 1000°C in order to melt the surface and rearrange the atoms in a regular structure having lower energy state that will produce regions with the (111) surface structure. However heating the sample evenly is difficult; it is very easy to heat some parts of the sample too much such that the metal layer can evaporate off. In trying to avoid this, it is normal that the sample only contains scattered regions with the (111) structure (see Figure 4.4). Use of a smoother single crystal sample (§4.5) would help to overcome this roughness issue.

An alternative approach is to make a partial layer of DMDS whilst heating the sample and conduct experiments of the type described in §5.3.2.1 on it. This would require careful choice of the topographical threshold in order to separate out the spectra since the vertical variation of topography on the sample would not be expected to be large in comparison to that experiment.

## 5.4 Conclusions

This chapter has described how self-assembled monolayers of octanethiol were manufactured on Au(111) substrates. STM images recorded at 78K show how the SAM reconstructed the Au(111) substrate. Some images are included that show

resolved molecules in the SAM. One of the STM images shows that the lack of molecular resolution in the images is due to the structure of the monolayer rather than any characteristic of the tip. Depressions are observed in the surfaces of the monolayer. Line profiles are included showing the diameter and depths of these holes. From these depth measures and images of the surfaces it was possible to determine that these depressions ('holes') are not due to missing thiolate molecules. Instead some depressions were attributed to changes in the packing of the thiolate molecules whereas others were attributed to missing atoms in the uppermost Au layer. Further depressions could be attributed to missing gold atoms if it was assumed that the tip could not reach the bottom of the holes as a consequence of its profile.

Scanning tunnelling spectroscopy (STS) experiments were conducted on a section of octanethiolate monolayer at 78K. A clear difference was observed between the shape of the curve for this SAM sample and a similar curve for an uncoated sample. There was some discussion into this difference in comparison to previous work. Features resulting from inelastic tunnelling processes are not seen. This is possibly due to the sample being too warm. The spectroscopic measurements made on the octanethiolate SAM sample were conducted in slightly different environments on the sample surface. Comparisons were made between the measurements from the different environments on the surface. No significant difference was detected between these different measurements.

From the STM images of the octanethiol SAM the 'holes' did not appear to contain bare regions of Au(111). As a consequence, a facility was developed to dose liquid chemicals onto a sample from vapour. STM images from preliminary experiments with dimethyl disulphide (DMDS) at 78K show the formation of low density phase that apparently shows the DMDS molecules aligning themselves with the underlying reconstruction of the gold atoms, although there is some uncertainty as to the structure of parts of this low density phase when considering the effect of the thiol molecules changing the local workfunction. STM images show that as a consequence of the experimental conditions used after a few days the initial phase was replaced with a surface of mostly unexposed Au(111) except for a few scattered molecules. These images were compared with calculated models of dimethyl disulphide and methylthiolate on Au(111) surfaces. Assuming that the STM images accurately represent the molecules on the surface the

methylthiolate group with a tilted S–C bond provides the best fit to the structures in the STM images.

STS experiments were conducted on a sample partially coated with DMDS in a grid pattern. Some of locations in the grid were on a feature initially considered to be a cluster of DMDS molecules where 13745 STS experiments were conducted. The rest were on an unexposed area of Au substrate where 47755 experiments were conducted. By comparing the data recorded on and off the feature it was possible to determine that the feature was most likely to be a cluster of Au atoms rather than DMDS molecules. The data recorded on the feature was noisier than that recorded off the feature due to the few number of experiments conducted on the feature compared to that off the feature. The analysis of this data was conducted in such a way as to be able to exclude this increased level of noise as a consequence of the locations where the data was collected.

The experimental method used to make the DMDS samples was modified by heating the sample during the dosing process. This produced samples with a complete methylthiolate SAM. STS experiments were conducted on one of these samples at 78K. The resulting spectrum contained features not seen in equivalent spectra on an uncoated sample recorded with the same tip. The features in the SAM sample spectrum do not contain the symmetry expected for inelastic tunnelling. This is consistent with the octanethiol data and is likely to be due to similar reasons. From comparisons between the methylthiolate spectrum and the uncoated gold spectra the dip in the  $\frac{dI}{dV}$  vs.  $V$  spectrum around zero volts can be attributed to the Au substrate, hence leaving the other features in the methylthiolate spectrum to be attributable to the thiolate monolayer. The presence of features in the  $\frac{dI}{dV}$  vs.  $V$  spectrum at energies less than 1eV is unexpected given that STS are normally dominated by modes higher than this due to the HOMO and LUMO states in the molecule. It is suggested that the presence of the thiolate molecules modifies the existing substrate energy states.

There is some discussion into the origin of the features in the STS spectrum in the light of information about alkanethiolates from previously published work. It is noted that there is a difference in shape between the curves for two sets of STS measurements on an uncoated sample and reasons are highlighted for the possible cause of this.

## 5.5 Future Work

From the STM images of octanethiolate monolayers it is clear that their current method of manufacture is not suitable for producing the partial layers that are best for studying any interactions between the laser and the STM. The next step for experiments involving octanethiol would probably be to dose it onto samples from vapour, as with dimethyl disulphide, in order to make partial layers. However, it probably would be best to conduct some further experiments with partial layers of DMDS before returning to working with longer chain alkanethiols.

From the STS experiments with octanethiolate layers the lack of any features in the spectra that correspond to molecular vibrational modes suggests that the samples were too warm to detect them. In  $\frac{d^2I}{dV^2}$  vs.  $V$  spectra the peaks broaden with temperature. It seems likely that at 78K they are too broad to be recorded with this equipment. In the future one possible future direction would be to try and record such peaks in  $\frac{d^2I}{dV^2}$  vs.  $V$  spectra. However experience of conducting experiments with  $\text{He}_{(l)}$  cooling suggests that using  $\text{He}_{(l)}$  routinely to provide the required conditions would significantly increase the running costs of the project.

It has been encouraging to be able to create low coverage samples of DMDS on Au(111) and learn new information about how these molecules arrange themselves on the surface. However there are still some issues that need to be resolved. It would be good to attempt to recreate these partial layers whilst ensuring that the sample was gently heated to ensure the stability of the structures created. For regions with individual scattered molecules further experiments would collect images at a range of voltages (e.g. -5V, -4V... +4V, +5V) to gain a better understanding of the electronic structure of these molecules. The issues raised in trying to analyse  $\frac{dI}{dV}$  vs.  $V$  spectra from a whole DMDS monolayer sample and compare them with similar spectra from uncoated samples show that the next step is to conduct such experiments with partial layers of DMDS. This would provide greater certainty that the characteristics of the tip had not changed between moving from uncovered to a covered part of the surface (or vice versa) minimising any tip effects in the spectra. By using similar analysis software to that described in §5.3.2.1 the spectra recorded in the two different areas on the

sample can be separated and one subtracted from the other to yield a more accurate spectrum for the thiolate adsorbate.

For both octanethiol and DMDS the issue of the change in workfunction has been raised as an issue to consider when analysing the results. Experiments to measure this change in workfunction on such surfaces (see §2.2.3.2 for details) would aid in the interpretation of the STM images and STS spectra.

## 5.6 References

1. Poirier, G.E. and M.J. Tarlov, *The C(4x2) Superlattice of N-Alkanethiol Monolayers Self-Assembled on Au(111)*. Langmuir, 1994. **10**(9): p. 2853-2856.
2. Roper, M.G., et al., *Atop adsorption site of sulphur head groups in gold-thiolate self-assembled monolayers*. Chemical Physics Letters, 2004. **389**(1-3): p. 87-91.
3. De Renzi, V., et al., *Metal Work-Function Changes Induced by Organic Adsorbates: A Combined Experimental and Theoretical Study*. Physical Review Letters, 2005. **95**(4): p. 046804.
4. Alloway, D.M., et al., *Interface Dipoles Arising from Self-Assembled Monolayers on Gold: UV-Photoemission Studies of Alkanethiols and Partially Fluorinated Alkanethiols*. J. Phys. Chem. B, 2003. **107**(42): p. 11690-11699.
5. Poirier, G.E., *Mechanism of Formation of Au Vacancy Islands in Alkanethiol Monolayers on Au(111)*. Langmuir, 1997. **13**: p. 2019-2026.
6. Cui, X.D., et al., *Making electrical contacts to molecular monolayers*. Nanotechnology, 2002. **13**(1): p. 5.
7. Wang, W.Y., T. Lee, and M.A. Reed, *Elastic and inelastic electron tunneling in alkane self-assembled monolayers*. Journal of Physical Chemistry B, 2004. **108**(48): p. 18398-18407.

8. Danisman, M.F., et al., *Structural investigation of monolayers prepared by deposition of (CH<sub>3</sub>S)<sub>2</sub> on the (111) face of single-crystal gold*. Journal of Physical Chemistry B, 2002. **106**(45): p. 11771-11777.
9. Grönbeck, H., A. Curioni, and W. Andreoni, *Thiols and disulfides on the Au(111) surface: The headgroup-gold interaction*. J. Am. Chem. Soc., 2000. **122**(16): p. 3839-3842.
10. Driver, S.M. and D.P. Woodruff, *Scanning tunnelling microscopy study of the interaction of dimethyl disulphide with Cu(111)*. Surf. Sci., 2000. **457**(1-2): p. 11-23.
11. Akinaga, Y., T. Nakajima, and K. Hirao, *A density functional study on the adsorption of methanethiolate on the (111) surfaces of noble metals*. The Journal of Chemical Physics, 2001. **114**(19): p. 8555-8564.
12. Dishner, M.H., J.C. Hemminger, and F.J. Feher, *Direct observation of substrate influence on chemisorption of methanethiol adsorbed from the gas phase onto the reconstructed Au(111) surface*. Langmuir, 1997. **13**(8): p. 2318-2322.
13. processed with WSxM® <http://www.nanotec.es>.
14. Lauhon, L.J. and W. Ho, *Effects of temperature and other experimental variables on single molecule vibrational spectroscopy with the scanning tunneling microscope*. Review of Scientific Instruments, 2001. **72**(1): p. 216-223.

## Chapter 6

### Laser Driven Scanning Tunnelling Microscopy

6.1	Chapter Introduction .....	143
6.2	Experimental Methods .....	143
6.2.1	General Principles .....	143
6.2.2	Specific Procedures Used.....	146
6.2.2.1	Laser Modulation Frequency .....	148
6.2.2.2	STM Electronics.....	148
6.2.2.3	Tunnelling Current.....	149
6.2.2.4	Applied Tunnelling Voltage.....	150
6.2.2.5	Laser Wavelength.....	150
6.2.2.6	Chemical Nature of the Sample .....	150
6.2.2.7	Surface Topography .....	150
6.3	Results and Discussion.....	151
6.3.1	Laser Modulation Frequency and Applied Tunnelling Voltage .	151
6.3.2	STM Electronics.....	153
6.3.3	Tunnelling Current.....	155
6.3.4	Chemical Nature of the Sample .....	157
6.3.5	Laser Wavelength.....	158
6.4	Conclusions and Future Work.....	160
6.5	References .....	163

## 6.1 Chapter Introduction

A key part of this work involved investigating the interaction between the OPO and the STM in order to look for responses dependent upon the relationship between the sample used and the wavelength of the OPO beam used. This chapter describes how the laser part of the apparatus was combined with the STM. Details are given of the experiments conducted as well as the results from these experiments.

## 6.2 Experimental Methods

### 6.2.1 General Principles

One of the key aims of this project was to investigate the interaction between the OPO and the STM. The interaction was expected to include thermal effects (see §2.5.1) as well as dependencies upon the surface energy states in the sample (see §2.5.2 and [1, 2]). From knowledge of the thermal effects it was expected that the modulation of the tunnelling current due to the incident laser radiation would decrease with increasing laser modulation frequency. From the work in [1, 2] it was expected that the tunnelling current would depend upon the wavelength of the laser in addition to any dependence upon the density of states of the sample.

Initially these effects were investigated by tuning the laser to the wavelength corresponding to the C-H stretch mode in a dimethyl disulphide (DMDS) molecule and the laser was allowed to illuminate the surface of a gold sample coated with DMDS, whilst the STM was used to record images of the topography of the surface. The presence of the laser did not appear to make any difference to these images.

This method was modified slightly by constraining the tip to just measure the tunnelling current at one point rather than across an area in a raster pattern. This modification was made in order to remove any potential effects due to the variation of the surface in the measurement of the current. Conducting

experiments in this way requires that the idler component of the OPO beam be centred on the tip. Despite the ability to see the tip and sample with a camera, this is of no use when trying to see an infrared laser beam. The visible component of the OPO beam can be used as an aid to alignment but the visible and idler components are only approximately co-linear. For the fine adjustment it is possible to use the STM itself to position the beam correctly. If the tip has been approached towards the sample for the purposes of imaging the surface, the tunnelling current is still measured even when no images are being recorded. This is necessary to ensure that the tip does not crash or drift away from the surface. If the laser beam is modulated in some way then this modulation will be present in the tunnelling current and can be detected with a lock-in amplifier. Although the tunnelling current is not being recorded by the STM data capture software it is still available as an external feed to input into other equipment such as a lock-in amplifier. The position of the beam can be adjusted to maximise the modulation of the tunnelling current.

Since it is possible to optimise the LDSTM response in this ‘standby’ mode it is also possible to conduct single point experiments in this state without having to activate the usual data capture mechanism. It is possible to conduct STM experiments at a single point with the STM data capture software but it was better to conduct LDSTM experiments in this standby mode since the signal to noise ratio of the modulation of the tunnelling current was greater. It is not clear what this difference is due to. Either there is an additional feedback setting that is deactivated when in the ‘standby’ mode due to not needing to respond to fast changes in the surface electron density or when the STM is setup to conduct experiments in single point mode the tip is able to ‘wander’ around its starting position leading to greater fluctuations in the tunnelling current recorded.

When conducting STM experiments across an area of the sample is usual to increase the sensitivity of the feedback loop by adjusting its ‘loop gain’ setting such that the tip is moved in response to the lateral changes of the surface electron density. The variation in the surface is recorded in the distance that the tip has to move to keep the tunnelling current constant. However when conducting LDSTM experiments in the ‘standby’ mode a larger signal to noise ratio was recorded in the tunnelling current with low feedback sensitivity, than in the topographic signal ( $z$ ) with high feedback sensitivity. Consequently the feedback loop was

configured with a low sensitivity such that the response to the laser was measured as a modulation in  $I$  but not too low such that the STM could still compensate for the relative drift of the tip and sample.

In order to increase the signal-to-noise ratio of the LDSTM response, the equilibrium current is sometimes set to around 4 to 5nA compared to the usual 0.4 to 0.5nA. This brings the tip closer to the surface and increases the signal to noise ratio of the modulation of the tunnelling current. With this decreased tip-sample separation it is not usually possible to scan across the surface in the usual way and collect topography images. By setting the equilibrium current this high the tip becomes close enough to the surface that if the tip is raster scanned it will drag atoms and molecules across the surface hence degrading the quality of the images recorded. Consequently when using a tunnelling current this high it is only currently practical to conduct LDSTM experiments at single points.

In the description of the STS experiments in §3.3.2, §3.4.3 & §3.4.5, the lock-in amplifier used is a Stanford Research Systems SR830 model. This model can manage input signals with amplitudes of up to  $\pm 1V$ . In the case of the STS experiments, the current signal (converted to a voltage) is larger than this limit and is passed through the compensation box which, amongst other things reduces the size of the signal so that it is within the limits of the SR830. The role played by the compensation box in STS experiments is not required during LDSTM experiments so it is not used in the latter. In LDSTM experiments, the problem of signal size is overcome by using a different lock-in amplifier, a Princeton Applied Research model 5210. This has a  $\pm 3V$  limit on its input and with care the tunnelling conditions can be chosen so that the current signal stays within these limits.

With the tip positioned in the required place readings of the  $x$  &  $y$  channels and noise can be recorded via the GPIB port and an HP-VEE program. The associated experimental conditions and lock-in configuration are recorded at the same time. With the HP-VEE program the readings are taken in batches (usually of 20) and averaged later, to improve signal-to-noise. LDSTM experiments were conducted over various different conditions. The parameters that can be varied are listed as follows:

- (a) Tunnelling current
- (b) Applied tunnelling voltage
- (c) Feedback setting
- (d) Laser wavelength used
- (e) Laser power
- (f) Laser modulation frequency
- (g) Sample type
- (h) Location of tip on surface
- (i) Lock-in amplifier time constant

Although it is best to modulate the laser beam and look for the corresponding response in the tunnelling current, in theory this might not be necessary. If the LDSTM response is expected to be mostly dependent upon the interaction of the laser with the surface adsorbate then illuminating the surface with an unmodulated laser beam and varying the wavelength might produce a corresponding change in the tunnelling current. Under different circumstances to those being studied as part of this work, this technique has been applied to investigate dyes on graphite illuminated with a monochromatic Xe lamp source.<sup>[3]</sup>

In a similar preliminary LDSTM experiment an Au(111) sample covered with a methylthiolate SAM was illuminated with an unmodulated laser beam. As the wavelength of the beam was tuned across the C–H stretching mode the tunnelling current was measured at 78K. No correlation was observed between changes in the tunnelling current and the change in laser wavelength. Interestingly groups who conducted LDSTM work prior to this (see §2.5) did not use such a simple technique suggesting that it was not successful for them either. Their experimental methods were much more complex.

### 6.2.2 Specific Procedures Used

The procedure used to conduct LDSTM experiments is as follows:

The laser is configured to emit the required idler wavelength and is directed at the surface near the tip. The tip is approached towards the surface until the required

tunnelling current is detected. The surface is then imaged and the tip is moved across the surface until a suitable part of the surface is found. This usually is an area  $(500\text{nm})^2$  where the vertical variation is less than  $2\text{nm}$ . Ideally within this area there would be a section of Au(111) terrace that is at least  $(100\text{nm})^2$  in size. The size of the area imaged is repeatedly reduced to about 50% of its previous size until the image is  $(20 \rightarrow 50\text{nm})^2$  in size. Then the tip is positioned in the centre or bottom left corner of this area, in the STM's 'standby' mode.

At this point if required the power of the idler beam can be reduced by means of an iris in an attempt to reduce the effect of the energy of the laser heating up the surface such that the adsorbed molecules are evaporated from the surface.

The tunnelling parameters ( $V$ ,  $I$ , feedback loop) are adjusted to increase the size of the response to the laser. The feedback loop is usually set to 3% (see below). The tunnelling current is set to  $\approx 4\text{nA}$  to increase the signal to noise ratio of the current modulation. The voltage was increased to  $0.4\text{V}$  to compensate for the decrease in the tip-sample separation due to the increase in tunnelling current. The position of the beam is then adjusted to maximise the modulation of the tunnelling current. The lock-in amplifier settings are optimised for the signal measured. An HP-VEE program then records a batch of readings from the lock-in.

One of the experimental variables is changed, such as the AOM frequency or the laser wavelength and another batch of readings is recorded. This process is continued until enough batches have been collected for the variable used.

Of the nine parameters that can be adjusted, (listed as (a) to (i) above) experiments were only conducted to see how five of them affected the modulation of the tunnelling current. In principle, the feedback setting could affect the lock-in response but for the purposes of this study it was fixed at 3%. This is a relatively low setting within the typical range of the feedback loop. Most of the changes in the tunnelling current are not compensated for and passed through to the lock-in amplifier but the tip is moved vertically in response to low frequency changes in order to stop the tip colliding into the surface.

The power of the laser beam before the final lens was fixed at  $10\text{mW}$ . Some initial experiments were conducted with the power greater than this but as the size of the beam on the sample was reduced with modifications to the arrangement of the optics there was some concern that the laser power was enough to remove some of

the thiol molecules. It was occasionally observed that STM images of areas of the sample exposed to the laser beam for  $\approx 10$  hours showed exposed areas of the Au(111) substrate. Consequently the laser power was reduced to a lower value of 10mW. Again as with the feedback setting it was expected that varying the laser power would affect the lock-in response but understanding the effect of the other variables was considered more important.

The lock-in time constant was fixed at 1s as a compromise between being long enough to average out the fluctuations and short enough to be able to make changes (for example to the beam position) and see the response almost immediately. In addition to the averaging performed by the lock-in, an average is taken of the batch of data recorded from it.

As far as the positioning of the tip on the sample is concerned, it is assumed that there is no special significance of any particular place on the sample chosen. The only criterion for a suitable location is the quality of the underlying gold substrate. This leaves the five parameters that are used as independent variables.

### 6.2.2.1 Laser Modulation Frequency

Some experiments were conducted where the modulation frequency of the laser is varied from 316 Hz to 100 kHz. It was expected that the response of the STM to the modulation frequency would be similar to that seen in previous LDSTM studies<sup>[4, 5]</sup> (see §2.5) but it was not clear how having a different laser wavelength and spot size would affect this. It was expected that at low frequencies thermal effects would dominate the LDSTM response but that as the modulation frequency was increased these would roll-off and any other effects would become visible. The experiments were conducted to investigate this and their data is discussed in §6.3.1.

### 6.2.2.2 STM Electronics

In addition to modulating the tip sample distance with the laser, a batch of data was recorded where the current was varied by varying the applied tunnelling

voltage in a similar way to the STS experiments. Although unlike the STS experiments, the modulation in the applied voltage is provided by an external signal generator. The compensation box is only able to modulate the tunnelling voltage up to a frequency of  $\approx 8$  kHz so this alternative facility was required to explore the frequency response of the STM electronics. The results from this experiment are discussed in §6.3.2.

### 6.2.2.3 Tunnelling Current

A series of experiments was conducted recording the effect of the equilibrium tunnelling current on the modulation of the tunnelling current. The tunnelling current was varied from 0.25nA to 5nA for a range of laser modulation frequencies from 316 Hz to 10 kHz. From §2.5.1, Equation 2.54 states that:

$$\frac{dI}{dz} = -cI \quad \text{Equation 6.1}$$

Given that  $c$  is positive, this equation predicts that  $\frac{dI}{dz}$  will be negative for positive values of the tunnelling current. Although for the LDSTM experiments the lock-in amplifier measures the change in  $I$  with respect to the changes in  $z$ , it measures this as a vector, either with  $x$  and  $y$  components or as  $R$  and  $\theta$ . However, the quantity  $\frac{dI}{dz}$  is a scalar but it can be related to  $R$  and  $\theta$  by:

$$\left| \frac{dI}{dz} \right| = R \quad \text{Equation 6.2}$$

When the lock-in response is plotted against a chosen variable, its magnitude  $R$  is used so from these relations  $R$  would be expected to be proportional to  $I$  with a positive constant of proportionality. The results from experiments investigating the effect of the equilibrium tunnelling current are discussed in §6.3.3.

#### 6.2.2.4 Applied Tunnelling Voltage

For most of the LDSTM experiments the tunnelling voltage chosen was 0.5V. Electrons at this potential have enough energy to excite an inelastic channel at  $\approx 0.36eV$  due to a C-H stretching mode in the thiol molecules on the sample. If the LDSTM response involves an inelastic process then it might be expected that if the tunnelling voltage was varied to include energies lower than  $0.36eV$  then a change in the LDSTM response might be observed. Consequently a batch of experiments was run in which the tunnelling voltage was varied from 0.1V to 0.6V to investigate this and the results are discussed in §6.3.1.

#### 6.2.2.5 Laser Wavelength

Another possibility is that processes such as inelastic tunnelling might also have some dependence upon the wavelength of the laser used. To explore this, a batch of experiments was run initially across three laser wavelengths corresponding to the  $29.5\mu m$ ,  $29.75\mu m$  and  $30\mu m$  gratings at  $100^{\circ}C$ . The results are discussed in §6.3.5.

#### 6.2.2.6 Chemical Nature of the Sample

In addition, for each of these variables, experiments were conducted on gold samples both coated with methylthiolate from DMDS and uncoated to look for differences due to the thiolate adsorbate. The results are discussed §6.3.4.

#### 6.2.2.7 Surface Topography

Finally, some experiments were conducted where the LDSTM lock-in response was measured whilst the tip was scanned across the surface. The tunnelling current was reduced to 1nA to minimise the effect of the tip dragging any

adsorbed molecules across the surface. No correlation could be seen between the output of the lock-in and the surface topography.

### 6.3 Results and Discussion

Experiments were conducted to study the effects of five variables; the laser modulation frequency, the applied voltage, the tunnelling current used, the laser wavelength used and the sample type. The details of the experiments conducted and the results obtained are given below.

#### 6.3.1 Laser Modulation Frequency and Applied Tunnelling Voltage

Figure 6.1 is a graph showing the LDSTM frequency response and the voltage dependence of this response. The data displayed in it were collected according to the procedure described in §3.7.7 on a methylthiolate on gold sample under the following conditions:

Tunnelling current ( $I$ ) = 2nA, Lock-in time constant ( $\tau$ ) = 1s,

STM feedback loop gain = 3%, Laser wavelength ( $\lambda$ ) =  $3.362\mu\text{m} = 2974\text{cm}^{-1}$

The equipment was configured to record the change in the tunnelling current due to the modulation of the laser. A value of 2nA for the equilibrium tunnelling current was chosen as a compromise between needing to have a large enough tunnelling current to provide a good signal-to-noise ratio and not wanting to bring the tip too close the surface and risk damage to the SAM. A value of 1s was chosen for the time constant of the lock-in amplifier to average out some of the noise in the tunnelling current signal but still allow frequent monitoring of the LDSTM response. The value of 3% for the feedback loop gain was chosen to only correct low frequency changes in the tunnelling current. This allowed the more rapid laser induced changes in the tunnelling current to be passed through to the lock-in amplifier but at the same time corrected for any slow drifting of the tip

relative to the surface. The wavelength of the laser was chosen to match the energy of the C–H vibrational mode in the methylthiolate molecules in the monolayer.<sup>[6]</sup> This vibrational mode is the most intense that can be reached by the available range of the OPO and it was anticipated that it would be best to investigate the LDSTM response using this wavelength.

The data in Figure 6.1 yields several important aspects of the LDSTM response: Firstly the roll-off with frequency is broadly consistent with that recorded by Grafström *et al.* for a gold on mica sample with a 1mW 514nm Ar<sup>+</sup> ion laser.<sup>[4]</sup> In their work they illuminated several samples (including one similar to the substrates used in the present work) with a 1mW 514nm Ar<sup>+</sup> ion laser modulated with a Pockels cell and a Glan-Thompson polarizer. They recorded the thermal expansion of Pt/Ir and W tips in response to the laser light. The roll off with frequency they recorded was similar to that shown in Figure 6.1.

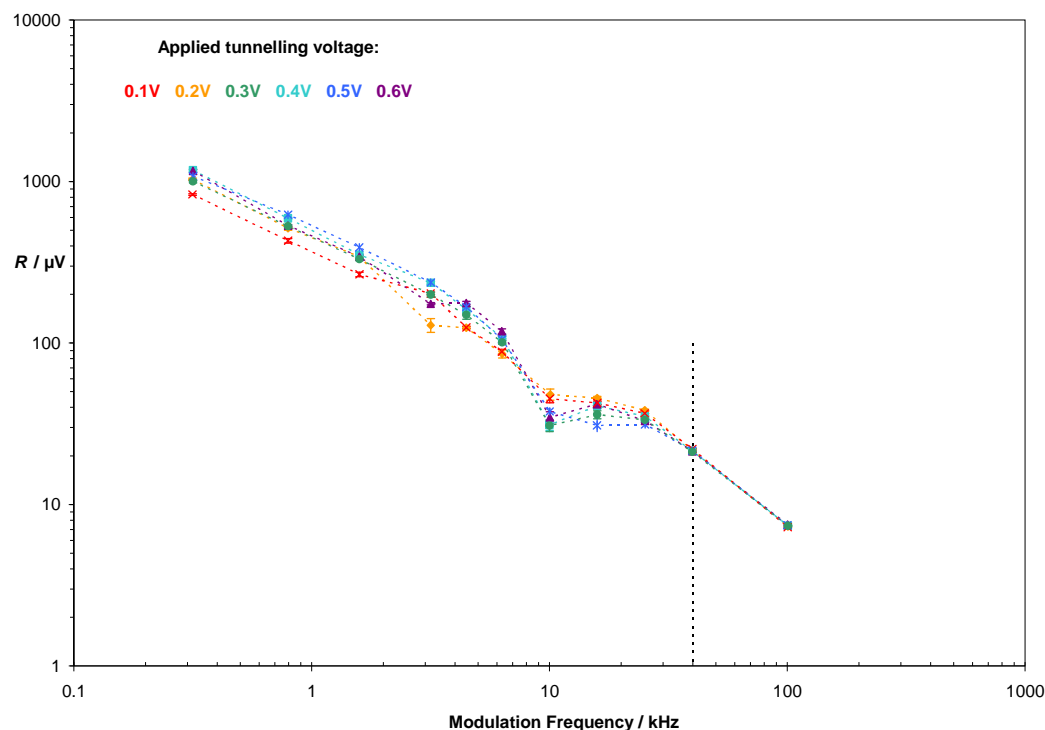


**Figure 6.1:** A plot showing the frequency and voltage dependence of the LDSTM response represented on the vertical axis as the magnitude output of the lock-in amplifier. The horizontal axis shows the modulation frequency of the AOM. Note the logarithmic scale on both axes. Experimental conditions:  $I = 2\text{nA}$ ,  $\tau = 1\text{s}$ , feedback loop gain = 3%, laser power = 10mW and  $\lambda = 2974\text{cm}^{-1} = 3.362\mu\text{m}$ .

Secondly there appears to be very little variation with applied voltage. This suggests that this response is due to thermal effects and not due to processes that depend upon the energy of the tunnelling electrons. This can be understood by realising that  $c$  in Equation 2.58 and Equation 6.1 ( $\frac{dI}{dz} = -cI$ ) is only weakly dependent upon  $V$  (see Equation 2.24  $\left(T \approx \frac{4E(V_0-E)}{V_0^2+4E(V_0-E)} e^{-\frac{2}{\hbar}\sqrt{2m(V_0-E)}L}\right)$ ). Although there is some variation in the different curves at lower modulation frequencies, the points recorded above  $\approx 40$  kHz are virtually identical (right-hand-side of dashed line in Figure 6.1). Closer investigation of the readings collected at these frequencies revealed that they did not appear to be dependent upon whether the tip and sample were illuminated with the laser or not revealing that they were just systematic noise.

Thirdly there is a dip at  $\approx 10$  kHz. It is not clear whether this is real or is linked to the artefact signal observed above 40 kHz.

### 6.3.2 STM Electronics

This analysis of the data in Figure 6.1 raises an important issue of whether this frequency response is due to an LDSTM process or to intrinsic properties of the STM. This can be resolved by examining Figure 6.2. This is identical to the previous Figure but with the addition of a curve (coloured black) showing the results of modulating the tunnelling voltage with a signal generator without illumination of the sample with the laser. The tunnelling voltage was 0.4V with a 40mV<sub>rms</sub> modulation provided by the signal generator. The other experimental conditions were  $I = 4$ nA,  $\tau = 300$ ms, Feedback loop gain = 3% and the sample was the same as used for the LDSTM experiments. The conditions are different to those used for the LDSTM experiments but as will be shown later this is probably not significant. The shorter time constant was used due to the greater signal-to-noise ratio compared to the LDSTM experiments.

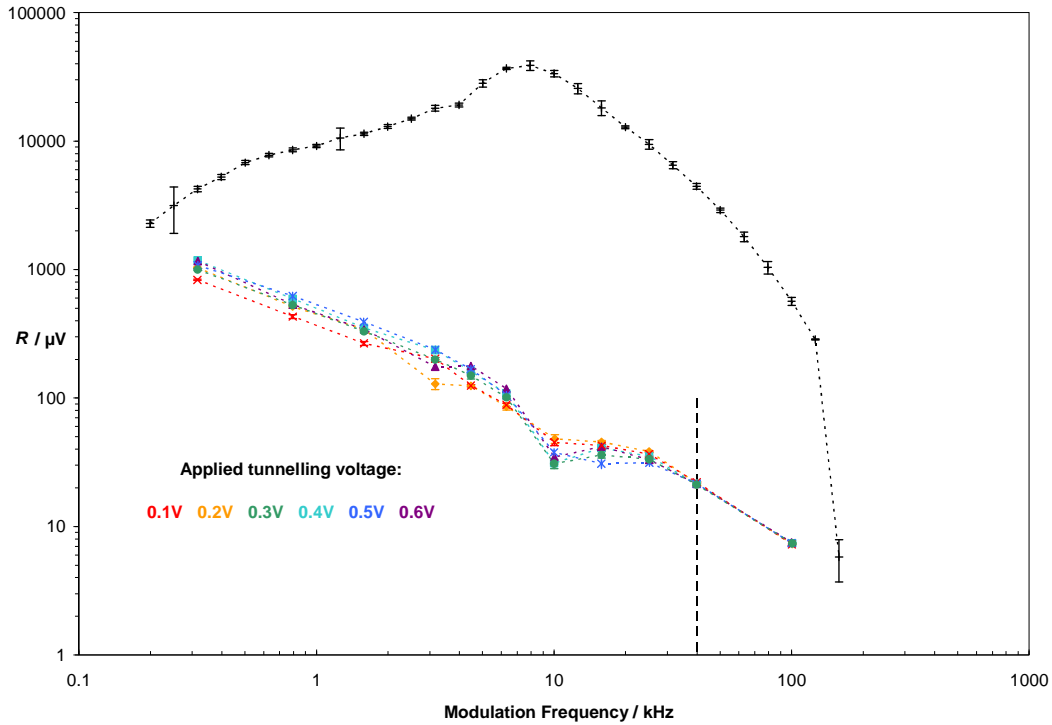


**Figure 6.2:** Identical to the previous Figure but with the addition of the black curve displaying data from an experiment in which the tunnelling current was varied by a modulated applied voltage rather than a modulated laser beam. This shows the frequency response of the STM electronics and allows the LDSTM data to be seen in context of the characteristics of the STM.

This curve shows that the response of the STM electronics increases between  $\approx 300$  Hz and  $\approx 10$  kHz and then decreases with increasing frequency up to above 100 kHz. The sensitivity of the STM electronics increases with increasing frequency so the roll-off of the LDSTM response in real terms is faster than the slope of the curves indicate. At frequencies higher than 10 kHz the decreasing sensitivity of the STM electronics provides a reason for the nature of the data at frequencies above  $\approx 39$  kHz. Despite there being a symmetry to the frequency response of the STM electronics either side of  $\approx 9$  kHz, LDSTM response rolls off from low frequencies to higher frequencies and above  $\approx 39$  kHz it is at the same level if not less than the noise of the of the STM electronics. Finally the sharp drop in the black curve at  $\approx 126$  kHz is due to the limit of the lock-in amplifier.

### 6.3.3 Tunnelling Current

The LDSTM data presented in Figure 6.2 was recorded with a different tunnelling current to the STM electronics response data in the same Figure. From the results of a second LDSTM experiment this difference in tunnelling current can be shown not to be a cause of the different shapes of the curves for these two types of experiments. In this experiment LDSTM measurements were conducted in a similar manner to the first LDSTM experiment described, except that for this experiment the gap voltage was fixed at 500mV and measurements of the LDSTM response (lock-in amplifier magnitude) were measured for a range of tunnelling currents at a selection of modulation frequencies. The data from this second experiment is shown in Figure 6.3. The data in this graph shows that the LDSTM response (shown as  $R$ , the magnitude output of the lock-in amplifier) increases linearly with increasing tunnelling current.

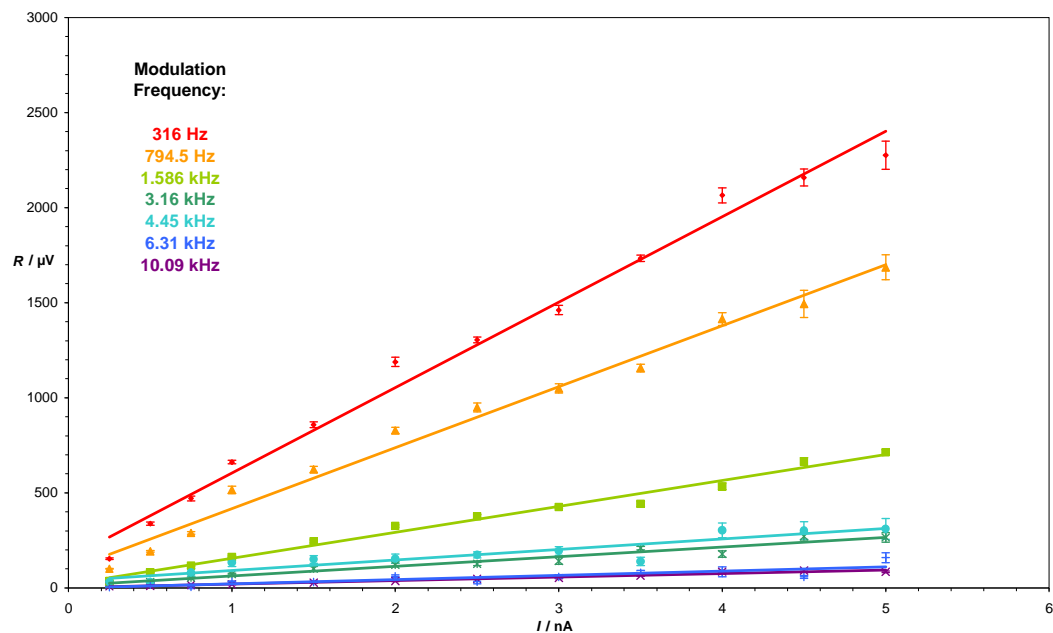


**Figure 6.3:** This shows the results of LDSTM experiments recording the effect of the tunnelling current on  $R$ . They were recorded with experimental conditions of: Methylthiolate on gold sample. Tunnelling voltage: 0.5V,  $\tau = 1$ s, feedback loop gain = 3%,  $\lambda = 2974\text{cm}^{-1} = 3.362\mu\text{m}$ , laser power = 10mW.

The gradient of this linear relationship increases with decreasing modulation frequency with the exception of the data at 4.45 kHz.

As discussed in §2.5 it was expected that the LDSTM response would be proportional to the tunnelling current and the linear fits seem to suggest this, at least to a first approximation. For the lower modulation frequencies at 316 and 794.5 Hz this fit fails at low values of the tunnelling current.

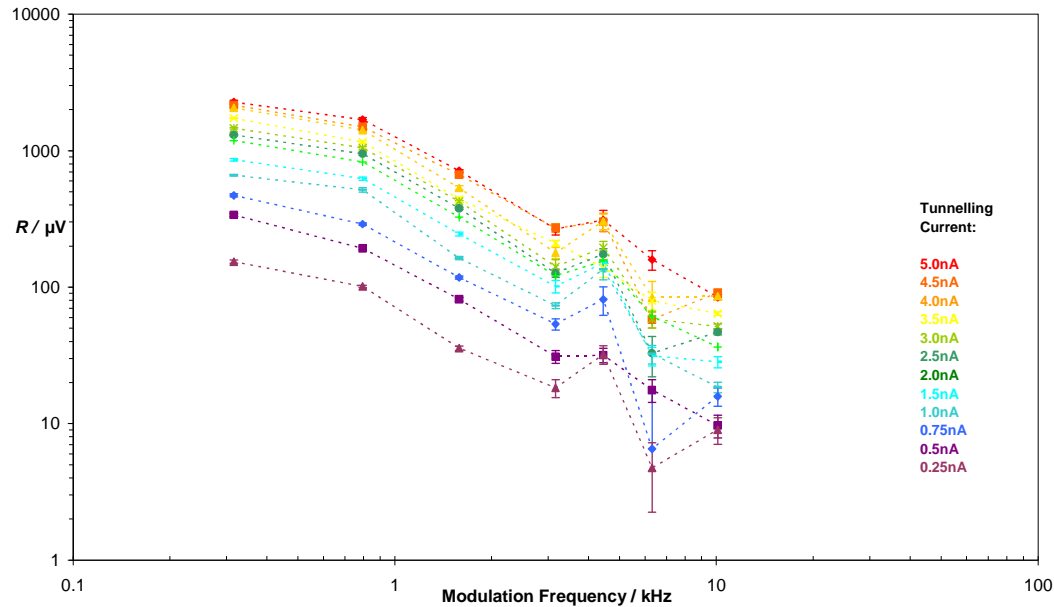


**Figure 6.4:** This shows the same data as in the previous Figure but with the lock-in magnitude output as a function of the modulation frequency. Experimental conditions as described in the caption for the previous Figure.

This is not unexpected given the approximation in Equation 2.53 that the tunnelling current is just exponentially dependent upon the tip-sample distance. These data can be plotted with the lock-in magnitude output as a function of laser modulation frequency as shown in Figure 6.4.

The data in Figure 6.4 shows that lock-in output magnitude just scales with increasing current meaning that the difference in shape between the LDSTM curves and the black curve in Figure 6.2 is not due to the differences in the values of  $I$  used.

### 6.3.4 Chemical Nature of the Sample

So far all these experiments have been conducted on a methylthiolate covered gold sample. To see the difference that methylthiolate makes to the response from the sample Figure 6.5 shows curves from an uncoated Au(111) sample and an Au(111) sample coated with methylthiolate.

Each of these two curves is an average of four curves conducted on each sample. They show a significant difference between the LDSTM responses of the two types of samples and intriguingly it is the gold sample that has the larger values of the lock-in output magnitude  $R$ . This difference is surprising given the modulation frequencies at which this difference occurs. Modulation at these frequencies is expected to induce thermal changes which are not expected to be sensitive to the presence of a monolayer of molecules on the substrate.

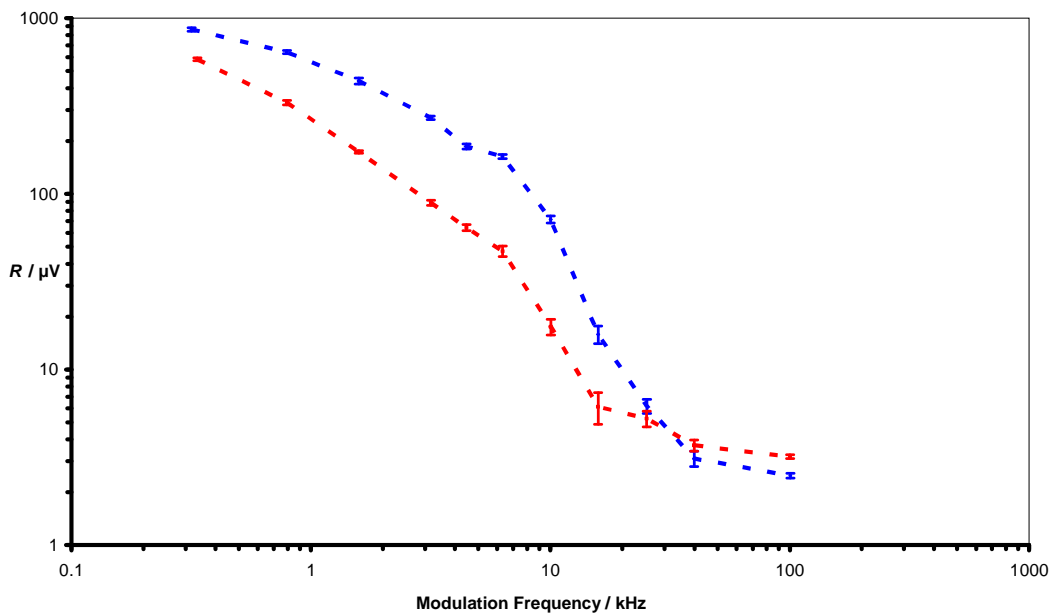


**Figure 6.5:** Showing the difference between the LDSTM responses for gold samples **coated** and **uncoated** with methylthiolate. Other experimental conditions: Tunnelling voltage = 0.5V, feedback loop gain = 3%,  $\lambda = 3.362\mu\text{m} = 2974\text{cm}^{-1}$ ,  $\tau = 1\text{s}$ ,  $I = 1\text{nA}$ , laser power = 10mW. The same tip was used for both samples.

### 6.3.5 Laser Wavelength

Although these experiments were conducted with  $\lambda = 3.362\mu\text{m}$  in expectation that there would be some wavelength dependent effects, it was possible that other effects would be manifested at other wavelengths. This was investigated with an experiment in which the laser wavelength was varied; the results of this are shown as the red and blue coloured data in Figure 6.6.

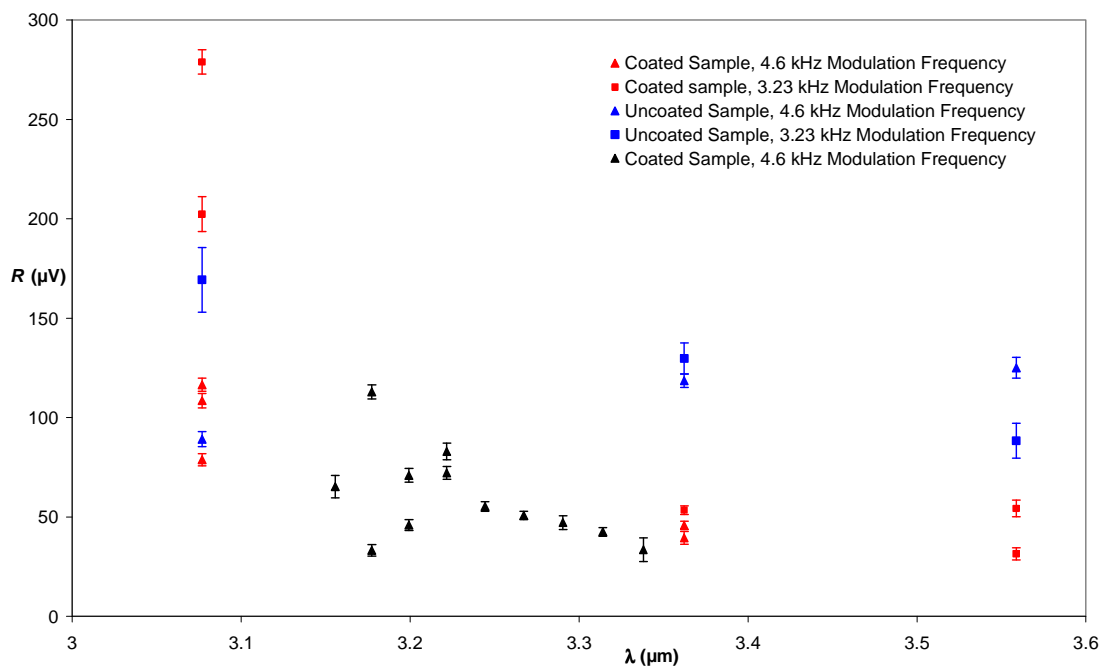


**Figure 6.6: Showing the LDSTM response to the wavelength of the laser. Samples: **coated** and **uncoated** Modulation frequency: ■ = 3.23 kHz, ▲ = 4.6 kHz. Other experimental conditions: Tunnelling voltage = 0.5V,  $\tau = 1\text{s}$ ,  $I = 1\text{nA}$ , feedback loop gain = 3%, laser power = 10mW. The black data points show additional data for laser wavelengths between  $3.16\mu\text{m}$  and  $3.36\mu\text{m}$ . These were generated by varying the temperature of the  $29.75\mu\text{m}$  grating from  $100^\circ\text{C}$  to  $190^\circ\text{C}$ .**

The three wavelengths chosen correspond to the  $29.5\mu\text{m}$ ,  $29.75\mu\text{m}$  and  $30.0\mu\text{m}$  gratings in PPLN crystal 2 (see Figure 2.22) at  $100^\circ\text{C}$ . As seen with the data in Figure 6.5 the response for the uncoated sample is greater than for the coated sample and wavelengths of  $3.36\mu\text{m}$  and  $3.56\mu\text{m}$ . For the coated sample there is a distinctive increase in the signal for  $\lambda = 3.08\mu\text{m}$  but not for the uncoated sample.

This response from the coated sample is unexpected. There is no feature in the vibrational spectrum for methylthiolate on gold at this energy.<sup>[6]</sup>

To investigate this feature further additional data were collected between  $3.07\mu\text{m}$  and  $3.34\mu\text{m}$  and are shown as the black coloured data points in Figure 6.6. These were collected by using the  $29.75\mu\text{m}$  grating and varying the temperature from  $100^\circ\text{C}$  to  $190^\circ\text{C}$ . The data at longer wavelengths seems to fit with the data in the previous Figure but at shorter wavelengths there is significant inconsistency. Ideally data would have been collected in the whole of the range between  $3.08\mu\text{m}$  and  $3.36\mu\text{m}$  but due to the design of PPLN crystal 2 this was not possible. According to Figure 2.22 the OPO can emit radiation in this range but it is only possible to configure the OPO to safely emit in the range  $3.16\mu\text{m}$  to  $3.36\mu\text{m}$ . The range of wavelengths between  $3.07\mu\text{m}$  and  $3.16\mu\text{m}$  are produced when the temperature of the PPLN crystal is less than  $100^\circ\text{C}$ . As described in §2.3.3 below this temperature the crystal suffers damage as a consequence of the incident pump beam and does not operate efficiently, hindering the ability to conduct experiments with radiation in this wavelength range.

Further LDSTM experiments of this type were also attempted with  $\lambda < 3.07\mu\text{m}$  but proved unsuccessful apparently due to another more fundamental limit of the OPO. When attempting to drive the OPO with the  $30.0\mu\text{m}$  grating at temperatures greater than  $100^\circ\text{C}$  the output idler power decreased dramatically. This seems to be due to a fundamental limit of the mirrors that form the OPO cavity. With the  $30.0\mu\text{m}$  grating at  $100^\circ\text{C}$  the wavelength of the signal photons (that oscillate in the OPO cavity) is  $1.59\mu\text{m}$ . This is outside the documented limits of the OPO mirrors of  $1.35\mu\text{m}$  to  $1.55\mu\text{m}$  so their effectiveness to reflect radiation at this wavelength will already be slightly diminished. Increasing the temperature of the oven further lengthens the wavelength of the signal photons such that the mirrors only reflect a small percentage of them. Although the OPO still emits some idler photons at the wavelengths described in Figure 2.20, the output power is dramatically reduced to only a few mW, too low to be used for experiments.

Despite these difficulties it is still possible to draw some conclusions from this wavelength dependent phenomenon in these LDSTM data. Figure 6.7 overlays the energies of the photons used to record the data Figure 6.6 with the electron energies in the  $\frac{dI}{dV}$  vs.  $V$  spectrum in Figure 5.27 and reveals that the increased

LDSTM response for the coated sample at  $3.07\mu\text{m}$  seems to occur at a similar energy to the decrease in the gradient at  $0.41\text{eV}$  in the  $\frac{dI}{dV}$  vs.  $V$  spectrum. In the equivalent  $\frac{dI}{dV}$  vs.  $V$  spectra for unexposed Au samples such a change in the gradient is not seen which seems to be consistent with the LDSTM data for the Au sample. This suggests that these features may have a common origin the details of which are as yet unclear.

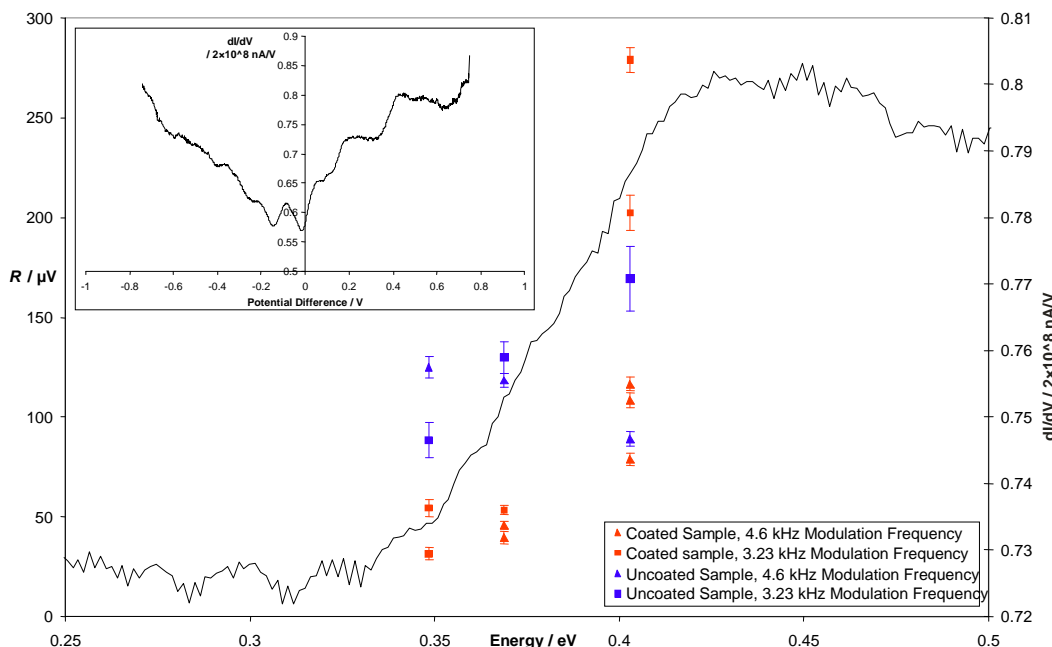


**Figure 6.7:** Showing how the change in gradient at  $0.42\text{V}$  in the methylthiolate  $\frac{dI}{dV}$  vs.  $V$  spectrum occurs at a similar energy to the increase in modulation of the tunnelling current of the coated sample. The insert is a copy of Figure 5.27. The main figure shows a section of this  $\frac{dI}{dV}$  vs.  $V$  curve from  $0.25\text{V}$  to  $0.5\text{V}$  (black curve, right axis) overlaid with data from Figure 6.6 (red and blue data, left axis).

## 6.4 Conclusions and Future Work

As anticipated, the LDSTM response of the STM seems to be dominated by thermal expansion. From previous work by Grafström *et al.* it seems that this is due to the sample.<sup>[4]</sup> Two differences were observed between the coated and

uncoated sample. Firstly the modulation of the tunnelling current for the coated sample was found to roll off faster than for the uncoated sample. Secondly the dependence upon the wavelength of the laser was different between the two samples. The modulation of the tunnelling current significantly increased with the coated sample compared to the uncoated sample for photons of energy  $\approx 0.4\text{eV}$ . However it is intriguing that there were not wavelength dependent features at the energy that matched a vibrational mode of the adsorbed species. There are several possible reasons for this some of which have already been raised for other reasons in the concluding remarks for other experiments in this thesis. It is possible that LDSTM processes involving molecular vibrational modes only appear if the sample is cold enough for inelastic modes to appear in  $\frac{d^2I}{dV^2}$  vs.  $V$  spectra.

Additionally, running LDSTM experiments at such low temperatures would present challenges in addition to those that already exist for conventional STM experiments. The power from the laser is likely to add significant energy to the sample and make it more difficult to maintain the base temperature of  $\approx 5\text{K}$ . Despite not seeing features at the expected energy of the C-H stretching mode possible inelastic resonance effects were seen at  $3.07\mu\text{m}$  ( $0.41\text{eV}$ ). However it is not clear what these effects are due to. In §6.2.2.4 it was described how the applied tunnelling voltage might play an important role in the laser-STM interaction if it involved inelastic tunnelling modes; however the data in Figure 6.1 does not support such a process. When electrons tunnel inelastically there is a change in the signal recorded as the energy of the tunnelling electrons increases above the energy of the mode in the molecule but no significant change is observed in the response of the STM as the tunnelling voltage is increased (see Figure 6.1). However these data were collected with a laser wavelength near  $0.36\text{eV}$  where the C-H stretching mode was expected to appear. If however the interaction of the molecules with the surface at  $\approx 78\text{K}$  produces a change in the density of states at a higher energy ( $> 0.4\text{eV}$ ) then this would explain why no difference was seen in these data. In order to clarify whether this change in the response of the STM to the laser at  $3.07\mu\text{m}$  ( $0.41\text{eV}$ ) depends upon the energy of the electrons a further experiment needs to be conducted with the laser wavelength set to  $3.07\mu\text{m}$  in which the LDSTM response is recorded for values of the tunnelling voltage above and below  $0.41\text{eV}$ . If a difference in response is

observed for applied voltages above and below  $0.41\text{eV}$  then this change in response at  $3.07\mu\text{m}$  is likely due to an inelastic tunnelling process. If however there is no change in the LDSTM response with respect to the tunnelling voltage then the change in response at  $3.07\mu\text{m}$  is not due to an inelastic tunnelling effect.

It was also disappointing not to be able to record any correlation of the LDSTM response with the features in a topography image of the surface. These two problems might be solved along with issues relating to spectroscopy experiments by using partial layers of adsorbates. As described in §5.4 by using these partial layers it should be easier to identify which features in spectroscopy curves are due to the adsorbate and which are due the substrate. The same reasoning may also apply to LDSTM experiments. Whether such a technique would work in practice depends upon the exact nature of the LDSTM response.

In addition there are a number of other laser related issues that arise as a consequence of these results. Firstly, the laser spot-size. In some of the previous studies laser spot sizes of  $40\mu\text{m}$ <sup>[4]</sup> and  $100\mu\text{m}$ <sup>[5]</sup> have been used but for this work it was closer to  $500\mu\text{m}$ . Due to the current constraints of not having any optical components inside the UHV chamber this is the smallest size the spot can be. With a large spot size a significant proportion of the laser radiation does not illuminate the sample near the tip, so any effect (other than thermal expansion) of this part of the beam on the sample is unlikely to be detected by the tip. However just decreasing the spot size with no change to the laser power will just increase the thermal response from a smaller area of the sample. It may be necessary to maintain the same intensity with a reduced spot size. Any attempt to reduce the laser spot size would require overcoming the existing limitations relating to the use of optics inside the UHV chamber. One solution would be to make use of an optical fibre transmissive both at idler and other wavelengths visible by the camera for alignment purposes. This would require a chalcogenide based fibre mounted on a feed-through in place of one of the windows and it would have to be routed past the rotating heat shield through a gap in the inner heat shield before being mounted onto the base of the STM piezoelectric stack to enable the end of the optical fibre to move in sync with the STM tip. However challenges remain in ensuring the UHV compatibility of such fibres.

From the outset it was expected that with increasing modulation frequency the thermal LDSTM effect would roll-off revealing other LDSTM effects at higher

modulation frequency but it seems that the frequency response of the STM may hinder this. At frequencies higher than  $\approx 10$  kHz the LDSTM response rolls off and it is here that there is the need for suitable electronics that will not perform any filtering to maximise the signal-to-noise ratio for the lock-in amplifier. To solve this problem will require replacement of the STM pre-amplifier from which the STM frequency response originates. Ideally its replacement would permit frequencies up to 120MHz allowing the repetition rate of the laser to be used as the modulation frequency of the LDSTM process.

Also it is not certain whether the current signal will effectively travel along the wires from the STM head to the feed-through connected to the pre-amplifier. From the need for UHV compatibility they have significant attenuation at high frequencies. These wires could be replaced by a cable that by design has lower losses at high frequencies, provided its new dimensions can be accommodated in the existing design of the STM.

If this is not possible two options remain for future designs of the pre-amplifier. The first would match the frequency characteristic of the wires from the STM head to the pre-amplifier, allowing the LDSTM response to be driven as fast as these wires would allow. The second would be mounted inside the UHV chamber much closer to the STM head. This would allow the processing of signals at the higher frequencies but would introduce further complications resulting from the need for UHV compatibility.

## 6.5 References

1. Yeyati, A.L. and F. Flores, *Photocurrent Effects in the Scanning Tunneling Microscope*. Physical Review B, 1991. **44**(16): p. 9020-9024.
2. Yeyati, A.L. and F. Flores, *Theory of Photovoltaic Effect in STM - Application to Graphite*. Ultramicroscopy, 1992. **42**: p. 242-249.
3. Möltgen, H. and K. Kleinermanns, *Resonance enhanced scanning tunneling (REST) spectroscopy of molecular aggregates on graphite*. Physical Chemistry Chemical Physics, 2003. **5**(12): p. 2643-2647.

4. Grafström, S., *Analysis and compensation of thermal effects in laser-assisted scanning tunneling microscopy*. J. Vac. Sci. Technol. B, 1991. **9**(2): p. 568-572.
5. Landi, S.M., *Avoiding photothermal noise in laser assisted scanning tunneling microscopy*. Ultramicroscopy, 1999. **77**: p. 207-211.
6. Nuzzo, R.G., B.R. Zegarski, and L.H. Dubois, *Fundamental-Studies of the Chemisorption of Organosulfur Compounds on Au(111) - Implications for Molecular Self-Assembly on Gold Surfaces*. Journal of the American Chemical Society, 1987. **109**(3): p. 733-740.

# Chapter 7

## Conclusions

This thesis describes the equipment and techniques developed to conduct LDSTM experiments on Au(111) coated and uncoated with thiol molecules. This chapter gives a summary of this work and highlights the significant results.

A key component of any STM is the tip used to image the surface. Early in this project techniques were developed to make STM tips using electrochemical etching with AC and DC power supplies and treatment with 40% HF<sub>(aq)</sub>. The etching procedures developed (as described in Chapter 3) were based upon guidelines provided by the manufacturer of the STM. Modifications were made to accommodate the experimental equipment available. In particular a special power supply was developed to facilitate DC etching.

Optical microscope and FEG-SEM images were collected of tips made with these techniques to determine their profiles and the optimum conditions for the etching processes. STM images recorded at 78K show the ability of both types of tip to resolve the atoms on sections of Au(111) surfaces. It was possible to make correlations between the microscopic shapes of the tips and the quality of the STM images obtained with those tips revealing that it is possible to screen the tips based upon their microscope shape. The radii of the tips as observed in the FEG-SEM images are large compared to the scale of the atoms imaged on the Au(111) samples indicating that the surface of the tips is rough on length scales smaller than that recorded by the STM. The apparent tip radii of the AC etched tips was larger than that of the DC etched tips and experimentally it was found that the probability of obtaining atomic resolution images was greater with the DC tips than the AC tips.

A key part of the experiments in this chapter was the Au(111) substrate used as the basis for all the samples studied. Chapter 4 describes how these substrates are manufactured using a hydrogen flame. Key to their manufacture is their removal from the flame for a brief period to cool down before being returned to the flame.

Experiments revealed that up to nine cycles of heating and cooling were required to reform the polycrystalline surface into larger domains containing good quality regions of Au(111). Despite only part of the surface undergoing reconstruction into the Au(111) structure it was not difficult to locate these regions on the surface and STM images are included showing this structure including the characteristic  $22 \times \sqrt{3}$  “herringbone” reconstruction.

Scanning tunnelling spectroscopy (STS) experiments were conducted upon the Au(111) surface at 5K. The shape of the  $\frac{dI}{dV}$  vs. V curve was similar to that of a quadratic curve, very different to that published previously. Work by Vázquez de Parga<sup>[1]</sup> suggests that the disparity can be understood if the arrangement of the atoms at the very end of the tip used to collect the data is different to that of other tips used to collect data in previously published work. In general the effect of the structure of the very end of the tip does not appear to affect how features appear in the STM images but images are presented suggesting that the tip structure may play a part in how the images appear in ways that are not ordinarily considered to be important. Given the sensitivity of the STS data to the structure of the tip it is possible that the tip structure changes as the tip is scanned across the surface particularly across the boundaries between the domains on the surface where there is greater variation of the surface topography. If this is the case then future work is suggested making use of flatter single crystal samples that would reduce this effect.

Chapter 5 describes experiments conducted on Au(111) substrates coated with self-assembled monolayers (SAMs) of alkanethiols. Samples of octanethiolate monolayers were made by immersion of gold substrates in dilute solutions of octanethiol in ethanol. STM images recorded at 78K of the octanethiolate monolayers show how the molecules arrange themselves on the surface and change the reconstruction of the atoms in the gold substrate. From measurements of the ‘holes’ observed in the surface of the SAM samples they are most likely to be due to the reconstruction of the underlying gold substrate by the thiolate molecules.

STS experiments were conducted on an octanethiolate SAM sample. Clear differences could be seen between the data from these experiments and those from the uncoated Au(111) sample. However it was found that the asymmetry present

in the octanethiolate data is consistent with previously published work<sup>[2]</sup>. There is an offset in the octanethiolate data the origin of which is not clear. No obvious features originating from inelastic tunnelling could be detected in the octanethiolate STS data. This is most likely due to the sample being too warm and so broadening the modes originating from inelastic processes. The spectroscopic measurements were recorded in slightly different environments on the SAM surface but no significant difference could be observed between the  $\frac{dI}{dV}$  vs.  $V$  spectra from the different environments. A small difference was seen between the  $I$  vs.  $V$  curves for the different environments at potentials approaching  $-1V$ . There is not enough information in the data to indicate an origin of this difference. Changes in local workfunctions, thiol layer thickness and resistance would only be expected to yield symmetric changes in the  $I$  vs.  $V$  curves contrasting with the slightly asymmetric curves recorded.

The method for making the octanethiol monolayers was found to be unsuitable for making samples that were partially coated with thiolate. Consequently the vapour dosing method was developed (see §2.2.5). Preliminary experiments involved the dosing of dimethyl disulphide (DMDS) onto Au(111) samples at room temperature. Low density coverage of DMDS can be seen on one set of STM images (recorded at 78K) of one of these samples showing evidence of the molecules aligning themselves with the underlying  $22\times\sqrt{3}$  “herringbone” reconstruction.

A later set of STM images from this sample shows individual molecules scattered across the surface. Their appearance in STM images at different voltages seemed to discount a typical tip convolution effect. This indicates that the images reveal information about the molecular substructure or indicate voltage dependent perturbation, revealing information about the tip structure. Under the assumption that the images show the shape of the molecules, structures and orientations are suggested in comparison with previously calculated models<sup>[3, 4]</sup>.

The results of topographically dependent STS experiments conducted at 78K on a sample partially coated with DMDS indicated that the feature in the STM images was most likely to be cluster of Au atoms rather than DMDS molecules. Despite this, the experiment demonstrates the viability of categorising the STS data by the topography of the surface in the vicinity of where the STS data was collected.

Future work is suggested involving the topographically dependent STS experiments conducted on Au(111) samples partially coated with methylthiolate prepared with sample heating.

The results of STS experiments conducted on a Au(111) substrate coated with a complete methylthiolate monolayer showed features not seen in data from uncoated samples. The anti-symmetric features expected as a consequence of inelastic tunnelling were not observed, most likely due to the temperature dependent broadening of the peaks in the  $\frac{d^2I}{dV^2}$  vs.  $V$  spectrum. Further experiments at lower temperatures ( $\sim 5\text{K}$ ) would be needed ideally with partially coated samples to clarify the situation.

Chapter 6 presents experiments investigating the interaction of the laser with the STM. The interaction is dominated by thermal effects but differences are still seen between the coated and uncoated samples. The modulation of the tunnelling current was found to roll off with increasing laser modulation frequency; although above  $\approx 40\text{ kHz}$  the recorded modulation of the tunnelling current seems to be an artefact of the electronic equipment used to record the LDSTM signal. At lower frequencies the response was confirmed to be genuine by comparing it with the response measured with a modulated voltage applied across the tunnelling junction with no laser illumination.

With laser illumination the fixed applied voltage had no effect on the modulation of the tunnelling current but the latter was linearly dependent upon the value of the tunnelling current set by the feedback loop. With a laser wavelength matched to the energy of one of the C–H stretching modes it was found that the modulation of the tunnelling current was greater for the uncoated sample but when the wavelength was increased to  $3.07\mu\text{m}$  (410meV) the modulation of the tunnelling current was greater for the coated sample than the uncoated sample. In the  $\frac{dI}{dV}$  vs.  $V$  spectrum for the methylthiolate coated sample there is a decrease in the gradient near this energy suggesting a common cause for these two phenomena. Future work is required to upgrade the laser source to investigate the LDSTM response at wavelengths not currently accessible. A key experiment for the future would be to re-examine the voltage dependence of the response of the STM to the laser at  $3.07\mu\text{m}$  (410meV) to determine whether the difference between the two samples at this wavelength is conditional upon the energy of the electrons.

Each of the chapters in this thesis highlights a key area of investigation in the task of studying the interaction of an infrared laser beam with thiolate molecules in a scanning tunnelling junction. This thesis has shown that the equipment used can be used to manufacture Au(111) substrates partially coated with thiolate. It has shown how such samples can be investigated with topographically dependent scanning tunnelling spectroscopy. The experiments with a thiolate sample and the OPO beam show the presence of wavelength and sample dependent effects.

Despite these achievements with the different types of experiments conducted clearly further work is necessary before these techniques can be combined together to form a useable method for identifying different species with molecular resolution. However there is also not enough information from the experiments conducted to rule out using an OPO and LTSTM to investigate single molecules in the future. A series of further experiments will need to be carried out to rule one way or the other whether it is useful to combine an OPO with a low temperature STM. The OPO will need to be reconfigured to ensure that it can emit radiation more consistently in the infrared ‘fingerprint’ region. It is also vital that the STM electronics are modified to not filter out high frequency signals so that the LDSTM response can be investigated at frequencies up to the repetition rate of the OPO pump laser. There are a range of issues relating to controlling the OPO beam parameters inside the UHV chamber which are more challenging but it should still be possible to further optimise the characteristics of the OPO beam.

Despite the results from these future experiments being far from certain, it is important that these remaining questions are answered because the prize of investigating the interaction of ‘fingerprint’ infrared radiation with organic species at the molecular scale is so valuable.

## 7.1 References

1. Vázquez de Parga, A.L., et al., *Electron Resonances in Sharp Tips and Their Role in Tunneling Spectroscopy*. Phys. Rev. Letters, 1998. **80**(2): p. 357-360.

2. Cui, X.D., et al., *Making electrical contacts to molecular monolayers*. Nanotechnology, 2002. **13**(1): p. 5.
3. Grönbeck, H., A. Curioni, and W. Andreoni, *Thiols and disulfides on the Au(111) surface: The headgroup-gold interaction*. J. Am. Chem. Soc., 2000. **122**(16): p. 3839-3842.
4. Akinaga, Y., T. Nakajima, and K. Hirao, *A density functional study on the adsorption of methanethiolate on the (111) surfaces of noble metals*. The Journal of Chemical Physics, 2001. **114**(19): p. 8555-8564.

## Appendix A: Manufacture of STM Tips

The Pt-Ir tips are made from 0.25 mm wire:

- A short section (1.5 → 2 cm) of wire is inserted into a tip holder. The wire is then clamped or welded in place
- The wire is then cut approximately 1 mm from the top of the tip holder at an angle of 45° with suitable wire cutters.
- As the wire is cut, the cutters are moved upwards along the direction of the wire, whilst maintaining the 45° angle.
- This action slightly stretches the newly cut end, so that it is slightly more likely to be atomically sharp than if it is not stretched.
- It may be surprising that this simple method is able to produce tips that are atomically sharp, however it does not produce such tips every time. In fact, the failure rate for such tips is very high. Consequently attempting to run the STM with such tips is difficult and slow.

Since the W tips are electrochemically etched and are more complicated to make:

- A section of 0.38mm or 0.010" W wire is electrochemically etched using equipment, identical or similar, to that shown in Figures 2.12 to 2.15. (The length of the wire is not that critical. It needs to be at least 4cm long but the longer the wire the greater the number of tips that can be made at one time.)
- Two different etching methods can be used, but their experimental set-ups are very similar to each other. Both use a shallow beaker containing an alkaline solution. In the solution is a piece of metal wire bent into a ring and an upright part that extends out of the water to be clamped in place. The W wire is positioned vertically (approximately) in the centre of the solution with about 4mm of wire under the surface of the liquid.

- If alternating current is to be used then the shallow beaker has a diameter of about 15cm. The ring is made of 0.5mm W metal wire and has a diameter of about 10cm. The alkaline solution is 200ml of 0.6M Potassium Hydroxide (KOH) solution. The voltage applied between the ring and straight wire is 15V ac.
- For direct current, etching the shallow beaker has a diameter of about 10cm. The ring has a diameter of about 7cm and is made of stainless steel. The alkaline solution is 100ml of 5M Sodium Hydroxide (NaOH) solution. The voltage applied between the W wire and the stainless steel ring is initially (at the start of etching) approximately 2V, with the + terminal connected to the W wire. As the etch progresses the voltage across the + & - terminals increases due to the resistance of the circuit increasing due to the removal of material from the end of the W wire. A special power supply is required to etch tips by the dc method so that the current supply is switched off at the correct moment in the etch process. As the etching process runs, the end of the W wire becomes very thin forming a sharp tip. If the electricity is allowed to flow for too long, then the etching process will make the tip blunt again, so the etch has to be stopped before this happens.
- The tip is then rinsed with deionised water to remove any traces of Hydroxide on the tip. The tip and about 2.5cm (1 inch) of the W wire is cut off to be stored in a labelled box on a piece of Blu-Tack or similar, whilst ensuring that the tip does not touch the walls of the box.
- Or the tip is dipped in 40%  $\text{HF}_{(\text{aq})}$  before being optionally being rinsed and inserted into a tip holder.

## Appendix B: Etching Circuit Diagrams

**Figure B.1: Circuit Diagram of DC Tip Etching Power Supply**

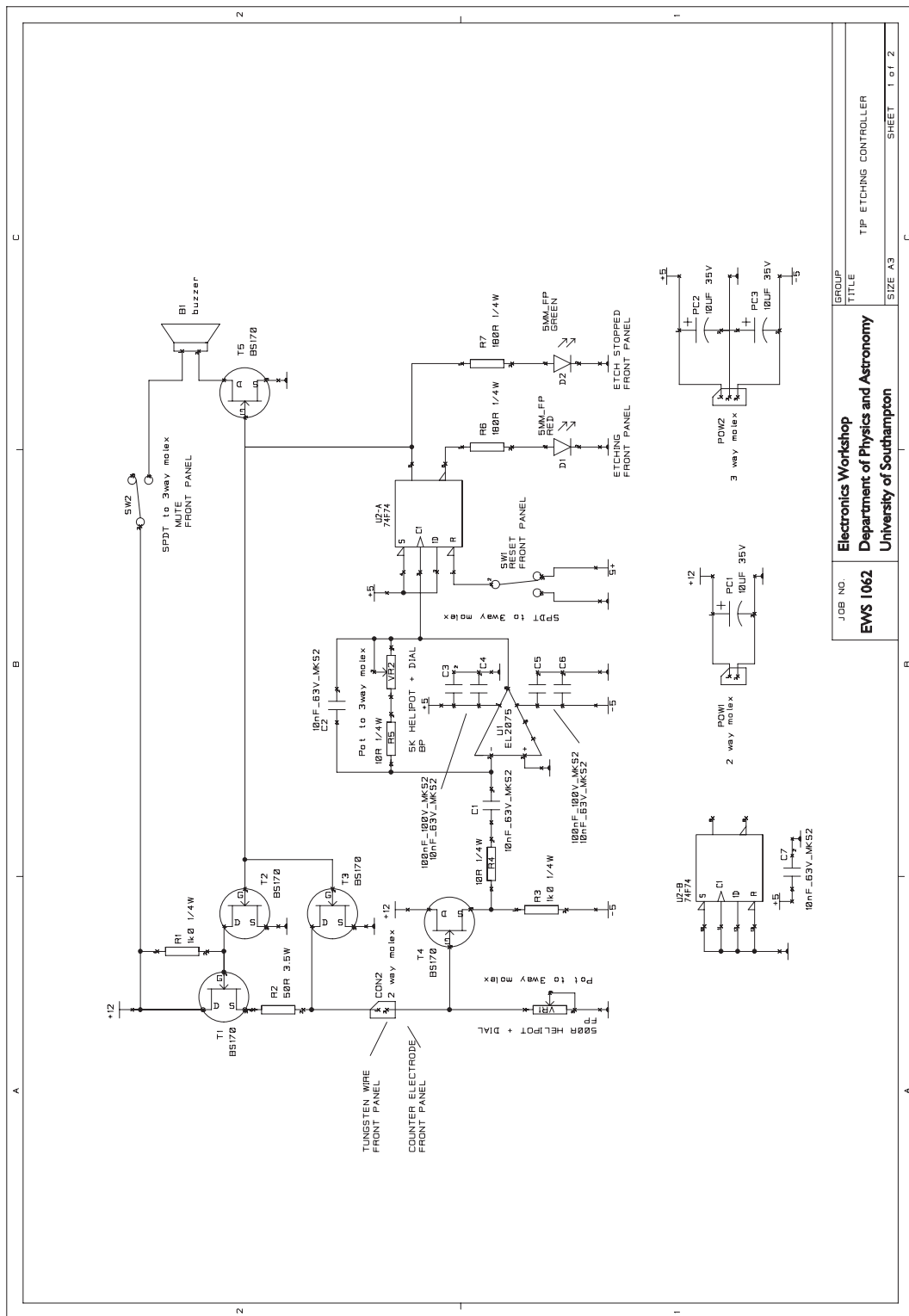
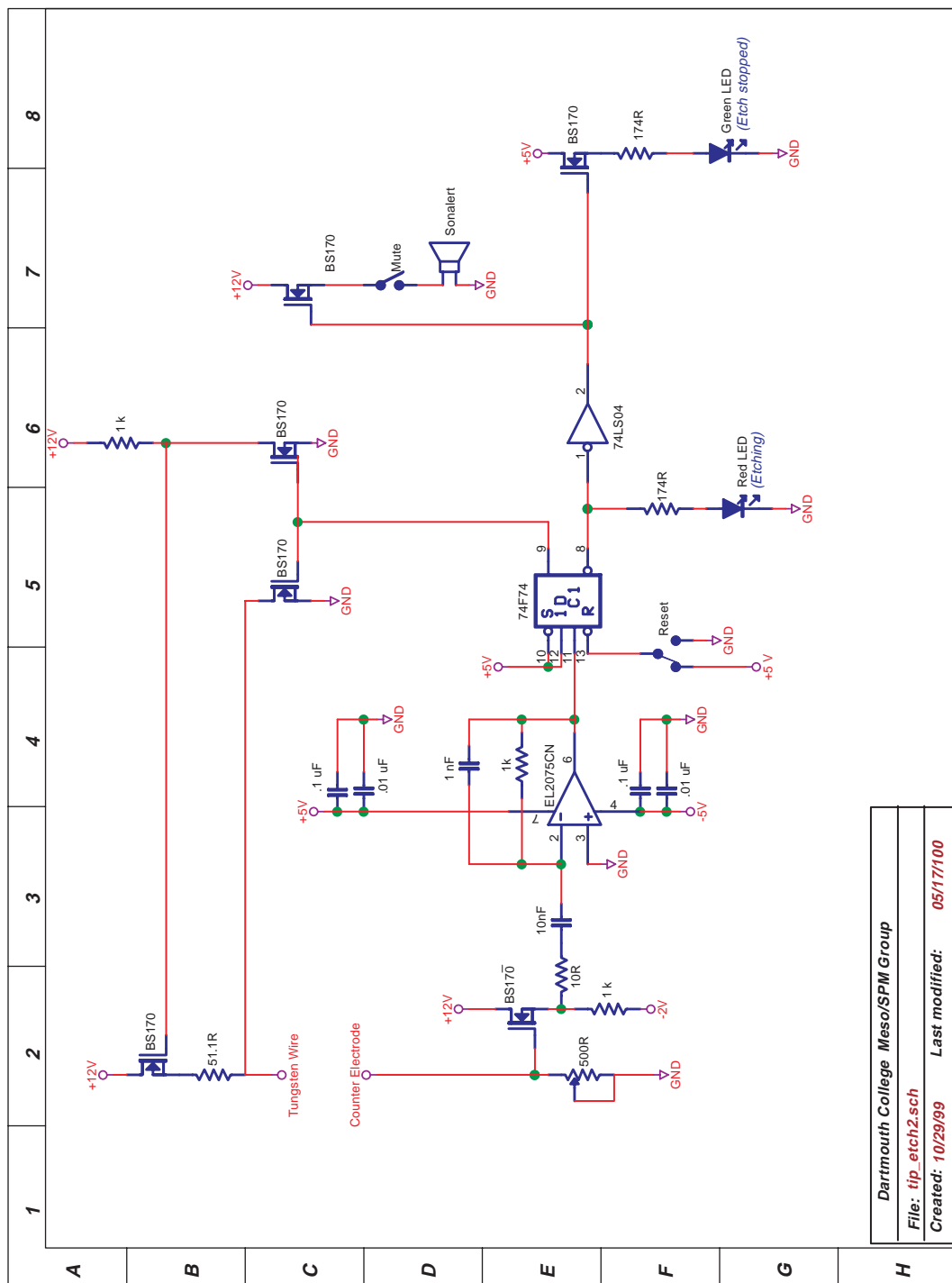


**Figure B.2: The circuit diagram from Dartmouth College, USA that was used as the basis for the circuit in Figure B.1**



## Appendix C: Microscope Images of the PPLN OPO Crystals

**Figure C.1 (Below Left):** A microscope image of PPLN2 (see Figure 2.20). The distance between the shorter markings at the bottom of the image is 100 $\mu$ m.

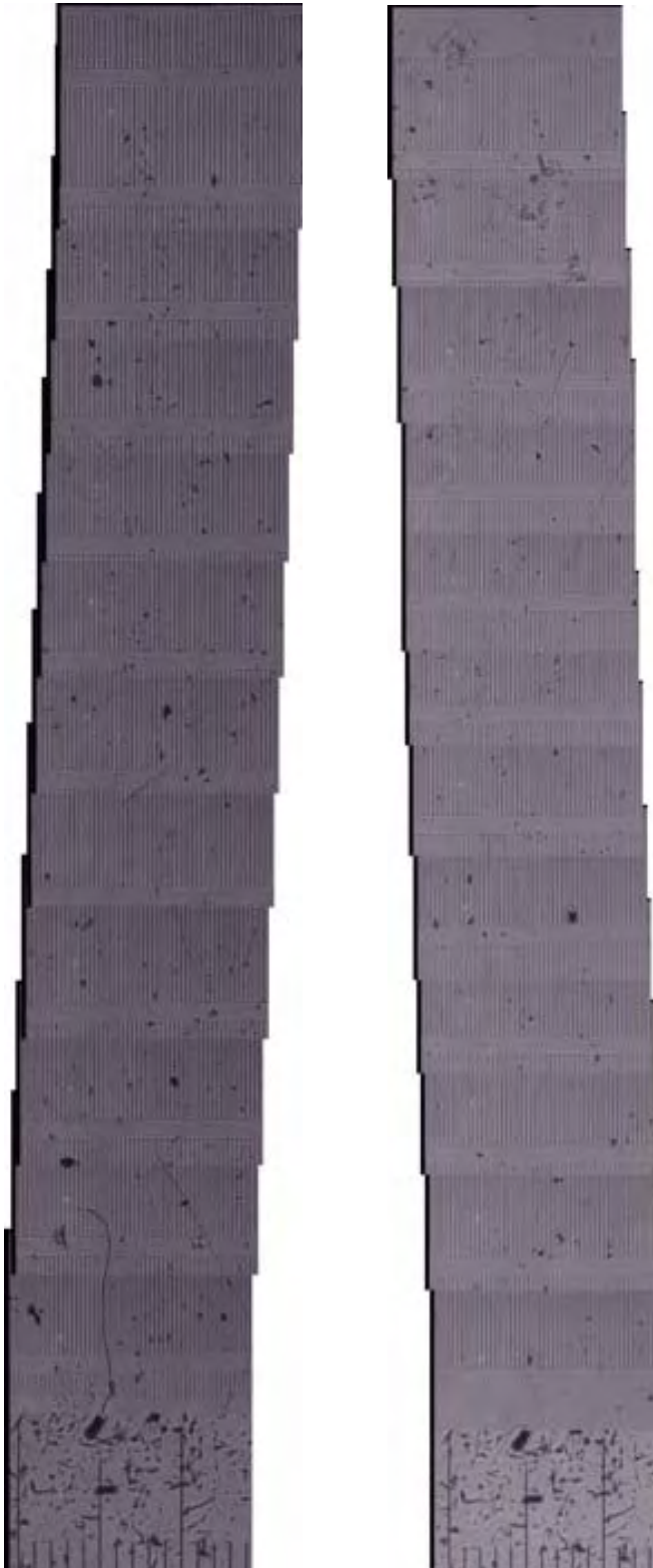


**Figure C.2 (Above Right):** A microscope image of PPLN1 (see Figure 2.19). The distance between the shorter markings at the bottom of the image is 100 $\mu$ m.

## Appendix D: MATLAB® Code for Processing Topographically Varying Scanning Tunnelling Spectroscopy Data

File 0:

```
%ldstm data processing
%function TopoStatsThresholdMoreOutputFiles_0_10x25x1000
%initial variables
FirstFile = 6
LastFile = 128
xpoints=10
ylines=25
image_y_size=400
image_x_size=400
TopoThreshold=25000
StatsThreshold=25
SpikeThreshold=5
fNumberOfSpecPoint=1000
bNumberOfSpecPoint=1000
StatisticalAnalysisStartPoint=2
%load x coordinates from 1st 2 csv files
FirstFilestr=num2str(FirstFile,2);
csvfname=strcat('m',FirstFilestr,'_ori.sf0.csv');
data=csvread(csvfname,1,0);
fx=data(:,1);
%fxWithLabel=csvread(csvfname,0,0,[0,0,1000,0]);
csvfname=strcat('m',FirstFilestr,'_ori.sb0.csv');
data=csvread(csvfname,1,0);
bx=data(:,1);
%calculate the number of files to load
fNumberOfFiles=LastFile-FirstFile+1; bNumberOfFiles=fNumberOfFiles;
%variables to count the number of 'bad' data sets
fSpecBadDataSetsCount=1; bSpecBadDataSetsCount=1;
%variables to list the failed data points
fBadDataSets=[]; bBadDataSets=[];
```

```

%variables to count the number of 'clean' grid points
fNumberCleanGridPoints=zeros(1,fNumberOfFiles);
bNumberCleanGridPoints=zeros(1,bNumberOfFiles);

%initialising blank variable for 'cleaner' total
fCleanerTotal=zeros(1,fNumberOfSpecPoint,fNumberOfFiles);
bCleanerTotal=zeros(1,1000,bNumberOfFiles);

fCleanerMean=zeros(fNumberOfSpecPoint,fNumberOfFiles+1);
fCleanerMean(:,1)=fx(:,1);

bCleanerMean=zeros(bNumberOfSpecPoint,bNumberOfFiles+1);
bCleanerMean(:,1)=bx(:,1);

%zstr_list=zeros(fnumberOfFiles);

size_fCleanerTotal=size(fCleanerTotal)
size_fx=size(fx)

%variables from Bill's program
specrow=ylines; speccol=xpoints;
col_spacing=image_x_size/xpoints; row_spacing=image_y_size/ylines;
spec=zeros(image_y_size,image_x_size);
for m=1:row_spacing:image_y_size
    for n=1:col_spacing:image_x_size
        spec(m,n)=1;
    end
end

fThresholdMatrix=zeros(image_y_size,image_x_size);
bThresholdMatrix=zeros(image_y_size,image_x_size);

%set up the column vectors for summing, ...
fSpecOn=zeros(fNumberOfSpecPoint,fNumberOfFiles+1);
bSpecOn=zeros(bNumberOfSpecPoint,bNumberOfFiles+1);

fSpecOn(:,1)=fx; bSpecOn(:,1)=bx;

fSpecOff=zeros(fNumberOfSpecPoint,fNumberOfFiles+1);
bSpecOff=zeros(bNumberOfSpecPoint,bNumberOfFiles+1);

fSpecOff(:,1)=fx; bSpecOff(:,1)=bx;

fSpecBoth=zeros(fNumberOfSpecPoint,fNumberOfFiles+1);
bSpecBoth=zeros(bNumberOfSpecPoint,bNumberOfFiles+1);

fSpecBoth(:,1)=fx; bSpecBoth(:,1)=bx;

fRandSpec=zeros(fNumberOfSpecPoint,fNumberOfFiles+1);
bRandSpec=zeros(bNumberOfSpecPoint,bNumberOfFiles+1);

fRandSpec(:,1)=fx; bRandSpec(:,1)=bx;

fNumberOn=zeros(fNumberOfFiles,1); fNumberOff=zeros(fNumberOfFiles,1);
bNumberOn=zeros(bNumberOfFiles,1); bNumberOff=zeros(bNumberOfFiles,1);

for z=1:1:(LastFile-FirstFile+1)

```

```

z=z

LoadingFileName=FirstFile+z-1

%convert file # to string for file reading

currentfilestr=num2str(FirstFile+z-1);

%Read forward spectroscopy file

ffname = strcat('m',currentfilestr,'_ori.sf0');

fid = fopen(ffname,'r','b');

fSpecData(:,:)= fread(fid,[250,1000],'int16');

%Read backward spectroscopy file

bfname = strcat('m',currentfilestr,'_ori.sb0');

fid = fopen(bfname,'r','b');

bSpecData(:,:)= fread(fid,[250,1000],'int16');

%Read forward topography file

ffname = strcat('m',currentfilestr,'_ori.tf0');

fid = fopen(ffname,'r','b');

fTopoData(:,:)=fread(fid,[400,400],'int16');

%Read backward topography file

bfname = strcat('m',currentfilestr,'_ori.tb0');

fid = fopen(bfname,'r','b');

bTopoData(:,:)=fread(fid,[400,400],'int16');

%Transpose TopoData to get the images the correct way round

fTopoData=fTopoData'; bTopoData=bTopoData';

%Mean correct topography files

fTotal=zeros(400); bTotal=zeros(400);

for x=1:400

    for y=1:400

        fTotal(x)=fTotal(x)+fTopoData(x,y);

        bTotal(x)=bTotal(x)+bTopoData(x,y);

    end

    fMean(x)=fTotal(x)/400;

    bMean(x)=bTotal(x)/400;

    for y=1:400

        fFlatterTopoData(x,y)=fTopoData(x,y)-fMean(x);

        bFlatterTopoData(x,y)=bTopoData(x,y)-bMean(x);

    end

end

%Convert to correct units

```

```

fSpecData = fSpecData * 50 / 32767; bSpecData = bSpecData * 50 / 32767;
%fSpecData(1,:,1)
%various size checks
[fNumberOfGridPoint,fNumberOfSpecPoint]=size(fSpecData);
[bNumberOfGridPoint,bNumberOfSpecPoint]=size(bSpecData);
%size(fSpecData)
%[bpoint,bspectrum]=size(bSpecData);
%plot graph of data before spike removal
figure(1);
subplot(2,2,1)
plot(fx,fSpecData(:,:,1))
subplot(2,2,3)
plot(bx,bSpecData(:,:,1))
%initialise the grid point counter
for GridPoint=1:1:fNumberOfGridPoint
    for SpecPoint=2:1:(fNumberOfSpecPoint-1)
        %logic to find spikes
        fbefore=fSpecData(GridPoint,SpecPoint-1);
        fmiddle=fSpecData(GridPoint,SpecPoint); fafter=fSpecData(GridPoint,SpecPoint+1);
        bbefore=bSpecData(GridPoint,SpecPoint-1);
        bmiddle=bSpecData(GridPoint,SpecPoint); bafter=bSpecData(GridPoint,SpecPoint+1);
        if ((abs(fmiddle-fbefore)>SpikeThreshold & abs(fafter-fmiddle)>SpikeThreshold)& ((fbefore-fmiddle>0&fafter-fmiddle>0)||((fbefore-fmiddle<0&fafter-fmiddle<0))))
            %change spike point to mean of adjacent points
            fSpecData(GridPoint,SpecPoint)=(fbefore+fafter)/2;
        else
            end
        if ((abs(bmiddle-bbefore)>SpikeThreshold & abs(bafter-bmiddle)>SpikeThreshold)& ((bbefore-bmiddle>0&bafter-bmiddle>0)||((bbefore-bmiddle<0&bafter-bmiddle<0))))
            %change spike point to mean of adjacent points
            bSpecData(GridPoint,SpecPoint)=(bbefore+bafter)/2;
        else
            end
        end
    end
%plot graphs of data after spike removal
figure(1);

```

```

subplot(2,2,2)
plot(fx,fSpecData(:,::))
subplot(2,2,4)
plot(bx,bSpecData(:,::))
%calculate mean & standard deviation
fStandardDev = std(fSpecData,1); fMean = mean(fSpecData);
bStandardDev = std(bSpecData,1); bMean = mean(bSpecData);
%calculate statistics matrix
for SpecPoint=1:1:fNumberOfSpecPoint;
    %SpecPoint=SpecPoint
    %size_fSpecData=size(fSpecData)
    %size_fmean=size(fmean)
    %size_fstandard=size(fstandard)
    fstats(:,SpecPoint)=(abs(fSpecData(:,SpecPoint)-
fMean(1,SpecPoint)))./fStandardDev(1,SpecPoint);
    bstats(:,SpecPoint)=(abs(bSpecData(:,SpecPoint)-
bMean(1,SpecPoint)))./bStandardDev(1,SpecPoint);
end
%First, smooth the image quickly to help with threshold identification
fSmoothenData=gauss_smooth(fFlatterTopoData,9,5);
bSmoothenData=gauss_smooth(bFlatterTopoData,9,5);
%set up for histograms
fReshape=reshape(fSmoothenData,image_x_size*image_y_size,1);
bReshape=reshape(bSmoothenData,image_x_size*image_y_size,1);
%get the histograms
[fn,f_x]=hist(fReshape,100); [bn,b_x]=hist(bReshape,100);
%plot the histograms
figure(2);
subplot(3,2,1),plot(f_x,fn)
figure(3);
subplot(3,2,1),plot(b_x,fn)
%plot the smoothed & original data
figure(2);
subplot(3,2,2), imagesc(fFlatterTopoData),axis xy, axis image,shading flat,
colorbar('vert'), colormap gray, title('Unsmoothed data')
subplot(3,2,3), imagesc(fSmoothenData),axis xy, axis image,shading flat,
colorbar('vert'), colormap gray, title('Smoothed data')
figure(3);

```

```

    subplot(3,2,2), imagesc(bFlatterTopoData),axis xy, axis image,shading flat,
    colorbar('vert'), colormap gray, title('Unsmoothed data')

    subplot(3,2,3), imagesc(bSmoothenData),axis xy,axis image,shading flat,
    colorbar('vert'), colormap gray, title('Smoothed data')

    %thresholding...

    %get the threshold value

    for i=1:image_y_size
        for j=1:image_x_size
            if (fSmoothenData(i,j)>TopoThreshold)
                fThresholdMatrix(i,j)=1;
            else
                fThresholdMatrix(i,j)=0;
            end
            if (bSmoothenData(i,j)>TopoThreshold)
                bThresholdMatrix(i,j)=1;
            else
                bThresholdMatrix(i,j)=0;
            end
        end
    end

    %plot up the thresholded data

    figure(2);

    subplot(3,2,4),imagesc(fThresholdMatrix),axis xy, axis image, colorbar('vert'),
    title('threshold map')

    figure(3);

    subplot(3,2,4),imagesc(bThresholdMatrix),axis xy, axis image, colorbar('vert'),
    title('threshold map')

    %now do the thresholding just by multiplying...

    fUsefulData=fThresholdMatrix.*spec; bUsefulData=bThresholdMatrix.*spec;

    %Now we convert useful_data back to a 10*25 array, and then use that as the index - how to
    do that?

    %use the inbuilt func find!!

    fs=sparse(fUsefulData); bs=sparse(bUsefulData);

    %plot up the data points we've selected

    figure(2)

    subplot(3,2,5),spy(fs),axis xy;title(strcat('threshold= ',num2str(TopoThreshold)))

    figure(3)

    subplot(3,2,5),spy(bs),axis xy;title(strcat('threshold= ',num2str(TopoThreshold)))

    [fRow,fCol,fRes]=find(fs); [bRow,bCol,bRes]=find(bs);

```

```

%put the sparse matrix back together by scaling the coords of the non-zero pts, and using the
spec grid dimensions

%Have to construct this differently!

fs2=sparse(((fRow-1)/(row_spacing)+1),(((fCol-
1)/col_spacing)+1),fRes,specrow,speccol);

bs2=sparse(((bRow-1)/(row_spacing)+1),(((bCol-
1)/col_spacing)+1),bRes,specrow,speccol);

%convert to a full array??? after dividing by spacings, which are specrow/image_size and
speccol/image_size

%now make that back into a regular array

fSmallSpec=full(fs2); bSmallSpec=full(bs2);

%ok - this is now the small matrix of zeros and ones we want, in (row,col) format

%possibility that these matrices will need to be transposed to get the indexing to work

fSmallSpec=fSmallSpec'; bSmallSpec=bSmallSpec';

%check out the number of useful spectra..... 

NumberUsefulForwardSpectra=size(fRes);
NumberUsefulBackwardSpectra=size(bRes);

%process the data with respect to topographical thresholds

GridPoint=1;

for GridPoint=1:1:fNumberOfGridPoint

    %process the data with respect to topographical threshold

    if fSmallSpec(GridPoint)==1
        fSpecOn(:,z+1)=fSpecOn(:,z+1)+fSpecData(GridPoint,:);
        fNumberOn(z)=fNumberOn(z)+1;
        fDataSetsOn(1,sum(fNumberOn))=GridPoint;
        fDataSetsOn(2,sum(fNumberOn))=z;
    else
        fSpecOff(:,z+1)=fSpecOff(:,z+1)+fSpecData(GridPoint,:);
        fNumberOff(z)=fNumberOff(z)+1;
        fDataSetsOff(1,sum(fNumberOff))=GridPoint;
        fDataSetsOff(2,sum(fNumberOff))=z;
    end
    fSpecBoth(:,z+1)=fSpecBoth(:,z+1)+fSpecData(GridPoint,:);

    %Process the data with respect to statistical threshold

    SpecPoint=StatisticalAnalysisStartPoint;

    while SpecPoint<=fNumberOfSpecPoint

        if (fstats(GridPoint,SpecPoint)<StatsThreshold)
            if SpecPoint==fNumberOfSpecPoint

                %record the fact that this grid point has passed the threshold test
                %size(fCleanerTotal)
            end
        end
    end
end

```

```

%size(fSpecData)
%fSpecData(GridPoint,SpecPoint,z)=fSpecData(GridPoint,SpecPoint,z)
fCleanerTotal(1,:,z)=fCleanerTotal(1,:,z)+fSpecData(GridPoint,:);
%add 1 to the total number of files used
fNumberCleanGridPoints(z)=fNumberCleanGridPoints(z)+1;
end
elseif (fstats(GridPoint,SpecPoint)>StatsThreshold)
    %record bad data grid point
    fBadDataSets(1,fBadSpecDataSetsCount)=GridPoint;
    fBadDataSets(2,fBadSpecDataSetsCount)=SpecPoint;
    fBadDataSets(3,fBadSpecDataSetsCount)=z;
    fBadSpecDataSetsCount=fBadSpecDataSetsCount+1;
    %exit the loop
    %GridPoint=GridPoint
    SpecPoint=fNumberOfSpecPoint;
end
SpecPoint=SpecPoint+1;
end
if bSmallSpec(GridPoint)==1
    bSpecOn(:,z+1)=bSpecOn(:,z+1)+bSpecData(GridPoint,:)';
    bNumberOn(z)=bNumberOn(z)+1;
    bDataSetsOn(1,sum(bNumberOn))=GridPoint;
    bDataSetsOn(2,sum(bNumberOn))=z;
else
    bSpecOff(:,z+1)=bSpecOff(:,z+1)+bSpecData(GridPoint,:)';
    bNumberOff(z)=bNumberOff(z)+1;
    bDataSetsOff(1,sum(bNumberOff))=GridPoint;
    bDataSetsOff(2,sum(bNumberOff))=z;
end
bSpecBoth(:,z+1)=bSpecBoth(:,z+1)+bSpecData(GridPoint,:)';
%Process the data with respect to statistical threshold
SpecPoint=StatisticalAnalysisStartPoint;
while SpecPoint<=bNumberOfSpecPoint;
    %[a,b]=size(bstats)
    %z=z
    %SpecPoint=SpecPoint
    %GridPoint=GridPoint
    %bstats(GridPoint,SpecPoint,z)=bstats(GridPoint,SpecPoint,z)

```

```

if (bstats(GridPoint,SpecPoint)<StatsThreshold)
    if SpecPoint==fNumberOfSpecPoint
        %record the fact that this grid point has passed the threshold test
        bCleanerTotal(1,:,z)=bCleanerTotal(1,:,z)+bSpecData(GridPoint,:);
        %add 1 to the total number of files used
        bNumberCleanGridPoints(z)=bNumberCleanGridPoints(z)+1;
    end
elseif (bstats(GridPoint,SpecPoint)>StatsThreshold);
    %record bad data grid point
    bBadDataSets(1,bBadSpecDataSetsCount)=GridPoint;
    bBadDataSets(2,bBadSpecDataSetsCount)=SpecPoint;
    bBadDataSets(3,bBadSpecDataSetsCount)=z;
    bBadSpecDataSetsCount=bBadSpecDataSetsCount+1;
    %exit the loop
    %GridPoint=GridPoint
    SpecPoint=fNumberOfSpecPoint;
end
SpecPoint=SpecPoint+1;
end
end
%create a random sum of that many columns:
%need some random numbers from 1-250
for i=1:1:fNumberOfSpecPoint
    %ceil just rounds up to next integer
    randindex=ceil(rand(1)*250);
    fRandSpec(:,z+1)=fRandSpec(:,z+1)+fSpecData(randindex,:)';
    %fTotalRandSpec=fTotalRandSpec+fSpecData(randindex,:);
end
for i=1:1:bNumberCleanGridPoints
    %ceil just rounds up to next integer
    randindex=ceil(rand(1)*250);
    bRandSpec(:,z+1)=bRandSpec(:,z+1)+bSpecData(randindex,:)';
    %bTotalRandSpec=bTotalRandSpec+bSpecData(randindex,:);
end
%plot the topographical processed data
figure(2)

```

```

    subplot(3,2,6), plot(fx,fSpecOn(:,z+1)/fNumberOn(z),'b'), hold on,
    plot(fx,fRandSpec(:,z+1)/fNumberOn(z),'r'),
    plot(fx,fSpecOff(:,z+1)/fNumberOff(z),'y'), plot(fx,fSpecBoth(:,z+1)/250,'g'),hold off;
    figure(3)

    subplot(3,2,6), plot(bx,bSpecOn(:,z+1)/bNumberOn(z),'b'), hold on,
    plot(bx,bRandSpec(:,z+1)/bNumberOn(z),'r'),
    plot(bx,bSpecOff(:,z+1)/bNumberOff(z),'y'), plot(bx,bSpecBoth(:,z+1)/250,'g'),hold off;

    %plot statistical data
    figure(4)

    subplot(1,2,1)
    plot(fx,fstats(:,::))
    subplot(1,2,2)
    plot(bx,bstats(:,::))

end

%Writing outputs to files
FirstFileString=num2str(FirstFile); LastFileString=num2str>LastFile);

TopoThreshString=num2str(TopoThreshold);
StatsThreshString=num2str(StatsThreshold);
SpikeThreshString=num2str(SpikeThreshold);

VariableString=strcat('Start=m',FirstFileString,'End=m',LastFileString,'TopoThresh=',TopoThreshString,'StatsThresh=',StatsThreshString,'SpikeThresh=',SpikeThreshString);

csvwrite(strcat('f0SpecOn',VariableString,'.csv'),fSpecOn)
csvwrite(strcat('f0SpecOff',VariableString,'.csv'),fSpecOff)
csvwrite(strcat('f0SpecBoth',VariableString,'.csv'),fSpecBoth)
csvwrite(strcat('f0RandSpec',VariableString,'.csv'),fRandSpec)
csvwrite(strcat('fNumberOn',VariableString,'.csv'),fNumberOn)
csvwrite(strcat('fNumberOff',VariableString,'.csv'),fNumberOff)
% csvwrite(strcat('f0NumberBoth',VariableString,'.csv'),fNumberBoth)
csvwrite(strcat('fDataSetsOn',VariableString,'.csv'),fDataSetsOn)
csvwrite(strcat('fDataSetsOff',VariableString,'.csv'),fDataSetsOff)
csvwrite(strcat('b0SpecOn',VariableString,'.csv'),bSpecOn)
csvwrite(strcat('b0SpecOff',VariableString,'.csv'),bSpecOff)
csvwrite(strcat('b0SpecBoth',VariableString,'.csv'),bSpecBoth)
csvwrite(strcat('b0RandSpec',VariableString,'.csv'),bRandSpec)
csvwrite(strcat('bNumberOn',VariableString,'.csv'),bNumberOn)
csvwrite(strcat('bNumberOff',VariableString,'.csv'),bNumberOff)
% csvwrite(strcat('b0NumberBoth',VariableString,'.csv'),bNumberBoth)
csvwrite(strcat('bDataSetsOn',VariableString,'.csv'),bDataSetsOn)

```

```

csvwrite(strcat('bDataSetsOff',VariableString,'.csv'),bDataSetsOff)
csvwrite(strcat('f0TotalCleanerMeans',VariableString,'.csv'),fCleanerMean)
csvwrite(strcat('f0#CleanGridPoints',VariableString,'.csv'),(fNumberCleanGridPoints))
csvwrite(strcat('b0TotalCleanerMeans',VariableString,'.csv'),bCleanerMean)
csvwrite(strcat('b0#CleanGridPoints',VariableString,'.csv'),(bNumberCleanGridPoints))
csvwrite(strcat('f0BadDataSets',VariableString,'.csv'),fBadDataSets)
csvwrite(strcat('b0BadDataSets',VariableString,'.csv'),bBadDataSets)

%Removing x coordinates from variables

fSpecOn(:,1)=[]; fSpecOff(:,1)=[]; fSpecBoth(:,1)=[]; fRandSpec(:,1)=[];
bSpecOn(:,1)=[]; bSpecOff(:,1)=[]; bSpecBoth(:,1)=[]; bRandSpec(:,1)=[];
size_fSpecOn=size(fSpecOn)

%Calculating totals

fTotalSpecOn=sum(fSpecOn,2); fTotalSpecOff=sum(fSpecOff,2);
fTotalSpecBoth=sum(fSpecBoth,2); fTotalRandSpec=sum(fRandSpec,2);

bTotalSpecOn=sum(bSpecOn,2); bTotalSpecOff=sum(bSpecOff,2);
bTotalSpecBoth=sum(bSpecBoth,2); bTotalRandSpec=sum(bRandSpec,2);

size_fTotalSpecOn=size(fTotalSpecOn)
size_fTotalSpecOff=size(fTotalSpecOff)
size_fTotalSpecBoth=size(fTotalSpecBoth)
size_fTotalRandSpec=size(fTotalRandSpec)

fTotalNumberOff=sum(fNumberOff)
fTotalNumberOn=sum(fNumberOn)
bTotalNumberOff=sum(bNumberOff)
bTotalNumberOn=sum(bNumberOn)

%plot the total topographical processed data

figure(5)

subplot(2,1,1), plot(fx,fTotalSpecBoth/(250*z),'g'), hold on,
plot(fx,fTotalSpecOff/fTotalNumberOff,'y'),
plot(fx,fTotalSpecOn/fTotalNumberOn,'b'), plot(fx,fTotalRandSpec/fTotalNumberOn,'r'),
hold off;

subplot(2,1,2), plot(bx,bTotalSpecBoth/(250*z),'g'), hold on,
plot(bx,bTotalSpecOff/bTotalNumberOff,'y'),
plot(bx,bTotalSpecOn/bTotalNumberOn,'b'),
plot(bx,bTotalRandSpec/bTotalNumberOn,'r'), hold off;

```

File 1:

```

%ldstm data processing
%function TopoStatsThresholdMoreOutputFiles_1_10x25x1000
%initial variables

```

```

FirstFile = 6
LastFile = 128
xpoints=10
ylines=25
image_y_size=400
image_x_size=400
TopoThreshold=25000
StatsThreshold=25
SpikeThreshold=5
fNumberOfSpecPoint=1000
bNumberOfSpecPoint=1000
StatisticalAnalysisStartPoint=2
%load x coordinates from 1st 2 csv files
FirstFilestr=num2str(FirstFile,2);
csvfname=strcat('m',FirstFilestr,'_ori.sf1.csv');
data=csvread(csvfname,1,0);
fx=data(:,1);
%fxWithLabel=csvread(csvfname,0,0,[0,0,1000,0]);
csvfname=strcat('m',FirstFilestr,'_ori.sb1.csv');
data=csvread(csvfname,1,0);
bx=data(:,1);
%calculate the number of files to load
fNumberOfFiles=LastFile-FirstFile+1; bNumberOfFiles=fNumberOfFiles;
%variables to count the number of 'bad' data sets
fSpecBadDataSetsCount=1; bSpecBadDataSetsCount=1;
%variables to list the failed data points
fBadDataSets=[]; bBadDataSets=[];
%variables to count the number of 'clean' grid points
fNumberCleanGridPoints=zeros(1,fNumberOfFiles);
bNumberCleanGridPoints=zeros(1,bNumberOfFiles);
%initialising blank variable for 'cleaner' total
fCleanerTotal=zeros(1,fNumberOfSpecPoint,fNumberOfFiles);
bCleanerTotal=zeros(1,1000,bNumberOfFiles);
fCleanerMean=zeros(fNumberOfSpecPoint,fNumberOfFiles+1);
fCleanerMean(:,1)=fx(:,1);
bCleanerMean=zeros(bNumberOfSpecPoint,bNumberOfFiles+1);
bCleanerMean(:,1)=bx(:,1);
%zstr_list=zeros(fnumberOfFiles);
size_fCleanerTotal=size(fCleanerTotal)

```

```

size_fx=size(fx)

%variables from Bill's program

specrow=ylines; speccol=xpoints;
col_spacing=image_x_size/xpoints; row_spacing=image_y_size/ylines;
spec=zeros(image_y_size,image_x_size);
for m=1:row_spacing:image_y_size
    for n=1:col_spacing:image_x_size
        spec(m,n)=1;
    end
end

fThresholdMatrix=zeros(image_y_size,image_x_size);
bThresholdMatrix=zeros(image_y_size,image_x_size);

%set up the column vectors for summing, ...
fSpecOn=zeros(fNumberOfSpecPoint,fNumberOfFiles+1);
bSpecOn=zeros(bNumberOfSpecPoint,bNumberOfFiles+1);

fSpecOn(:,1)=fx; bSpecOn(:,1)=bx;

fSpecOff=zeros(fNumberOfSpecPoint,fNumberOfFiles+1);
bSpecOff=zeros(bNumberOfSpecPoint,bNumberOfFiles+1);

fSpecOff(:,1)=fx; bSpecOff(:,1)=bx;

fSpecBoth=zeros(fNumberOfSpecPoint,fNumberOfFiles+1);
bSpecBoth=zeros(bNumberOfSpecPoint,bNumberOfFiles+1);

fSpecBoth(:,1)=fx; bSpecBoth(:,1)=bx;

fRandSpec=zeros(fNumberOfSpecPoint,fNumberOfFiles+1);
bRandSpec=zeros(bNumberOfSpecPoint,bNumberOfFiles+1);

fRandSpec(:,1)=fx; bRandSpec(:,1)=bx;

fNumberOn=zeros(fNumberOfFiles,1); fNumberOff=zeros(fNumberOfFiles,1);
bNumberOn=zeros(bNumberOfFiles,1); bNumberOff=zeros(bNumberOfFiles,1);

for z=1:1:(LastFile-FirstFile+1)
    z=z

    LoadingFileName=FirstFile+z-1

    %convert file # to string for file reading
    currentfilestr=num2str(FirstFile+z-1);

    %Read forward spectroscopy file
    fname = strcat('m',currentfilestr,'_ori.sf1');

    fid = fopen(fname,'r','b');

    fSpecData(:,:)= fread(fid,[250,1000],'int16');

    %Read backward spectroscopy file
    bfname = strcat('m',currentfilestr,'_ori.sb1');

    fid = fopen(bfname,'r','b');

    bSpecData(:,:)= fread(fid,[250,1000],'int16');

```

```

%Read forward topography file
ffname = strcat('m',currentfilestr,'_ori.tf0');
fid = fopen(ffname,'r','b');
fTopoData(:,:)=fread(fid,[400,400],'int16');

%Read backward topography file
bfname = strcat('m',currentfilestr,'_ori.tb0');
fid = fopen(bfname,'r','b');
bTopoData(:,:)=fread(fid,[400,400],'int16');

%Transpose TopoData to get the images the correct way round
fTopoData=fTopoData'; bTopoData=bTopoData';

%Mean correct topography files
fTotal=zeros(400); bTotal=zeros(400);
for x=1:400
    for y=1:400
        fTotal(x)=fTotal(x)+fTopoData(x,y);
        bTotal(x)=bTotal(x)+bTopoData(x,y);
    end
    fMean(x)=fTotal(x)/400;
    bMean(x)=bTotal(x)/400;
    for y=1:400
        fFlatterTopoData(x,y)=fTopoData(x,y)-fMean(x);
        bFlatterTopoData(x,y)=bTopoData(x,y)-bMean(x);
    end
end

%Convert to correct units
fSpecData = fSpecData * 10 / 32767; bSpecData = bSpecData * 10 / 32767;
%fSpecData(1,:,:)
%various size checks
[fNumberOfGridPoint,fNumberOfSpecPoint]=size(fSpecData);
[bNumberOfGridPoint,bNumberOfSpecPoint]=size(bSpecData);
%size(fSpecData)
%[bpoint,bspectrum]=size(bSpecData);
%plot graph of data before spike removal
figure(1);
subplot(2,2,1)
plot(fx,fSpecData(:,:))
subplot(2,2,3)
plot(bx,bSpecData(:,:))

```

```

%initialise the grid point counter
for GridPoint=1:1:fNumberOfGridPoint
    for SpecPoint=2:1:(fNumberOfSpecPoint-1)
        %logic to find spikes
        fbefore=fSpecData(GridPoint,SpecPoint-1);
        fmiddle=fSpecData(GridPoint,SpecPoint); fafter=fSpecData(GridPoint,SpecPoint+1);
        bbefore=bSpecData(GridPoint,SpecPoint-1);
        bmiddle=bSpecData(GridPoint,SpecPoint); bafter=bSpecData(GridPoint,SpecPoint+1);
        if ((abs(fmiddle-fbefore)>SpikeThreshold & abs(fafter-fmiddle)>SpikeThreshold)& ((fbefore-fmiddle>0&fafter-fmiddle>0)|(fbefore-fmiddle<0&fafter-fmiddle<0)))
            %change spike point to mean of adjacent points
            fSpecData(GridPoint,SpecPoint)=(fbefore+fafter)/2;
        else
            end
        if ((abs(bmiddle-bbefore)>SpikeThreshold & abs(bafter-bmiddle)>SpikeThreshold)& ((bbefore-bmiddle>0&bafter-bmiddle>0)|(bbefore-bmiddle<0&bafter-bmiddle<0)))
            %change spike point to mean of adjacent points
            bSpecData(GridPoint,SpecPoint)=(bbefore+bafter)/2;
        else
            end
        end
    end
    %plot graphs of data after spike removal
    figure(1);
    subplot(2,2,2)
    plot(fx,fSpecData(:, :))
    subplot(2,2,4)
    plot(bx,bSpecData(:, :))

    %calculate mean & standard deviation
    fStandardDev = std(fSpecData,1); fMean = mean(fSpecData);
    bStandardDev = std(bSpecData,1); bMean = mean(bSpecData);
    %calculate statistics matrix
    for SpecPoint=1:1:fNumberOfSpecPoint;
        %SpecPoint=SpecPoint
        %size_fSpecData=size(fSpecData)
        %size_fmean=size(fmean)
        %size_fstandard=size(fstandard)

```

```

fstats(:,SpecPoint)=(abs(fSpecData(:,SpecPoint)-
fMean(1,SpecPoint)))./fStandardDev(1,SpecPoint);

bstats(:,SpecPoint)=(abs(bSpecData(:,SpecPoint)-
bMean(1,SpecPoint)))./bStandardDev(1,SpecPoint);

end

%First, smooth the image quickly to help with threshold identification

fSmoothenData=gauss_smooth(fFlatterTopoData,9,5);
bSmoothenData=gauss_smooth(bFlatterTopoData,9,5);

%set up for histograms

fReshape=reshape(fSmoothenData,image_x_size*image_y_size,1);
bReshape=reshape(bSmoothenData,image_x_size*image_y_size,1);

%get the histograms

[fn,f_x]=hist(fReshape,100); [bn,b_x]=hist(bReshape,100);

%plot the histograms

figure(2);

subplot(3,2,1),plot(f_x,fn)

figure(3);

subplot(3,2,1),plot(b_x,fn)

%plot the smoothed & original data

figure(2);

subplot(3,2,2), imagesc(fFlatterTopoData),axis xy, axis image,shading flat,
colorbar('vert'), colormap gray, title('Unsmoothed data')

subplot(3,2,3), imagesc(fSmoothenData),axis xy,axis image,shading flat,
colorbar('vert'), colormap gray, title('Smoothed data')

figure(3);

subplot(3,2,2), imagesc(bFlatterTopoData),axis xy, axis image,shading flat,
colorbar('vert'), colormap gray, title('Unsmoothed data')

subplot(3,2,3), imagesc(bSmoothenData),axis xy,axis image,shading flat,
colorbar('vert'), colormap gray, title('Smoothed data')

%thresholding...

%get the threshold value

for i=1:image_y_size

for j=1:image_x_size

if (fSmoothenData(i,j)>TopoThreshold)

fThresholdMatrix(i,j)=1;

else

fThresholdMatrix(i,j)=0;

end

if (bSmoothenData(i,j)>TopoThreshold)

bThresholdMatrix(i,j)=1;

else

```

```

bThresholdMatrix(i,j)=0;
end
end
end
%plot up the thresholded data
figure(2);

subplot(3,2,4),imagesc(fThresholdMatrix),axis xy, axis image, colorbar('vert'),
title('threshold map')

figure(3);

subplot(3,2,4),imagesc(bThresholdMatrix),axis xy, axis image, colorbar('vert'),
title('threshold map')

%now do the thresholding just by multiplying...
fUsefulData=fThresholdMatrix.*spec; bUsefulData=bThresholdMatrix.*spec;

%Now we convert useful_data back to a 10*25 array, and then use that as the index - how to
do that?

%use the inbuilt func find!!
fs=sparse(fUsefulData); bs=sparse(bUsefulData);

%plot up the data points we've selected
figure(2)
subplot(3,2,5),spy(fs),axis xy;title(strcat('threshold= ',num2str(TopoThreshold)))
figure(3)
subplot(3,2,5),spy(bs),axis xy;title(strcat('threshold= ',num2str(TopoThreshold)))
[fRow,fCol,fRes]=find(fs); [bRow,bCol,bRes]=find(bs);

%put the sparse matrix back together by scaling the coords of the non-zero pts, and using the
spec grid dimensions

%Have to construct this differently!
fs2=sparse(((fRow-1)/(row_spacing)+1),(((fCol-
1)/col_spacing)+1),fRes,specrow,speccol);
bs2=sparse(((bRow-1)/(row_spacing)+1),(((bCol-
1)/col_spacing)+1),bRes,specrow,speccol);

%convert to a full array??? after dividing by spacings, which are specrow/image_size and
speccol/image_size

%now make that back into a regular array
fSmallSpec=full(fs2); bSmallSpec=full(bs2);

%ok - this is now the small matrix of zeros and ones we want, in (row,col) format

%possibility that these matrices will need to be transposed to get the indexing to work
fSmallSpec=fSmallSpec'; bSmallSpec=bSmallSpec';

%check out the number of useful spectra.....
NumberUsefulForwardSpectra=size(fRes);
NumberUsefulBackwardSpectra=size(bRes);

%process the data with respect to topographical thresholds

```

```

GridPoint=1;
for GridPoint=1:1:fNumberOfGridPoint
    %process the data with respect to topographical threshold
    if fSmallSpec(GridPoint)==1
        fSpecOn(:,z+1)=fSpecOn(:,z+1)+fSpecData(GridPoint,:);
        fNumberOn(z)=fNumberOn(z)+1;
        fDataSetsOn(1,sum(fNumberOn))=GridPoint;
        fDataSetsOn(2,sum(fNumberOn))=z;
    else
        fSpecOff(:,z+1)=fSpecOff(:,z+1)+fSpecData(GridPoint,:);
        fNumberOff(z)=fNumberOff(z)+1;
        fDataSetsOff(1,sum(fNumberOff))=GridPoint;
        fDataSetsOff(2,sum(fNumberOff))=z;
    end
    fSpecBoth(:,z+1)=fSpecBoth(:,z+1)+fSpecData(GridPoint,:);
    %Process the data with respect to statistical threshold
    SpecPoint=StatisticalAnalysisStartPoint;
    while SpecPoint<=fNumberOfSpecPoint
        if (fstats(GridPoint,SpecPoint)<StatsThreshold)
            if SpecPoint==fNumberOfSpecPoint
                %record the fact that this grid point has passed the threshold test
                %size(fCleanerTotal)
                %size(fSpecData)
                %fSpecData(GridPoint,SpecPoint,z)=fSpecData(GridPoint,SpecPoint,z)
                fCleanerTotal(1,:,z)=fCleanerTotal(1,:,z)+fSpecData(GridPoint,:);
                %add 1 to the total number of files used
                fNumberCleanGridPoints(z)=fNumberCleanGridPoints(z)+1;
            end
        elseif (fstats(GridPoint,SpecPoint)>StatsThreshold)
            %record bad data grid point
            fBadDataSets(1,fBadSpecDataSetsCount)=GridPoint;
            fBadDataSets(2,fBadSpecDataSetsCount)=SpecPoint;
            fBadDataSets(3,fBadSpecDataSetsCount)=z;
            fBadSpecDataSetsCount=fBadSpecDataSetsCount+1;
            %exit the loop
            %GridPoint=GridPoint
            SpecPoint=fNumberOfSpecPoint;
        end
        SpecPoint=SpecPoint+1;
    end
end

```

```

end

if bSmallSpec(GridPoint)==1
bSpecOn(:,z+1)=bSpecOn(:,z+1)+bSpecData(GridPoint,:)';
bNumberOn(z)=bNumberOn(z)+1;
bDataSetsOn(1,sum(bNumberOn))=GridPoint;
bDataSetsOn(2,sum(bNumberOn))=z;

else bSpecOff(:,z+1)=bSpecOff(:,z+1)+bSpecData(GridPoint,:)';
bNumberOff(z)=bNumberOff(z)+1;
bDataSetsOff(1,sum(bNumberOff))=GridPoint;
bDataSetsOff(2,sum(bNumberOff))=z;
end

bSpecBoth(:,z+1)=bSpecBoth(:,z+1)+bSpecData(GridPoint,:');

%Process the data with respect to statistical threshold

SpecPoint=StatisticalAnalysisStartPoint;
while SpecPoint<=bNumberOfSpecPoint;

% [a,b]=size(bstats)

%z=z

%SpecPoint=SpecPoint
%GridPoint=GridPoint

%bstats(GridPoint,SpecPoint,z)=bstats(GridPoint,SpecPoint,z)

if (bstats(GridPoint,SpecPoint)<StatsThreshold)

if SpecPoint==fNumberOfSpecPoint

%record the fact that this grid point has passed the threshold test
bCleanerTotal(1,:,z)=bCleanerTotal(1,:,z)+bSpecData(GridPoint,:);

%add 1 to the total number of files used
bNumberCleanGridPoints(z)=bNumberCleanGridPoints(z)+1;

end

elseif (bstats(GridPoint,SpecPoint)>StatsThreshold);

%record bad data grid point
bBadDataSets(1,bBadSpecDataSetsCount)=GridPoint;
bBadDataSets(2,bBadSpecDataSetsCount)=SpecPoint;
bBadDataSets(3,bBadSpecDataSetsCount)=z;
bBadSpecDataSetsCount=bBadSpecDataSetsCount+1;

%exit the loop
%GridPoint=GridPoint

SpecPoint=fNumberOfSpecPoint;

end

SpecPoint=SpecPoint+1;

```

```

    end
end

%create a random sum of that many columns:
%need some random numbers from 1-250
for i=1:1:fNumberOn(z)
    %ceil just rounds up to next integer
    randindex=ceil(rand(1)*250);
    fRandSpec(:,z+1)=fRandSpec(:,z+1)+fSpecData(randindex,:);
    %fTotalRandSpec=fTotalRandSpec+fSpecData(randindex,:);
end

for i=1:1:bNumberOn(z)
    %ceil just rounds up to next integer
    randindex=ceil(rand(1)*250);
    bRandSpec(:,z+1)=bRandSpec(:,z+1)+bSpecData(randindex,:);
    %bTotalRandSpec=bTotalRandSpec+bSpecData(randindex,:);
end

%plot the topographical processed data
figure(2)
subplot(3,2,6), plot(fx,fSpecOn(:,z+1)/fNumberOn(z),'b'), hold on,
plot(fx,fRandSpec(:,z+1)/fNumberOn(z),'r'),
plot(fx,fSpecOff(:,z+1)/fNumberOff(z),'y'), plot(fx,fSpecBoth(:,z+1)/250,'g'),hold off;
figure(3)
subplot(3,2,6), plot(bx,bSpecOn(:,z+1)/bNumberOn(z),'b'), hold on,
plot(bx,bRandSpec(:,z+1)/bNumberOn(z),'r'),
plot(bx,bSpecOff(:,z+1)/bNumberOff(z),'y'), plot(bx,bSpecBoth(:,z+1)/250,'g'),hold off;
%plot statistical data
figure(4)
subplot(1,2,1)
plot(fx,fstats(:,:,1))
subplot(1,2,2)
plot(bx,bstats(:,:,1))

end

%Writing outputs to files
FirstFileString=num2str(FirstFile); LastFileString=num2str>LastFile);
TopoThreshString=num2str(TopoThreshold);
StatsThreshString=num2str(StatsThreshold);
SpikeThreshString=num2str(SpikeThreshold);

VariableString=strcat('Start=m',FirstFileString,'End=m',LastFileString,'TopoThresh=',Top
oThreshString,'StatsThresh=',StatsThreshString,'SpikeThresh=',SpikeThreshString);

```

```

csvwrite(strcat('f1SpecOn',VariableString,'.csv'),fSpecOn)
csvwrite(strcat('f1SpecOff',VariableString,'.csv'),fSpecOff)
csvwrite(strcat('f1SpecBoth',VariableString,'.csv'),fSpecBoth)
csvwrite(strcat('f1RandSpec',VariableString,'.csv'),fRandSpec)
csvwrite(strcat('fNumberOn',VariableString,'.csv'),fNumberOn)
csvwrite(strcat('fNumberOff',VariableString,'.csv'),fNumberOff)
% csvwrite(strcat('fNumberBoth',VariableString,'.csv'),fNumberBoth)
csvwrite(strcat('fDataSetsOn',VariableString,'.csv'),fDataSetsOn)
csvwrite(strcat('fDataSetsOff',VariableString,'.csv'),fDataSetsOff)
csvwrite(strcat('b1SpecOn',VariableString,'.csv'),bSpecOn)
csvwrite(strcat('b1SpecOff',VariableString,'.csv'),bSpecOff)
csvwrite(strcat('b1SpecBoth',VariableString,'.csv'),bSpecBoth)
csvwrite(strcat('b1RandSpec',VariableString,'.csv'),bRandSpec)
csvwrite(strcat('bNumberOn',VariableString,'.csv'),bNumberOn)
csvwrite(strcat('bNumberOff',VariableString,'.csv'),bNumberOff)
% csvwrite(strcat('bNumberBoth',VariableString,'.csv'),bNumberBoth)
csvwrite(strcat('bDataSetsOn',VariableString,'.csv'),bDataSetsOn)
csvwrite(strcat('bDataSetsOff',VariableString,'.csv'),bDataSetsOff)
csvwrite(strcat('f1TotalCleanerMeans',VariableString,'.csv'),fCleanerMean)
csvwrite(strcat('f1#CleanGridPoints',VariableString,'.csv'),(fNumberCleanGridPoints))
csvwrite(strcat('b1TotalCleanerMeans',VariableString,'.csv'),bCleanerMean)
csvwrite(strcat('b1#CleanGridPoints',VariableString,'.csv'),(bNumberCleanGridPoints))
csvwrite(strcat('f1BadDataSets',VariableString,'.csv'),fBadDataSets)
csvwrite(strcat('b1BadDataSets',VariableString,'.csv'),bBadDataSets)

% Removing x coordinates from variables
fSpecOn(:,1)=[]; fSpecOff(:,1)=[]; fSpecBoth(:,1)=[]; fRandSpec(:,1)=[];
bSpecOn(:,1)=[]; bSpecOff(:,1)=[]; bSpecBoth(:,1)=[]; bRandSpec(:,1)=[];
size_fSpecOn=size(fSpecOn)
% Calculating totals
fTotalSpecOn=sum(fSpecOn,2); fTotalSpecOff=sum(fSpecOff,2);
fTotalSpecBoth=sum(fSpecBoth,2); fTotalRandSpec=sum(fRandSpec,2);
bTotalSpecOn=sum(bSpecOn,2); bTotalSpecOff=sum(bSpecOff,2);
bTotalSpecBoth=sum(bSpecBoth,2); bTotalRandSpec=sum(bRandSpec,2);
size_fTotalSpecOn=size(fTotalSpecOn)
size_fTotalSpecOff=size(fTotalSpecOff)
size_fTotalSpecBoth=size(fTotalSpecBoth)
size_fTotalRandSpec=size(fTotalRandSpec)
fTotalNumberOff=sum(fNumberOff)

```

```
fTotalNumberOn=sum(fNumberOn)
bTotalNumberOff=sum(bNumberOff)
bTotalNumberOn=sum(bNumberOn)

%plot the total topographical processed data
figure(5)
subplot(2,1,1), plot(fx,fTotalSpecBoth/(250*z),'g'), hold on,
plot(fx,fTotalSpecOff/fTotalNumberOff,'y'),
plot(fx,fTotalSpecOn/fTotalNumberOn,'b'), plot(fx,fTotalRandSpec/fTotalNumberOn,'r'),
hold off;
subplot(2,1,2), plot(bx,bTotalSpecBoth/(250*z),'g'), hold on,
plot(bx,bTotalSpecOff/bTotalNumberOff,'y'),
plot(bx,bTotalSpecOn/bTotalNumberOn,'b'),
plot(bx,bTotalRandSpec/bTotalNumberOn,'r'), hold off;
```

## Appendix E: MATLAB® Code for Processing Scanning Tunnelling Spectroscopy Data

File 0:

```
%ldstm data processing
%function biggerdatapro(firstfname,lastfname)
firstfile =19
lastfile =21
StatsThreshold=4
SpikeThresh=1
StartPointSpectroscopy=0.74999964
IncrementPointSpectroscopy=-0.0014954952
StatisticalAnalysisStartPoint=2
%load data
currentfile = firstfile;
%load x coordinates from 1st 2 csv files
    % firstfilestr=num2str(firstfile,2);
    % csvfname=strcat('m',firstfilestr,'_ori.sf0.csv');
    % data=csvread(csvfname,1,0);
for SpecPoint=1:1:1000
fx(SpecPoint)=StartPointSpectroscopy+((SpecPoint-1)*IncrementPointSpectroscopy);
    % csvfname=strcat('m',firstfilestr,'_ori.sb0.csv');
    % data=csvread(csvfname,1,0);
bx(SpecPoint)=StartPointSpectroscopy+((SpecPoint-1)*IncrementPointSpectroscopy);
end
fnumber_of_files=lastfile-firstfile+1;
bnumber_of_files=fnumber_of_files;
fdata_sets_count=1;
bdata_sets_count=1;
fBadDataSets=[];
bBadDataSets=[];
fNumberCleanGridPoints=zeros(1,fnumber_of_files);
bNumberCleanGridPoints=zeros(1,bnumber_of_files);
fcleaner_total=zeros(1,1000,fnumber_of_files);
bcleaner_total=zeros(1,1000,bnumber_of_files);
fCleanerMean=zeros(1000,fnumber_of_files+1);
```

```

fCleanerMean(:,1)=fx(:);
bCleanerMean=zeros(1000,bnumber_of_files+1);
bCleanerMean(:,1)=bx(:);
zstr_list=zeros(fnumber_of_files);
size_fcleaner_total=size(fcleaner_total)
size_fx=size(fx)
fBigData=[];
bBigData=[];
for z=1:1:(lastfile-firstfile+1)
    currentfilestr=num2str(firstfile+z-1);
    fname = strcat('m',currentfilestr,'_ori.sf0');
    fid = fopen(fname,'r','b');
    fdata(:, :) = fread(fid,[250,1000],'int16');
    size_fdata=size(fdata)
    bfname = strcat('m',currentfilestr,'_ori.sb0');
    fid = fopen(bfname,'r','b');
    bdata(:, :) = fread(fid,[250,1000],'int16');
    LoadingFileNumber=currentfile
    currentfile =currentfile+1;
    %size_fdata=size(fdata)
    %data=csvread(csvfname,0,0);
    %bxlist=data(:,1);
    %sizeofxdata=size(x)
    %Convert to correct units
    fdata = fdata * 50 / 32767;
    bdata = bdata * 50 / 32767;
    csvwrite(strcat(fname,'.csv'),fdata');
    csvwrite(strcat(bfname,'.csv'),bdata');
    %fdata(1,:,:)
    %calculate mean & standard deviation
    fstandard = std(fdata,1);
    %size_fstandard=size(fstandard)
    %size_fStandardDeviation=size(fStandardDeviation)
    fStandardDeviation(z,:)=fstandard;
    fmean = mean(fdata);
    %size_fmean=size(fmean)
    bstandard = std(bdata,1);

```

```

bStandardDeviation(z,:)=bstandard;
bmean = mean(bdata);
%various size checks
%size(bstandard)
%Size_bmean=size(bmean)
[fnumber_of_GridPoint,fnumber_of_SpecPoint]=size(fdata);
[bnumber_of_GridPoint,bnumber_of_SpecPoint]=size(bdata);
%size(fdata)
%[bpoint,bspectrum]=size(bdata);
z=z
%plot graph of data before spike removal
figure(1)
subplot(2,2,1)
plot(fx,fdata(:,,))
subplot(2,2,3)
plot(bx,bdata(:,,))
%initialise the grid point counter
for GridPoint=1:1:fnumber_of_GridPoint
    for SpecPoint=2:1:(fnumber_of_SpecPoint-1)
        %logic to find spikes
        %GridPoint=GridPoint
        %SpecPoint=SpecPoint
        %z=z
        fbefore=fdata(GridPoint,SpecPoint-1);
        fmiddle=fdata(GridPoint,SpecPoint);
        fafter=fdata(GridPoint,SpecPoint+1);
        bbefore=bdata(GridPoint,SpecPoint-1);
        bmiddle=bdata(GridPoint,SpecPoint);
        bafter=bdata(GridPoint,SpecPoint+1);
        if ((abs(fmiddle-fbefore)>SpikeThresh & abs(fafter-fmiddle)>SpikeThresh)&
        ((fbefore-fmiddle>0&fafter-fmiddle>0)|(fbefore-fmiddle<0&fafter-fmiddle<0)))
            %SpecPoint=SpecPoint
            %x(GridPoint)
            %middle=middle
            %change spike point to mean of adjacent points
            fdata(GridPoint,SpecPoint)=(fbefore+fafter)/2;
        else
    end
end

```

```

    end

    if ((abs(bmiddle-bbefore)>SpikeThresh & abs(bafter-bmiddle)>SpikeThresh)&
((bbefore-bmiddle>0&bafter-bmiddle>0)||((bbefore-bmiddle<0&bafter-bmiddle<0)))

        %SpecPoint=SpecPoint

        %x(GridPoint)

        %middle=middle

        %change spike point to mean of adjacent points

        bdata(GridPoint,SpecPoint)=(bbefore+bafter)/2;

    else

        end

    end

    end

    %plot graphs of data after spike removal

    figure(1)

    subplot(2,2,2)

    plot(fx,fdata(:, :))

    subplot(2,2,4)

    plot(bx,bdata(:, :))

    %calculate statistics matrix

    for SpecPoint=1:1:fnumber_of_SpecPoint;

        %      size_fdata=size(fdata)

        %      size_fmean=size(fmean)

        %      size_fstandard=size(fstandard)

        fstats(:,SpecPoint)=(abs(fdata(:,SpecPoint)-
fmean(1,SpecPoint)))./fstandard(1,SpecPoint);

        bstats(:,SpecPoint)=(abs(bdata(:,SpecPoint)-
bmean(1,SpecPoint)))./bstandard(1,SpecPoint);

    end

    for GridPoint=1:1:fnumber_of_GridPoint

        %'grid point='

        %SpecPoint=SpecPoint

        SpecPoint=StatisticalAnalysisStartPoint;

        while SpecPoint<=fnumber_of_SpecPoint

            if (fstats(GridPoint,SpecPoint)<StatsThreshold)

                if SpecPoint==fnumber_of_SpecPoint

                    %record the fact that this grid point has passed the statistical threshold test

                    %size(fcleaner_total)

                    %size(fdata)

```

```

%fdatal(GridPoint,SpecPoint,z)=fdatal(GridPoint,SpecPoint,z)
fcleaner_total(1,:,z)=fcleaner_total(1,:,z)+fdatal(GridPoint,:);
fBigData=[fBigData,fdatal(GridPoint,:)];
%add 1 to the total number of files used
fNumberCleanGridPoints(z)=fNumberCleanGridPoints(z)+1;
end

elseif (fstats(GridPoint,SpecPoint)>StatsThreshold)
    %record bad data grid point
    fBadDataSets(1,fdatal_sets_count)=GridPoint;
    fBadDataSets(2,fdatal_sets_count)=SpecPoint;
    fBadDataSets(3,fdatal_sets_count)=z;
    fdatal_sets_count=fdatal_sets_count+1;
    %exit the loop
    %GridPoint=GridPoint
    SpecPoint=fnumber_of_SpecPoint;
end
SpecPoint=SpecPoint+1;
end

SpecPoint=StatisticalAnalysisStartPoint;
while SpecPoint<=fnumber_of_SpecPoint;
    %fnumber_of_GridPoint=fnumber_of_GridPoint
    %[a,b]=size(bstats)
    %bstats
    %z=z
    %SpecPoint=SpecPoint
    %GridPoint=GridPoint
    %bstats(GridPoint,SpecPoint,z)=bstats(GridPoint,SpecPoint,z)
    if (bstats(GridPoint,SpecPoint)<StatsThreshold)
        if SpecPoint==fnumber_of_SpecPoint
            %record the fact that this grid point has passed the statistical threshold test
            bcleaner_total(1,:,z)=bcleaner_total(1,:,z)+bdata(GridPoint,:);
            bBigData=[bBigData,bdata(GridPoint,:)];
            %add 1 to the total number of files used
            bNumberCleanGridPoints(z)=bNumberCleanGridPoints(z)+1;
        end
    elseif (bstats(GridPoint,SpecPoint)>StatsThreshold);
        %record bad data grid point

```

```

bBadDataSets(1,bdata_sets_count)=GridPoint;
bBadDataSets(2,bdata_sets_count)=SpecPoint;
bBadDataSets(3,bdata_sets_count)=z;
bdata_sets_count=bdata_sets_count+1;
%exit the loop
%GridPoint=GridPoint
SpecPoint=fnumber_of_SpecPoint;
end
SpecPoint=SpecPoint+1;
end
end
%plot statistical data
figure(2)
subplot(1,2,1)
pcolor(fx,1:250,(((fstats(:,::)))), shading flat, colormap hot
colorbar;
subplot(1,2,2)
pcolor(bx,1:250,(((bstats(:,::)))), shading flat, colormap hot
figure(3)
subplot(1,2,1)
plot(fx,fstats(:,::))
subplot(1,2,2)
plot(bx,bstats(:,::))
zstr=num2str(z);
for SpecPoint=1:1:fnumber_of_SpecPoint

fCleanerMean(SpecPoint,z+1)=fcleaner_total(1,SpecPoint,z)/fNumberCleanGridPoints(
z);

bCleanerMean(SpecPoint,z+1)=bcleaner_total(1,SpecPoint,z)/bNumberCleanGridPoint
s(z);
end
end
%size(fNumberCleanGridPoints)
%size(fCleanerMean)
%fCleanerMean=cat(1,[(::)], [fCleanerMean]);
%size(fCleanerMean)
%Writing outputs to files

```

```

FirstFileString=num2str(firstfile); LastFileString=num2str(lastfile);
StatsThresholdString=num2str(StatsThreshold);
SpikeThreshString=num2str(SpikeThresh);
VariableString=strcat('Start=m',FirstFileString,'End=m',LastFileString,'StatsThreshold=',
StatsThresholdString,'SpikeThresh=',SpikeThreshString);
csvwrite(strcat('f0TotalCleanerMeans',VariableString,'.csv'),fCleanerMean)
csvwrite(strcat('f0#CleanGridPoints',VariableString,'.csv'),(fNumberCleanGridPoints))
csvwrite(strcat('b0TotalCleanerMeans',VariableString,'.csv'),bCleanerMean)
csvwrite(strcat('b0#CleanGridPoints',VariableString,'.csv'),(bNumberCleanGridPoints))
csvwrite(strcat('f0BadDataSets',VariableString,'.csv'),fBadDataSets)
csvwrite(strcat('b0BdDataSets',VariableString,'.csv'),bBadDataSets)
fStandardDeviation=std(fBigData,1)
bStandardDeviation=std(bBigData,1)
% csvwrite('f0StandardDeviation.csv',fStandardDeviation)
% csvwrite('b0StandardDeviation.csv',bStandardDeviation)
fCleanerMean(:,1)=[]; bCleanerMean(:,1)=[];
figure(4)
subplot(2,1,1)
plot(fx,fCleanerMean)
subplot(2,1,2)
plot(bx,bCleanerMean)
%display analysis information
fNumberCleanGridPoints=fNumberCleanGridPoints
bNumberCleanGridPoints=bNumberCleanGridPoints
%fBadDataSets=fBadDataSets
%bBadDataSets=bBadDataSets

```

File 1:

```

%ldstm data processing
%function biggerdatapro(FirstFname,lastfname)
FirstFile =19
LastFile =21
statsthreshold=4
SpikeThreshold=10
StatisticalAnalysisStartPoint=2
StartPointSpectroscopy=0.74999964
IncrementPointSpectroscopy=-0.0014954952

```

```

%load data
currentfile = FirstFile;
%load x coordinates from 1st 2 csv files
    % FirstFilestr=num2str(FirstFile,2);
    % csvfname=strcat('m',FirstFilestr,'_ori.sf1.csv');
    % data=csvread(csvfname,1,0);
for SpecPoint=1:1:1000
    fx(SpecPoint)=StartPointSpectroscopy+((SpecPoint-1)*IncrementPointSpectroscopy);
    %fxWithLabel=csvread(csvfname,0,0,[0,0,10000,0]);
    % csvfname=strcat('m',FirstFilestr,'_ori.sb1.csv');
    % data=csvread(csvfname,1,0);
bx(SpecPoint)=StartPointSpectroscopy+((SpecPoint-1)*IncrementPointSpectroscopy);
end
fnumber_of_files=LastFile-FirstFile+1;
bnumber_of_files=fnumber_of_files;
fdata_sets_count=1;
bdata_sets_count=1;
fBadDataSets=[];
bBadDataSets=[];
fNumberCleanGridPoints=zeros(1,fnumber_of_files);
bNumberCleanGridPoints=zeros(1,bnumber_of_files);
fcleaner_total=zeros(1,1000,fnumber_of_files);
bcleaner_total=zeros(1,1000,bnumber_of_files);
fCleanerMean=zeros(1000,fnumber_of_files+1);
fCleanerMean(:,1)=fx(:,1);
bCleanerMean=zeros(1000,bnumber_of_files+1);
bCleanerMean(:,1)=bx(:,1);
zstr_list=zeros(fnumber_of_files);
size_fcleaner_total=size(fcleaner_total)
size_fx=size(fx)
fBigData=[];
bBigData=[];
for z=1:1:(LastFile-First
FirstFile+1)
    currentfilestr=num2str(First
FirstFile+z-1);
    fname = strcat('m',currentfilestr,'_ori.sf1');

```

```

fid = fopen(ffname,'r','b');
fdata(:,:)= fread(fid,[250,1000],'int16');
bfname = strcat('m',currentfilestr,'_ori.sb1');
fid = fopen(bfname,'r','b');
bdata(:,:)= fread(fid,[250,1000],'int16');
LoadingFileNumber=currentfile
currentfile =currentfile+1;
%size_fdata=size(fdata)
%data=csvread(csvfname,0,0);
%bxlist=data(:,1);
%sizeofxdata=size(x)
%Convert to correct units
fdata = fdata * 10 / 32767;
bdata = bdata * 10 / 32767;
% csvwrite(strcat(ffname,'.csv'),fdata');
% csvwrite(strcat(bfname,'.csv'),bdata');
%fdata(1,:,1)
%calculate mean & standard deviation
fstandard = std(fdata,1);
%size_fstandard=size(fstandard)
fmean = mean(fdata);
bstandard = std(bdata,1);
bmean = mean(bdata);
%various size checks
%size(bstandard)
%Size_bmean=size(bmean)
[fnumber_of_GridPoint,fnumber_of_SpecPoint]=size(fdata);
[bnumber_of_GridPoint,bnumber_of_SpecPoint]=size(bdata);
%size(fdata)
%[bpoint,bspectrum]=size(bdata);
z=z
%plot graph of data before spike removal
figure(1)
subplot(2,2,1)
plot(fx,fdata(:,:))
subplot(2,2,3)
plot(bx,bdata(:,:))

```

```

%initialise the grid point counter
for GridPoint=1:1:fnumber_of_GridPoint
    for SpecPoint=2:1:(fnumber_of_SpecPoint-1)
        %logic to find spikes
        %GridPoint=GridPoint
        %SpecPoint=SpecPoint
        %z=z
        fbefore=fdata(GridPoint,SpecPoint-1);
        fmiddle=fdata(GridPoint,SpecPoint);
        fafter=fdata(GridPoint,SpecPoint+1);
        bbefore=bdata(GridPoint,SpecPoint-1);
        bmiddle=bdata(GridPoint,SpecPoint);
        bafter=bdata(GridPoint,SpecPoint+1);
        if ((abs(fmiddle-fbefore)>SpikeThreshold & abs(fafter-fmiddle)>SpikeThreshold)& ((fbefore-fmiddle>0&fafter-fmiddle>0)||((fbefore-fmiddle<0&fafter-fmiddle<0))))
            %SpecPoint=SpecPoint
            %x(GridPoint)
            %middle=middle
            %change spike point to mean of adjacent points
            fdata(GridPoint,SpecPoint)=(fbefore+fafter)/2;
        else
            end
        if ((abs(bmiddle-bbefore)>SpikeThreshold & abs(bafter-bmiddle)>SpikeThreshold)& ((bbefore-bmiddle>0&bafter-bmiddle>0)||((bbefore-bmiddle<0&bafter-bmiddle<0))))
            %SpecPoint=SpecPoint
            %x(GridPoint)
            %middle=middle
            %change spike point to mean of adjacent points
            bdata(GridPoint,SpecPoint)=(bbefore+bafter)/2;
        else
            end
        end
    end
    %plot graphs of data after spike removal
    figure(1)
    subplot(2,2,2)

```

```

plot(fx,fdata(:,::))
subplot(2,2,4)
plot(bx,bdata(:,::))

%calculate statistics matrix
for SpecPoint=1:1:fnumber_of_SpecPoint;
    fstats(:,SpecPoint)=(abs(fdata(:,SpecPoint)-
fmean(1,SpecPoint)))./fstandard(1,SpecPoint);
    bstats(:,SpecPoint)=(abs(bdata(:,SpecPoint)-
bmean(1,SpecPoint)))./bstandard(1,SpecPoint);
end

for GridPoint=1:1:fnumber_of_GridPoint
    %'grid point='
    %SpecPoint=SpecPoint
    SpecPoint=StatisticalAnalysisStartPoint;
    while SpecPoint<=fnumber_of_SpecPoint
        if (fstats(GridPoint,SpecPoint)<statsthreshold)
            if SpecPoint==fnumber_of_SpecPoint
                %record the fact that this grid point has passed the threshold test
                %size(fcleaner_total)
                %size(fdata)
                %fdata(GridPoint,SpecPoint,z)=fdata(GridPoint,SpecPoint,z)
                fcleaner_total(1,::,z)=fcleaner_total(1,::,z)+fdata(GridPoint,:);
                fBigData=[fBigData,fdata(GridPoint,:)];
                %add 1 to the total number of files used
                fNumberCleanGridPoints(z)=fNumberCleanGridPoints(z)+1;
            end
        elseif (fstats(GridPoint,SpecPoint)>statsthreshold)
            %record bad data grid point
            fBadDataSets(1,fdata_sets_count)=GridPoint;
            fBadDataSets(2,fdata_sets_count)=SpecPoint;
            fBadDataSets(3,fdata_sets_count)=z;
            fdata_sets_count=fdata_sets_count+1;
            %exit the loop
            %GridPoint=GridPoint
            SpecPoint=fnumber_of_SpecPoint;
        end
        SpecPoint=SpecPoint+1;
    end
end

```

```

end

SpecPoint=StatisticalAnalysisStartPoint;
while SpecPoint<=bnumber_of_SpecPoint;
    %fnumber_of_GridPoint=fnumber_of_GridPoint
    %[a,b]=size(bstats)

    %bstats

    %z=z

    %SpecPoint=SpecPoint
    %GridPoint=GridPoint
    %bstats(GridPoint,SpecPoint,z)=bstats(GridPoint,SpecPoint,z)
    if (bstats(GridPoint,SpecPoint)<statsthreshold)
        if SpecPoint==fnumber_of_SpecPoint
            %record the fact that this grid point has passed the threshold test
            bcleaner_total(1,:,z)=bcleaner_total(1,:,z)+bdata(GridPoint,:);
            bBigData=[bBigData,bdata(GridPoint,:)];
            %add 1 to the total number of files used
            bNumberCleanGridPoints(z)=bNumberCleanGridPoints(z)+1;
        end
    elseif (bstats(GridPoint,SpecPoint)>statsthreshold);
        %record bad data grid point
        bBadDataSets(1,bdata_sets_count)=GridPoint;
        bBadDataSets(2,bdata_sets_count)=SpecPoint;
        bBadDataSets(3,bdata_sets_count)=z;
        bdata_sets_count=bdata_sets_count+1;
        %exit the loop
        %GridPoint=GridPoint
        SpecPoint=fnumber_of_SpecPoint;
    end
    SpecPoint=SpecPoint+1;
end
end

%plot statistical data
figure(2)
subplot(1,2,1)
pcolor(fx,1:250,((fstats(:,::))), shading flat, colormap hot
colorbar;
subplot(1,2,2)

```

```

pcolor(bx,1:250,(((bstats(:,::)))), shading flat, colormap hot
figure(3)
subplot(1,2,1)
plot(fx,fstats(:,::))
subplot(1,2,2)
plot(bx,bstats(:,::))
for SpecPoint=1:1:fnumber_of_SpecPoint

fCleanerMean(SpecPoint,z+1)=fcleaner_total(1,SpecPoint,z)/fNumberCleanGridPoints(z);

bCleanerMean(SpecPoint,z+1)=bcleaner_total(1,SpecPoint,z)/bNumberCleanGridPoint
s(z);
end
end
% size _fBigData=size(fBigData)
fStandardDeviation=std(fBigData,1)
bStandardDeviation=std(bBigData,1)
%size(fNumberCleanGridPoints)
%size(fCleanerMean)
%fcleanerMean=cat(1,[(::)],fCleanerMean);
%size(fCleanerMean)
%Writing outputs to files
FirstFileString=num2str(FirstFile); LastFileString=num2str>LastFile);
StatsThreshString=num2str(StatsThreshold);
SpikeThreshString=num2str(SpikeThreshold);
VariableString=strcat('Start=m',FirstFileString,'End=m',LastFileString,'StatsThresh=',Sta
tsThreshString,'SpikeThresh=',SpikeThreshString);
csvwrite(strcat('f1TotalCleanerMeans',VariableString,'.csv'),fCleanerMean)
csvwrite(strcat('f1#CleanGridPoints',VariableString,'.csv'),(fNumberCleanGridPoints))
csvwrite(strcat('b1TotalCleanerMeans',VariableString,'.csv'),bCleanerMean)
csvwrite(strcat('b1#CleanGridPoints',VariableString,'.csv'),(bNumberCleanGridPoints))
csvwrite(strcat('f1BadDataSets',VariableString,'.csv'),fBadDataSets)
csvwrite(strcat('b1BadDataSets',VariableString,'.csv'),bBadDataSets)

fCleanerMean(:,1)=[]; bCleanerMean(:,1)=[];
figure(4)
subplot(2,1,1)
plot(fx,fCleanerMean)

```

```
subplot(2,1,2)
plot(bx,bCleanerMean)
%display analysis information
fNumberCleanGridPoints=fNumberCleanGridPoints
bNumberCleanGridPoints=bNumberCleanGridPoints
%fBadDataSets=fBadDataSets
%bBadDataSets=bBadDataSets
```